Technische Universität München
Lehrstuhl für Carbon Composites

Matrix dominated effects of defects on the mechanical properties of wind turbine blades

Andreas Peter Josef Altmann

Vollständiger Abdruck der von der Fakultät für Maschinenwesen
der Technischen Universität München zur Erlangung des akademischen Grades eines

Doktor-Ingenieurs

genehmigten Dissertation.

Vorsitzender: Univ.-Prof. Dr. med. Dr.-Ing. habil. Erich Wintermantel

Prüfer der Dissertation:

1. Univ.-Prof. Dr.-Ing. Klaus Drechsler
2. Univ.-Prof. Dr.-Ing. Horst Baier

Die Dissertation wurde am 27.11.2014 bei der Technischen Universität München eingereicht und durch die Fakultät für Maschinenwesen am 04.05.2015 angenommen.

Technische Universität München
Fakultät für Maschinenwesen
Lehrstuhl für Carbon Composites
Boltzmannstraße 15
D-85748 Garching bei München

Tel.: +49 (0) 89 / 289 – 15092
Fax.: +49 (0) 89 / 289 – 15097
Email: info@lcc.mw.tum.de
Web: www.lcc.mw.tum.de

ACKNOWLEDGMENT

My sincere thank goes to Prof. Dr.-Ing. Klaus Drechsler who supervised this thesis and has spent several hours of discussion to give valuable suggestions. I gratefully acknowledgement Prof. Dr.-Ing. Horst Baier for serving as second advisor and for his time and interest to review the thesis. A thank goes to Dr. Roland Hinterhölzl for numerous organizational and technical discussions and for counterchecking and correcting this thesis.

My special thank goes to Prof. Dr. Ramesh Talreja for his acknowledge and time during my two-month stay at Texas A&M University, College Station, TX, USA.

I thank my colleagues for very valuable discussions und their great support! Robin, Uli, Marina, Peter, Ben, Clemens, Swen, Max S., Daniel T., Reinhold, Roland L. and David. A special thank to my friend and former classmate Stephan. Thank you! I also would like to thank Elisabeth, Çiğdem, Mrs. Uruk, Michi R. and Thomas W. for your support during the daily business.

The research was conducted at the Institute for Carbon Composites, Faculty of Mechanical Engineering, Technische Universität München, Germany and was financially supported by BASF AG, Ludwigshafen, Germany. I gratefully thank the members of the business units of BASF AG "Advanced Materials & Systems Research" and "Epoxy Systems" Dr. René Arbter, Dr. Holger Ruckdaeschel, Dr. Archim Besser, Andreas Wüst and Dr. Gregor Daun for their encouragement, cooperation and their valuable input during our monthly project meetings. I also had excellent technical discussions with Mr. Thomas Merzhäuser from GE Global Research. Thank you, Thomas!

During my work at the Institute, I have supervised several student theses. I am grateful to thank all of my supervised students for their efforts and technical support: Lukas, Blaise, Pascal, Marcel, Mario, Jonathan, Herbert, Max, Nina, Daniel, Simon, Markus, Ricarda, Phillip, Marc, Larissa, Christian, David, Philipp, Arturo, Florian and Stefan. Thank you!

On a more personal note I would like to thank my family Ingrid, Peter and Susanne, my lovely girlfriend Rebecca and my friends for never letting me doubt myself and for reminding me that there is a whole world outside of my PhD.

ABSTRACT

Nowadays, wind energy rotor blades exceed the length of 70 meters. Composite materials offer enormous savings compared to metallic material due to lower weight and excellent mechanical properties. The manufacturing of wind turbine blades is subjected to extraordinary demands for low costs of production. It is not extraordinary that both, structural penalties in the selection of material are made, and fabrication inaccuracies are tolerated to keep production costs low.

Besides the interaction between design concepts and manufacturing technologies, material systems that are especially tailored to the structural requirements of a wind turbine blade (WTB) are inheriting more and more important roles in the development process of innovative rotor blades. Using the numerical model outlined in this thesis, matrix dominated effects on the structural performance are highlighted. The sensitivity analyses and parametric studies show that the composite materials of blades derive much of their structural performance from the fiber reinforcement. However, several key properties are dominated by the matrix systems such as the strength property (R_{11}^{-}, R_{22}^{+}), whereas the stiffness and stability properties are slightly affected.

After studying the influence of the matrix system on the global structure, the matrix dominated effects on a local level taking fabrication effects such as ply waviness are reviewed. Ply waviness poses a commonly occurring fabrication defect of rotor blades at which the strength behavior of the composite is essentially influenced by the matrix systems and their properties. The present work engages in a phenomenological understanding of the structural mechanical influence of ply waviness with a particular emphasis on the effects of matrix systems. The behavior of stiffness and strength parameters are determined analytically and numerically. Utilizing these findings, a wavy specimen`s geometry is derived. A convenient fabrication method is developed and installed to fabricate specimens containing artificially induced waviness in reproducible quality. Numerical simulations validated by experiments show that the failure mechanisms for compression and tensile loads are both driven by the matrix properties. Especially, the nonlinear shear behavior of the matrix strongly influences the failure mechanisms.

The outcomes presented here provide a valuable exposure to the development of matrix systems that are damage tolerant to common fabrication defects. The trade-off between a cost-efficient material selection and sufficient structural properties tenders an individual infusion of the subcomponents *spar caps* and the *aerodynamic shells* using two different matrix systems that are adapted to the structural and manufacturing needs.

Tags: Composites, structural analysis, matrix systems, ply waviness, manufacturing defects

ÜBERSICHT

Rotorblätter von Windkraftanlagen überschreiten heutzutage Blattlängen von 70 Metern. Faserverbundwerkstoffe bieten dabei enorme Gewichtsvorteile mit exzellenten mechanischen Eigenschaften gegenüber metallischen Konstruktionswerkstoffen. Die Herstellung von Rotorblättern unterliegt dabei einem enormen Kostendruck. Daher werden gewöhnlich sowohl strukturelle Einschränkungen in der Materialauswahl sowie Fertigungsintoleranzen in Kauf genommen, um die Produktionskosten gering zu halten.

Neben dem Zusammenspiel aus Bauteilauslegung und Produktionsverfahren nehmen Materialsysteme, die speziell den strukturellen Anforderungen von Rotorblättern angeglichen sind, eine immer wichtigere Rolle im Entwicklungsprozess innovativer Rotorblätter ein. Die Einflüsse von Harzsystemen auf das Strukturverhalten der Blattstruktur werden anhand des in der Arbeit entwickelten numerischen Models diskutiert. Es wird gezeigt, dass die mechanischen Eigenschaften der Harzsysteme einen großen Einfluss auf das Festigkeitsverhalten der Struktur haben, während das Steifigkeits- und Stabilitätsverhalten der Struktur nur geringfügig von den Harzeigenschaften beeinflusst werden.

Neben Untersuchungen auf Strukturebene werden die mechanischen Auswirkungen von Harzsystemen auf lokaler Ebene betrachtet. Faserwelligkeiten stellen dabei einen häufig auftretenden Fertigungsdefekt dar, wobei das Festigkeitsverhalten wesentlich von den Harzsystemen und deren Eigenschaften bestimmt wird. In der vorliegende Arbeit werden phänomenologischen Untersuchungen an welligen Laminaten hinsichtlich deren Steifigkeits- und Festigkeitsverhaltens angestellt. Das Hauptaugenmerk liegt diesbezüglich auf der Einflussnahme der Harzsysteme. Dazu werden analytische und numerische Verfahren entwickelt und vorgestellt. Es wird eine Methode beschrieben, womit Coupons mit gezielt eingebrachten Faserwelligkeit reproduzierbar hergestellt werden können. Numerische Modelle, die mit Experimenten abgeglichen sind, zeigen, dass die Versagensmechanismen sowohl bei Druck- als auch Zugbeanspruchung von den Harzeigenschaften dominiert werden. Speziell das nichtlineare Schubverhalten des Harzes beeinflusst die Versagensmechanismen stark.

Die hier dargestellten Ergebnisse geben Aufschluss zur Entwicklung neuer Harzsystemen, die möglichst schadenstolerant gegenüber gängigen Fertigungsdefekte sind. Der gegenwärtige Kompromiss zwischen kosteneffizienter Materialauswahl und ausreichendender Struktureigenschaften offeriert, die Bauteilkomponenten *Gurt* und *Blattschale* mit unterschiedlichen Harzsystemen, deren Eigenschaften auf die Bedürfnisse der jeweiligen Komponenten zugeschnitten sind, zu infiltrieren.

Stichworte: Faserverbundwerkstoffe, Strukturanalyse, Matrixsystem, Faserwelligkeiten, Bewertung von Fertigungsmerkmalen

Contents

Glossary

Symbol	Unit	Short term
$\boldsymbol{A}$	-	Extensional stiffness matrix
$\boldsymbol{B}$	-	Bending-extension coupling stiffness matrix
c_d	-	Drag coefficient
c_l	-	Lift coefficient
c_m	-	Torsional coefficient
$\boldsymbol{D}$	-	Bending stiffness matrix
E_{11}	MPa	Longitudinal Young Modulus
E_{22}	MPa	Transversal Young Modulus
E_{33}	MPa	Young modulus in out-of-plane direction
f	-	Stress exposure
f_y	N/mm	Line loads (y-values) transformed into blade coord. system
$f_{y,i}^{FE}$	N/mm	Line loads (y-values) at the relevant distance
f_z	N/mm	Line loads (z-values) transformed into blade coord. system
G_{ij}	MPa	Shear Modulus in ij plane
g	m/s²	Gravity (9.81)
l_{chord}	mm	Chord length of profile
M_b	Nmm	Simplified bending moment
M_{bz}	Nmm	Flapwise (y) bending moment
M_{by}	Nmm	Edgewise (z) bending moment
M_t	Nmm	Torsional moment
M_x	Nmm	Torsional (x) moment
$M_{x,i}^{FE}$	Nmm	Torsional moment at the relevant distance
m	Nm/m	Aerodynamic moment coefficient

Q_x	N	Shear force
r_i	mm	Distance between cross-section and rotational axis
R_{11}^+	MPa	Longitudinal tensile strength
R_{11}^-	MPa	Longitudinal compressive strength
R_{22}^+	MPa	Transverse tensile strength
R_{22}^-	MPa	Transverse compressive strength
R_{12}^s	MPa	Longitudinal shear strength
R_{13}^s	MPa	Transverse shear strength
RF	-	Reserve factor
t	s	Time
v_{eff}	m/s	Effective wind speed
v_{tip}	m/s	Wind speed at tip of the blade
v_u	m/s	Peripheral speed
v_w	m/s	Wind speed
x	m	Distance

Greek letters

α	°	Angle of attack
β	°	Sum of angles
ε_{ij}		Strain
θ'		Curvature
δ	°	Pitch angle
ϱ_{air}	kg/m³	Density of the air ($\varrho = 1.20\ \frac{kg}{m^3}\ at\ T = 20°C$)
σ_{ij}		Stress
ν_{ij}[1]	-	Poisson`s ratio in ij-plane

[1] Cf. to ν_{ij} (VDI 2014): The first index indicates the direction of the transverse contraction. The second index denotes the stress, which causes the contraction.

υ	°	Twist angle
φ	°	Torsion angle
ω	r/s	Rounds per seconds

List of Abbreviations

ATL	Automated tape laying process
BSF	Buckling safety factor
CAD	Computer aided design
CAI	Compression after impact
CFD	Computational fluid dynamics
CFRP	Carbon fiber reinforced plastics
CS	Cross section(s)
CLT	Classical laminate theory
CME	Coefficient of moisture expansion
CoE	Cost of energy
CT	Computer tomography
CTE	Coefficient of thermal expansion
CoE	Costs of energy
DCB	Double cantilever beam
DIC	Digital image correlation
DoE	Design of Experiments
DS	Dassault Systèmes
ENF	End notched flexure
GFRP	Glass fiber reinforced plastics
FE	Finite element(s)
FF	Fiber failure
FEM	Finite element method
FPF	First ply failure
FVC	Fiber volume content
GL	German Lloyd
GUI	Graphical user interface
HM	Hypermesh
IEC	Electro-technical Commission
IFF	Inter-fiber failure

ILTS	Interlaminar tensile stresses
ILSS	Interlaminar shear stresses
IP	In-plane waviness
LPF	Last ply failure
MD	Multidirectional
MPC	Multiple point constraints
MCT	Multi-continuum theory
NDI	Non-destructive inspection
NREL	National Renewable Energy Laboratory
OP	Out-of-plane waviness
PEEK	Polyetheretherketone
PET	Polyethylenterephthalat
PID	Process induced deformations
PP	Polypropylene
PPS	Polyphenylensulfid
PW	Ply waviness
RSA	Response surface approximation
RoM	Rule of Mixture
UD	Unidirectional
SDV	Solution-dependent variables
RIFT	Resin infusion under flexible tooling
RFI	Resin film infusion
RVE	Representative volume element
Scrimp	Seaman composites resin infusion molding process
VAP®	Vacuum-assisted process®
VARTM	Vacuum-assisted resin transfer molding
WTB	Wind turbine blade
WPP	Wind power plants

List of Figures

List of Tables

1. Introduction

"Wind and solar have gone from green dreams to economic realities", according to [1]. Nowadays, modern wind energy plants essentially contribute an economic and environmental supply to a sustainable and CO_2 neutral energy policy. Thus, it is essential to enhance current technologies constantly and focus research on new technologies.

Current blade structures form one of the largest structures made of composite materials. "Knowledge of operation conditions and requirements of the embedded materials are essential for new innovations and developments. Thus, suitable simulation tools play a central role in the analysis and design process of composite structures. The evaluation of rotor blades on a virtual platform allows a cost-efficient and rapid examination and validation of new material systems." [2]

Brief background information of wind energy related to composite materials is given to classify the context of the present thesis. This is followed by the motivation and cause of the thesis. In chap.1.3, the scope and the modus operandi are defined.

1.1. Background

As a consequence of the global climate warming`s discussions in the 21st century, renewable energies are one attempt to counteract the current climate changes. Consequently, an increasing number of state governments[2] are starting to constitute laws and publish letters of intent to reduce CO_2 emissions worldwide. Key technologies, such as wind energy especially, are being used to achieve the issued and ambitious goals. In recent years, there have been great technical efforts to enhance available technologies with the fundamental goal to produce energy more efficiently. Wind power plants (WPP) are subjected to an extraordinary demand for cost efficiency and are still increasing in dimensions. To economically produce wind energy in weak wind areas[3] plants with blade lengths of at least 60 meters are essential.

Fig. 1.1: Wind energy plant (5MW) [112]

The challenges of blade manufacturers include the need to increase the dimensions of blade length and increase productivity in order to attain an ultimate goal: the

[2] Key markets in 2014/2015: China, Brazil, India and Russia
[3] Regions prevailing average wind speeds less than 2 m/s at ground level; e.g. Bayern and Baden-Württemberg

reduction of costs of energy[4] (CoE). Besides new developments in tower architectures, gearboxes, grid connections and generators, the research of this thesis concentrates on potentials and challenges in wind turbine blades (WTB) and the behavior of its composite materials. WTBs are mainly manufactured from long fiber reinforced plastic materials.

There are current innovations in recent material systems, new design concepts, and advanced process technologies of composite materials. Composite materials offer enormous savings due to a lower weight along with excellent mechanical properties, such as stiffness, strength and fatigue behavior. Especially with WTB applications, composite materials have to be cost-efficient, easy to handle and easy to manufacture. Generally, composite materials consist of two constituents such as the fiber and the matrix system. Conventional blades are comprised of sandwich structures.

This thesis will work on the evaluation of recent material systems using a finite element (FE) model based on a composite blade structure. Both the use of different fiber materials in the form of glass fiber reinforced plastics (GFRP), carbon fiber reinforced plastics (CFRP) and the use of diverse core materials in the sandwich structures are discussed with a particular focus put on matrix systems.

1.2. Motivation of the thesis

In 1983, the project GROWIAN[5] revealed that the design and structure of the blade has to be customized to the used materials. In contrary to a smooth and continuous development process at that time, the blade length has been increased erratically in accordance with previously developed plants. Simultaneously, metallic alloys were still used for the blade structure. The material was not able to fulfill the mechanical requirements[6] and thus, the blade structure failed.

The effects of matrix properties within the composite material on the structural performance of a conventional and state-of-the-art WTB haven't been examined extensively. During a common industrial design process, manufacturers revert to well-tried and commonly used matrix systems. This thesis attempts to tune the matrix properties to the ideal structural performance of the composite structure. (reverse material selection) Further, the aim of the thesis is to understand the effects that possible improvements of the matrix systems offer in different aspects of the overall mechanical behavior. The conclusions drawn are intended to be used as a guideline to refocus the material development towards the most promising matrix systems identified.

Because current manufacturing techniques are dominated by manual labor, many defects will commonly occur. Ply waviness is one dominant defect. Taking a distinct look at the matrix

[4] Approx. CoE: Onshore 8 cents/kWh, offshore 13 cents/kWh. (Europe)
[5] GROWIAN: BMFT project in the years between 1977-1983.
[6] It has been demonstrated that rotor blade of metals longer than 25m are critical due to a comparison of S/N curves between metal alloys and GFRP/CFRP.

systems, ply waviness has a substantial influence on the mechanical properties of the WTB. In particular, the ply waviness in the load carrying spar caps is studied. “Less research related to these and other structural details has been performed for WTB materials. Further, it must be noted that much of this research has been performed for industries where manufacturing is on a smaller scale where expense is less critical.” [3] Studying the effects of matrix systems on ply waviness serves to comprehend the matrix`s behavior in detail. Hence, this awareness can be used to assimilate the matrix properties during the material development process.

Retrospective to GROWIAN, the focus is on the analysis and advancements of matrix materials based on a conventional WTB in order to derive future trends rather than - as pursued in GROWIAN - the development of WTBs by convenient materials. The output of the thesis contributes to the improvement of the reliability of a WTB`s matrix systems. While the design process described herein is applied to a blade structure, the framework is also applicable to the evaluation of any composite structure.

1.3. Outline of the thesis

Contemporary trends in the development of rotor blades are given in chap.2. Besides basic knowledge of wind energy plants (WEP), recent material systems, design concepts and manufacturing processes are also described. A catalog of requirements is generated and supplemented by recent findings. In this framework, it is important to allude that the blade design strongly interacts with the manufacturing process and the material properties.

Chap.3 describes the analysis and design process of the WTB conducted within this work. After boundary conditions of a virtual facility have been determined, the geometry and the loads are defined. The composite layup is determined (Fig. 1.2). Further, the FE-based modeling of a conventional wind turbine blade is described. This includes the computer-aided design modeling (CAD), the FE-modeling, and the load implementation. The numerical model and its assumptions are evaluated and checked by the German Lloyd (GL) to ensure the correctness of the prevailing assumptions.

On the basis of the numerical model, sensitivity analyses and parametric studies (chap.4) are conducted in order to highlight the matrix dominated effects on the structural performance of the blade structure. Therefore, a detailed evaluation and interpretation of the stiffness, strength and stability properties of the structure are conducted. In chap.4.3, the usage of low-cost CFRP is debated using two FE-based case studies.

While the previous context of this work considers the influence of matrix systems on a component level (macroscopic level) observing the structural response of a blade structure, the subsequent chap.5 deals with the effects of matrix systems on a local level taking fabrication effects such as ply waviness into consideration. These effects may also yield to global effects.

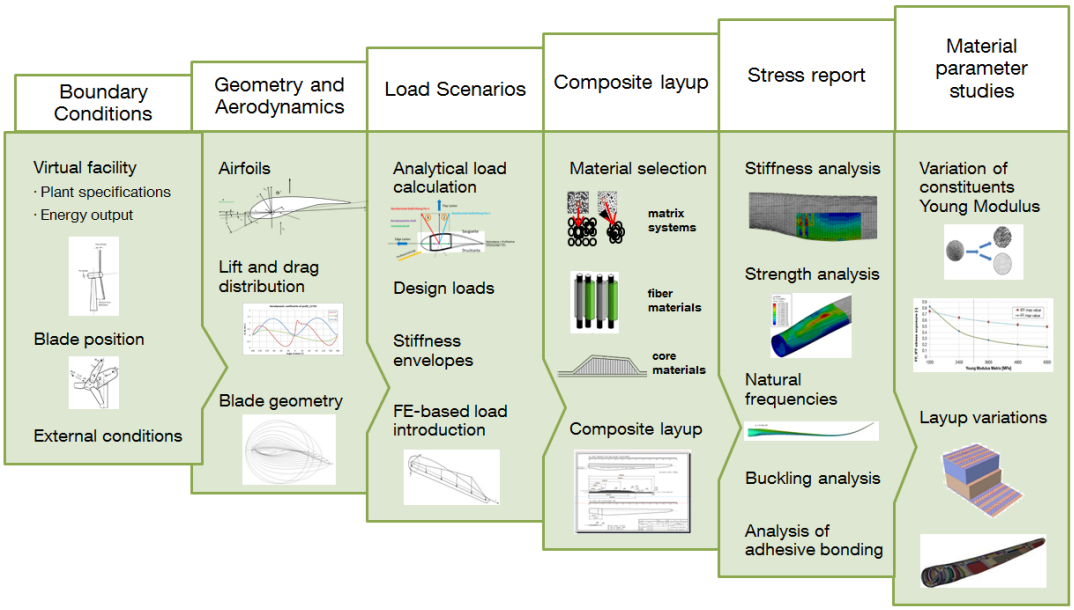

Fig. 1.2: Modus Operandi

Ply waviness[7] (PW) is a commonly observed fabrication defect in composite parts. Ply waviness is known as a wave-formed ply and/or fiber deviation from a straight alignment in a unidirectional laminate. A decrease in the material performance (stiffness, strength and fatigue properties) is expected. Both, the fiber architecture and the material affect the mechanical properties. A literature review is conducted focusing on the occurrence of ply waviness in WTBs (chap.5.1.1) and its characteristics (chap.5.1.2). The failure mechanisms under compression and tensile loads are described in chap.5.1.3.

An analytical approach derived from [4] and enhanced by a PUCK failure criterion is implemented within a GUI that enables a quick and quantitative tool to evaluate ply waviness. (chap.5.2.1) The failure mechanisms occurring in wavy composites are studied in detail using a numerical model enhanced by a material user subroutine containing a continuum damage model (chap.5.2.2). Both, the analytical and the numerical model are developed in order to assess the composite material`s stiffness and strength behavior for given geometrical shape and on the material data of ply waviness. A particular emphasis is on the matrix relevant (dominated) properties of the laminate.

Utilizing previous findings, a wavy specimen`s geometry is derived. (chap.5.3.1) A convenient fabrication method (chap.5.3.2) is developed and installed to fabricate specimens containing artificially induced waviness in reproducible quality. Experiments (chap.5.4.1) of compression and tensile tests are carried out for specimens of neat resin, planar specimens and wavy specimens. Results of tests are discussed and validated against numerical results. Finally, these observations are taken to evaluate the stiffness and strength behavior of a wavy spar cap section in chap.5.6. A conclusion and an outlook are given in chap.6 and chap.7 respectively.

[7] Alternative terms: marcel, fiber waviness, fiber wrinkle, undulation

2. State of the art: Trends in the development of rotor blades

The blade lengths of recent WTBs are increased continuously to reduce the CoE. Cost-efficient material systems, design concepts and manufacturing technologies are continuously enhanced. This chapter gives an excerpt of past developments. Shifting requirements in the field of the development environment of WTBs are opening up novel development strategies. Essential boundary conditions are:

- Decreasing market prices of matrix, fiber and core materials
- Enhanced mechanical properties of low-cost composite materials; substitution of GFRP through CFRP
- High demand of WTBs leads to raising demand of automatization
- High demand of robust manufacturing processes
- Exploitation of new manufacturing strategies
  - On-site manufacturing: flexible plant
  - Modular blade designs [5] [6]
- Introduction of quality assessment systems

The composition of these boundary conditions may show the influence on current trends. E.g., new manufacturing technologies, which may dramatically raise the grade of automatization, are accompanied by designs that actually have to be replaced. Defects are mainly caused by hand-lamination. Alternatively, e.g. the high demand of GFRP has been accounting for very low material prices, which in turn exacerbate the use of CFRP.

A brief summary of the basic knowledge of wind energy plants is given. It is pointed out to the reader that a precise research of the further discussed composites structure – the rotor blades – can only be conducted with a preexisting and comprehensive understanding of the global system. Thus, important topics related to the main research fields are highlighted. The significance of composite materials for WTB applications is carved out.

WIND ENERGY: PRODUCTION OF ENERGY

A wind energy plant (WEP) is prompted by the energy that can be extracted from the current wind conditions. Modern sites usually start the production of energy at a defined wind speed (cut-in speed). When reaching a maximum wind speed (cut-out speed), the production of energy is stopped by pitching the blade profiles out of the wind or stopping the rotation through a mechanical brake. (Fig. 3.2) This is conducted to avoid any overloading that may damage the structure. Typically, a wind plant operates between wind speeds of about 5m/s – 25m/s.[8] Ideally, every wind plant is individually designed for wind conditions and distributions that are most common at a defined site. The analysis and design process of the

[8] The cut-in and cut-out speed is accounted for the FE-model introduced in chap. 3.1.

blade structure is strongly reliant on the relative occurrence of wind speed. Test measurements monitor both the probability and the turbulence factor of the present wind conditions. A site with generally constant wind conditions would be more eligible than a site possessing temporarily high wind speed of low diffusion. Fig. 2.1 illustrates a representative curve of the relative distribution of the prevailing wind speed at a defined site that has its maximum at about 7 m/s. Further, the electrical output power is plotted over the actual wind speed. It can be distinguished between pitch and stall regulated plants. Typically, multi-megawatt (MW) plants reach their maximum power output at about 12 m/s. Pitch regulated systems adjust the angle of attack of the rotor blade to the current wind conditions. The objective is to design plants in a manner that a maximum energy output can be achieved over a preferably large sector of different wind speeds. Fig. 2.1 shows a constant energy output in the range of wind speeds between 13m/s to 25m/s. According to BETZ [7], it is not possible to transfer the total energy of the wind into mechanical energy. The maximum value is 0.595. It is an aerodynamic efficiency constant. (Fig. 2.2)

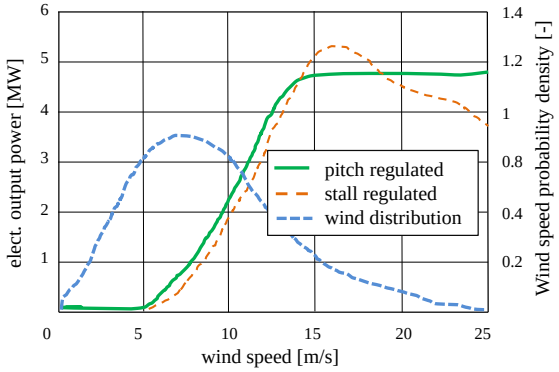

Fig. 2.1: Electrical output power vs. wind speed [8]

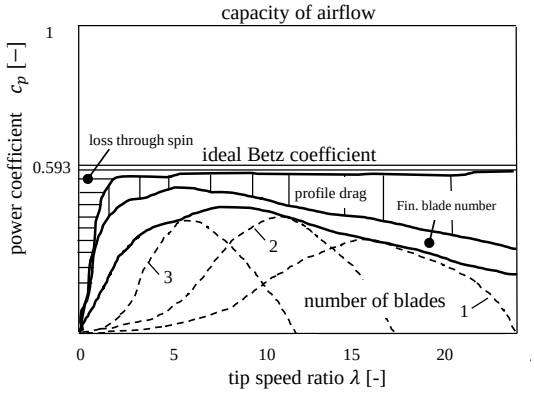

Fig. 2.2: Power coefficient vs. tip speed ratio [8]

Equ. (2.1) indicates the relationship between the electrical power output, the air density, the diameter of the rotor and the wind speed. The energy output depends linearly on the radius and cubically on the wind speed. It can be seen that a doubled wind speed could octuplicate the energy output. Nevertheless, a conventional plant reaches its maximum energy output at 13m/s - 16 m/s by pitching the blades. (Fig. 2.1) As a reference point it is stated that the "rated wind speed should be about a factor of 1.5 greater than the site mean wind speed." [8, p. 157]

$$P = \frac{1}{2} \cdot \dot{m} \cdot v_0^2 \cdot c_p = \frac{1}{2} \cdot \varrho_l \cdot A_{rotor} \cdot v_0^3 \cdot \ c_p = \ c_p \cdot \frac{\pi}{8} \cdot \varrho_L \ \cdot D \ \cdot v^3 \qquad (2.1)$$

ρ: Density

$\dot{m} = \ \varrho \cdot A_{rotor} \cdot v_0$: Flow stream of air

$A_{rotor} = \ R^2 \cdot \pi$: Circular area of rotor

P: Power

c_p: Coefficient of Betz

There is an upcoming discussion about the quantity of blades mounted on a wind site. In general, both configurations of two blades and three blades on a site can extract a comparable amount of energy out of the wind. (Fig. 2.2, right) Indubitably, two blades are cheaper than three blades. The rotational frequency (rpm) of a two-blade design must be higher to retain the same energy output. This affects a lower torque at the main shaft. Unfortunately, the aerodynamic noise (high tip speed) is greater than a three blade design. Another disadvantage of two blade designs is "the cyclic aerodynamic loads on the main shaft due to wind shear and especially yaw motion." [9] In contrast with that, a three-blade design is "gyroscopically balanced and gives a better visual comfort." [9]

Continuative literature concerning a comprehensive understanding of the functionalities of a WTP and the coaction of the components can be studied in the customary works of GASCH, HAU, JAMIESON, GOLFMAN and MANWELL. [10, 11, 12, 13, 8]

LONGER BLADES

According to GOLFMAN [12, p. 8], costs of rotor blades are about 20-30% of total costs of an energy plant. JAMIESON [8, p. 155] portions the blade costs to be about 17% of total costs. The information varies because different assumptions of recent material prices, technology standards, etc. are likely made. According to [8, p. 59], "the rotor blade capital value may be about 1/10th of lifetime cost on land based sites and less offshore. Thus, each percentage of energy captured is at least ten times more valuable than one percent of the cost of a blade and any trade-off in aerodynamic efficiency for structural comfort must be very carefully considered." Tab. 2.1 shows the relative cost portions of WTP components. It is outlined that the blades belong to the most costly components of a WEP.

Tab. 2.1: Relative cost portions of WTB components [8, p. 155]

Component	Portion	Component	Portion
Blades (3)	**0.177**	Tower	0.219
Hub	0.077	Variable speed system	0.073
Gearbox	0.143	Pitch system	0.043
Generator	0.076	Rotor brake	0.006
Yaw system	0.019	Couplings	0.003
Nacelle cover	0.020	Shaft	0.041
Nacelle structure	0.040	Others	0.063
		Total turbine	1.000

So why is longer blade length sought after? According to (2.1), a ten percent increase of the wind speed causes a 33% increase in electrical energy output. Because the wind speed cannot be influenced, the aim is to increase the blade length to a maximum. Throughout this enterprise, the break-even point of the economic feasibility study has to be found. The particular blade design has to be attuned to both the plant and environmental conditions.

At present, the major arguments for designing longer blades are summarized:

- Enhanced energy output
- Attracting weak wind areas
- Repowering[9]
- Reducing noise emissions

Fig. 2.3 [12, p. 56] shows the blade weight as a function of the corresponding blade length. The blade mass is dependent on the material selection, the design, the composite layup, the manufacturing technology, and the accuracy of the processes. The parabolic trend line can be imitated by an exponent of approximately 2.65. It is obvious that "the largest blades are the more recent and at a more advanced stage of manufacturing technology." [8, p. 87]

Longer blades induce greater bending moments, which are detrimental for the strength behavior and fatigue strength. Otherwise, longer blades lead to a reduced number of rotations during operation life. The reason for limiting the maximum wind speed at the blade tip (v_{max}= 80 m/s) is that the acoustic emission easily exceeds the threshold value on the landline. Acoustic emission incurs with the third exponent regarding the wind speed. Otherwise, this means that the maximum number of fatigue loadings may be reduced from $2 \cdot 10^9$ to 10^9. [14] Offshore plants are unaffected by acoustical considerations.

In 2014, the world`s largest rotor blades are from Samsung with a diameter of 170 meters, Vestas with 164 meters, and Siemens with 154 meters. A schematic sketch is shown in Fig. 2.4 [15] to categorize current dimensions of wind energy plants.

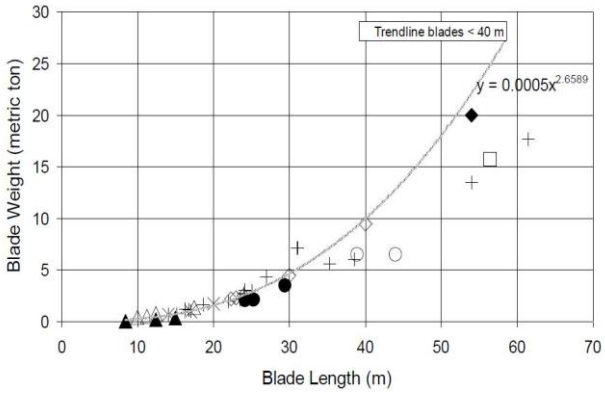

Fig. 2.3: Blade weight vs. blade length [12]

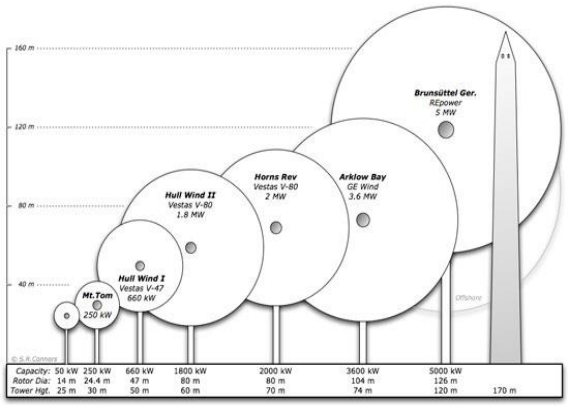

Fig. 2.4: Growing dimensions of WTBs [15]

Common approaches to increase the distance between the blade tip and the tower during the operation are to cone the rotor or to design the blade with a pre-deflection. The rotor plane could also be tilted. "A tilt angle of about 5° between the rotor axis and the horizontal plane is quite common." [16, p. 121]

[9] Replacement and/or substitution of an existing plant through a new plant with a higher efficiency.

Considering the individual subcomponents such as the load carrying spar caps, the trends towards longer blades leads to an increase in the thickness of the laminates. This results in lower quality, such as ply waviness or voids, and higher production cycles. [17]

In summary, recent development can be classified into three areas: Composite materials, design concepts and manufacturing technologies. While the application of composite materials in a WTB are discussed in chap.2.1, design concepts are treated in chap.2.2. Relevant manufacturing technologies are argued in chap.2.3.

2.1. Recent material systems

Composite materials have subsequently substituted metals that could no longer resist the prevailing material stresses due to increasing blade lengths. Commonly used composite fabrics are non-crimp fabrics (NCF), such as biaxial, triaxial, and quadraxial clutches. For the sandwich materials, BALSA wood and foam materials are widespread. These lightweight materials are primarily used to minimize the loads that arise from the rotating masses. The inertia plays a crucial role. Composite material, such as glass fibers and low-cost carbon fibers, may be used in all structural components of a rotor blade. The material causes about 55% of total blade costs. Fig. 2.5 shows that material costs are the main cost driver next to labor.

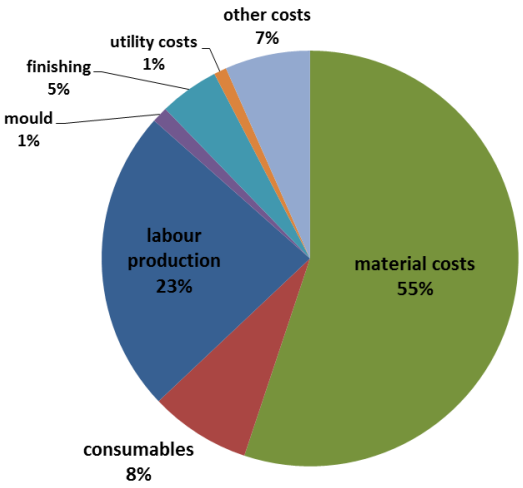

Fig. 2.1: Cost distribution of a blade manufacturing process

According to [18], composite material can cause up to 65% of total blade costs. Therein, 25% of total costs are caused by the matrix system. An approximate ratio of 10€ per used kilogram of material in a modern blade structure is assumed to include into a cost-efficient design. [14] This reference value relates to a smeared consideration of the complete material used for a blade structure. Simultaneously, the cost of material is quite sensitive to the current market situation and can greatly alternate. The APAC states are capable to compete with approx. 30% lower prices in total compared to European and US market prices. Local manufacturers use indigenous glass fiber materials. Moreover, labor costs are far more inexpensive. Particularly with composite materials, there exists a trade-off for the selection of the material between cost-efficient properties and sufficient high mechanical performance. Compared to industry branches like the aerospace, automotive, or leisure sectors, composite materials operate under a considerable cost-effecting pressure. It is not extraordinary that both, structural penalties in the selection of material are made, and fabrication inaccuracies are tolerated to keep costs low. The latter, however, is discussed in chap.5.

C**omposite materials**, such as glass and carbon fibers, are suitable to a WTB due to its properties:

+ High mass specific stiffness and strength properties
+ Fiber-adapted fabrication method: The orthotropic behavior of the material allows it to adjust the material into load path locally.
+ Superior fatigue properties compared to metals
+ Locally variable part thickness
+ Good drapability

Composite materials reveal the following disadvantages:

- Higher material costs compared to conventional steel or Aluminum
- Availability, especially of CFRP
- Medium level of process maturity (relatively new process technologies)

Glass fibers are the most processed fibers. They hold good strength properties and a moderate Young's Modulus. Although, carbon fibers exhibit excellent stiffness and strength properties, glass fibers are predominately used due to its lower price. [10, p. 259] Nevertheless, low-cost carbon fibers are increasingly used in very long blades. Subsequent enumeration prioritizes the requirements of composite materials for rotor blades in descending importance:

- **Prio 1**: High strength-to-cost ratio, high material stiffness and strength, material price, low density, processability (handling, infiltration and curing) and high fatigue properties.
- **Prio 2**: Low material degradation, high strength-to-density ratio and good fatigue properties, prone to environmental influence, good erosion resistance, especially where leading edge erosion is common; and availability (especially for BALSA wood and low-cost CFRP).
- **Prio 3**: Prone against electromagnetic fields, good adhesion for painting to substitute the gel-coat, compression after impact (CAI), damage tolerance (bird strike), impacts, aging (moisture and temperature, wood can rot, fungus), creep, storage (prepregs are not best), environmental influences (lightning, corrosion, temperature and moisture).

The aim is to enhance an optimum balance of a cost-efficient, light, stiff and strong fabric that at the same time fulfills the requirements of the process technology. Fig. 2.6 illustrates the changing application of lightweight materials in a WTB over the last three decades.

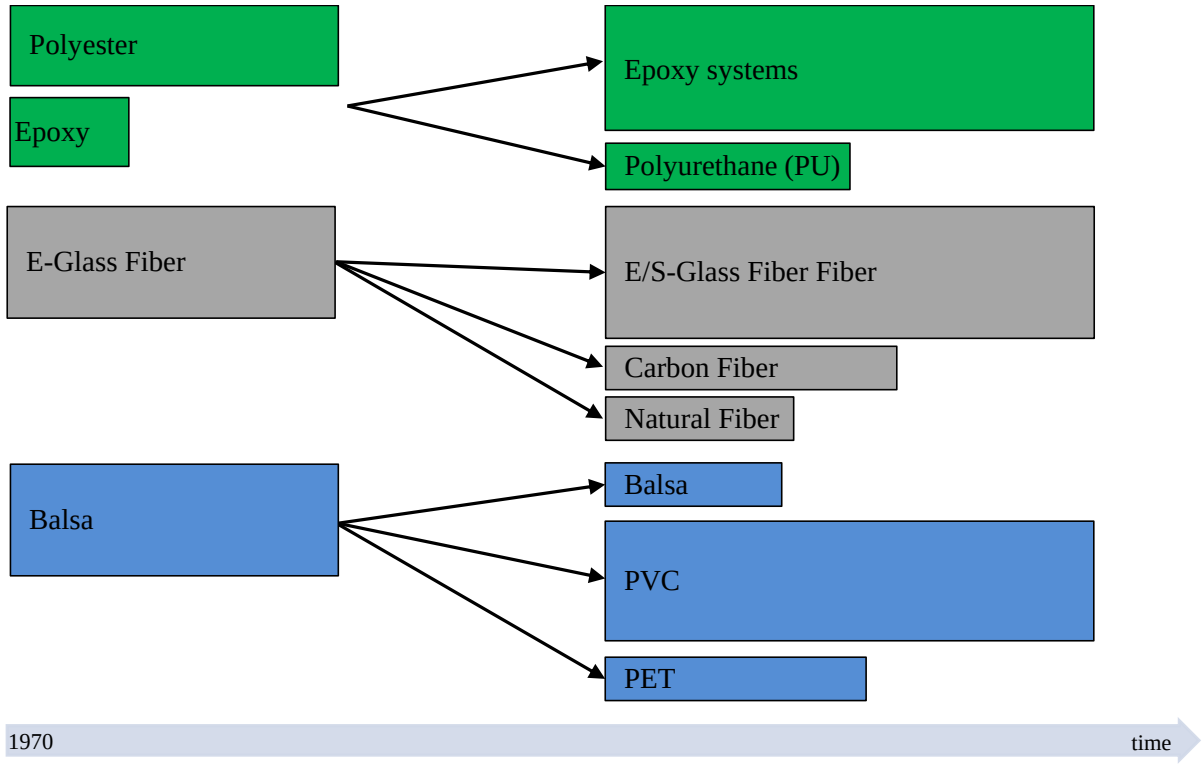

Fig. 2.6: Trends in the development of lightweight materials for matrix, fiber and core materials in WTBs over the last three decades

Matrix systems are classified into thermoset and thermoplastic systems. Thermoset matrix systems are EPOXY, POLYESTER and VINYL ester. VINYL ESTER has good fatigue properties; its Young's Modulus does not exceed 4GPa. The matrix systems EPOXY and POLYESTER are mostly used in WTBs. The selection is strongly driven by the manufacturing technologies, such as the infiltration and the curing properties. Basic parameters for selecting matrix systems are their viscosity and curing time. While POLYURETHANE systems are cost-efficient and may cure at room temperature, EPOXY systems are more expensive and primarily cure at elevated temperatures. However, primarily EPOXY resins are utilized due to their enhanced mechanical properties compared to POLYESTER systems. Additional advantages of EPOXY systems to POLYESTER systems are: higher strength and fatigue properties, lower density, less shrinkage and better bonding behaviors. [10, p. 259] In Tab. 2.2, typical component materials used in a WTB are constituted.

Tab. 2.2: Typical composite materials used in WTB

Material properties		**Fiber material**		**Matrix system**		**Core material**	
		E-Glass	C-Fiber	Epoxy	Vinyl ester	Balsa	Foam
Stiffness	[N/mm²]	72000	230000	3000	4000	270	70
Density	[kg/m³]	2540	1800	1200	1140	150	60

It is pointed out that the stiffness of CFRP is about 3 times greater than GFRP. The tensile strength is about one third greater. The combination of GFRP and CFRP in blade applications is called hybrid blade design. A compromise between a cost-efficient and a high-performance laminate is an objective. Chap.4.3 discusses a purposeful use of low-cost CFRP.

PROCESSING OF MATRIX SYSTEMS

The relative process time in Fig. 2.7 reveals that the manufacturing process is dominated by the curing time of the composite parts. [19] Thus, an ubiquitous aim is to accelerate this process step. Matrix systems in WTB applications are more and more tailored to production requirements, especially due to changing requirements of longer blade lengths.

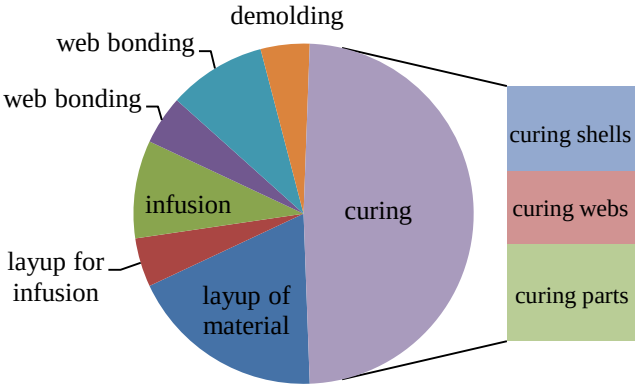

Fig. 2.7: Process time of singular process steps [-]

Fig. 2.8 classify the matrix systems into three groups related to their processing and mechanical behavior. While snap-curing systems are more used for *resin transfer molding* (RTM) applications that commonly require low cycle times, slow curing systems are applied to the *resin infusion under flexible tooling* (RIFT) applications that come along with a low number of units. Since WTBs constitute a very large and thick composite structure, latent curing systems have been developed recently. These systems allow a long pot life with good fiber wetting properties below conventional infiltration temperatures (T<55°C) and a short reaction time once the temperature is raised (T>70°C). The infusion of a 61.5m blade typically lasts about 75 minutes.

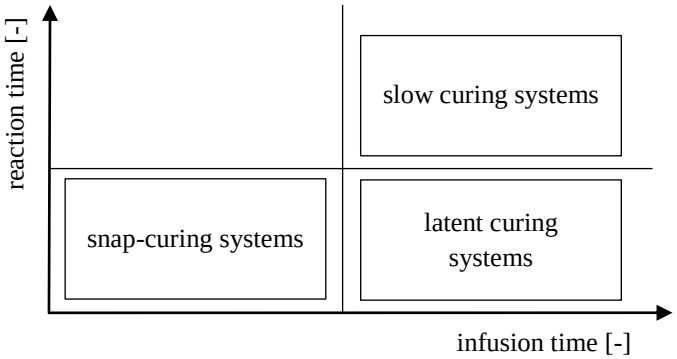

Fig. 2.8: Classification of epoxy based matrix systems

According to DARCY'S LAW, the flow rate of an incompressible[10] NEWTON`s fluid can be estimated for a one-dimensional consideration by:

$$v_m = -\frac{K_x}{\eta} \cdot \frac{\Delta p}{\Delta x} \tag{2.2}$$

v_m: Flow rate of incompressible fluid

K_x: Permeability of textile

η: Dynamic viscosity

Δp: Pressure

Δx: Distance

Further, a subtle stream (Re<1), an isothermal process (η=const.), and a constant permeability are assumed.

The aim is both to keep the matrix`s viscosity low during the infiltration process and to cure parts rapidly. The chemical mixture provides a long infusion time and a short curing time concurrently. This leads to remarkable reduction of the process time. Fig. 2.9 shows the trend of viscosities at an infiltration temperature of 40°. Both a traditional EPOXY matrix system and a latent EPOXY system are illustrated. It can be seen that the latent system holds a lower viscosity over time. (Fig. 2.9 left) Thus, thicker composite structures are more feasible to infiltrate. (Fig. 2.9 right)

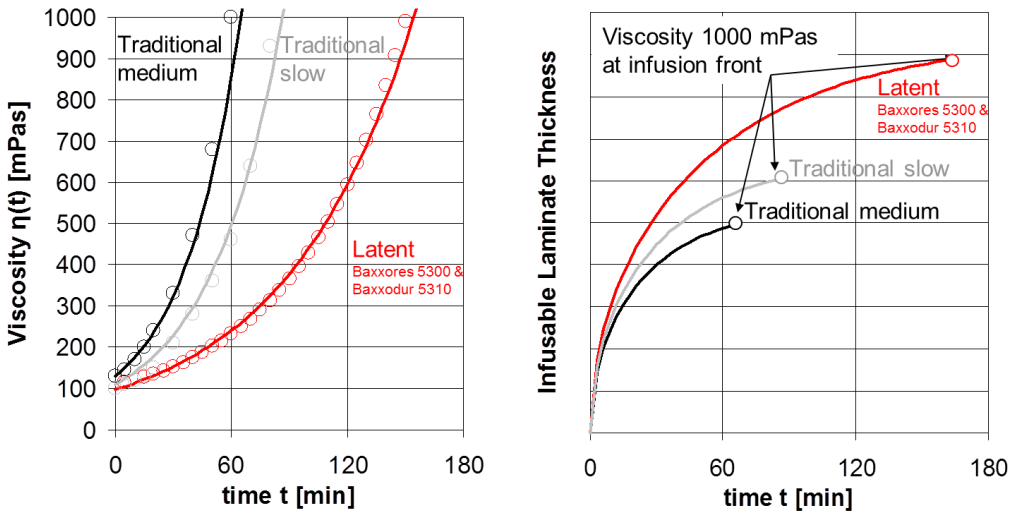

Fig. 2.9: Viscosity and infusible laminate thickness against infusion time [20] [21]

In Fig. 2.9 (left), peak temperatures in the middle of a 50mm thick laminate are depicted. Both the temperature during curing and the matrix system are varied. Corresponding to that, Fig. 2.10 (right) shows the temperature gradation against curing time for a convential and a latent system at a curing temperature of 50°. Latent epoxy matrix systems release lower

[10] $\varrho = const.$

exothermal energies than traditional epoxy systems. That leads to lower temperatures during the curing process. Therefore, it is important that, in general, higher exothermal energies tend to increase the likelihood of the occurrence of process induced deformations (PID), such as spring-in effects.

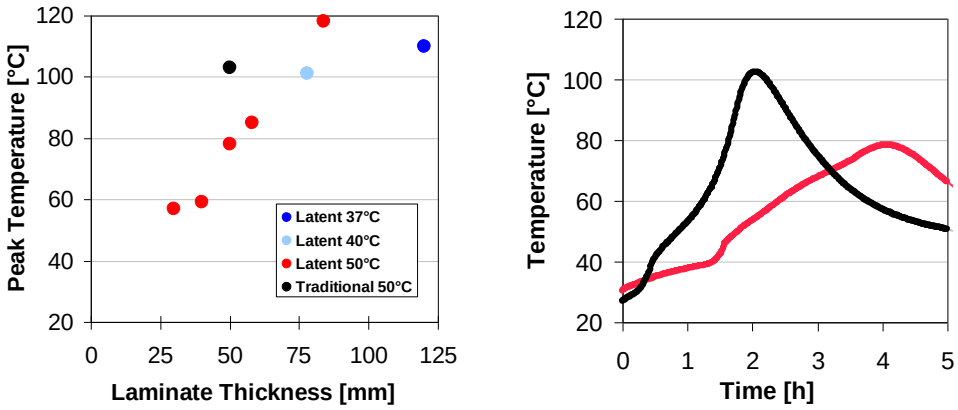

Fig. 2.10: Nascent temperature during curing process [20] [21]

Increasing the temperature above 70°C within the laminate, the latent curing process starts and leads to shorter infusion times than traditional systems. Latent EPOXY systems contain inactive reactants that are activated above a temperature threshold. Using latent matrix systems, the infusion time may be reduced by around 40%. [22] Next, experiments of the viscosity and the shear rate are carried. [23] Therefore, the matrix system RIM135/RIMH137 and the latent matrix system BAXXODUR are compared to each other. In Fig. 2.11 (left), the curves of viscosity of the two matrix systems are plotted against the time. A constant shear rate (1000 *1/s*) is held under 25°*C*. Equivalent to Fig. 2.9 (left), the latent matrix systems exhibit a lower viscosity over a specific time needed for the infusion. In addition, the change of viscosity of the latent and standard matrix systems is analyzed against various shear rates in Fig. 2.11 (right). It is observed that a shear rate dependency persists especially within the low shear rates of 1*/s* to 100*/s*. Further, the latent matrix system shows a lower viscosity within this zone.

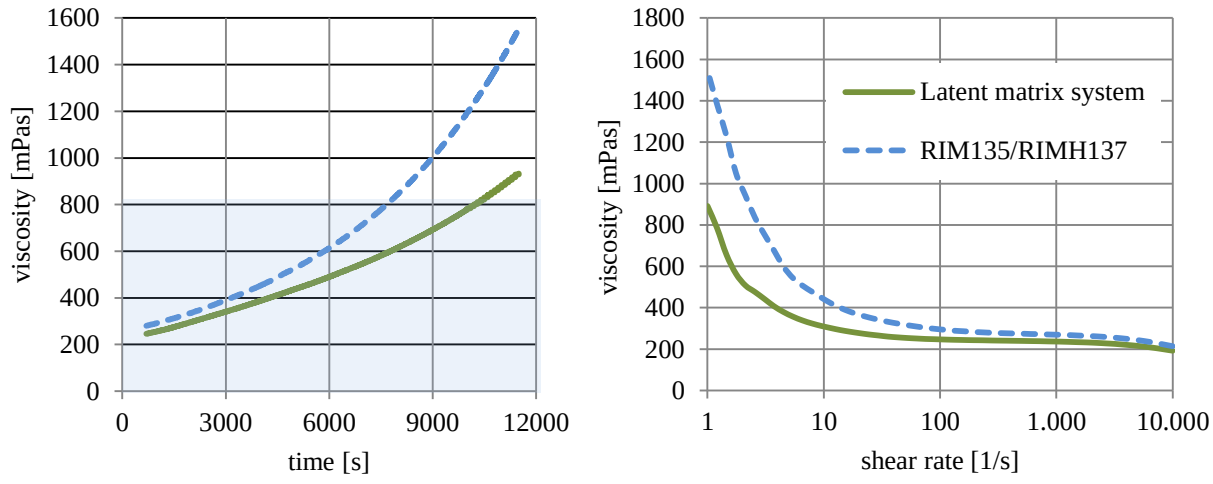

Fig. 2.11: Viscosity and shear rate dependence of a conventional and a latent matrix system

2.2. Design concepts of WTBs

The design corresponds intensely to the manufacturing process. Achievements in process technology can justify new design concepts. A state-of-the-art blade structure consists of seven main components: spar caps (1, 3), aerodynamic shells (2, 4), the shear webs (5, 6) and the blade root section (not visualized). The substructure of the aerodynamic shells implies leading and trailing edges. In chap.3.3, the single components of the preferred design are discussed in detail. Fig. 2.13 displays aero-elastic effects, e.g. how the structure, aerodynamic, and load scenarios are mutually influenced during the design process. The prevailing position of the blade during rotation directly affects the loads that in turn influence the aerodynamics. The structure also interacts with both the aerodynamics and the load scenario. While the aerodynamic conditions deliver the geometrical data of the profiles, the corresponding wind conditions induce loads upon the structure. It is stated that lowering the loads directly reduces the overall costs. Additionally, the manufacturing process affects the structure. Costs of material and manufacturing are the key factors in the development process.

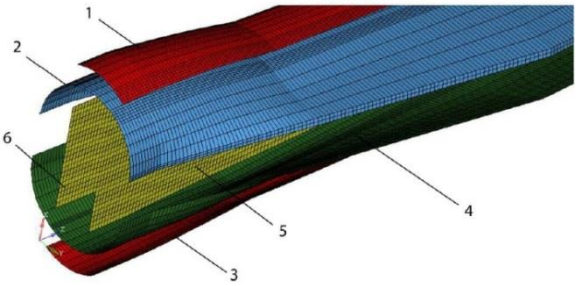

Fig. 2.2: FE-model: Exploded assembly of a WTB [5]

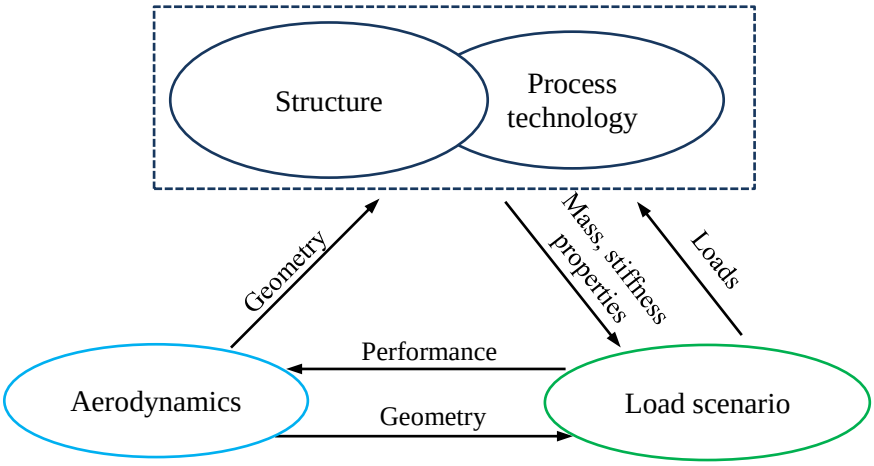

Fig. 2.13: Design and analysis process [24]

To consider the interactions of the above-mentioned categories, an iterative developing process is mandatory. Fig. 2.14 shows the outline history of design concepts from 1975 to this day. While the blade length has continuously been increased within the last 30 years, modifications of the design have been led to new structural concepts. Beginning with a single monolithic skin, a single, and now, a double shear web concept has been integrated. Secondly, achievements in the choice of material have been accomplished. GFRP has substituted for metals. Sandwich structures have been integrated. In comparison, airplane wings are

commonly reinforced by stringers and rips to withstand bending and shear forces and to prevent buckling modes. Sandwich structures are thought to be a cost-efficient alternative to attain the same effects. Since the 1980s, NCFs of S-glass fiber material were used. At the same time, matrix systems of VINYL ESTER were substituted by EPOXY systems because of both improved mechanical properties and healthier labor conditions. As blade designs increased 50 meters in length, alternative fiber and matrix systems were applied. Recently, the use of high stiffness glass fibers and carbon fibers were primarily discussed.

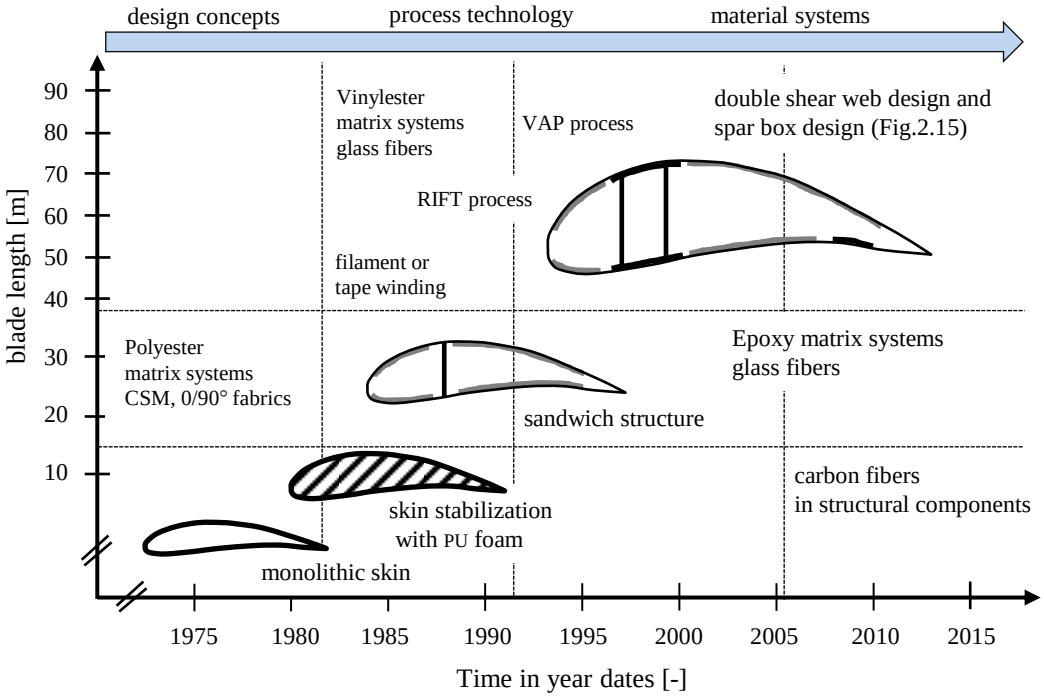

Fig. 2.14: Development of blade design over years (approximated by [25])

The process of developing a revised blade design regularly takes 12 to 24 months. If the latest process technology is introduced, the development process may last up to 36 months. [26] Two distinct designs are currently present in Fig. 2.15:

- Double shear web design
- Spar cap box design

The numerical model implemented in chap.3.4 is aligned to the double shear web design. Parts are separately manufactured and additionally bonded. This is currently the most established design, while the spar box design allows the adaption of automated manufacturing methods. A pultrusion process may fabricate spar caps.

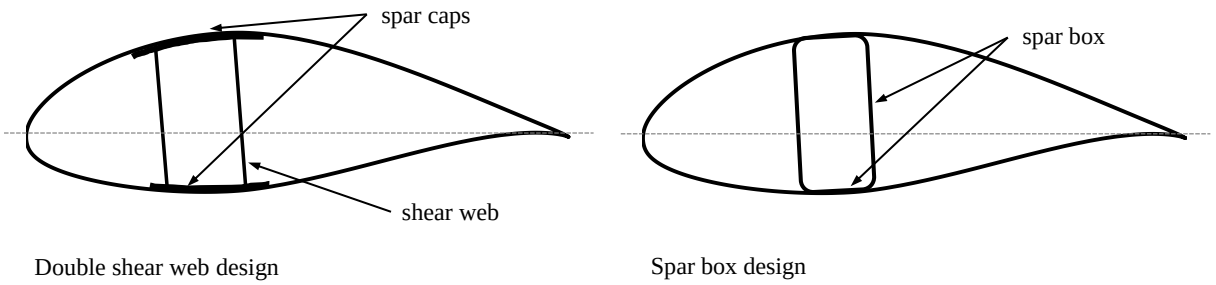

Fig. 2.15: Double shear web design and spar box design

Thus, the design concepts are continuously adapted to the variable boundary conditions. Recent developments in design concepts are listed:

- Modular blade design
  - for new manufacturing technologies
  - for transportable blade designs[11]
- Minimizing the number of shear webs [12]
- Development of a solid laminate versus sandwich or stiffened panels for unsupported areas [12]
- Flatter properties: Blades tend to have a slighter design, which may be prone to flatter properties.

While the most relevant structural requirements are stiffness, strength and fatigue properties, natural frequencies and stability (chap.4.2), the weight of the blade plays a superior role. Low weight comes along with lower material usage, lower induced loadings and stresses and with good responding behavior for low wind conditions. Further, a lighter blade shows positive effects on the fatigue behavior.

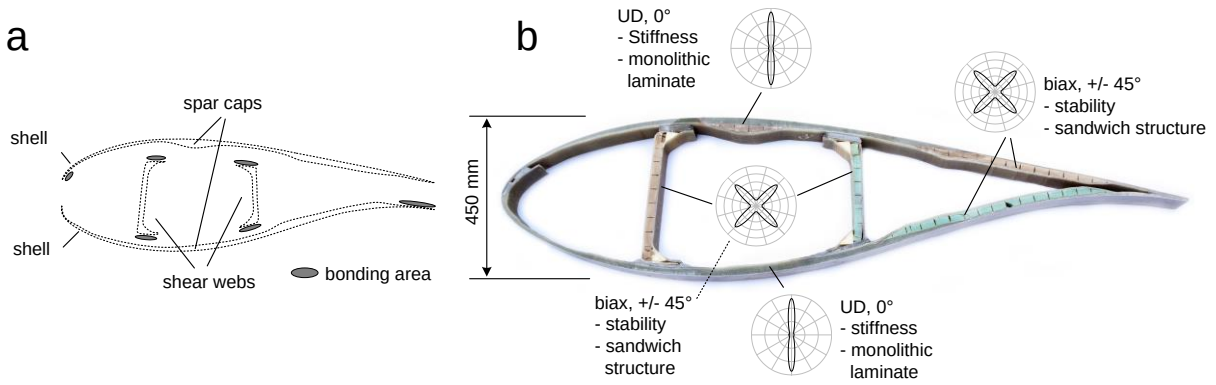

Fig. 2.16: Cross-sections of a conventional blade structure

[11] The transportation costs increase dramatically at about 52m blade length. [120]

2.3. Manufacturing processes and automatization concepts

The expanding industrialization of the wind energy sector has promoted the development of manufacturing technologies. While prior blades were manufactured by hand-layup techniques, there have been several attempts to produce blades by a filament or tape winding technique in the early 1980s. [10] Nowadays, the vacuum assisted process (VAP®) poses a widespread technique to fabricate blades. Ambitious concepts of automatization still collapse owing to excessive investment costs. Nonetheless, a trend towards incremental automatization of single process steps reigns.

The blade manufacturing process is driven by costs more than any other composite branches. Current processes are labor intensive. Defects induced by the manufacturing process may lead to further complications during operation, maintenance, and blade life. The amount of defects is strongly dependent on the manufacturing process. Common defects are ply wavinesses (chap.5), fiber misalignments, porosities, delaminations, unbonded joints, and resin rich areas. "Cycle times vary depending on the quality of equipment, the level of automatization and the cure time acceleration assumed." [8, p. 70] According to [27], the production time of a single blade is about 36 hours whereat finishing time is already included. The fabrication steps can roughly be separated into preforming, infiltration, curing, assembling, and finishing.

A prospect of recent manufacturing techniques aimed toward the impulsion of new ideas is given. The processes are briefly discussed, and then introduced beginning with the most common. Additional reading of the manufacturing processes can be studied in [28, 29, 30, 31].

RESIN INFUSION UNDER FLEXIBLE TOOLING

The process "resin infusion under flexible tooling" (RIFT) is a widely used industrial manufacturing process of wind turbine blades. Enhancing the content of porosity, RIFT is improved by a semi-permeable membrane. The vacuum assisted process (VAP®) may further accelerate the infiltration process.

A schematic layup of the process RIFT is shown in Fig. 2.17. Due to the large dimensions of the components, the mold is commonly built up as a sandwich structure. The mold is heated by air. There are efforts on designing the mold out of sandwich structures combined with embedded heated filaments. A single mold may be used about 2000 times until it has to be renewed due to abrasion. A gel-coat is applied for the ease of removing the cured component and protecting the mold`s surface. The comprehensive dry composite lay-up is deposited and stacked on the semi-shell of the tooling. Subsequently, a peel ply, a flow promoter, a VAP® membrane and a suction fleece is put upon the preform. Finally, the layup is covered by an airtight sheet. Particular manufacturers use a second airtight sheet to ensure the imperviousness of the build-up. The vacuum is drawn. The matrix system provided premixed in containers is transferred via pipes through the dry preform by the pressure difference.

Especially for large-scale composite structures, it should be guaranteed that the matrix has sufficient time to fully fill the mold before the viscosity significantly increases and the exothermal reaction starts. The aerodynamic shell includes perforated core materials that allow the matrix to flow through the thickness. In contrast to the aerodynamic shells, holes are drilled into the shear webs (chap.3.3.4) at defined areas to enable the matrix flow. The challenge of the infusion process is the infusion of the spar caps due to their thick laminate.

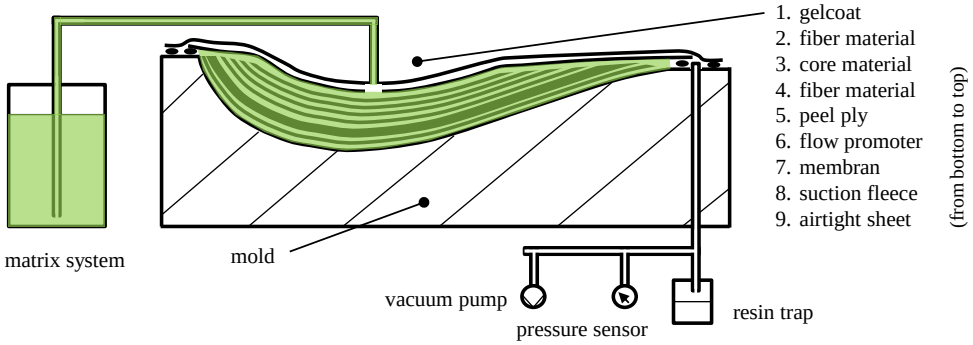

Fig. 2.17: Schematic VAP® setup

The current infiltration strategy of large scaled composite structures is driven by expert`s knowledge. Commercial software tools provide insufficient results due to the high complexity of the composite layup and its varying permeability. To control the exothermal energy during curing, unconventional methods, like depositing of humid rags on local warmed-up regions, are ubiquitous. The vacuum assisted resin transfer molding (VARTM), and Seeman composites resin infusion molding process (SCRIMP) are alternative processes for the blade structures.

In Fig. 2.18, a schematic sequence of the production is shown. In the first step, parts are individually manufactured. After the parts have been cured, the components are bonded to each other.

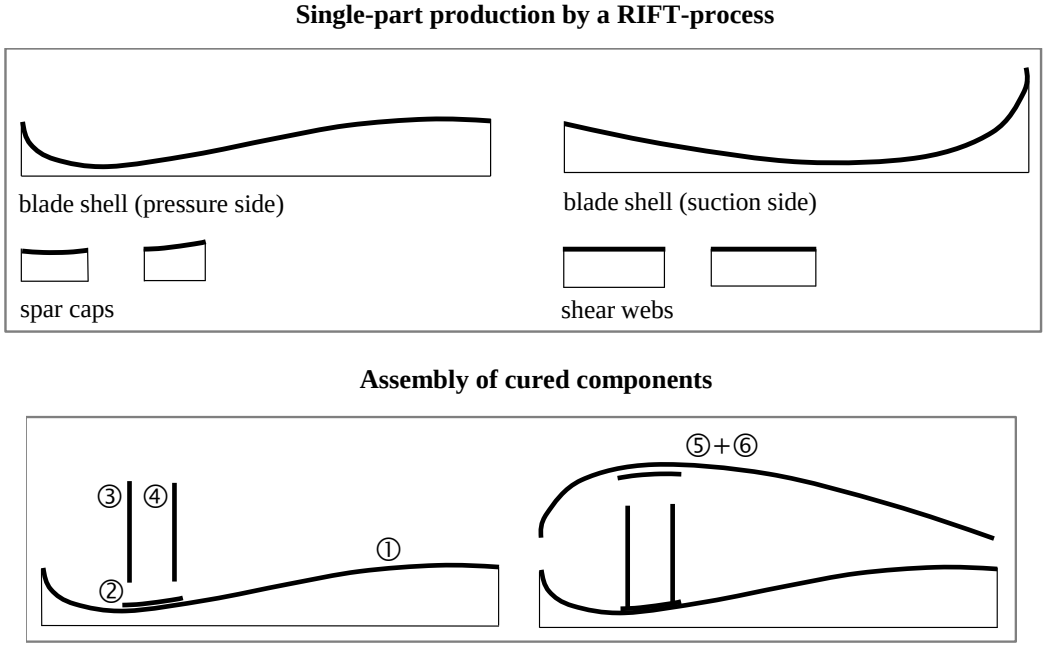

Fig. 2.18: Schematic sketch of single parts` production and assembling

Fig. 2.19 shows a typical production line of a WTB.

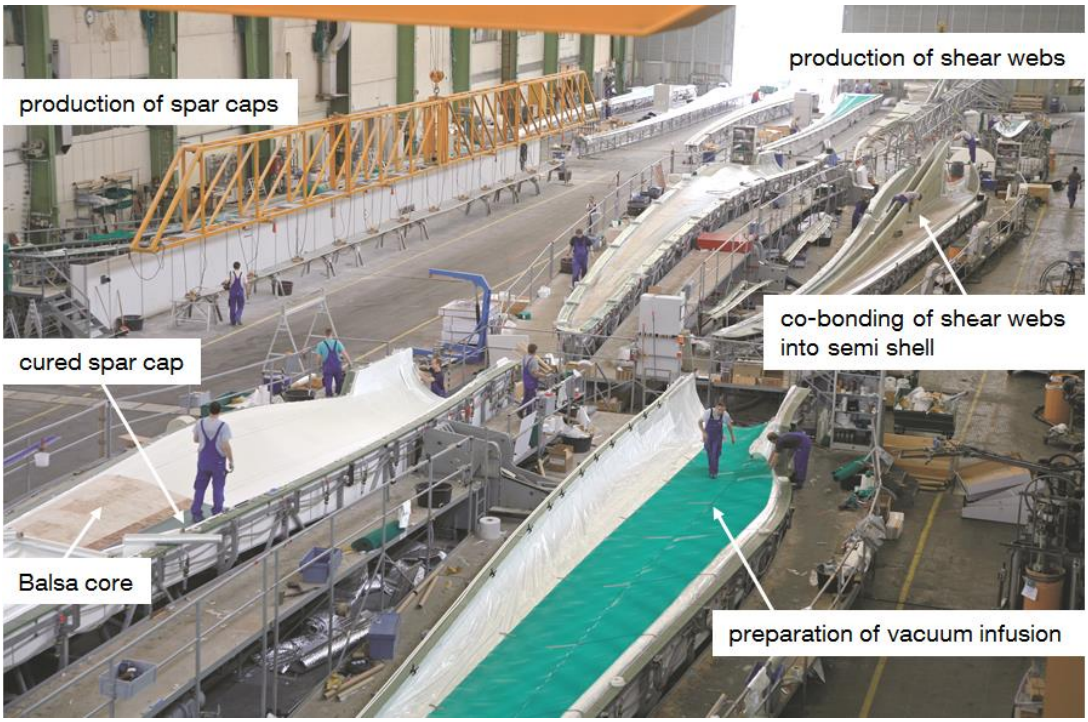

Fig. 2.19: WTB production line [32]

In Fig. 2.20, the single process steps are depicted. First, the composite material is draped into the mold, and then the setup for the infiltration process is prepared. Having assembled the cured parts are assembled, the blade is finally painted.

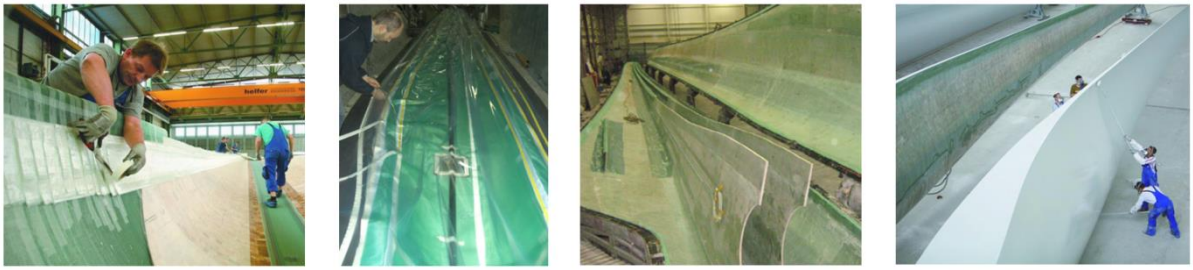

Fig. 2.20: Process steps: Draping, infusion and curing, assembling and finishing [32]

INTEGRAL BLADE PROCESS

Using the RIFT process, the blade`s subcomponents (chap.3.3) are infiltrated separately and bonded additionally. Adhesive bonding – especially when stressed – poses a potential risk of structural weakness. Designs manufactured by RIFT occasionally feature defects at the bonding areas. This may have several reasons:

- Erroneous bonding, manufacturing intolerances (weakest structural part)
- Invisible bonding area (thus, detection is improbable)
- Low fatigue properties of adhesives compared to composite material

Thus, over-dimensioned bond lines are arranged to balance manufacturing intolerances. As a result of this, STIESDAL and JENSON[12] have developed an innovative manufacturing technique in recent years. This manufacturing technology allows a design without adhesive bonding. This is possible due to a novel fabrication strategy. The composite fabrics are not laid down into lengthwise direction of the blade. Furthermore, the preforms are put orthogonal to the lengthwise direction and – after a removable core (Fig. 2.21) has been applied – the preforms are laid over the core. Equipment in the form of a flow promoter, etc. is arranged at the surface of the integrated core. The composite structure is infiltrated by one shot.

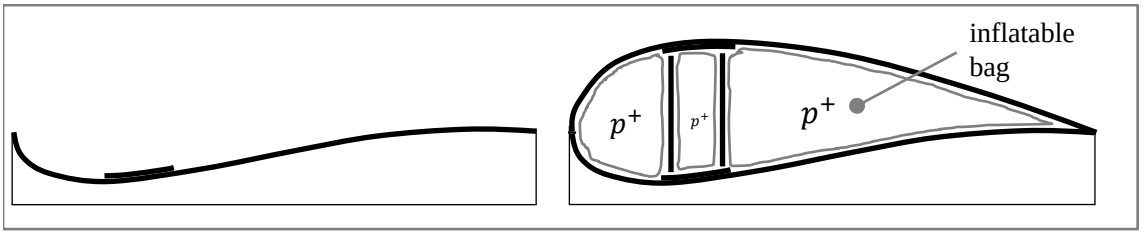

Fig. 2.21: Integral blade process - layup step

Next, a second mold is applied to the exposed layup. Due to infiltration issues, the closed mold is turned into position according to Fig. 2.22 (left). After the structure has been infiltrated and cured, the inflatable bags are removed.

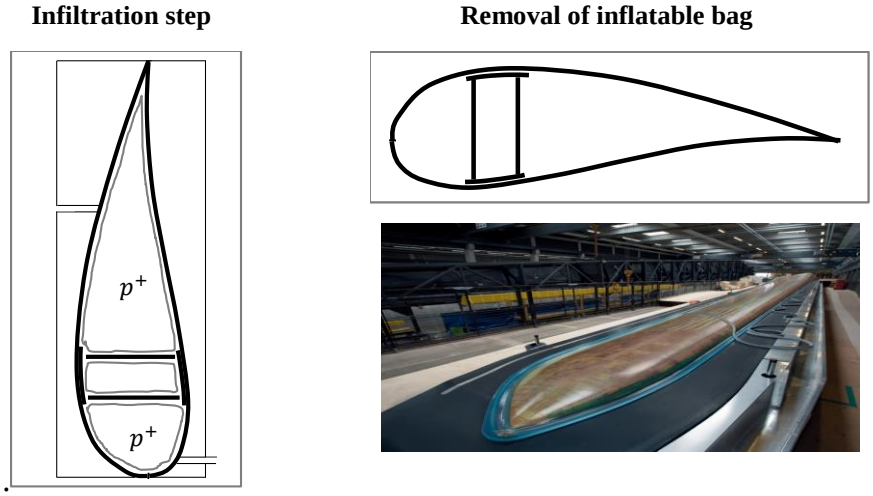

Fig. 2.22: Integral blade process - infiltration and curing step

A disadvantage of the integral blade process is the major risk of wastage (chap.5), if the manufacturing process is not robust.

PULTRUSION PROCESS

The fabrication of spar caps poses superior requirements. The composite layup of the spar caps is dominated by plies orientated in one direction. Total laminate thickness of the

[12] Siemens Windpower holds the patent US 20030116262 A1 (filed 26.06.2003).

structure may exceed 40mm for a modern 61.5m rotor blade. (chap.3.3) There are ventures to utilize the pultrusion process for manufacturing unidirectional dominated spar cap structures. The pultrusion process gains high fiber volume contents (FVC) of about 0.65 - 0.75, combined with an extraordinary automatization rate. Further, the occurrence of ply wavinesses can be dramatically reduced. A novel preform material of aligned fiber reinforcement for wind blade spar caps has currently been developed by the company NEPTCO.

FILAMENT OR TAPE WINDING PROCESS

In 1980, government funded projects planned to manufacture rotor blades by a filament and tape winding process. [10] The purpose was to lay down the composite layers upon the aerodynamic shell. The blade is fixed on a mandrel and rotated around its length axis. It turned out that it is challenging to reproduce a concave form by a filament winding process.

One method could be the integration of an air bag upon the concave shape. Successively, it is winded over the air bag. The bag is removed after the winding process and the filaments and/or tapes are pressed up to the final geometric shape. [33, 5] Another restriction of the tape winding process is that the deposition of tapes, the orientation of which is close to the blade length axis, is limited. E.g., tapes of various widths can be deposed at an angle to the length axis between around 10°-80°. In contrast, detached manufacturers use the tape winding process solely for selected components: the blade root section of very large structures and the spar box for blade structures up to 20 meters (Fig. 2.15 (right)). Large rotor blades require thick laminates at the blade root section. A laborious layup process is arranged to guarantee a definite deposition. The tape winding process allows an automated layup in short cycle times. The blade root is suited for the process due to its circular shape. The laminate of the root sections is mostly quasi-isotropic. This fact even facilitates the application of the process.

AUTOMATED TAPE LAYING PROCESS

Automated tape laying (ATL) and automated fiber placement processes (AFP) are processes that use computer-guided robotics to position composite material tapes onto a mold. Typical applications include aircraft wing skins and fuselages. Composite fabrics and core materials in WTB are already prefabricated and custom-tailored. Thus, in the predominant fabrication process using RIFT, decomposition and slight draping into the mold is carried out promptly. Nevertheless, the grade of automatization is very low; investments of automated process technologies have to be justified. Companies, such as MAG and MTORRES have recently developed automated portal machines adapted to the needs of blade manufacturers. The facilities are able to deposit fiber material automatically into the mold. It becomes apparent that the purchase of an automated layup device for blade manufacturers is still unprofitable and has to be justified economically. A comparison between required labor works - by means of draping time - has to be conducted according to the fact that the fabrics are already bought in custom-tailored shape. Further, the occupation time of the molds is still the same. As a consequence, additional molds have to be acquired.

2.4. Miscellaneous trends

The mutual effects of material selection, design concepts, and manufacturing technologies may be vast. A list of contemporary developments and innovations in blade structures is broadened:

- **GFRP-/CFRP hybrid design**: A purposeful adoption of CFRP, instead of GFRP, may dramatically improve the structural mechanical properties of the blade. Case studies are conducted to evaluate the influence of the use of CFRP. The adoption of CFRP is verified in terms of a cost-efficient design.
- **Bend-twist-couplings**: The smart intentional alignment of the fiber filaments induces bend-twist-couplings under pure bending. This effect assists the pitching mechanism. Finally, this may lead to reduced structural loadings of the composite material.
- **Structural optimization method**: A structural optimization routine may be initiated to improve the present composite layup and stacking order. An optimization technique should be used as a preliminary design tool. [5] This should imply the integration of load, shape, and material modification into the optimization process.
- **NDI testing methods**: The manufacturing process causes nine out of ten failure modes that occur during a blade life.
- **Active pitch regulations:** The electronic control is responsible for power control and the avoidance of overloads and damages to the structure. The individual pitch control could further decrease occurring loads upon the blade structure.
- **Embedded fiber optic sensoring systems** for condition monitoring systems.
- **Slender blade designs** for low wind regions and higher annual energy capture.
- **Blade-hub-connection**: New hybrid joining concepts are pursued. The connection between the metal hub and the composite structure gains a fiber-fair load introduction.

The itemized trends stated above are to be understood as a summary.

3. Analysis, design & modeling of rotor blades

The chapter describes the analysis and design process of WTBs. Design loads are defined by an analytical approach in chap.3.1. The blade design of a conventional WTB is outlined in chap.3.2. The blade`s components are individually described in chap.3.3. The study of literature has shown that the composite layup of the conventional WTB is rarely published in a detailed manner, much less information about a distinct composite layup is available. Currently, no comprehensive database has been published.
Finally, a finite element model and the corresponding analysis of the blade structure representing a conventional and state-of-the art design are described in chap.3.4 and validated in chap.3.5.

3.1. Design loads

Horizontal WTBs use the principle of lift to produce energy. Steady, cyclic, transient, stochastic and resonance-induced loads occur during operations. [13, p. 158ff] The loads emerge from aerodynamics, gravity, dynamic interactions, interactions of mechanical control systems, emergency stops etc. While a mean value of the wind speed is crucial for the energy efficiency of a WEP, the short-term extreme loads, blasts, emergency stops, are the dimensioning factor for the structural design. [10] [2] Since the blade system is highly dynamic, wind conditions vary at every blade`s position. Therefore, wind distributions are more strongly affected in the lower area than in the most upper area a blade circulates. Especially, the transit close to the tower induces complex flow conditions. Actual prevailing load conditions are complex to estimate. Therefore, generally accepted idealizations are made (see GL and IEC61400 guidelines). An analytical tool is composed to determine simplified design loads. This is followed by the application of the load to the FE-model. Finally, the resulting load envelopes are compared to load curves of contrastable blades.

The boundary conditions such as the assignment to wind class I[13], the adjustment and positions of the blades are defined and may be reviewed in the Appendix A.

According to [34, p. 11f], the blade design process commonly starts with the definitions of its aerodynamics and its corresponding loads. Having defined performance of the rotor blade, the design of the aerodynamic shape is fixed. While the load envelopes are established, the power curve is defined. Simultaneously, the threshold value of noise emission has to be observed. Common practice is the simulation of at least 100 load cases, which are particularly traced for 600 seconds. Therefore, commercial multi-body simulation tools[14] (MBS) are used.

[13] Wind classes: Wind classes define which WEP is suitable for normal wind conditions of a particular site. Wind classes (I-IV) are classified by the average wind speed, extreme 50-year gust and turbulence.
[14] Commercial multi-body tools: FOCUS6, FLEX5, FAST, HAWC2, ADAMS, SAMCEF for WTB, BLADED, etc.

The resulting curves of bending moments are compared to existing and comparable data in the literature. A plausibility check is conducted by GL. Guidelines and inspection requests for load calculations are found at the International Electrotechnical Commission (IEC). The following types of loads are considered:

- Aerodynamic loads (constant)
- Gravity loads (dependent on blade position)
- Centrifugal loads (constant)
- Functional loads
- Dynamics
- Loads due to impact, icing and etc.

According to the aforementioned type of loads, functional loads are produced by the controlling and regulations of the plant. The emergency shutdown has to be considered. According to GL, the maximum deceleration of the rotating blade has to be elected in that way, that the allowable strength values of the blade material are not exceeded. Fig. 3.1 shows a simplified sketch of the occurring forces on a blade structure.

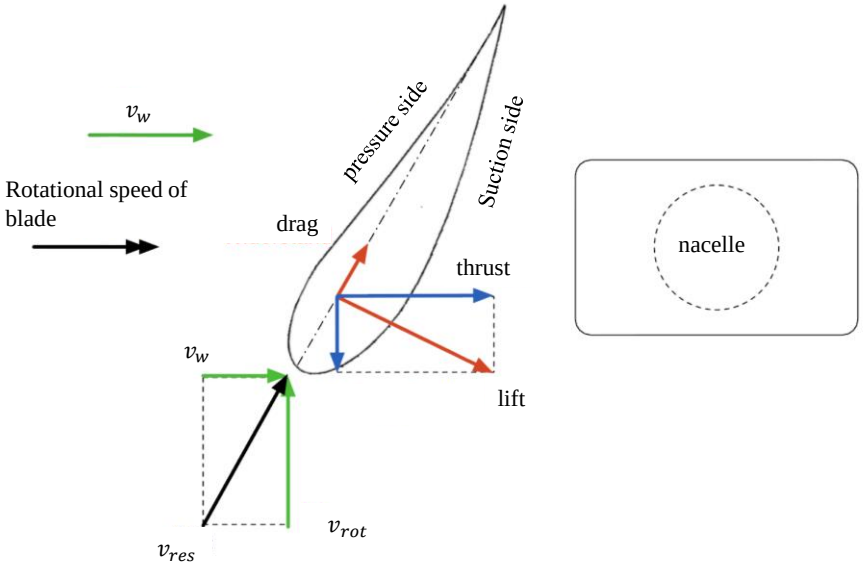

Fig. 3.1: Occurring forces at blade`s cross section

For a very detailed wind load calculation, fluid-structure-inaction methods (FSI) are recommended. FSI can be used to estimate the interaction of various wind conditions to the geometry and composite layup structure. This method is recommended to research on bend-twist couplings with respect to smart structures and active pitch control. Nevertheless, current MBS do not analyze the material`s structure very accurately. Focusing on the behavior of the composite`s constituents, an FE-based model is essential.

ANALYTICAL LOAD CALCULATION

The aerodynamic loads are apportioned into its three components, which consist of a lift, drag, and a torsional portion. Gravity and centrifugal loads are additionally applied in the FE model. The following assumptions are made:

- Quasi-static load scenario is assumed,
- Interpolation of the lift distribution along cross sections,
- Neglecting of turbulences and wind discontinuities,
- Constant wind speed (v_w) along blade length,
- Time-independent variance of wind speed.

An analytical approach is used to generate quasi-static aerodynamic loads. Discrete aerodynamic loads are calculated for corresponding cross-sections. C_p-values of a two-dimensional circulation are used. The load envelopes of the aerodynamic forces and moments along the blade length axis are determined by linearization between two adjacent cross sections. This method is also a common approach for a preliminary design and layout of aircraft wings. [35] [36]

The calculation of the aerodynamic loads are related to the aerodynamic center of the individual profiles. The following aerodynamic loads will be calculated for every cross-section according to Tab. 3.3.

According to Betz the effective wind speed v_{eff}:

$$v_{eff} = \frac{2}{3} \cdot v_w \tag{3.1}$$

with:

v_{eff} : effective wind speed

v_w : wind speed

The local peripheral speed v_u is computed by the rotor speed ω and the local radius of the blade r:

$$v_u = 2 \cdot \pi \cdot r \cdot \omega \tag{3.2}$$

The resultant blade-tip velocity v_{res} of the profile i is determined by the axial effective wind speed and the peripheral speed v_u.

$$v_{res,i} = \sqrt{v_{eff,i}^2 + v_{u,i}^2} \tag{3.3}$$

The resulting aerodynamic angle of attack α of a cross-section is calculated by following geometrical expression:

$$\beta[rad] = arctan\frac{v_{eff}}{v_u} \tag{3.4}$$

$$\alpha_i = \beta_i[°] - v_i - \delta \tag{3.5}$$

with:

β : angle of sum

υ : twist angle

δ : pitch angle

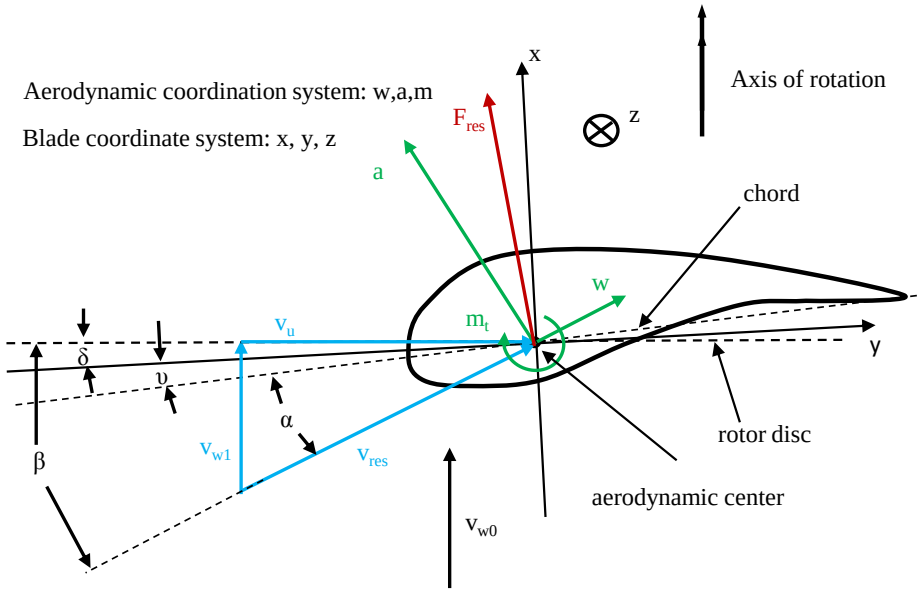

Fig. 3.2: Aerodynamic loads by inflow [37]

The aerodynamic loads are estimated at each cross-section in unit length by chord length $l_{cs,i}$ and the resultant blade-tip velocity v_{res}. The loads are imposed at the aerodynamic center that is defined constantly at a fourth of the chord length of profile i. The lift and drag characteristics[15] are calculated.

$$l_i = \frac{1}{2} \cdot \varrho_{air} \cdot {v_{res,i}}^2 \cdot c_{l,i} \cdot l_{cs,i} \tag{3.6}$$

$$d_i = \frac{1}{2} \cdot \varrho_{air} \cdot {v_{res,i}}^2 \cdot c_{d,i} \cdot l_{cs,i} \tag{3.7}$$

$$m_i = \frac{1}{2} \cdot \varrho_{air} \cdot v_{res,i}^2 \cdot c_{m,i} \cdot l_{cs,i} \tag{3.8}$$

l : lift [N/m]

d : drag [N/m]

m : aerodynamic moment coefficient [Nm/m]

c_l : lift coefficient [-]

c_d : drag coefficient [-]

c_m : coefficient of moment [-]

l_{cs} : chord length of profile [mm]

[15] Relationship between static and dynamic pressure: static pressure of wanted pressure and static pressure of the inflow divided by dynamic pressure: $c_p = (p - p_\infty)/(1/(2\varrho v_\infty^2))$

Loads are transformed in the blade coordinate system. On the basis of the linearized line loads with its basic values at 19 cross sections, distributions of transversal forces and bending moments in flap- and edgewise direction can be drawn. The distribution of torsional loads is estimated by transforming the aerodynamic loads e.g. to use the length axis of the blade as a reference axis. [37]

The design loads are calculated by an analytical tool considering previously mentioned assumptions. The rotor speed ω, the wind speed v_w and the pitch angle of the blade δ can be varied individually and, thus, specified quasi-static load scenarios can be estimated. Four blade positions and their resulting forces are shown in Fig. 3.3. Considering the taken assumptions, the aerodynamic and centrifugal loads are constant during a circle. However, the loading of the structure is dependent on the gravity during a cycle. The prefix of the loading changes between position 2 and position 4. Thus, because in position 4 the aerodynamic and the gravity loads show in the same direction, position 4 poses the most stressed blade position. Furthermore, the angle of attack effects the resulting bending loads due to changing gravity conditions in flap- and edgewise direction. [37]

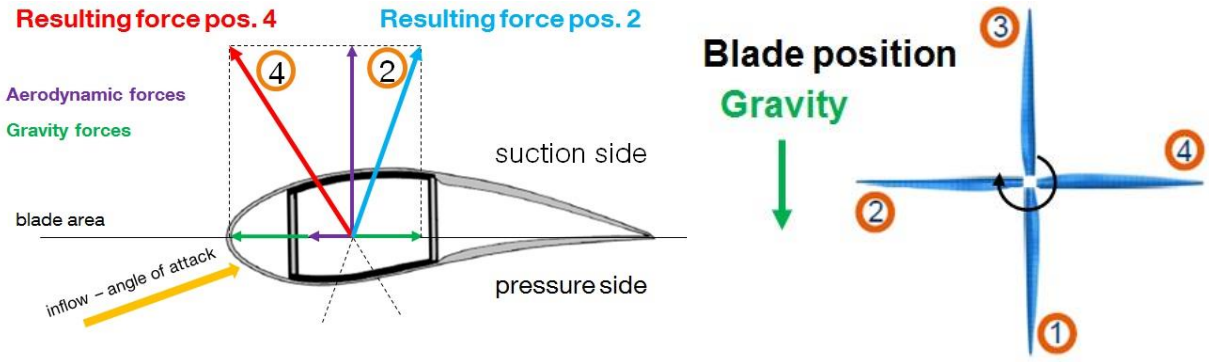

Fig. 3.3: Resulting forces in dependence on the blade position [37]

APPLICATION TO FE-MODEL

The calculated loads are transformed to blade coordinate systems of the specified cross-section by:

$$f_{y,i} = -\cos(\alpha_i + v) \cdot l_i - \sin(\alpha_i + v) \cdot d_i \tag{3.9}$$

$$f_{z,i} = \sin(\alpha_i + v) \cdot l_i - \cos(\alpha_i + v) \cdot d_i \tag{3.10}$$

$f_{y,z}$: line loads

The shear force distribution along the x-axis is estimated by

$$Q_x = \int q(x)dx. \tag{3.11}$$

A predefined number of nodes are used as nodes of load introduction (NLI). Thus, it is interpolated by:

$$F_{y,i}[N] = (r_{i+1} - r_i) \cdot f_{y,i+1} + \frac{(r_{i+1} - r_i) \cdot (f_{y,i} - f_{y,i+1})}{2} + F_{y,i+1} \tag{3.12}$$

$$F_{z,i}[N] = (r_{i+1} - r_i) \cdot f_{z,i+1} + \frac{(r_{i+1} - r_i) \cdot (f_{z,i} - f_{z,i+1})}{2} + F_{z,i+1} \tag{3.13}$$

Equivalent to the previous, the torsional moment distribution along the x-axis is determined by

$$M_{bz}(x) = \int Q_y(x)dx, \tag{3.14}$$

$$M_{by}(x) = \int -Q_z(x)dx \text{ and} \tag{3.15}$$

$$M_t(x) = \int m_t(x)dx. \tag{3.16}$$

Flapwise (y) bending moment:

$$M_{bz,i}[Nmm] = (r_{i+1} - r_i) \cdot F_{y,i+1} + \frac{(r_{i+1} - r_i) \cdot (F_{y,i} - F_{y,i+1})}{2} + M_{bz,i+1} \tag{3.17}$$

Edgewise (z) bending moment:

$$M_{by,i}[Nmm] = (r_{i+1} - r_i) \cdot F_{z,i+1} + \frac{(r_{i+1} - r_i) \cdot (F_{z,i} - F_{z,i+1})}{2} + M_{by,i+1} \tag{3.18}$$

Torsional (x) moment:

$$M_{x,i}[Nmm] = (r_{i+1} - r_i) \cdot m_{i+1} + \frac{(r_{i+1} - r_i) \cdot (m_i - m_{i+1})}{2} + m_{x,i+1} \tag{3.19}$$

Q_x : transverse shear force

M_{bz} : flapwise (y) bending moment [Nmm]

M_{by} : edgewise (z) bending moment [Nmm]

M_x : torsional (x) moment [Nmm]

r_i : distance between crossection and rotational axis

Five load scenarios according to Tab. 3.2 are considered. The operating conditions and environmental conditions are stated in Tab. A1. The aerodynamic loads are calculated by the previous formula relating to the reference point of the respective cross section. A constant wind speed v_w is assumed. The inflow is affected orthogonal to the rotor disk. The distribution of normal forces is depicted, too. Centrifugal forces are estimated by the mass distribution analytically. [37]

Having transferred the aerodynamic into its corresponding coordinate system the loads are applied to twelve cross sections of the structure via both discrete forces in flap- and edgewise direction and discrete torsional moments. Gravity and centrifugal forces are directly applied in the model via the corresponding load type. [37] [5]

A polygon is created to connect the load introduction points, representing the aerodynamic centers, to a flexible and massless beam. The loads (flap- and edgewise) are applied upon the beam via a linear function. The discrete moments are upset to the load instruction points. The aim is to exclude any stress concentrations at the load introductions. ABAQUS offers several possibilities to implement coupling constraints and/or multi point constraints (MPC). The constraints are used to limit predefined displacements and/or rotations in dependence to the movement of a reference node. [38] The recommended constraint that fits best to the above mentioned requirements are the *continuum distributing coupling*. This constraint distributes the forces and moments which appear on the reference point to the coupled nodes. Forces only affect the coupled nodes. The loads are distributed in such a way that the resulting forces in the coupled nodes are equal to the forces and moments acting at the reference point. The function "weighting method" allows weighting the load distribution at the coupling points with respect to the distance of the referring coupled node. Fig. 3.4 depicts the schematic sketch of the load introduction to the FE-based model. For a better illustration the load distribution in edgewise direction is not shown here.

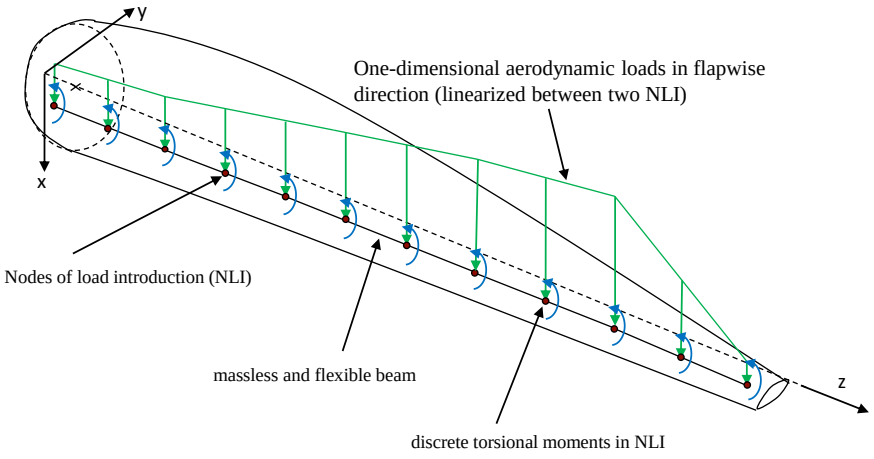

Fig. 3.4: Load introduction in FE-model (schematic illustration) [37]

The resulting bending moments in flap- and edgewise direction are compared to available literature data. It is stated that the resulting bending moments are in good correlation to literature data.

Characteristic loads are charged by the safety factors from Tab. 3.1. and emerge as design loads.

Tab. 3.1: Safety factors of loads

Load type	Aerodynamic loads	Gravity loads	Centrifugal loads
Safety factor γ_F	1.35	1.35	1.25

The comparison of the bending moment is one validation step. It shows that the analytical approach is applicable to pre-design consideration.

Tab. 3.2: Definition of the load scenarios

Load scenario (LC)	Status and description
1	Standstill, 50-year-blast, pitch angle 0°, position blade 270°
2	In operation, maximum rotation speed 12.2 U/min, wind speed at cut-off speed 25m/s, pitch angle 8°, blade position 4
3	In operation, maximum rotation speed 12.2 U/min, wind speed at cut-off speed 25m/s, pitch angle 8°, blade position 2
4	Modal analysis
5	Linear buckling analysis (loads of LC2)

The resulting bending moments are shown in Fig. 3.5 for the load case LC2. Further, bending moments influenced by the gravity are shown in flap- and edgewise direction and in dependence on the pitch angle at blade position 4.

a) Bending moments in flap- and edgewise directions

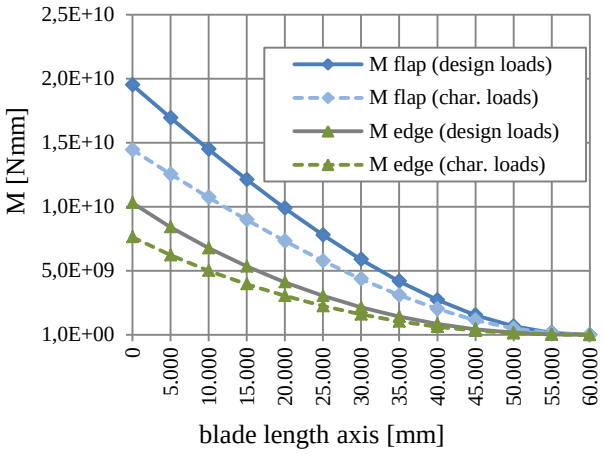

b) Bending moments in torsional directions

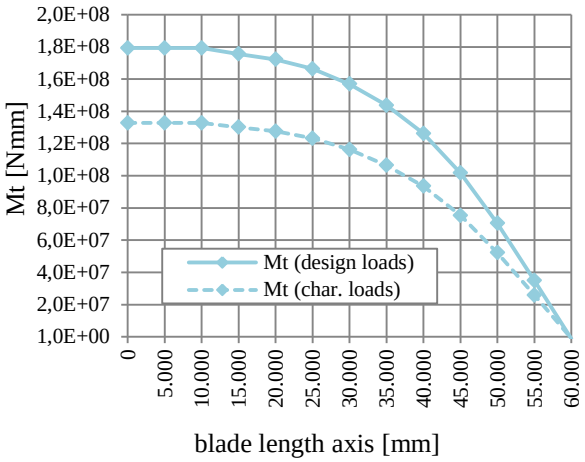

c) Centrifugal loads

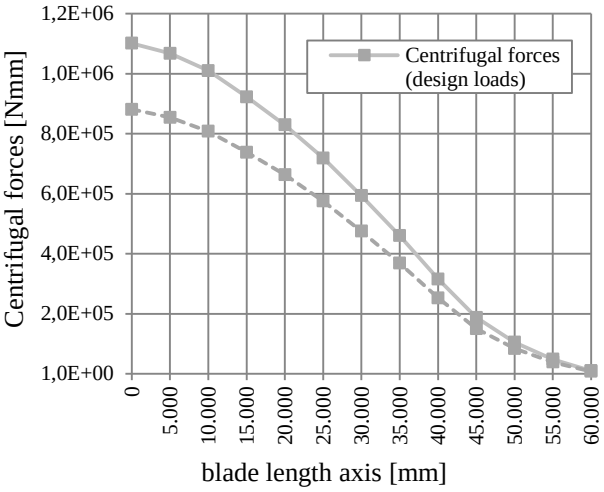

d) Flapwise bending loads in dep. on pitch angle

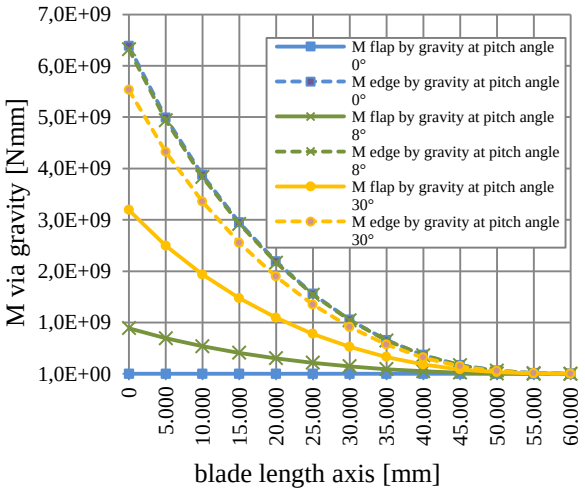

Fig. 3.5: Design loads and characteristic loads

MULTI-DISCIPLINARY OPTIMIZATION METHODS

While a straightforward load analysis and its corresponding load implementation process to an FEA are described in chap. 3.1, further work try to refine the load analysis process. Therefore, multi-disciplinary optimization tools (MDO) should be fast and fully-integrated tools that can be handled by standard software tools. [39]

The aim in [2] is to estimate the occurring stresses up to the composite structures directly depending on the wind speed and the angle of attack by applying a fluid structure interaction simulation (FSI). The co-simulation method may be defined as the interaction between the fluid mechanics and the structural analysis. Unfortunately, the work in [2] shows that this method using ABAQUS seems to be too elaborate concerning computational and modeling complexities in order to apply this method to the blade structure (Tab. 3.3). Nevertheless, the possibility of combining the computational fluid dynamics (CFD) and the finite element analysis (FEA) is shown on an oversimplified blade`s cross-section.

The work conducted in [40] uses an analytical method in order to estimate a simplified composite layup by using the tool MATLAB. The blade structure is separated into 20 cross-sections, while each cross-section is separated in several structural sub-structures in turn. The analytical based optimization method using the MATLAB tool OPTIMIZATION TOOLBOX varies the initial thicknesses of the plies in order to hit predefined bending stiffness curves according to Fig. 3.5 in flap- and edgewise direction. Results show that this method can be used as a preliminary design tool, especially to analyze the bending stiffnesses along the blade axis and the effects of CFRP spar caps. Strength properties haven`t been considered.

Fig. 2.13 shows the interactions between the structure, the geometry, and the loads. The work carried out in [41] presents a structural and aerodynamic coupled optimization method in order to determine a simplified composite layup depending on the occurring loads. The structural design is adapted to the equivalent blade shape, whereas loads and the layup are optimized iteratively by an implemented routine that connects a multi-body simulation tool FOCUS6 to the FEA tool NASTRAN.

3.2. Blade geometry

Once the aerodynamic outer shape is identified, the structural mechanical requirements are to be fulfilled. The blade structure consists of seven components: two shells, two spar caps, two shear webs and the root section. Several reinforcements, especially at the leading and trailing edges that are embedded into the shells. The aerodynamic outer contour consists of two slightly curved shells that are co-bonded during the manufacturing process. (chap.2.3) The shells are primarily responsible to generate lift and drag forces. Secondly, the shells absorb a minor part of the bending loads and torsional loads. To withstand the demanding bending forces and moments in flap- and edgewise direction, spar caps are placed along the middle axis of the shells. Spar caps, the fiber material of which is nearly exclusively aligned to the load carrying direction, accommodate the major portion of the prevailing load. Finally, the shear webs transfer the tensile and compressive forces via shear from the suction side to the pressurized side. Both, the spar caps and the shear webs also restrain the blade structure against buckling. For a preliminary analysis, the blade structure may be simplified as a bending beam. The structure, which is close to the root of the blade, has to withstand the greatest bending moments in all three spatial directions. The root section itself has to fit into the hub of the turbine. With an increasing distance from the hub along the blade, the aerodynamic properties become more and more important. The blade profiles become thinner towards the blade tip in order to obtain acceptable aerodynamic properties. Since the blade speed increases along the blade axis, the lift forces also increase towards the tip. To receive a desirable and acceptable distribution of lift forces the chord width is decreased towards the tip to counteract this effect. The shorter the distance is to the tip of the blade, the faster the effective flow rate will be. Thus, the blade geometry is the result of the trade-off between the aerodynamics and the corresponding structure. Moving along the blade length axis, aerodynamic concerns become more important. (Fig. 3.6)

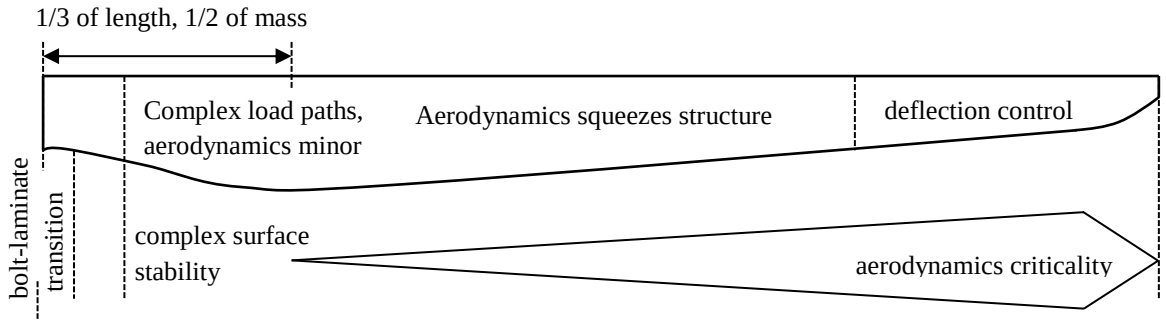

Fig. 3.1: Aerodynamics vs. structural performance (reproduced from [7])

The profile sections in Tab. 3.3 are twisted along their length axis to blade tip to receive an almost constant resulting angle of attack along the cross section to the blade tip. Irrespective of these predefined twist angles for every cross section, the blade can be pitched during

operations. This angle is designated as a pitch angle. The geometry data for the blade is listed in Tab. 3.3.

Tab. 3.3: Geometry data of the virtual blade [42]

Cross section	Radius	Chord length	Twist	Airfoil	Thick-ness	Cross section	Radius	Chord length	Twist	Airfoil	Thick-ness
[-]	[m]	[m]	[°]	[-]	[%]	[-]	[m]	[m]	[°]	[-]	[%]
1	1.500	3.542	13.308	Circle	100%	**11**	36.350	3.502	5.361	DU21	21%
2	2.867	3.542	13.308	Circle	100%	**12**	40.450	3.256	4.188	DU21	21%
3	5.600	3.854	13.308	Pro5600	90%	**13**	44.550	3.010	3.125	NACA64	18%
4	8.333	4.167	13.308	Pro8333	70%	**14**	48.650	2.764	2.319	NACA64	18%
5	11.750	4.557	13.308	Pro11750	50%	**15**	52.750	2.518	1.526	NACA64	18%
6	15.850	4.652	11.480	DU40	40%	**16**	56.167	2.313	0.863	NACA64	18%
7	19.950	4.458	10.162	DU35	35%	**17**	58.900	2.086	0.370	NACA64	18%
8	24.050	4.249	9.011	DU30	30%	**18**	61.633	1.419	0.106	NACA64	18%
9	28.150	4.007	7.795	Pro28150	27%	**19**	63.000	0.920	0.000	NACA64	18%
10	32.250	3.748	6.544	DU25	25%						

Geometry data is provided by [42, 43, 8] and slightly adapted. Essential geometry information is given in [42, p. 18ff]. The coordinates of the airfoil profiles that are disposed along the longitudinal axis, the twist angle, and the aerodynamic lift coefficients are taken from [42]. The shear webs of the blade are positioned in a parallel direction. A third web is added. More information can be found in the appendix. NACA profiles exhibit good aerodynamics.

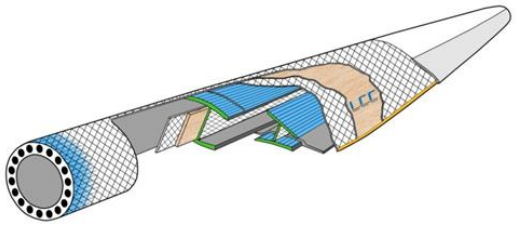

Fig. 3.2: Schematic layup of a conventional WTB

Stiffness properties can be crucial. “In the desire to make large blades as light and economical as possible, it is hard to avoid increased flexibility. This can be an asset leading to load reductions but flexibility is certainly limited in conventional upwind rotor designs by the key requirement to avoid tower strike by the blade tip in the most critical load case.” [8]

Composite design recommendations for the structure are described in the following part.

3.3. Blade components

The blade structure consists of seven individual subcomponents that are described in the subsequent context. (Fig. 2.12) Depending on the design philosophies, the structure is primarily designed to withstand either stiffness, strength, or fatigue properties. This is vastly dependent on the material used and the preferred design concepts. The blade structure described here is fully made of GFRP and, thus, primarily driven by stiffness properties. The subsequent context describes the essential design considerations of the individual components.

3.3.1. Blade root section

The circular blade root section provides the transition between the metallic hub of the plant and the composite structure. It is exposed to the highest bending moments in flap-, edge- and torsional direction occurring to the composite structure. Particularly, this section may be critical to fatigue loadings in the edgewise direction. The connection of the blade to the hub is realized via pin joints across the circular blade root section. Holes for the fasteners are commonly drilled into the laminate.[16] The mechanical fasteners cause a complex load path at the areas of the load introduction. Therefore, a quasi-isotropic composite layup is preferred. It is significant to provide an adequate number of plies orientated in circumferential directions (90°) in the root section to prevent a shear-out of the bolts. The blade model composed in this thesis is performed with a layup sequence $[0°, \pm 45°, 90°]$ and a corresponding percentage rate of [20%, 55%, 25%]. The GFRP composite layup is related to a "black metal design".

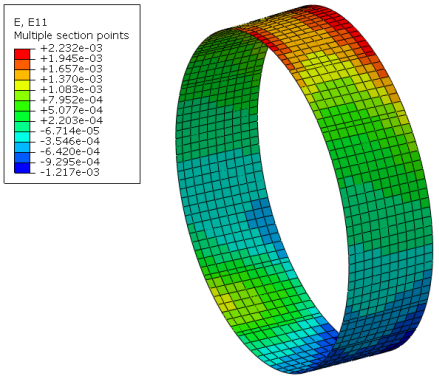

Fig. 3.3: Blade root section (load case LC2)

Modern blade designs that use a filament winding process to manufacture the blade root section do exist. This is especially done at structures that exceed 50m of blade length. The numerical model described within this thesis weighs 2.6 tons until the first 2 meters of blade length. That is approx. 10.9 percent of the total blade mass. The maximum thickness of the root section is 83mm. In this case, the component is manufactured separately and assembled on the blade structure. The corresponding joint patches are tapered. The transmission must be placed between the root section and the initiation of the spar cap very carefully. Smooth transition must be guaranteed.

[16] Common type: IKEA type root connection

3.3.2. Spar caps

The spar cap composes the main structural component of a WTB. The spar caps are allocated along the blade length axis on the top and bottom side of the blade`s shell and transfer bending moments via tensile and compression forces. While on the suction side, it is mainly designed to be stressed by compression loads, the pressure side is primarily designed to be stressed by tension loads.

The fibers are almost aligned in the direction of the blade length axis to carry the loads. Therefore, unidirectional preform material is used. The thickness of the spar caps varies with the blade length. It is stated that the spar cap commonly has the thickest area at about a third of the blade length due to the high occurring tensile and, especially, compression loads. At this area, the spar cap consists of approx. 60mm thickness for the 61.5m long blade. The unidirectional dominated NCFs should contain a small ratio of 90° layers, which act as crack arresters[17].

The width of the spar caps is constant along the blade length axis in the latest blade designs. In the majority of modern blade designs, this is because a design of constant width facilitates the manufacturing of the spar caps. Fig. 3.9 shows the (un)deformed shape of the stressed spar cap in load case LC2 (chap.3.1).

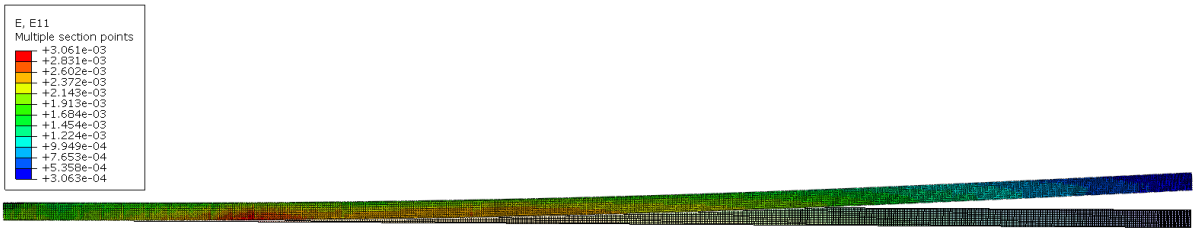

Fig. 3.9: FE-model of an (un)deformed spar cap (load case LC2)

Spar caps are mainly manufactured separately and assembled to the aerodynamic shells in a subsequent process step. A co-curing process[18] can also be employed.

Concerning the dimensions for the spar caps, two design philosophies regarding the spar cap design are applied in state-of-the-art blade structures. While the thickness of the spar cap`s laminate is not constant along the blade length axis, the width-to-thickness ratio can be discussed. While one fabricator utilizes broad and relatively thin spar caps (option A), the other utilizes slight and relatively thick spar caps (option B). Option A induces that broad spar caps fill out a good portion of the aerodynamic shell, especially in the area of the blade tip. In turn, UD fabrics in blade length direction do not account to withstand the edgewise and torsional stiffness, which is actually the task of the aerodynamic shells. Thin structures tend to

[17] A NCF [0°, 90°] with a ratio of [90%, 10%] is recommended and used for the model.
[18] Co-curing: The process step of curing a composite laminate and simultaneously bonding it to another uncured composite material.

buckle or lead to local wrinkling. In contrast to option A, thick composite structures – as mentioned in option B – are very prone to process induced deformations (PID). The nascent exothermal temperature during the curing process causes residual stresses. Due to both the infusion process and the varying thickness, it is not unusual that the matrix system in the end sections has already started to gel, while the matrix system in the very thick cross-sections has not yet been saturated. The occurring exothermal temperature leads to undesirable deformations of the structure.

Another central point is the selection of the matrix system. Spar caps belong to the thickest and largest composite structures that are generally infiltrated in industrial composite applications. Therefore, on the one hand, matrix systems of a low-viscosity are beneficial for the infiltration of thick and large structures; on the other hand, it should be guaranteed that the exothermal temperature during curing does not lead to undefined deformations during the curing process. Using a low viscosity matrix system can lead to a high fiber volume content. In fact, this has positive influence on the stiffness of the component, but may have negative influence on the strength and fatigue behavior.

Spar caps are generally prone to fiber failure. The design criterion of a GFRP layout tends to result in stiffness properties, while a CFRP layout may rather be prone to strength properties. Layouts comprised of POLYESTER systems instead of EPOXY systems are more prone to fatigue issues. Further failure modes may occur due to ply waviness. (chap.5)

Additional unidirectional reinforcements are commonly placed at the trailing edge and are further described in chap.3.3.3.

3.3.3. Aerodynamic shells

The main task of the aerodynamic shells is to affect the aerodynamic lift. Further tasks of the shells are to carry the torsional loadings due to aerodynamic, gravitational and centrifugal forces. Nevertheless, the aerodynamic shells also admit a portion of loadings in flap- and edgewise direction. From a structural perspective, the shell is separated in four sections: a) the leading edge, b) the main, c) the spar cap and d) the trailing edge area. The leading and trailing edge is primarily made of UD fabrics oriented in the blade length axis to absorb the loadings in edgewise direction. Additional fabrics of ±45° orientations are placed in the inner side of the leading and trailing edge to strengthen the adhesive bonds connecting the semi-halves. Secondarily, the ±45° fabrics improve the impact behavior at the leading edge. This area is exposed to corrosion, airdrops, grains of sand, and particles flying through the air. The main area (b) consists of a sandwich structure. Top and bottom layers are oriented in such a way as to withstand torsional loadings and to take shear stresses. NCFs containing ±45° oriented plies (biaxial clutches) feature good draping properties, while NCFs containing 0° and ±45° orientated plies (triaxial clutches) are relatively poor for draping into the mold. The use of the combination of BIAX and TRIAX clutches is not recommended. [26] The type and thickness of the embedded sandwich materials are strongly dependent on the prevailing loading conditions and design considerations. In general, it is stated that sandwich structures located at the beginning of the blade structures are made of the core material BALSA, while for the subsequent structure the core material PVC and PET are used. It should be mentioned that the core material belongs to the most expensive material in WTBs, in the case that CFRP is not used.

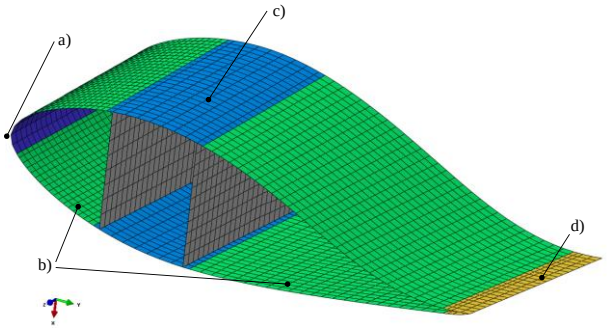

Fig. 3.4: FE-model of an aerodynamic shell

Aerodynamic shells are prone to inter-fiber failure due to their complex loading conditions. Depending on the prevailing blade design buckling can also be a critical failure mode. Further failure modes may occur at the ply-drops due to inter-laminar tensile stresses (ILTS) and inter-laminar shear stresses (ILSS).

The blade model is composed of a symmetrical layup, on both the suction and pressure side. The shells are manufactured separately in parallel and jointed after they have been cured. The spar caps are joined into the shells (see also chap.2.3)

A critical region of the aerodynamic shell is the trailing edge in particular; mainly between 0 - 35 meters at edgewise loading. In addition to inter-fiber failure, the shell is critical to buckling modes. A relatively high torsional stiffness is given due to its closed geometrical shape and the presence of ±45° orientated plies.

3.3.4. Shear webs

Shear webs are designed to transfer shear forces that originate from the bending moments. The webs are disposed in a parallel manner to the lengthwise axis. The blade model uses a distance 700mm between the two webs. In many designs, the spar caps are placed within the endings of the webs. The width of the spar caps also slightly exceeds the distance between the two webs. Alternatively, designs using dihedral dispositions of the shear webs and architectures, which allot 2.5 shear webs, are present. This means that two webs run parallel to the blade length axis from about 1.5 meters to 55 meters of the blade length. A third shear web is added at the thickest area of the trailing edge. The origins of the webs are endued with a circular cut-out. This is done to minimize the compression forces at this area.

Sandwich structures are used to prevent buckling. The face sheets are mainly designed by $\pm 45°$ plies. The $\pm 45°$ plies are forced to uptake the prevailing shear forces. Additional 0° plies in the lengthwise direction absorb minor portions of bending moments, which is primarily the task of the spar caps. Core materials are mainly imposed to in-plane shear stresses.

The shear webs are separately manufactured and finally bonded with the aerodynamic shells. Beginning at the blade root, the sandwich structure has a linear decreasing core thickness (35 to 30mm). The end fittings of the top and bottom layers are straightened appropriate to Fig. 3.11 (right) in order to assure a sufficiently large adherent.

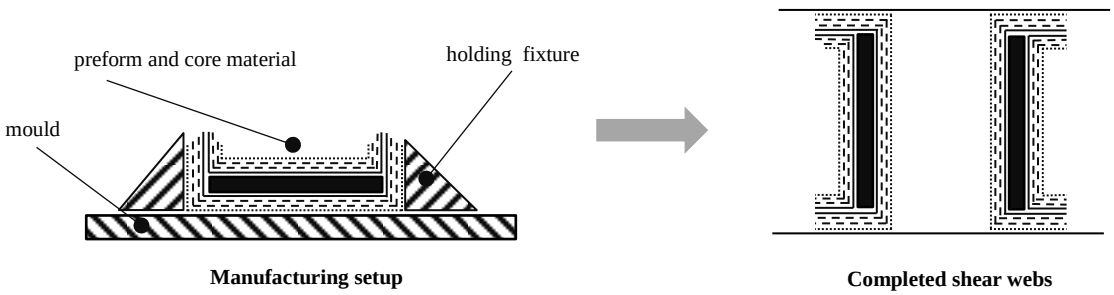

Fig. 3.11: Shear webs: Manufacturing setup and completed parts (cross-sectional views)

The extended layers are adjusted to the outer side of the cross section. It has to be guaranteed that the shells are bonded to the webs along the whole contact surface. The issue is that the bonding mechanism cannot be controlled because some areas are not accessible during and after the assembling process.

3.4. Description and implementation of the numerical model

The computer-aided design (CAD) software CATIA V5R19, the finite element (FE) environments ABAQUS 6.11.2 CAE of the company DASSAULT SYSTEMS (DS) and the FE software HYPERWORKS 11.0 of the company ALTAIR ENGINEERING are utilized for the implementation of the numerical model. It should be indicated that simplifications are rendered in order to reduce the complexity:

- A quasi-static load scenario is assumed (chap.3.1).
- Strains and stresses in in-plane directions are considered, 3D stress states are not considered. A layered shell element model is used.
- Ply drop-offs in the chord-wise direction are not incorporated within the model.

The geometry is created as a three dimensional surface model. The profile points are imported by a macro[19] to CATIA V5 R19. It is recommended to create a surface model instead of a solid model[20]. The reason for that is that surfaces are highly suited for a composite structure, which is implemented to layered shell elements. Due to a high complexity of the composite layup, the use of volume elements is unconvertible. For analyzing the three-dimensional stress states, shell elements are restricted. Nevertheless, transverse shear stresses in the out-of-plane direction can be approximated. [38] For an analysis considering 3D stress states, a sub-model of a representative cross-section with volume elements, which describe the geometry more precisely than shell elements, is recommended.

The geometrical model is imported both to the finite element environment HYPERMESH (HM) and ABAQUS. Thus, the geometrical model is exported by using the format ".stp", because the geometry is transferred more precisely than with the other formats. Complex geometrical shapes are especially prone to corrupt geometry import. The option to export the model first to HYPERMESH and later to ABAQUS is done to evaluate different pre-processing techniques. The result is that the software HM offers both superior methods of geometrical finishing and precious meshing methods compared to ABAQUS. Having finished on refining the geometrical partitions, the geometry is partitioned with respect to the imposed composite layup design that is integrated into the model in a later implementation step. In addition, the structure is partitioned in constant and orthogonal distance to the longitudinal axis.

[19] Software tool *GeometryFromExcel* by DASSAULT SYSTEMS
[20] Usage of the software module GENERATIVE SHAPE DESIGN

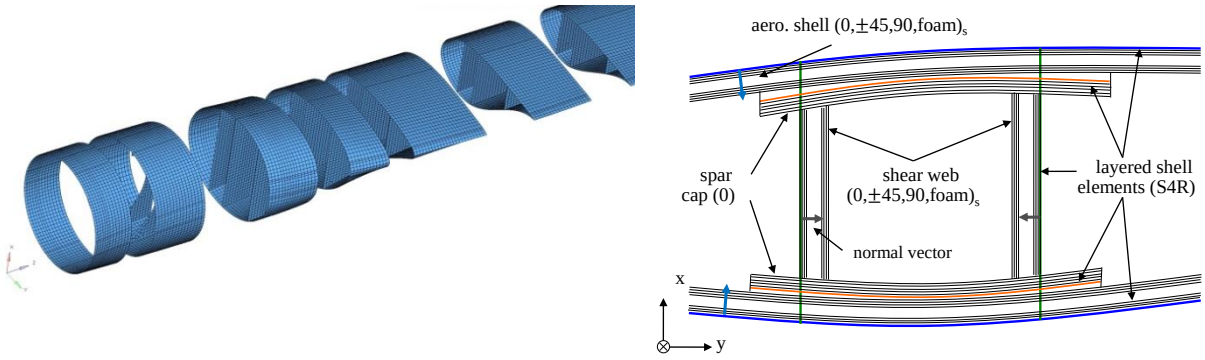

Fig. 3.12: Meshed structure (left); cross-section of WTB (right)

It is secured that the mesh accords to the imposed composite layup. A convergence study considering the mesh element size is conducted [44, p. 34]. The change of displacements and natural Eigenfrequencies are analyzed while the average element size is decreased. The result is that a characteristic element size of 160mm provides sufficient results (divergencies <<1%). Although the GL recommends a characteristic element length of 100mm, the characteristic element length of the model presented in this thesis is of approx. 70mm. The number of the degree of freedom is approx. 700,000.

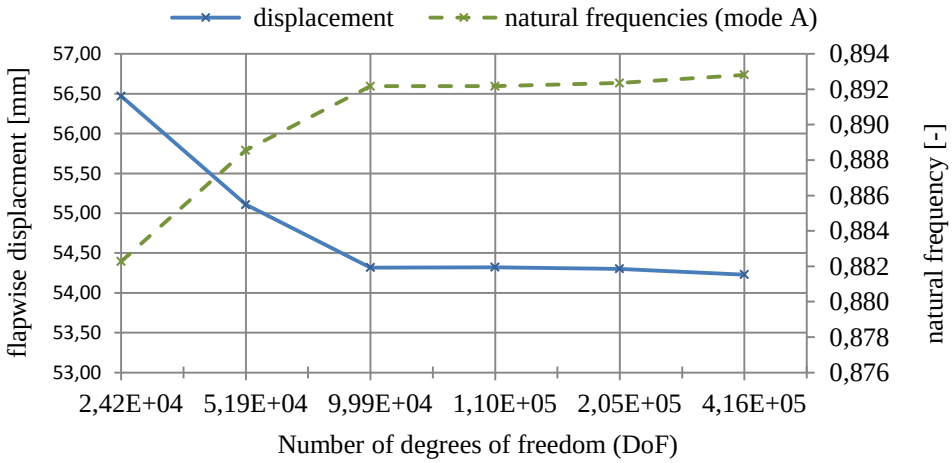

Fig. 3.13: Convergence study

Finally, the part is meshed using conventional shell elements (S4R). A ply-based implementation of the composite layup is considered. Therefore, the geometrical sets, which facilitate the implementation of the composite layup in further steps, are generated. Fig. 3.14 shows the geometric shape as the CAD-model (left) and the finite element model (right).

Fig. 3.14: CAD-model (left); FE-model (right)

The material data is provided[21] in the form of smeared ply data: E_{11}, E_{22}, G_{12}, ν_{12}, ϱ. This data is required to calculate composite material using the CLT. For analyzing the failure behavior of the composite material, specific strength criteria are appended. Hence, the failure behavior of composite material differs both in tensile/compression and in along/orthogonal fiber direction, the strength parameters R_{11t}, R_{11c}, R_{22t}, R_{22c}, R_{12} are required.

The information of the composite layup is documented in a plybook and imported to ABAQUS by a text file. The lack of information concerning a modern composite layup operates to a highly iterative procedure. For the initial position, a cardinal selection of standard components – the spar caps, the shear webs, the aerodynamic shells, the root section, leading- and trailing edge – is made. Furthermore, its prime fiber orientations are also mentioned. Available information about a detailed composite layup of a modern WTB is restricted. The quantity of parameters and the possibilities of parameter variation are so intensive that it is unfeasible to create a modern composite design without specific precognitions about the composite layup. An approximate composite layup of a WTB is generated in cooperation with industrial partners[22] due to their expertise on design issues. The results of the cooperation are used to reproduce a revised composite layup design that is adapted to the applied load scenarios.

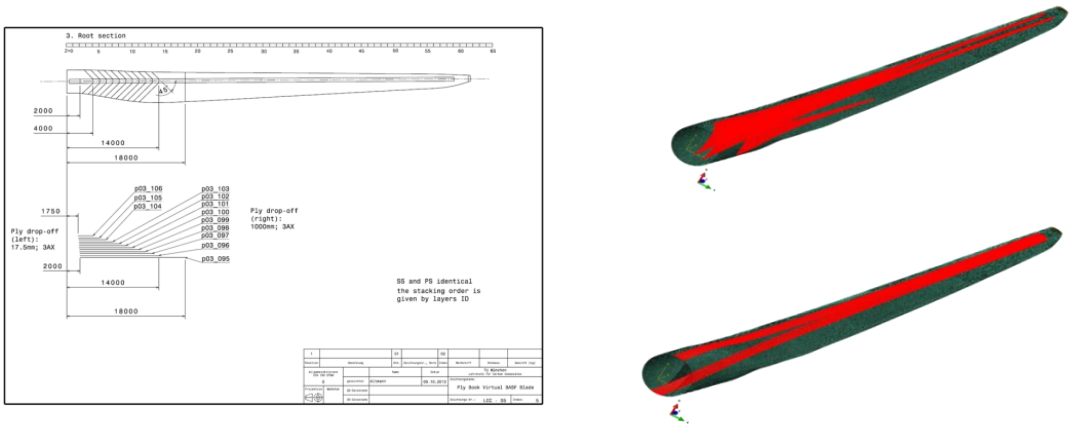

Fig. 3.15: Exemplary excerpt of the plybook (left), geometrical sets (right)

It is recommended to implement the composite layup using a text file due to the intensive computational costs. To give an idea: 550 single plies are implemented. The generation of the composite layup is a tremendous iterative design process. The laminate composition, stacking

[21] By BASF AG, System Integration Group Wind Energy
[22] Industrial partners: *Robert Bosch GmbH* and *Aero Dynamik Consult mbH*

order, sequence, ply location, and orientation are interactively adapted to predefined requirements.

The resulting forces and moments calculated by the analytical method in chap.3.1 are implemented into the numerical model. This is done via multi-point constraints (MPC) at numerous cross sections. The method is also described in chap.3.1. The MPC interface gives the option to resume load scenarios that are determined by multi-body-simulations for wind turbine blades.

The preprocessing steps of the model are completed by requesting the designated output values. The main-processing steps comprise the solving of the finite element equations. In this case, it is recommended to use a linear solver, assuming a linear elastic material behavior til the failure of the first ply. Non-linearities occurring in the matrix system are neglected. Geometrical nonlinearities can also be neglected due to the dimensions of the structure. ($u_{max} > t_{structure}$) Finally, the numerical model is used to conduct material parametric studies that allow evaluating the structural mechanical effects of matrix, core, and fiber properties related to the structural requirements in chap.4. The design process is summarized in Fig. 3.16.

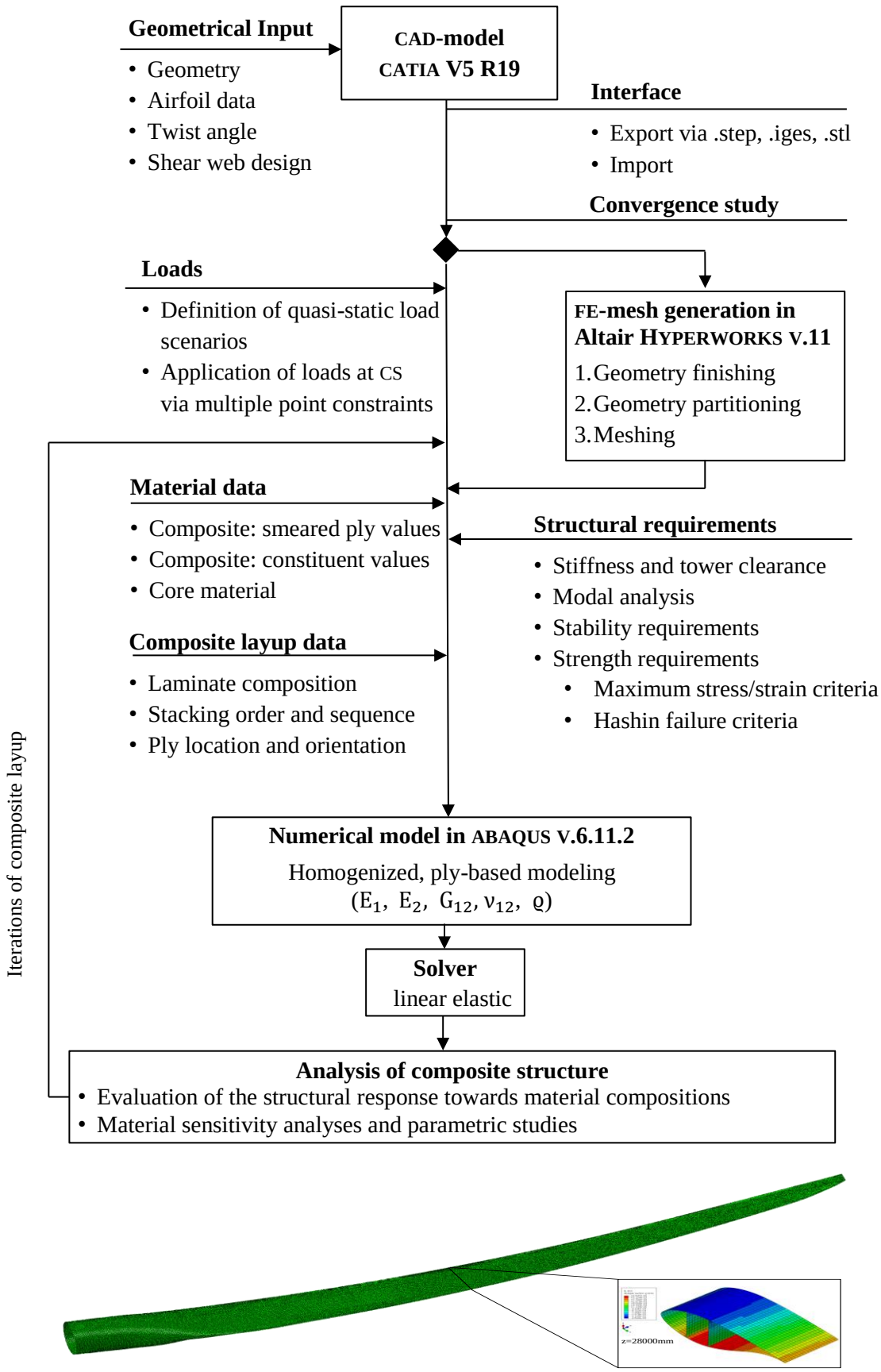

Fig. 3.5: Iterative design process - schematic routine

3.5. Validation of the numerical blade model

Assumptions, boundary conditions, geometry, loads, and composite layup have been double-checked by GL and project partners. The stiffness, strength, modal and buckling analyses are been carried out and fulfil the requirements. Within this context the determination of the bending stiffness is further described. The stiffness distribution of a WTB along its length is a crucial structural characteristic. Thereby, the consistency of the conventional and state-of-the-art rotor blade can be proven. Its curve highlights potential changes in stiffness by discontinuities. Since the bending stiffnesses are dependent on geometry, material properties, and composite layup, its characteristics are comparative parameters.

Commercial tools like ABAQUS, ANSYS and HYPERWORKS do not offer the option to determine the bending stiffness at defined cross-sections that consist of composite material. The anisotropic behavior of a composite structure exacerbates its determination. Thus, a method to estimate the bending stiffness is developed and described in the following.

With the aid of the beam theory, bending stiffnesses EI of predefined cross-sections are determined by the quotient of a simplified uniaxial bending moment $M_b(z)$ and the curvature $\theta'(z)$ of the structure:

$$EI(z) = \frac{M_b(z)}{\theta'(z)} = \frac{M}{u''(z)} \tag{3.20}$$

The specified angle $\theta' = d\theta/dz$ may also be determined by the second derivation of the bending in z-direction $u''(z)$. A defined uniaxial bending load is applied to the structure by a function of forces in flapwise direction. The torsion angle θ is determined by the displacements of predefined nodes (3.21):

$$\theta_n = \frac{u_{n+1} - u_n}{\Delta z} \tag{3.21}$$

$$\theta_{n-1} = \frac{u_n - u_{n-1}}{\Delta z} \tag{3.22}$$

$$\theta'_n = \frac{\theta_n - \theta_{n-1}}{\Delta z} \tag{3.23}$$

Alternatively, the torsion angle θ' may also be determined by using the finite difference method:

$$\theta' = u'' = \frac{u_{n+1} - 2u_n + u_{n-1}}{\Delta z^2} \tag{3.24}$$

Fig. 3.17 shows schematically the determination of the bending stiffness EI in flapwise direction. The equivalent procedure is conducted to determine the bending stiffness EI in edgewise direction.

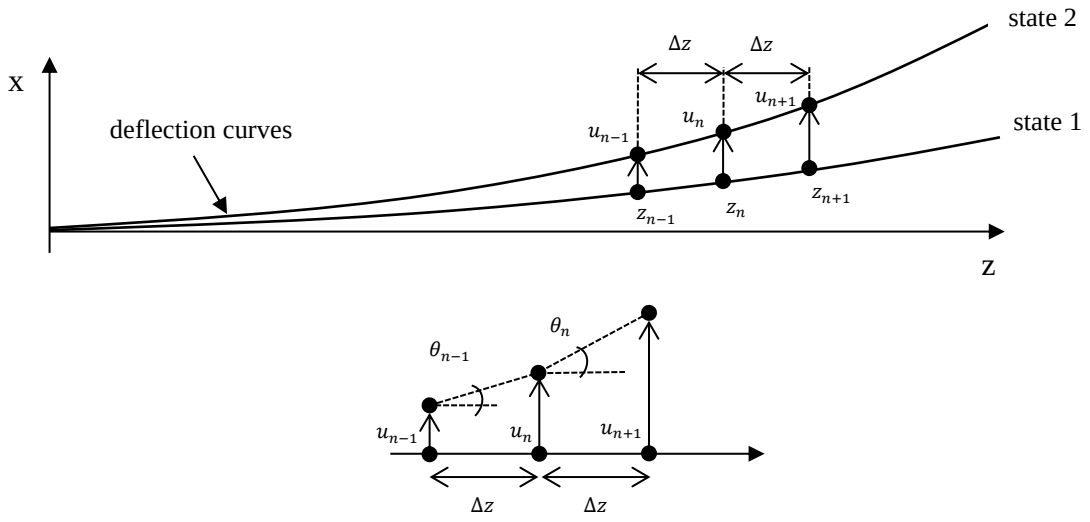

Fig. 3.17: Determination of bending stiffness EI in flapwise direction

A python script is implemented and used to determine the bending stiffnesses in flap- and edgewise directions. This method can be adapted to any composite structure in order to evaluate its bending stiffness. Results shown in Fig. 3.18 are in good accordance with stiffness curves determined by the MBS software FOCUS6. [45]

a) flapwise direction

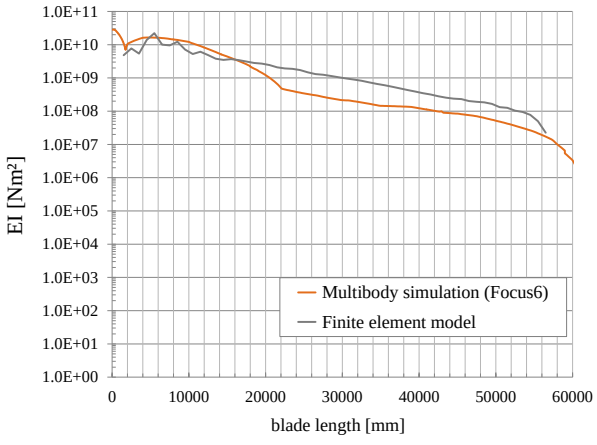

b) edgewise direction

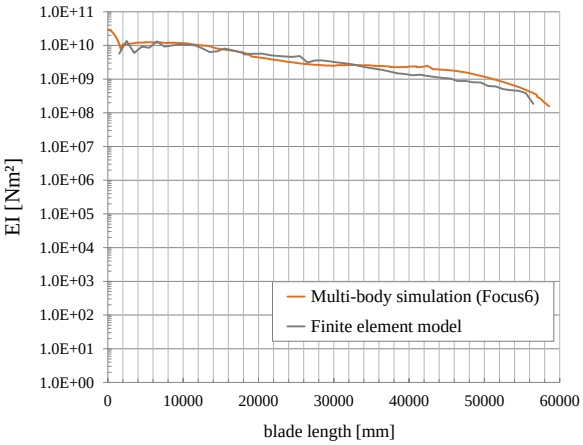

Fig. 3.18: Bending stiffness EI [Nm²] in flap- and edgewise directions

4. Sensitivity analyses and parametric studies considering matrix dominated effects

The objective is to determine the matrix dominated effects (chap.4.1) on the structural performance of the blade structure (chap.4.2). A two-stage approach is taken: First, sensitivity analyses are performed to identify how the matrix properties influence the structural behavior of a conventional WTB. (chap.3.4) Based on these findings, the most influential variables are identified over a series of analyzed responses. Second, parametric analyses are carried out to generate response surface approximation models (RSA). While a distinct focus is on the effect of the matrix properties on ply and especially on structural level, sensitivity studies are also carried out for selected sandwich core materials.

Two different hybrid GFRP/CFRP design studies considering a cost-optimized design using low-cost CFRP (chap.4.3.1) and the use of low-cost CFRP for bend-twist coupled blades (chap.4.3.2) are carried out. Once the potentials of the studied materials` properties are identified, the research in the material development can be refocused towards their specific requirements.

4.1. Matrix dominated effects on ply level

The Young`s Moduli E_{11}, E_{22} and the Shear Modulus G_{12} are calculated by using ROM and displayed against varying fiber orientation under tensile loading in Fig. 4.1. While E_{11} significantly decreases with raising fiber orientation til a minimum is reached, the G_{12} reaches its maximum at 45° fiber orientation. The spectra of the depicted curves (E_{11}, E_{22}, G_{12}) represent the effects of the matrix systems. Thus, the lower and upper bounds illustrate a 50% decrease and a 50% increase of matrix stiffness properties respectively. Observing E_{11}, the more the angle of rotation increases, the more the properties of the matrix system affect the properties of a UD ply. The Shear Modulus G_{12} is influenced most at the 45° orientation.

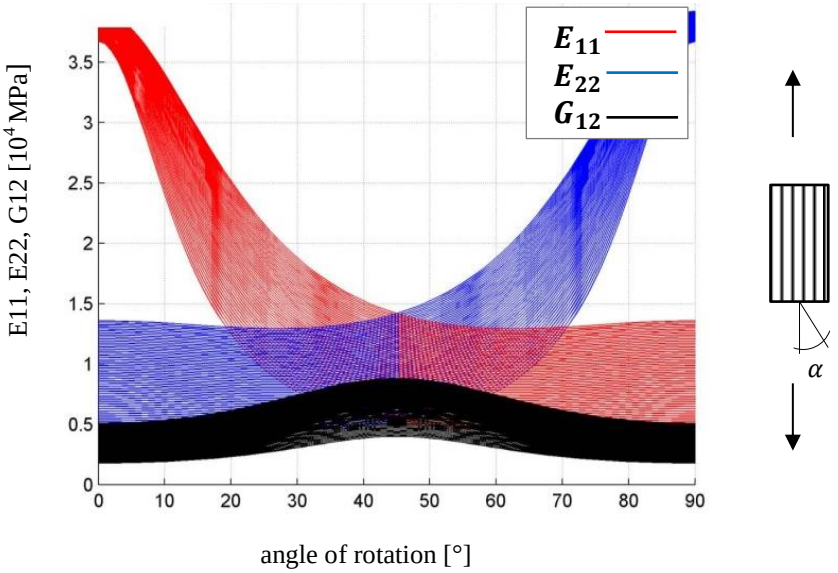

Fig. 4.1: Stiffness vs. angle of rotation [37] using the rule of mixture

Next, the stiffness and strength properties of a homogenized UD ply depending on the Young`s Modulus of the matrix system are plotted in Fig. 4.2. The lower and upper bounds are much wider than those currently commercially available in the industry, which spread around the nominal value of 3000MPa. By means of ROM and by use of experimental data, the curves are extrapolated to the aforementioned scope. Nowadays, the Young's Modulus of technically producible EPOXY matrix systems ranges around 3000MPa. In the medium term, given the current investigations, this range is expected to widen up between 2000 and 4500MPa. In the long term, a scope between 1200MPa to 6000MPa may be covered by novel technical improvements and is therefore considered in the subsequent analyses. Results show that matrix properties strongly affect the UD properties in transversal and shear direction, while properties in fiber direction are slightly affected. The influence of matrix systems on the strength properties (Fig. 4.2) is based on assumptions considering single experimental test data due to missing experiments and the impreciseness of current simulation methods. Especially, the transversal tensile strength (R_{11}^{c}), the transversal compressive strength (R_{22}^{c}) and the shear strength (R_{12}) are affected most by the matrix system.

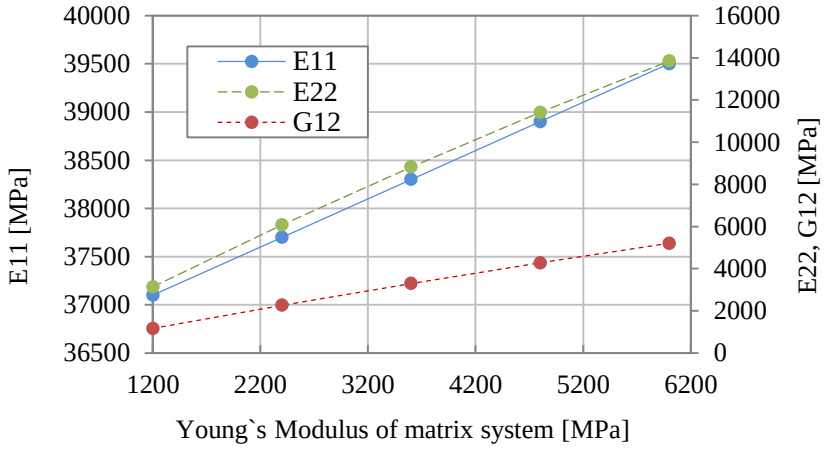

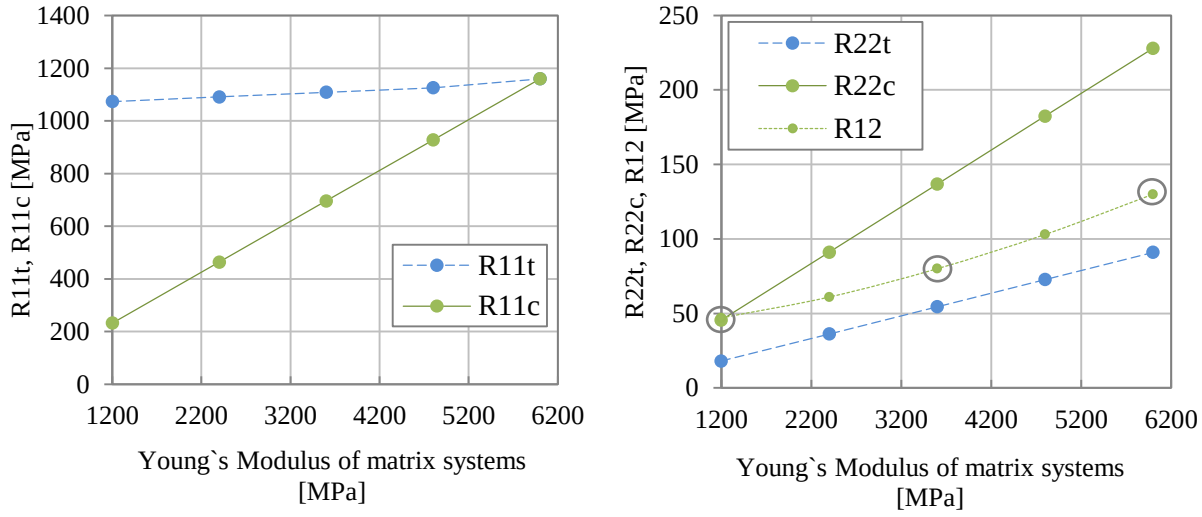

Fig. 4.2: Homogenized properties of a UD ply against Young Modulus of matrix system – stiffness properties (top) and strength properties (left and right)

The strong influence of the matrix properties on ply level manifests the intention to analyze its effects on structural level. The material data shown in Fig. 4.2 is utilized for the subsequent sensitivity and parametric studies.

4.2. Matrix dominated effects on structural level

While varying the matrix properties, a series of parametric studies are performed. The relevant findings are divided into three structural responses:

- Stiffness analyses,
- strength analyses and
- stability analyses.

Mass effects are also considered. Material data (chap.4.1) is inserted within the numerical model described in chap.3. Every simulation is carried out under the equivalent load conditions of scenario 2. (see Tab. 3.2) The geometry of the blade remains unchanged.

The analysis of the influence of each one of the variables is performed using a two-step approach. First, **sensitivity analyses** are carried out in order to define the parameters that influence the corresponding study most on each one of the corresponding responses. So, the number of variables (dimensions of design space[23]) is reduced without compromising the accuracy of the model. A 2^{k-p} fractional factorial design of experiments (DoE) [46] provides an efficient sampling pattern keeping the number of simulations low. By this way, the dimension of the original design space is reduced without compromising the accuracy of the subsequent studies. [46] [47]

[23] Maximum and minimum values comprise the design space.

In order to analyze the central effects and interactions of effects, a useful and widespread tool is the Pareto analysis. The Pareto analysis is a formal decision-making analysis method enabling the identification of the most significant effects. The Pareto plot consists of two overlaying diagrams, namely a histogram and a curve. Every pillar of the histogram corresponds to the absolute value of the main effect or interaction. Results are carried out by FE-analyses. The cumulative percentage value of each effect is depicted on the secondary axis. Effects that are lower than 5% are removed for clarity in the subsequent studies.

Based on the findings of the corresponding sensitivity studies by screening significant variables for a determined response, detailed analyses using a full factorial design method [46] are carried out. The number of numerical simulations taken along every variable depends on its impact factor. RSA-models are constructed using an extended meta-modeling technique called Kriging interpolation algorithm. RSA-models enable the prediction of every response as a function of the most influential global variables. [48] Hence, **parametric studies** are derived and finally discussed.

The high complexity of the FE model used requires the definition of multiple variables. The materials' parameter variables analyzed and varied within this study are listed in Tab. 4.1. According to their nature two main groups can be identified: ply-thickness related variables and variables related to the material properties. The former refer to and modify the original thicknesses of the plies depending on the material of which they are made. The latter are incorporated within the analysis as the homogenized stiffness and strength properties according to Fig. 4.2.

Although a distinct focus is on the effects of matrix systems on the structural performance, thickness effects of the individual plies and the mechanical properties of core materials are also analyzed because of their strong interaction and influencing character on the blade structure. The density of the core materials is linked to the mechanical properties in Appendix B. For the sake of simplicity, the material parameters are assigned to a nomenclature, to which it is referred in the latter.

Tab. 4.1: Description of materials' parametric variables

Material variable	Design space	Unit	Nomenclature
Thickness of plies (except of spar caps)	±50%	[-]	A
Thickness of spar cap plies	±50%	[-]	B
Thickness of foam core	±50%	[-]	C
Thickness of Balsa core	±50%	[-]	D
Mechanical properties of plies (effected by matrix systems in chap. 4.1)	[1200,6000]	[MPa]	E
Mechanical properties of spar cap plies (effected by matrix systems in chap. 4.1)	[1200,6000]	[MPa]	F
Density of foam core	[40,250]	kg/m³	G
Density of Balsa core	[110,318]	kg/m³	H

4.2.1. Stiffness properties

The stiffness behavior is indicated by the displacement of the blade tip in Fig. 4.3. It depends mainly on three material parameters: the thickness of the ordinary plies (A), the thickness of the spar caps (B) and the matrix properties (E). However, there are important differences among the different displacement modes, as shown in the Pareto analyses.

Displacement in flap-wise direction is about 4 times higher than in edgewise direction and is clearly dominated by the thickness of the load-carrying spar cap plies (60% of the variability) having ordinary ply properties a much lower influence. In contrast, edgewise and torsional deformations depend fundamentally on the thickness of the ordinary plies and on the Young`s Modulus of the matrix system. The reason for this is that the shells (chap.3.3.3) under edgewise and torsional loading are mainly stressed by shear.

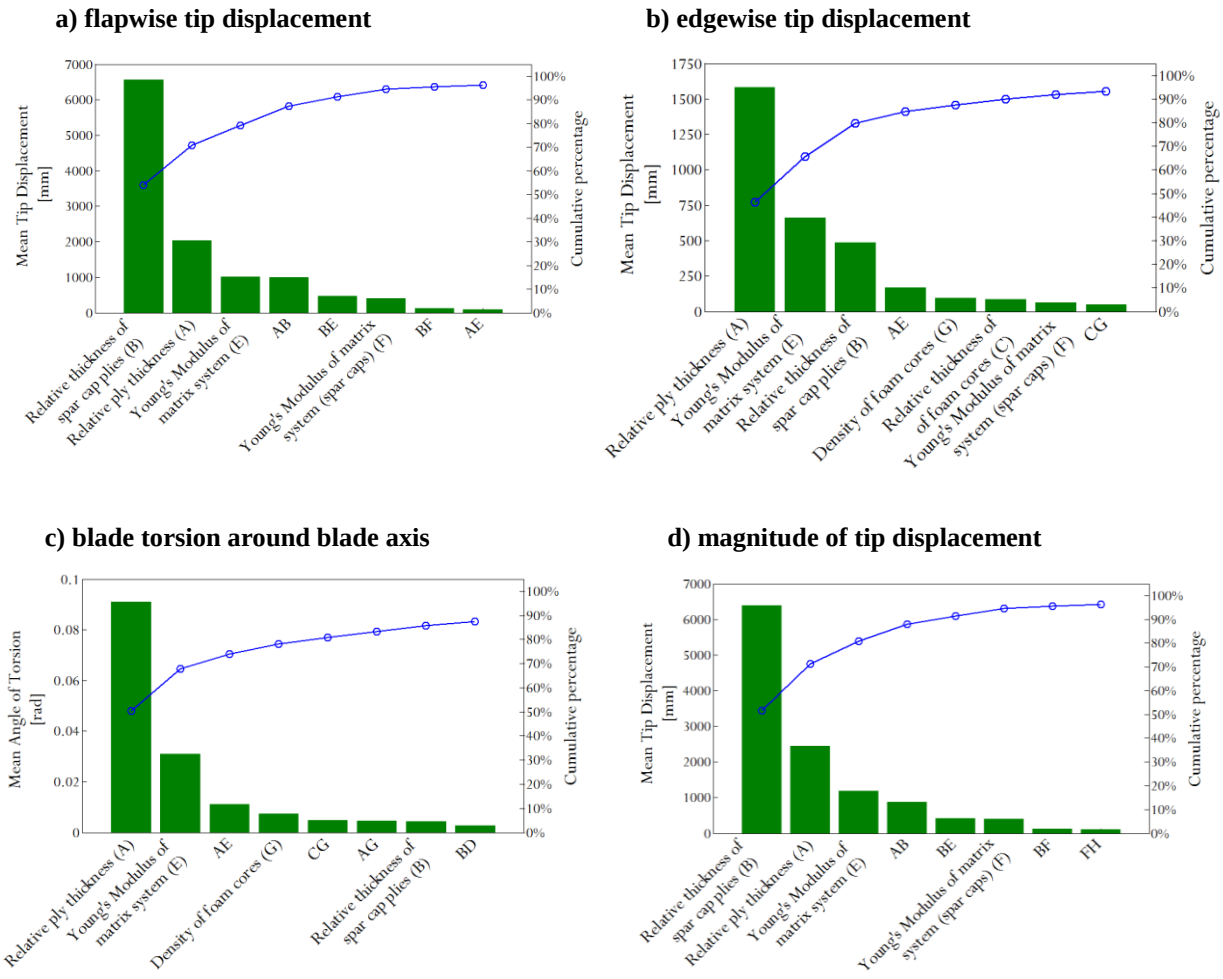

Fig. 4.3: Pareto analysis of the blade deformation (Effects are shown til a 95% variability is explained.)

The corresponding RSA-model computed by a full factorial design method is depicted in Fig. 4.4. The blade displacement is plotted in dependence on the three most significant variables

outlined in previous sensitivity studies. As the magnitude is dominated by the flapwise component, so is its dependence on the spar cap ply thicknesses.

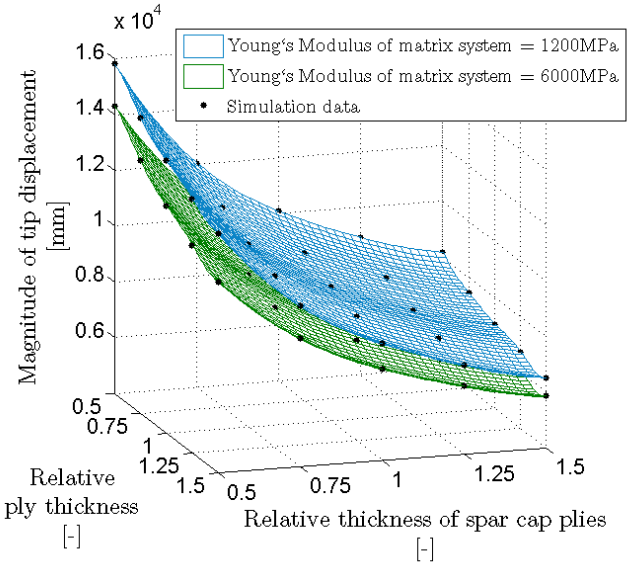

Fig. 4.4: RSA-model for the blade deformations by kriging interpolation [47]

Further, the natural frequencies rise with increasing matrix stiffness properties, too. While the frequencies in flap- and edgewise direction only increase minimally, the effect is greater on torsional frequencies.

4.2.2. Strength properties

The strength behaviour of the blade is analysed by the total number of ply failures within each element occurring on the GFRP plies according to both the maximum stress criterion and Hashin's 2D failure criterion. The maximum stress criterion considers no interaction among the stresses and does not distinguish between fiber failure (FF) and inter-fiber or matrix failure (IFF). The failure function f is computed at every ply of every FE according to Equ. (4.1). If the value is greater than 1, a ply failure occurs.

$$f = max\left(\frac{|\sigma_1|}{R_{11}^{t/c}}, \frac{|\sigma_2|}{R_{22}^{t/c}}, \frac{|\tau_{12}|}{R_{12}}\right) = 1 \tag{4.1}$$

The Pareto analysis in Fig. 4.5 reveals the strong effects of the matrix properties on the strength behavior. These, together with the thickness of the plies (A) and the interaction between the thickness and the mechanical properties of the plies (AE) dominate the strength behaviour of the structure.

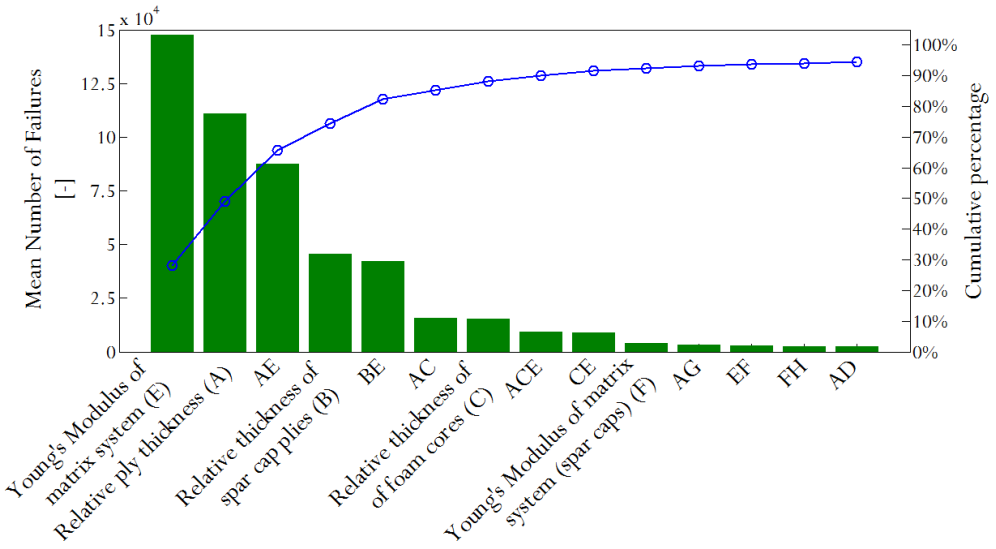

Fig. 4.5: Pareto analysis according to max. stress criterion

The partly interactive failure criterion according to Hashin [49] is applied in order to differentiate between FF and IFF, for each tension and compression. IFF can also be referred to as matrix failure. Equ. (4.2) - (4.5) are evaluated at every element and predict each ply failure.

FF tension
$$\left(\frac{\sigma_{11}}{R_{11}^{t}}\right)^{2}+\left(\frac{\tau_{12}}{R_{12}}\right)^{2}=1 \qquad \sigma_{11}\geq 0 \tag{4.2}$$

FF compression
$$\frac{-\sigma_{11}}{R_{11}^{c}}=1 \qquad \sigma_{11}<0 \tag{4.3}$$

IFF tension
$$\left(\frac{\sigma_{22}}{R_{22}^{c}}\right)^{2}+\left(\frac{\tau_{12}}{R_{12}}\right)^{2}=1 \qquad \sigma_{22}\geq 0 \tag{4.4}$$

IFF compression
$$\left(\frac{\sigma_{22}}{2R_{22}}\right)^{2}+\left[\left(\frac{Y_{c}}{2R_{22}}\right)^{2}-1\right]\frac{\sigma_{22}}{R_{22}^{c}}+\left(\frac{\tau_{12}}{R_{12}}\right)^{2}=1 \qquad \sigma_{22}<0 \tag{4.5}$$

Focusing on the different failure modes according to Hashin`s criterion (Fig. 4.6), it reveals that the strength behavior of the blade structure is driven by the failure modes of *fiber compression failure* and *matrix tension failure*. Considering the failure mode *fiber compression failure* the properties of the matrix system are crucial. If one regards the failure mode *matrix tension failure* the matrix properties are second in significance.

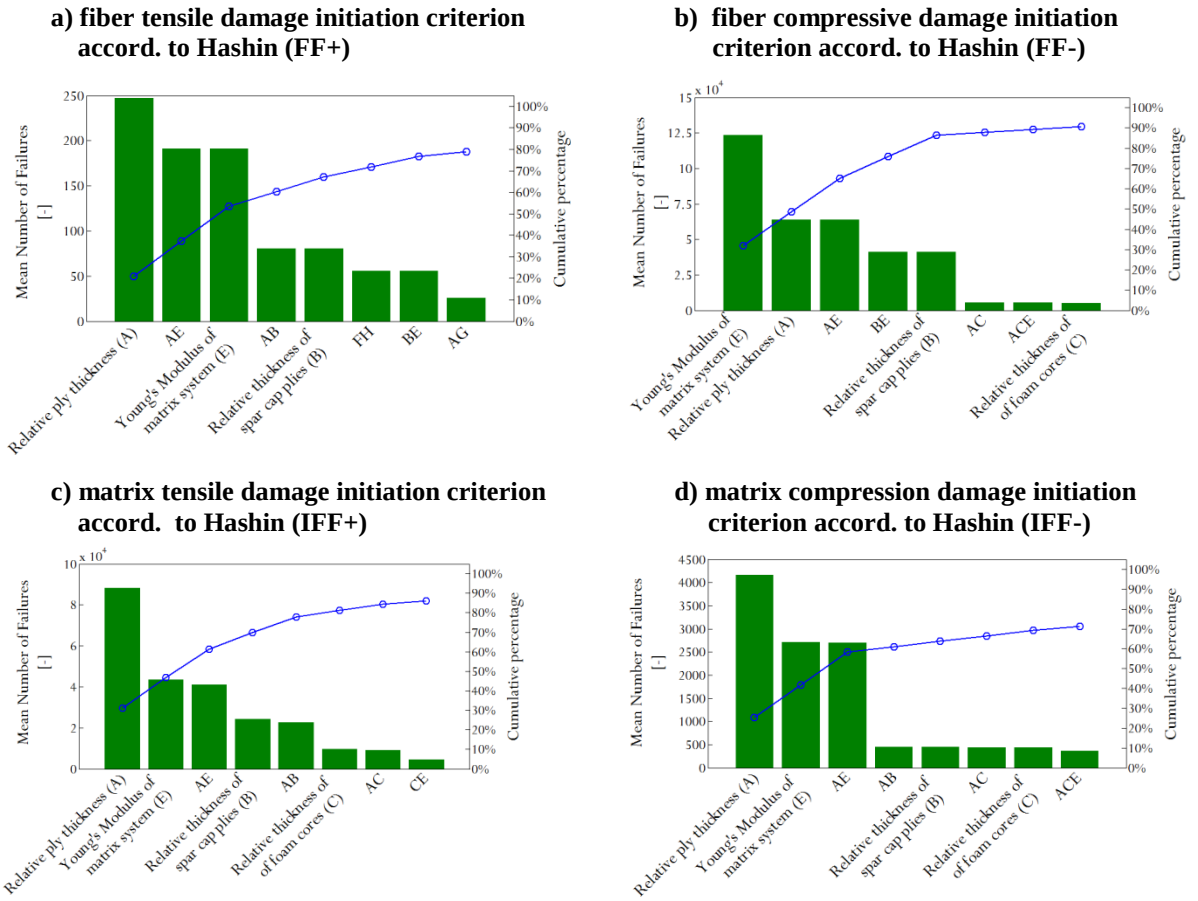

Fig. 4.6: Pareto analysis of number of failures in GFRP plies according to the different failure modes of Hashin Failure Criterion [47]

The number of failures according to the maximum stress is depicted in Fig. 4.7. Results are displayed against the two main parameters, i.e. Young`s Modulus of the matrix system (E) and the relative thickness of the plies (A), in four surfaces, each one corresponding to a different combination of the levels of the less significant variables: thickness of the spar cap plies (B) and of the foam cores (C). It can be appreciated that what boosts the failure rate, is not the factors alone, but their simultaneous setting, which reflects the strong interaction effect (AE) shown in Fig. 4.6.

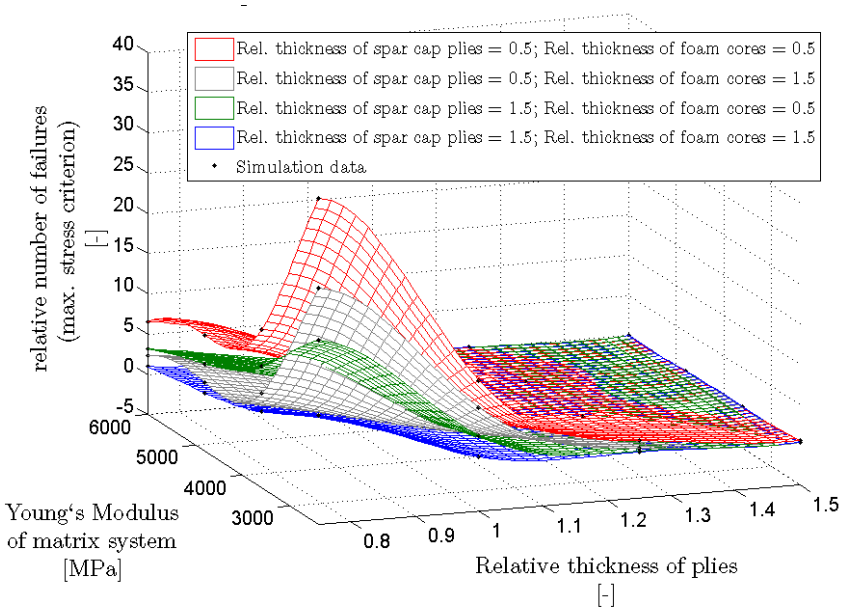

Fig. 4.7: RSA-model for strength properties indicated by the max. stress criterion

4.2.3. Stability properties

The structural stability of the blade is evaluated by the buckling safety factor (BSF). This index, computed by a linear perturbation analysis, takes positive values, which indicate structural stability (if BSF > 1) or predicts a buckling failure if BSF ≤ 1. Fig. 4.8 shows the corresponding results of the Pareto analysis. In contrast to previous sensitivity analyses, the stability behaviour depends fundamentally on the thickness (C) and density (G) of the foam cores. The thickness of the ordinary GFRP plies (A) is the third most important cause. These factors and their interactions explain more than a 75% of the response variability. Notice that matrix dominated effects play a minor part considering the stability performance.

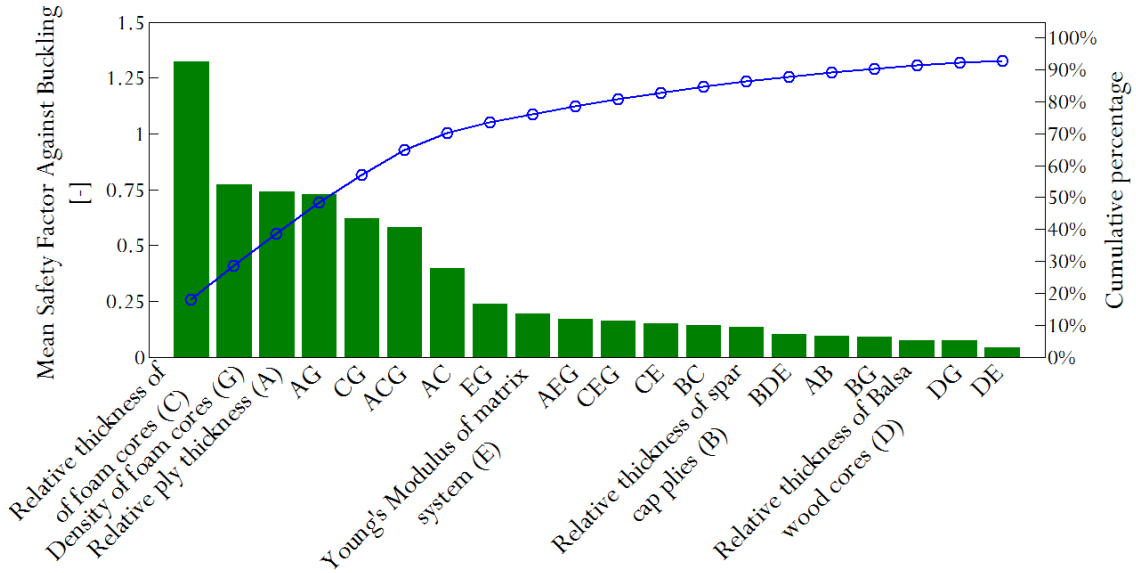

Fig. 4.8: Pareto analysis of safety factor ag. buckling

Current commercially available foam cores of sandwich structures typically present a density spectrum around 100kg/m³, but future foam materials are expected to cover soon the range between 40 kg/m³ and 250 kg/m³ considered in the RSA-models depicted below.

Several conclusions shall be drawn at the sight of Fig. 4.9: First, it must be emphasized the high degree of interactions among the most influencing variables as expected from the Pareto analysis. It can be shown that only with a suitable combination of these three factors structural stability can be guaranteed. Although higher levels of any of them increase the BSF, none of them independently can ensure it.

Second, it has been observed that high enough densities of foam cores (G) can provoke dramatic increases of the BSF provided that a proper - thick enough - combination of the core and skin thicknesses is provided. Nevertheless, beyond a threshold - determined by those thicknesses - the effect is limited and no further improvement can be obtained. This can be observed in the overlapping of surfaces corresponding to high foam densities, Fig. 4.9 (left) or in the plateau-shaped surfaces of Fig. 4.9 (right).

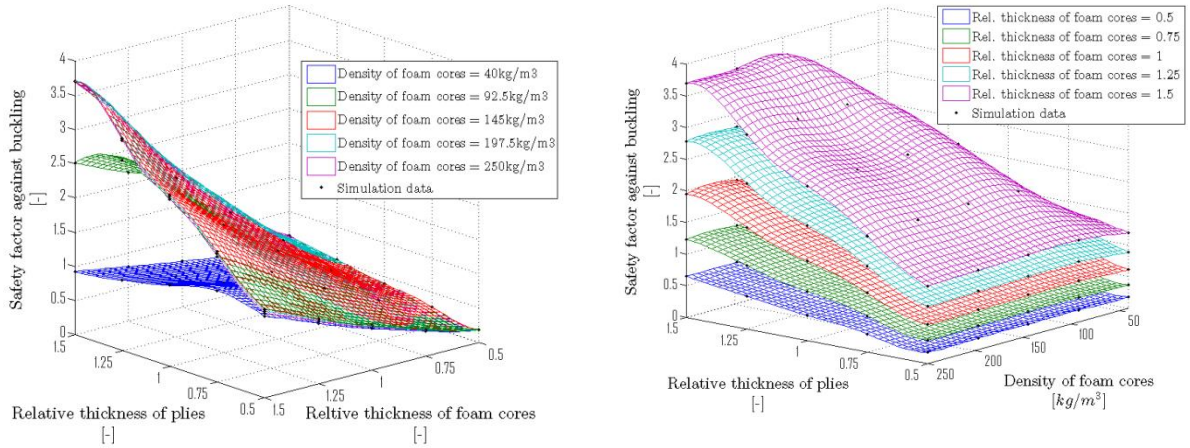

Fig. 4.9: RSA-models for stability properties: Safety buckling factors ag. ply thickness, core thickness and density of foam core

The contour plot in Fig. 4.10 shows a cross-section of the latter and illustrates the dependence of the core thickness and core density based on the safety factor against buckling. The diagram reveals that an increasing density of the foam core increases the stability performance until a plateau is reached based on a defined thickness of a foam core.

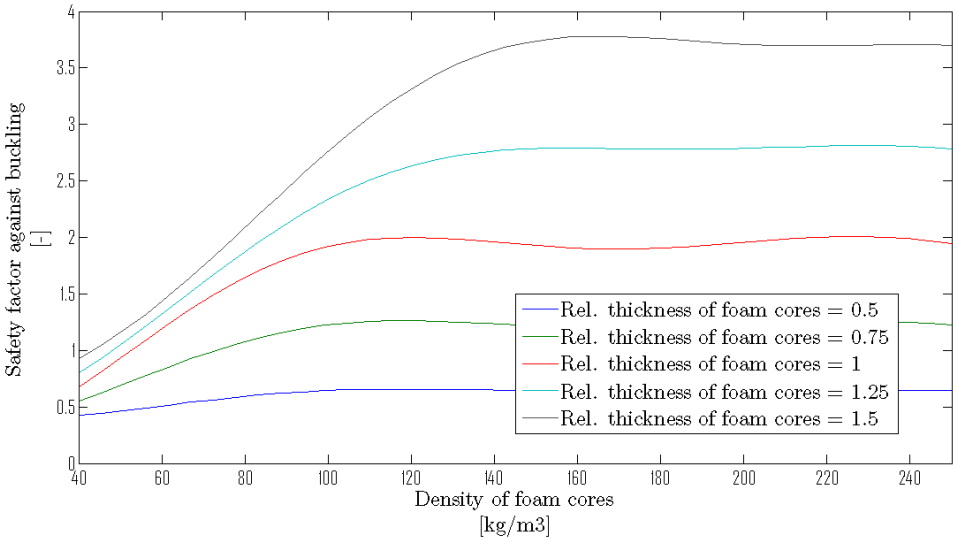

Fig. 4.10: Buckling safety factor: Thickness and density of foam core

By overlapping contour plots of the buckling safety factor and blade mass for given values of the ordinary GFRP ply thickness, their evolution with respect to the mechanical properties and thickness of foam cores are shown in Fig. 4.11. So, proper combinations of these parameters can be found in order to maximize the BSF and minimize mass simultaneously.

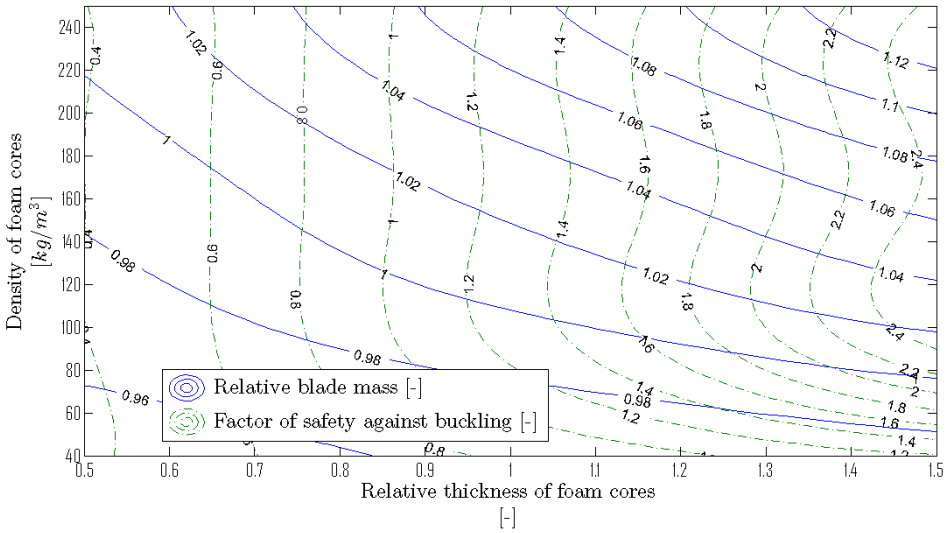

Fig. 4.11: Buckling safety factor and blade mass dependence: Thickness and density of foam core

It can be shown that the thickness and density of the foam cores are crucial for the stability performance, while matrix dominated effects can almost be neglected.

4.2.4. Mass effects

Next, the impact of the design factors (Tab. 4.1) on the blade mass is investigated. Findings show that the thicknesses of both the ordinary and the spar cap plies are responsible for more than 75% of the variability of the blade mass, Fig. 4.12 (left). The thickness and density of foam cores do influence the mass but in a much less significant way. (Fig. 4.12, right)

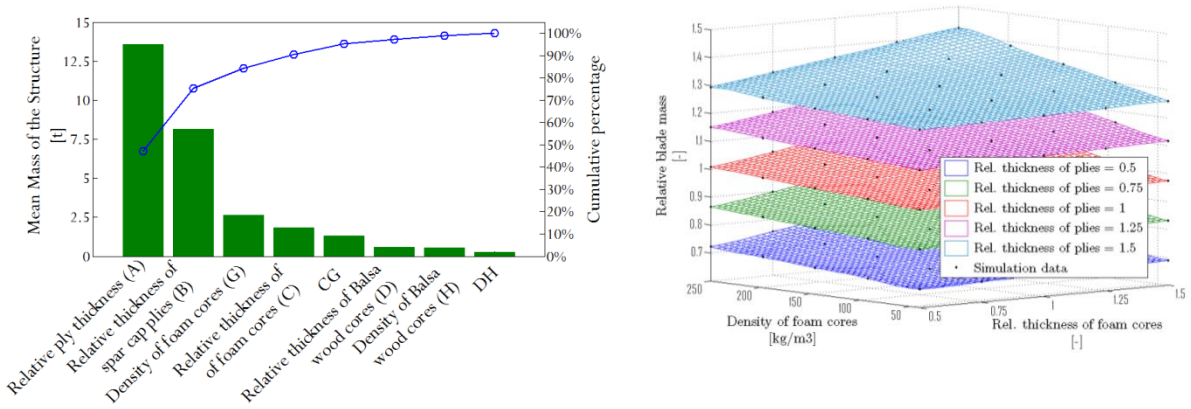

Fig. 4.12: Blade mass: Pareto analysis (left), RSA-model (right)

In fact, the influence of the resin uptake has to be considered, too. It can be supposed that a core material with a low density assimilates more of the matrix system compared to a core material with a higher density.

4.2.5. Conclusion

The study of the matrix-dominated effects on the mechanical behavior of a conventional WTB has provided various findings: The strength behavior is found to be clearly dominated by the properties of the matrix systems. However, the properties of the matrix systems are of little significance for the stability and mass performance.

Matrix properties play a crucial role on the strength performance of the structure. *Fiber compression failure* and *matrix tension failure* stand out as the two dominant failure modes.

For every criterion analysed, a low number of failures can be achieved only by ensuring simultaneously a sufficiently high matrix properties and thick enough plies. Especially, the dominant occurrence of the failure modes *fiber compression failure* and *matrix tension failure* show the strong effect of the matrix properties. Too low levels of any of them will boost failures with regard to any of these criteria; however there exists a relatively wide design zone where the trade-off should be carefully explored due to its important improvement potentials.

Blade stiffness is dominated by the flapwise deformation, which fundamentally depends on the thickness of the load-carrying spar cap plies. Nevertheless, whenever high in-plane shear stresses are induced, as in the case of the *edgewise* and *torsional* components of the

deformation, matrix properties show a much bigger influence on the blade composite structure.

Analysing the stability performance of WTBs, the following conclusion is drawn: Once the sandwich core and the skin thicknesses are set to thick enough levels, the *safety against buckling* will rise with increasing foam densities until a threshold is reached, beyond which no further improvement is achieved. This thickness-dependent maximum limits the potentials of core foam developments.

Mass effects are governed fundamentally by the thicknesses of the ordinary GFRP plies and secondly by that of the spar cap plies. Both the thickness and density of the foam cores are significant, but to a much lower extent given the small density of the cores.

Due to the blade structure itself, the thickness of the ordinary plies is a determining parameter over every response. All desirable structural results, i.e. low number of ply failures, low deformation and safety against buckling are associated with thick plies, which at the same time dramatically increase the blade mass. To avoid this, taking advantage of the relatively uncoupled nature of the responses, its influence can be compensated by setting other parameters that have a lower effect on mass: Excessive deformations can be tackled by increasing thickness of the spar cap plies while the reduction on failure rates should be sought by improving matrix-dependent mechanical properties and using thinner plies. High buckling security factors can be achieved with a proper combination of thick and strong cores thicknesses which are much lighter.

The material research should be focused on the development of EPOXY resins with higher values of the Young's modulus, which are basic to reduce the specific weight of blade sections and consequently to reduce production costs. On the other hand, results show that the potentials of core foam developments are limited by a thickness-dependent threshold.

4.3. Hybrid GFRP/CFRP designs of the WTB

The purposeful use of low-cost CFRP in WTBs is outlined next based on two numerical case studies. Currently, the carbon market in WTB applications is in a transitional state. The increasing demand in longer WTB should stimulate the development of extra supply capacity that could lead to lower CFRP prices. “The supply of carbon and potential cost reductions will not however be realized unless the demand from WTB manufacturers can reach a dominant level in the world market and wean the main carbon suppliers from a main focus on the sporadic demand levels of the aerospace industries.” [8, p. 62] Discounting costs by long-term partnerships between manufacturers and material suppliers are crucial for the blade design practice. Raw material prices are spot prices, which means that prices can rise and fall constantly. Long-term contracts that may enable certain foreseeability for new design concepts are seldom. So, the dilemma is that CFRP cannot be replaced by GFRP without changing the blade design in the form of geometry and composite layup. [8, p. 67]
Considering the design process there are contrary design philosophies. Spar cap made of CFRP have to withstand much higher stresses than a GFRP spar cap due to its revised design. A spar cap of CFRP is purposely designed to withstand greater stresses; otherwise the higher performance of the CFRP material cannot be exploited. While blade lengths were exceeding 70 meters, a common statement in recent years was that a sufficient stiffness of these structures may only be achieved by the use of CFRP. [10] In contrast with GFRP, CFRP has advanced stiffness and strength properties combined with a lower density (Tab. 2.2). This leads to the following benefits of CFRP in wind turbine blades:

- Reduction of blade mass reduces the overall loads occurring at the WEP. Lower loads lead to a “slighter” design that finally reduces the overall costs.
- CFRP allows the design of thinner blades that may reduce the aerodynamic drag and result in a higher power output.
- Eigenfrequencies can be reduced. This may be crucial for repowering aspects.
- Next to its higher mechanical fatigue properties, lighter blades have lower fatigue loads.

Thus, there are several blade manufacturers using CFRP in their load carrying blade structures. However, the crucial items that ultimately decide on the use of CFRP in WTBs are the material costs. Blades are designed with the lowest price possible in mind even more so than most of the other structural components made of composite material. The performance of the properties is drilled to the lowest possible costs. Carbon fiber is currently about 5-8 times more costly than glass fibers for blade applications. Even the effects of matrix systems are more sensitive.

Hence, the majority of current blade structures exceeding 60 meters are still fully made of GFRP. This may primarily be achieved through recent processes in enhanced glass fiber properties and in advancements of the process technologies. Further, there are design

considerations for designing downwind[24] plants. Thus, an increased flexibility of the blade structure is tolerated due to the fact that the requirement of tower clearance can be omitted.

4.3.1. Cost optimized design using low-cost carbon fibers

The first study shows the effect of CFRP in a WTB considering the blade mass and its material costs. A 40 meter reference blade is used. [5] In the subsequent scenarios, it is assumed that a low-cost CFRP is 4-times more expensive than GFRP. In Fig. 4.13, four different designs are shown. The geometry is unaltered. All designs fulfill the equivalent boundary conditions such as general structural constraints of static stiffness, strength behavior, Eigenfrequencies, and safety against buckling. The design "GFRP" shows a blade fully made of GFRP. Its adjacent pillar illustrates the corresponding material costs. The second design is fully made of CFRP.

Next, the design in which CFRP is used only for the spar caps is shown. The mass is reduced by about 27% compared to the design fully made of GFRP. Costs are almost equivalent to the design "GFRP".

To determine the fourth design a composite optimization tool is used. Its design variables are the selection of material. It can be chosen between GFRP and CFRP. In this case, a cost function is determined as the objective function. The result is that a purposeful use of CFRP - not only in the spar caps – can reduce the overall mass and finally the materials costs. [5]

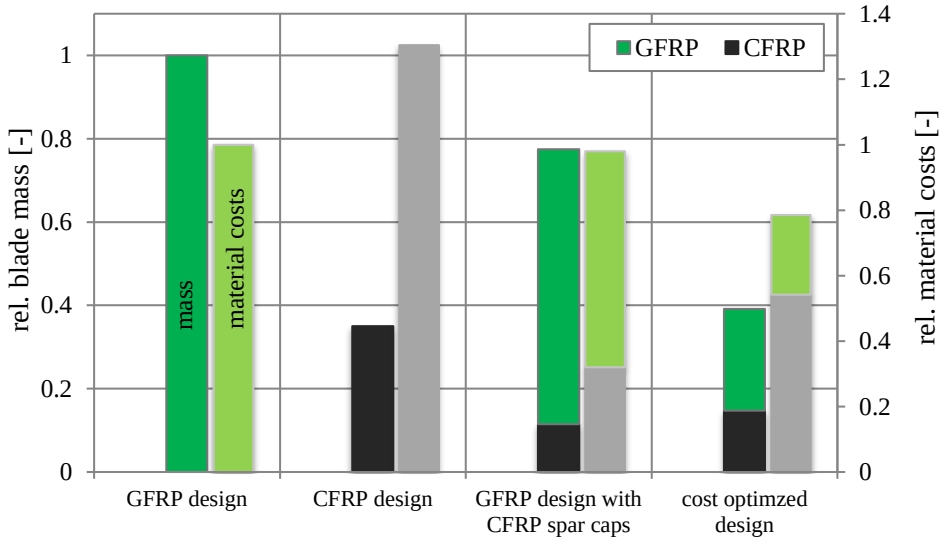

Fig. 4.13: Hybrid design studies using GFRP and CFRP

[24] The disk area is placed behind the tower. Thus, the blowing wind passes the tower first, before reaching the disk area.

4.3.2. Hybrid design for bend-twist coupled blades

The anisotropic behavior of composites is used to purposefully induce bend-twist couplings. A structure reveals bend-twist couplings by the time a load is introduced. An additional torsional structural response occurs. A convenience of bend-twist couplings in a WTB is that this structural-mechanical effect assists the electro-mechanical executed pitch control and reduces occurring structural loads. Further, according to [50], an adequate coupling can reduce fatigue loads up to 10% due to the reason that bend-twist coupled blades can conform to the prevailing environmental conditions more efficiently than pitched blades. While electro-mechanical pitch mechanisms react to changing environmental conditions, such as wind speed, wind direction, turbulences, etc., with a short retardation, a smart structure attunes immediately to changing conditions.

Here, bend-twist couplings are introduced into the spar caps by using off-axis plies instead of unidirectional plies that are situated parallel to the blade`s lengthwise axis. Additionally, CFRP fibers substitute GFRP fibers in the spar caps.

The coupling can be achieved by three methods. [44, p. 10] First, an unsymmetrical layup is built up within the aerodynamic shells. Second, fibers in the off-axis direction are placed within the spar caps and, third, previous layups are combined. A typical adjustment of the pitch angle is between 0-15 degrees. According to [51, p. 26, 44], a "beam theory model was used to evaluate the effect of replacing the spar cap unidirectional (…) material with carbon fiber oriented at an angle θ". The beam theory model relates N, the axial force per unit width in the spar caps, to the axial strain, ε , and the shear flow, q :

$$N = \beta_1 \varepsilon + \beta_2 q \tag{4.6}$$

The parameter β_1 is called "axial stiffness coefficient", β_2 is called "coefficient of torsional coupling". Constants β_1 and β_2 are defined as:

$$\beta_1 = A_{11} - \frac{A_{12}^2}{A_{22}} - \frac{\beta_2^2}{\beta_4} \tag{4.7}$$

$$\beta_2 = \left(A_{16} - \frac{A_{12} \cdot A_{26}}{A_{22}}\right)\beta_4 \tag{4.8}$$

$$\beta_4 = \left(\mathrm{A}_{66} - \frac{\mathrm{A}_{26}^2}{\mathrm{A}_{22}}\right)^{-1} \tag{4.9}$$

The coefficients A_{ij} are taken from the ABD matrix for N numbers of plies:

$$A_{ij} = \sum_{k=1}^{N} \left(\bar{Q}_{ij}\right) \cdot t_k \tag{4.10}$$

Where $[\bar{\mathrm{Q}}]$ is determined by:

$$[\overline{Q}] = [T][Q][T]^T \tag{4.11}$$

Matrix [A] is of interest for the application to the spar caps. Matrix [A] leads to a tension-shear coupling. The matrix [D] (if full) leads to the bend-twist coupling. Due to the fact that the bending of the blade induces tension in the upper spar cap and compression in the lower spar cap, these loadings induce a distortion (shear) of the single spar cap, which finally leads to a global torsion of the blade. That is the reason why the bend-twist coupling is primarily considered on the spar cap level. Furthermore, to introduce bend-twist couplings, the fibers of both spar caps have to be oriented in the same direction. [44, p. 10] This configuration is called *mirror symmetric layup*. (Fig. 4.14) If the fiber orientation is in the contrary direction, it will be called *helical layup*. This would lead to a tension-torsion couplings.

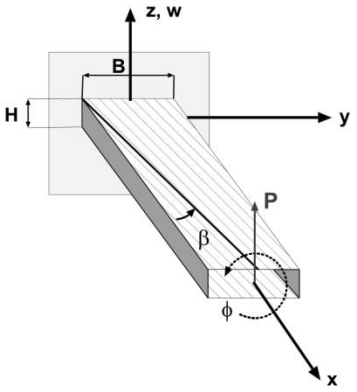

Fig. 4.14: Bend-twist coupling on a cantilever beam [52]

In the subsequent study, the 0° oriented GFRP plies that represent the spar caps are substituted by CFRP plies. The CFRP plies are misaligned stepwise in the xy-plane. In order to receive an equivalent deflection in flapwise direction, fibers that are positioned more and more off-axis have to be thickened. (see Fig. 4.16 left) Fig. 4.15 shows the effects of various arranged fiber orientations (0°, 5°, 10°, 15° and 20°). While the deflection of a blade in the flapwise direction remains constant, an increasing ratio of off-axis plies induces larger bend-twist couplings.

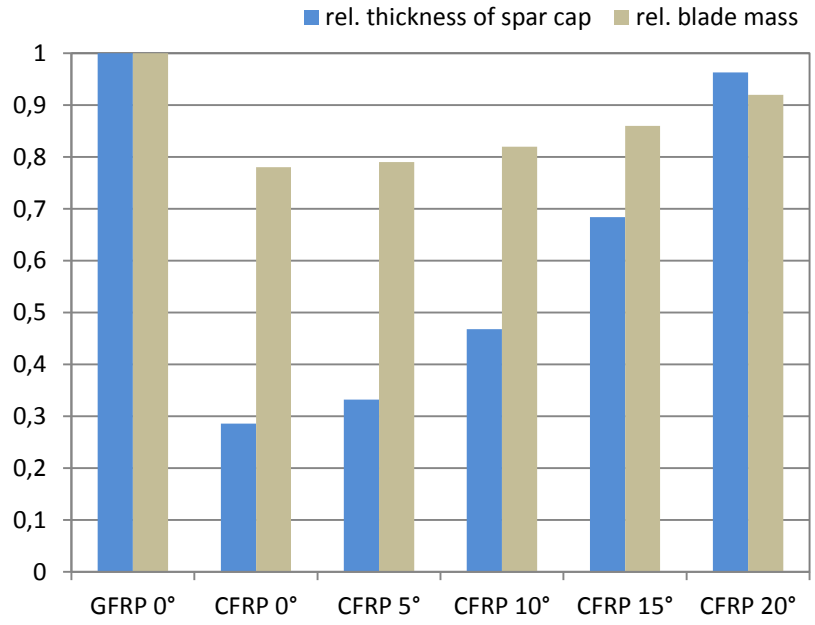

Fig. 4.15: Spar cap thickness and blade mass against increasing off-axis plies

The study shows that the fibers` declinations of 10 degrees to the blade length axis causes a distortion of the blade structure of approx. 13 degrees. (Fig. 4.16, right). This torsional component is used to actively support the pitching of the blades.

It is observed that an increase of the fiber deflection from 10° to 15° causes an increase of the twist angle of about 15%. This results in an increase of total blade weight of 5.4%. The break-even point is hit at about 10% of fiber deflection in the spar caps. [53]

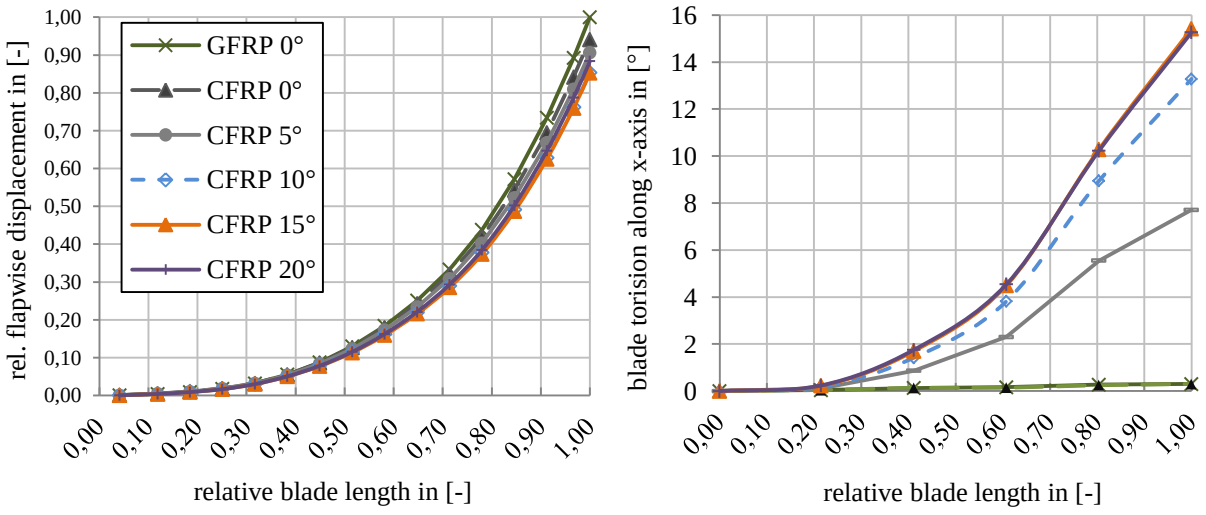

Fig. 4.16: Flapwise displacement and blade torsion along x-axis

5. Ply waviness – Influence of matrix systems

While the previous context of the work considers the effects of matrix systems on a component level (macroscopic level) observing the structural response of a blade structure, the present chapter deals with the effects of matrix systems on a local level taking fabrication effects such as ply waviness into consideration. These effects may also yield to global effects.

Ply waviness (PW) is, next to delaminations, porosities and etc., a commonly observed fabrication defect in composite parts, such as in spar caps (chap.3.3.2) of WTBs. Ply waviness is known as a wave-formed ply and/or fiber deviation from a straight alignment in a unidirectional laminate. A decrease in the material performance (stiffness, strength and fatigue properties) is expected. Both the fiber architecture and the material affect the mechanical properties.

Apart from ply waviness in WTBs, ply waviness is also commonly detected in filament winding and fiber placement applications. Irrespective of undesired wavy composites due to the fabrications intolerances, typical inherent wavinesses are present in composite material, namely in weaves and braids.

A literature review has been conducted focusing on the occurrence of ply waviness in WTBs (chap.5.1.1) and its characteristics (chap.5.1.2). The focus is exclusively on out-of-plane waves due to their higher relevance on WTB structures. Further, the critical failure mechanisms under compression and tensile loads (chap.5.1.3) are described.

An analytical approach derived from [4] and enhanced by a PUCK failure criterion is implemented within a GUI that enables a quick and quantitative tool to evaluate the mechanical properties of ply waviness. (chap.5.2.1) The failure mechanisms occurring in wavy composites are studied in detail using a numerical model within the FE software ABAQUS enhanced by a material user subroutine containing a continuum damage model. (chap.5.2.2) Both, the analytical and the numerical model are developed in order to assess the composite material`s stiffness and strength behavior for a given geometrical shape and on the material properties. A particular emphasis is on the matrix relevant (dominated) properties of the laminate. Utilizing these findings, a wavy specimen`s geometry is derived. (chap.5.3.1) A fabrication method (chap.5.3.2) is developed and installed to fabricate a specimen containing artificially induced waviness in reproducible quality.

Experiments (chap.5.4.1) of compression and tensile tests are carried out for a neat resin specimen (chap.5.4.2), planar specimens (chap.5.4.3) and wavy specimens (chap.5.4.4 - chap.5.4.6). Numerical results are validated against experiments in chap.5.5.

These findings are utilized to analyse the structural behavior in thick wavy laminates in chap.5.6. The effects of these fabrication-induced effects can be evaluated by a damage tolerance approach. “In fact, the effect of (…) fiber waviness and irregular fiber distribution in initiating damage and the interaction between damage and defects have prompted a new field called *defect damage mechanics*.” [54]

5.1. Literature review of wavy composites

The occurrence of ply waviness in WTB components is described in chap.5.1.1. The characteristics of wavy composites are shown in chap.5.1.2 categorized into its geometrical shape and its structural mechanical meaningfulness. Further, the critical failure mechanisms under compression and tensile loads are described. (chap.5.1.3)

5.1.1. Occurrence of ply waviness in WTBs

The enormous cost pressure of the fabrication process forces blade manufacturers to incur production inaccuracies. Thereby, ply waviness is inevitably induced during the fabrication process of a WTB. [55]
Fig. 5.1 indicates structural parts of a WTB that are typically prone to ply waviness. PW is commonly observed and most critical in the thick load carrying structures. The conventional spar cap`s geometry is prone to cause fiber misalignments. Due to the fact that the spar cap is the load carrying component, ply waviness is most sensitive in this component. Further, the trailing edge comprises a complex geometry for draping issues. UD plies tend to induce fiber misalignment at the area of maximum curvature. The UD ply has to be placed along the blade length axis to 90° and additionally bended around the rim. The butt joint of the slightly drapable core material may also generate ply wavinesses. A graded shape (Fig. 5.3) is commonly observed.

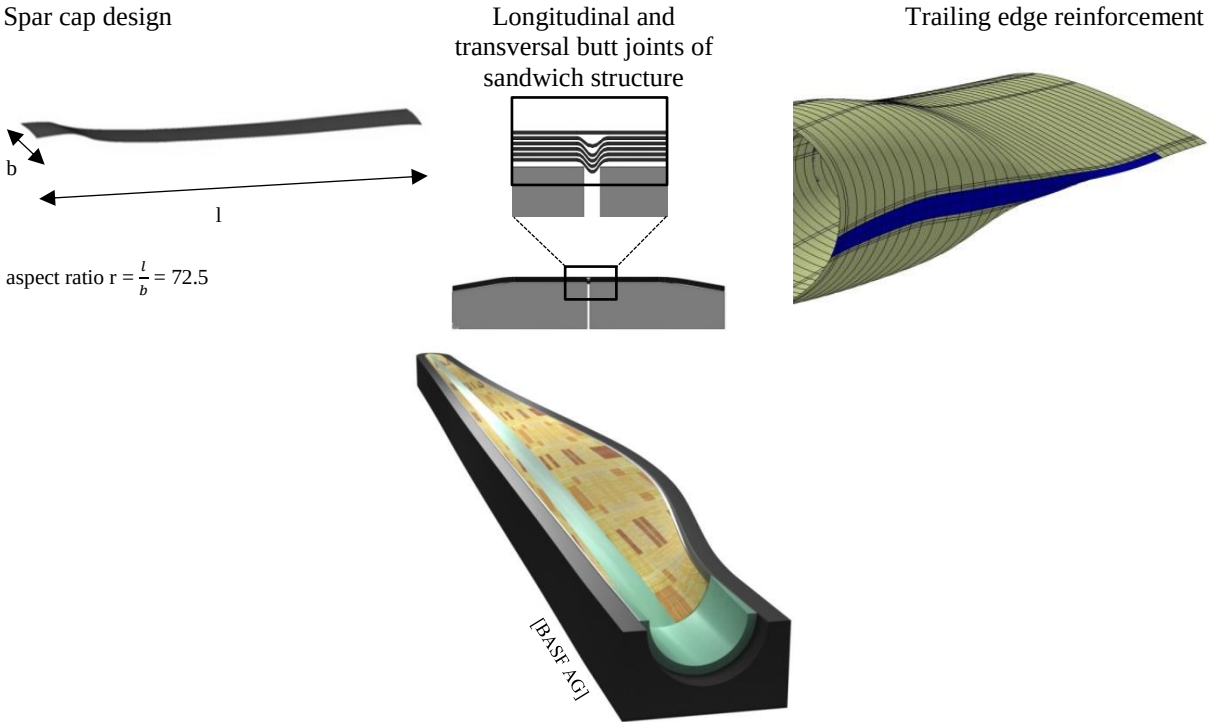

Fig. 5.1: PW-prone parts: spar caps, butt joint and trailing edge reinforcement

The composite root section of a WTB exhibits a cylindrical shape. Due to gravity influences, the draped clutches tend to slip towards each other and generate ply waviness in the chordwise blade direction.

The main defect`s originations are caused by events occurring during following process steps:

1. **Layup process**: The cost-efficient production that is driven by handwork is highly prone to impreciseness of ply deposition. The inappropriate aspect ratio of the spar cap (r >70) easily leads to ply waviness during the draping process.
2. **Infiltration process**: Fiber washing effects may occur and misalign draped composite material. Occasionally, irregular infiltration settings also induce ply waviness.
3. **Curing process**: Ply waviness is localized in the thick laminate of spar caps as a consequence of residual stresses built up during post consolidation and cure shrinkage. Process induced deformations are subject to various influencing parameters.

A ranking of previous defect`s originations is difficult and not documented completely. It mainly depends on the respective composite material, the layup design (chap.3.3.2) and the manufacturing processes (chap.2.3).

Fig. 5.2: Wavy spar cap laminate [56]

For the sake of completeness, mis-kitting of ply drop-off [57] [55], iniquitous draping material, an inappropriate deposition of the flow promoter, local temperature differences due to heating channels are broader sources in terms of the occurrence of ply waviness in a WTB. Ply waviness is usually accompanied by an increased void content, resin rich areas and/or various FVCs. E.g. a decreasing FVC may also increase nonlinearities within the wavy section.

5.1.2. Characteristics of ply waviness

Ply waviness appears in arbitrary shapes and locations and can principally be classified into in-plane (IP) and out-of-plane waves (OP). It is stated in [58] that in-plane and out-of-plane waves show similar strength degradations. Herein, the focal point is on out-of-plane waves in UD-dominated thick laminates due to the fact that out-of-plane stresses occur more frequently in WTBs. In-plane waviness is studied in [58].

It is differentiated between uniform and graded forms. While a uniform shape is characteristic for constant amplitude to length ratio, the wavy shape weakens towards free edges. Fig. 5.3 shows a uniform and a graded shape of ply waviness through the thickness of a laminate. Uniform shapes are commonly detected in spar caps. It is assumed that the formation originates from the curing process. Graded shapes mainly originate from complexities in draping and are detected in the trailing edges of a WTB (Fig. 5.1). The shapes are generally described by the ratio *r*.

$$r = \frac{A}{l} \tag{5.1}$$

A: height of amplitude

l: length of wave

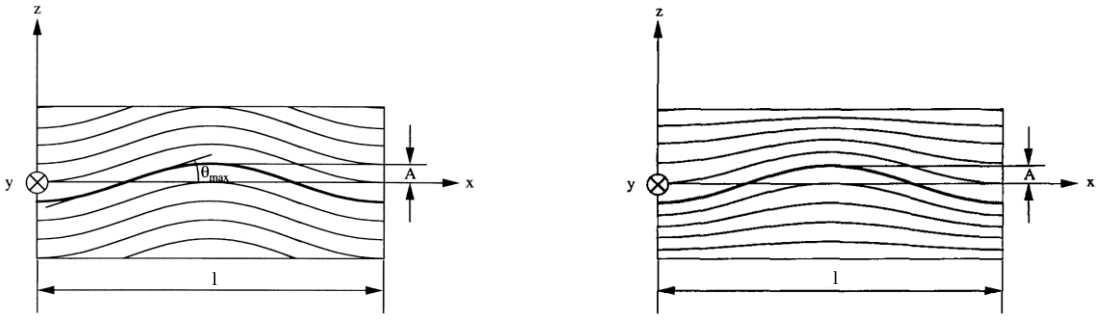

Fig. 5.3: Uniform (left) and graded (right) shape of ply waviness [4]

Certainly, several wavy shapes can occur back-to-back or in quick succession. Results in [57] indicate that the location of wavy plies within a cross-section of a laminate significantly influences the strength knock-down. A wavy ply "located at the lower laminate surface produced a greater strength knock-down than a similar size defect at the laminate mid-plane." The reason of this is that the plies at the edge of the laminates are single supported and therefore tend to fail rather than plies located within the laminate.

5.1.3. Failure mechanisms in wavy composites

Ply waviness induces a three-dimensional stress field based on its geometrical shape. Fig. 5.4 shows the local average of stresses within a representative slice of an inclined ply. It is stated in [59] that interlaminar tensile stresses normal to the fibers are induced as a consequence of transverse strains induced by the geometry. The resulting stresses at a wavy laminate section subjected to a load in x-direction are a combination of interlaminar normal (ILTS) and interlaminar shear stresses (ILSS). The occurring transverse shear force varies at each location along the wavy course.

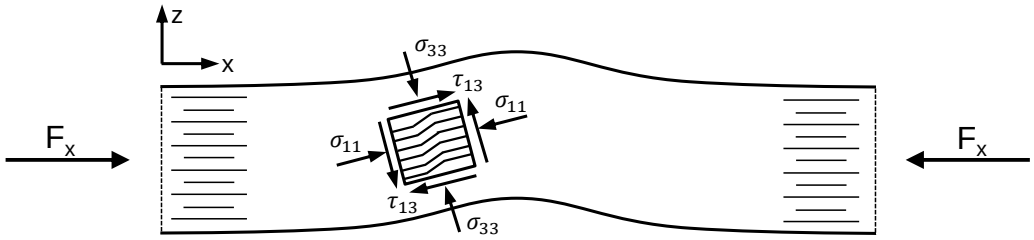

Fig. 5.4: Occurring stress states in a wavy ply

While a tensile load tries to straighten the single fibers, a compressive load will increase the amplitude-to-wavelength ratio. [60]

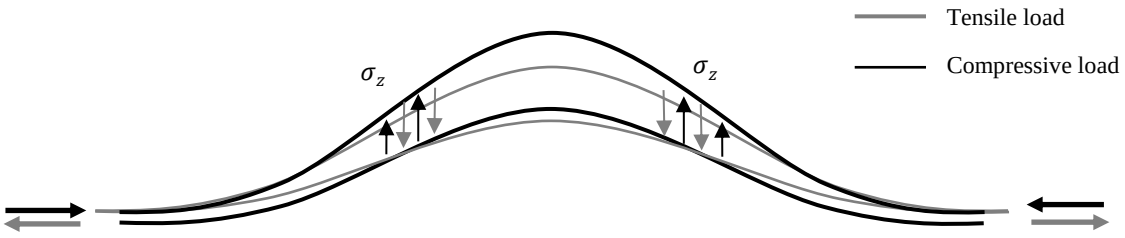

Fig. 5.5: Tensile and compressive load introduced to wavy ply

It is assumed by [61] that the failure initiations for compression and tensile loads are dominated by matrix failure. Especially the non-linearities of the matrix systems [62] govern the stiffness and strength behavior of wavy composites. The failure mechanisms are analyzed individually under compression (chap.5.1.3.1) and tensile loads (chap.5.1.3.2).

5.1.3.1. Failure mechanisms under compression load

When applying a compression load on uni-directional aligned composites, the following five failure mechanisms have been observed and studied in [63] [64] [65] [66] [67] [68] [59] [69] [70] [71] [72]: elastic microbuckling, plastic microbuckling, matrix failure, fiber crushing and longitudinal cracking. Fig. 5.6 schematically shows the corresponding failure mechanisms under a compression load. Although similar failure mechanisms are expected at wavy composites, insufficient data are present in literature.

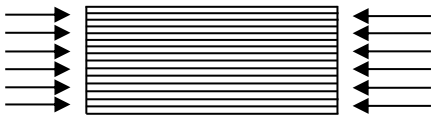

Failure mechanisms:

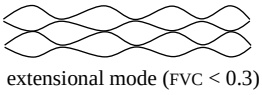

elastic microbuckling

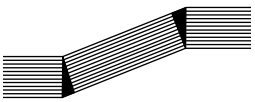

plastic microbuckling

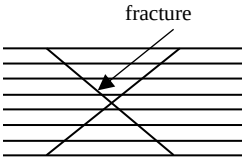

matrix failure

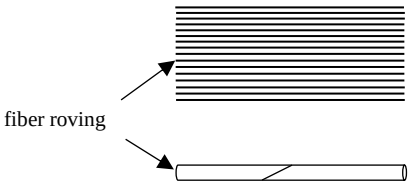

fiber crushing

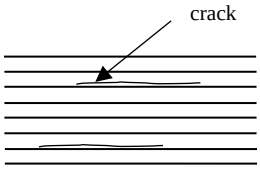

longitudinal cracking (delamination)

Fig. 5.6: Failure mechanism in aligned composites under compression (aligned to [63])

Composites containing a low FVC ($v_f < 0.3$) exhibit an extensional mode rather than a shear mode. [63] [73] Therefore, JELF and FLECK [63] use various material models to trigger individually one of the five failure mechanisms depicted in Fig. 5.6. It is verified that for polymer EPOXY systems plastic microbuckling is most presumable. SLAUGHTER [67] comes to

similar results studying the microbuckling effects of ply waviness. It is stated that "microbuckling is the failure mechanism by which the composite suffers localized with a kink band." It is also shown that the non-linear shear behavior of the matrix systems is of crucial interest. VOGLER and KYRIAKIDES [65] study the composite failure under a combined compression and shear loading by experimental observations and numerical models. Two load histories - namely first compression stresses and then shear stresses are applied (and vice versa) - show similar failure modes. NIU and TALREJA [64] introduce an advanced mechanism based on shear instability using a modified ARGON-BUDIANSKY kinking formula. While BUDIANSKY et al. use an initial fiber misalignment angle, TALREJA postulates a method applying a kink band formation without initial misalignment. CHAI and KNAUSS [66] describe a one-dimensional modeling approach of failure in composites by delamination buckling. The trade-off between delamination and buckling mode is studied. A critical delamination length is determined.

Physically-based, homogenized methods to model the composite behavior under a compression load are utilized in [69]. Therein, the initial failure mode under compression loadings of a perfectly aligned specimen is delamination, followed by microbuckling of the wavy plies. This succeeds in further delaminations. In [70], an interfiber/interlaminar failure theory is developed, especially for the superposition of shear and compression loads. A MOHR-COULOMB criterion for estimation of the fracture plane is used. PINHO et al. [71] [72] develop a fiber kinking model and implemented an appropriate FE-code based on the commercial software ANSYS.

Further, DAVIDSON and WAAS [68] show that fiber kinking is the initial failure mode in thick wavy laminates. This failure mechanism is followed by delaminations. Although previous observations have shown, that - after these mechanisms are coined - interactions between these failure mechanisms may occur. Having formatted a kink band the structural part cannot absorb any further loads.

In conclusion, the effects of shear non-linearities under compressive loading even increase with the severity of present ply waviness and, therefore, play an essential role for the initiation and propagation of the failure mechanisms (Fig. 5.6). Related to the previous findings in the literature, the initial and critical failure mode occurring in wavy composites is supposed to be the formation of a kink band. Subsequently, the formation of a kink band is discussed in detail.

Formation of a kink band

Kink band [74] is defined as the rotation of fibers in a band within a degrading matrix. Further, kinking is a localized shear deformation of the matrix accompanied by fiber fracture. [75] While the intrinsic initial failure mechanism in conventional GFRP and CFRP under compression is plastic microbuckling (Fig. 5.6), this plastic microbuckling process ends up in a well-defined kink band formation. It is expected that the kink bands occur at the regions of wavy composites that are imposed by the maximum shear stress field. This is mainly at the maximum inclination of wavy composites.
ROSEN postulates that, at a present buckling stress σ_c, a kink band oriented at a right angle to the loading direction suffers an average shear strain γ equal to the small rotation ϕ. The associated shear stress τ is given by the elastic law $\tau = G\gamma = G\phi$. Fiber bending stiffness is neglected.

$$\sigma_c = \frac{G_{12}}{1 - \nu_f} \tag{5.2}$$

Later, both the plasticity and the misalignment are considered by ARGON announcing the following equation for the kinking stress:

$$\sigma_c = \frac{\tau_y}{\phi} \tag{5.3}$$

τ_y: shearing yield stress of the composite

ϕ: initial maximum angular misalignment of the fibers

BUDIANSKY and FLECK enhance the formula by ROSEN and ARGON by a RAMBERG-OSGOOD shear stress-strain relation

$$\frac{\gamma}{\gamma_y} = \frac{\tau}{\tau_y} + \frac{3}{7}\left(\frac{\tau}{\tau_y}\right)^n \tag{5.4}$$

to

$$\frac{\sigma_c}{G} = \frac{1}{1 + n\left(\frac{3}{7}\right)^{\frac{1}{n}}\left(\frac{\frac{\phi}{\gamma_y}}{n-1}\right)^{\frac{n-1}{n}}} \tag{5.5}$$

σ_c: Composite limit-point of kinking under compression/buckling stress

G: Shear modulus of composite

γ_y: Shearing yielding strain

ϕ: Initial maximum angular misalignment of fibers

n: Constant, which depend on the considered material.

Further, it is noted that the kinking starts most likely from the surface. [61] [68] Because the fibers on the surface are only supported from one side, they tend to buckle easier. LEE and WAAS [76] postulate that "kink bands are formed on account of the synergy due to the misalignment induced during the axial splitting and the large amount of strain energy that is released. (…) When kink bands were found, they were always accompanied by longitudinal fiber/matrix splitting cracks. It is, however, quite possible that kinking in conjunction with low interfacial fracture toughness can induce axial splits."

SCHULTHEISZ [75] poses the question "whether the important matrix property in the failure process (of kink band formation) is the Young`s Modulus or the yield stress, as these two properties are strongly correlated. "The traditional elastic microbuckling analyses would point to the former, while kinking analyses and some microbuckling analyses that include initial imperfections would point to the latter." He further points out that the matrix stress crucially influences the kink band formation.

Fig. 5.7 shows the formation of a kink band that is sectioned into a shear-dominated and a bending-dominated region.

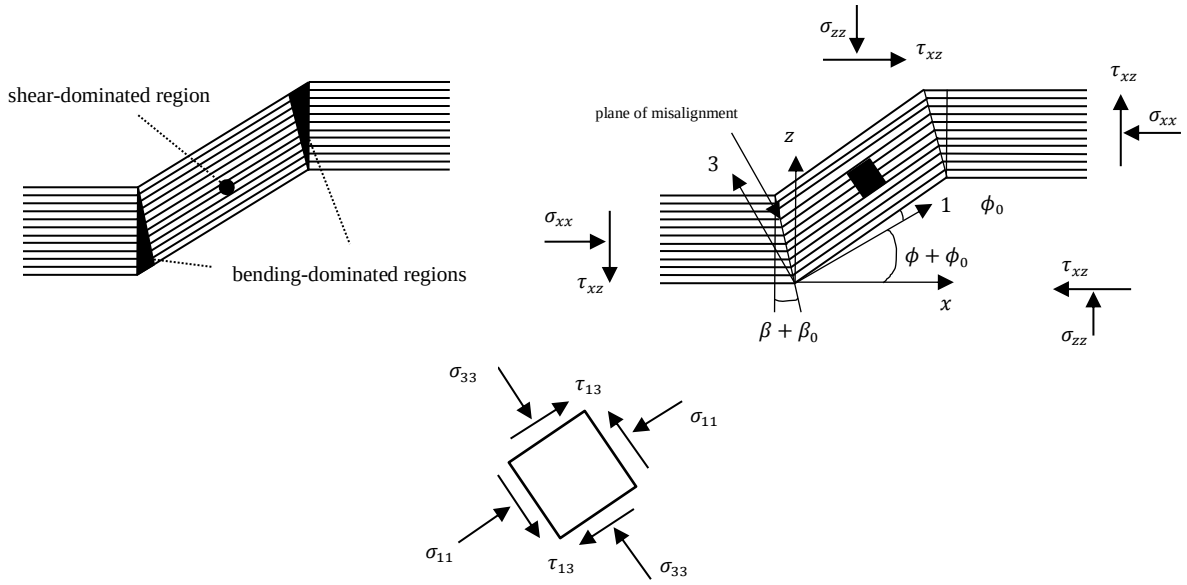

Fig. 5.7: Kink band geometry (aligned to [74])

DAVIDSON, WAAS [68] and FLECK [67] postulate that in-plane and out-of-plane kink band formations can occur in wavy composites. According to [67], "the fibers buckle either in the plane of the specimen or out-of-plane, depending on the constraints on the free surface." Time dependent effects of the kink formation are postulated by SCHAPERY "who also introduced the possibility of matrix cracking and its manifestation to soften the matrix response." [73]

5.1.3.2. Failure mechanisms under tensile load

It is pointed out by ASP and TALREJA [61] [77] [78] that two failure mechanisms may primarily occur in EPOXY matrix systems assuming a three-dimensional stress state, such as dilatation failure and shear failure of the matrix system. It is emphasized that both primary failure modes in wavy composites are initiated by matrix failure. It is well known that a polymer embedded between fibers behaves dramatically different than its original unconstrained state (pure matrix): First, the matrix failure may be modeled by a dilatation criterion through the growth of a cavity that becomes unstable. Second, shear failure may occur where a shear band is formed. Further, [77] states that "under stress states resembling those in matrix constrained between fibers, e.g. equi-biaxial and equi-triaxial tension, yielding is suppressed while brittle failure, presumably caused by crack growth from cavitation, occurs. A criterion for this mode of failure is proposed as the critical dilatational strain energy density." It is assumed that the initial fiber mechanism under tension is debonding.
In [78], an RVE-model representing fibers and matrix individually is loaded in tension normal to the fiber. The authors assume for this load case that the failure mechanism is initiated by debonding of fiber and matrix. Applying both criteria, cavitation-induced brittle failure and yielding of the matrix [77] show that the cavitation-induced brittle failure is the primary failure mechanism under these boundary conditions. Further, it is shown that a uni-axially loaded epoxy matrix system features different yield stresses under tension and compression. "This is attributed to the effect of hydrostatic stress on shear-driven yielding." Within this paper, "the classical yield criterion, e.g. von Mises and Tresca, which are insensitive to the hydrostatic stress, have thus been modified to account for this effect."

KARAMI and GARNICH [79] use an RVE model of a wavy fiber embedded in a matrix system in order to determine the effective moduli and failure considerations for composites with periodic fiber waviness. VOGLER and KYRIAKIDES [65] uses a volume model assuming an isotropic and linear elastic behavior of the fibers and the matrix is modeled by "a finitely deforming J2-type elasto-plastic solid which hardens isotropically." They show that while the matrix is plasticized, the shear modulus of the composite is reduced as a result. Further, it is shown that the maximum reduction of the shear modulus is observed at the location where the initial fiber orientation is most severe. NEDELE and WISNOM [80] uses a three-dimensional finite element analysis of the stress concentration at a single fiber break in order to study the effects of the matrix systems. A similar approach may be applied to a wavy sub-model.

The previous references suggest that the first failure mechanism of a tensile loaded ply waviness is debonding. Fiber/matrix debonding may be caused due to in-plane shear and stresses normal to the fiber. In order to analyze this failure mechanism a micro-scale modeling approach[25] considering fiber and matrix systems individually is convenient. In order to model

[25] Micro-scale: fiber, matrix; macro-scale: composite

the failure mechanism of debonding a meso-scale approach is required. Globally occurring boundary conditions in the form of displacements and reaction forces are transferred to a sub-model in which fibers and matrix are individually modeled. Therein, a failure criterion is applied to the matrix system. NEDELE and WISNOM [80] use a volume model in order to simulate the stress conditions around a single fiber. Therefore, the single fiber is surrounded by a matrix region. Subsequently, the surrounded fibers are homogenized and modeled as a ring region of the thickness of one fiber diameter. This is followed by a matrix region that is neighbored by a region representing the homogenized composite.

Next, the analyses of stiffness and strength prediction are described.

5.2. Analysis of stiffness and strength degradation

An analytical approach according to [4] is used to analyze the stiffness and strength behavior of wavy laminates considering various amplitude ratios and material properties. The theory is implemented in a code using MATLAB. [81] The GUI is presented. The analytical approach enables a quick and quantitative tool to evaluate ply waviness.

The failure mechanisms occurring in wavy composites are studied in detail using a numerical approach employing a material user subroutine containing a continuum damage model. (chap.5.2.2) Results are validated against experiments in chap.5.5.

5.2.1. Analytical method

Under loading along fiber orientation, ply waviness leads to the development of interlaminar shear stress and interlaminar tensile or compressive stress perpendicular to the fiber. These stresses may lead to inter-fiber failure (IFF), which can be influenced by the properties of the matrix and fiber coating. Hence the effects of matrix systems on the strength behavior of unidirectional laminates containing ply wavinesses are analyzed. Tensile and compressive loads are subjected. A linear elastic behavior is assumed. Taking into account [4] and [82], the approach is reproduced and extended by the PUCK failure criterion. [29] The analytical calculation is implemented as a GUI using the software MATLAB. The GUI allows an analytical estimation of the stiffness and strength behavior depending on waveform and material of the lamina.

LOCAL AND GLOBAL STIFFNESS PREDICTION

The calculation of the stiffness is carried out by a reproduction of [4] and [82]. A sinusoidal, in-phase, global, out-of-plane ply wavinesses with uniform and graded amplitudes (Fig. 5.3) is considered. The calculation is based upon a representative volume element of length l and height h. It includes one period of a uniform or graded waviness with the amplitude A. The local inclination of the plies is defined by the angle θ:

$$\theta = \tan^{-1}\left(2\pi\frac{A}{L}\left(1-2\frac{|z|}{h}\right)\cos\left(\frac{2\pi x}{L}-\frac{\pi}{2}\right)\right) \tag{5.6}$$

Whereby angle θ for a uniform waviness arises at the special case of $z = 0$.

The local stiffnesses are determined by a location-dependent transformation of the compliance matrix ${}_F\boldsymbol{S}$, from the fiber coordination system F to the global coordination system G. The transformed compliance matrix ${}_G\boldsymbol{S}$ is written by:

$$ {}_{G}\boldsymbol{S} = \boldsymbol{R} \cdot {}_{FG}\boldsymbol{T}^{-1} \cdot \boldsymbol{R}^{-1} \cdot {}_{F}\boldsymbol{S} \cdot {}_{FG}\boldsymbol{T} \tag{5.7} $$

Assuming transverse isotropy, Reuter matrix $\boldsymbol{R}$, transformation matrix ${}_{FG}\boldsymbol{T}$ and compliance matrix ${}_{F}\boldsymbol{S}$ are:

$$ \boldsymbol{R} = \begin{bmatrix} 1 & 0 & 0 & 0 & 0 & 0 \\ 0 & 1 & 0 & 0 & 0 & 0 \\ 0 & 0 & 1 & 0 & 0 & 0 \\ 0 & 0 & 0 & 2 & 0 & 0 \\ 0 & 0 & 0 & 0 & 2 & 0 \\ 0 & 0 & 0 & 0 & 0 & 2 \end{bmatrix}, \tag{5.8} $$

$$ {}_{FG}\boldsymbol{T} = \begin{bmatrix} m^2 & 0 & n^2 & 0 & 2mn & 0 \\ 0 & 1 & 0 & 0 & 0 & 0 \\ n^2 & 0 & m^2 & 0 & -2mn & 0 \\ 0 & 0 & 0 & m & 0 & -n \\ -mn & 0 & mn & 0 & m^2 - n^2 & 0 \\ 0 & 0 & 0 & n & 0 & m \end{bmatrix}, \tag{5.9} $$

$$ \text{with } m = \cos\theta \qquad n = \sin\theta $$

$$ {}_{F}\boldsymbol{S} = \begin{bmatrix} \frac{1}{E_{11}} & -\frac{\nu_{12}}{E_1} & -\frac{\nu_{12}}{E_1} & 0 & 0 & 0 \\ & \frac{1}{E_{22}} & -\frac{\nu_{23}}{E_2} & 0 & 0 & 0 \\ & & \frac{1}{E_{22}} & 0 & 0 & 0 \\ & & & \frac{2(1+\nu_{23})}{E_{22}} & 0 & 0 \\ & \text{sym} & & & \frac{1}{G_{12}} & 0 \\ & & & & & \frac{1}{G_{12}} \end{bmatrix}. \tag{5.10} $$

The local transformed stiffnesses result from the compliances with:

$$ {}_{G}\boldsymbol{S} = \begin{bmatrix} \frac{1}{E_x} & -\frac{\nu_{xy}}{E_x} & -\frac{\nu_{xz}}{E_{xx}} & 0 & 0 & 0 \\ & \frac{1}{E_y} & -\frac{\nu_{yz}}{E_y} & 0 & 0 & 0 \\ & & \frac{1}{E_z} & 0 & 0 & 0 \\ & & & \frac{1}{G_{yz}} & 0 & 0 \\ & \text{sym} & & & \frac{1}{G_{xz}} & 0 \\ & & & & & \frac{1}{G_{xy}} \end{bmatrix}. \tag{5.11} $$

Global compliances or rather stiffnesses of the representative volume element are determined by integration over the contemplated area:

$$ {}_G\overline{\boldsymbol{S}} = \frac{1}{h}\frac{1}{L}\int_{-h/2}^{h/2}\int_{0}^{L} {}_G\boldsymbol{S}\, dxdz \tag{5.12} $$

LOCAL STRESSES

Based on the previously determined stiffnesses, respective stress distributions, arising out of an x-direction loading can be determined. Firstly the more general case of graded waviness is considered. Fig. 5.8 shows the discretization of the representative volume element.

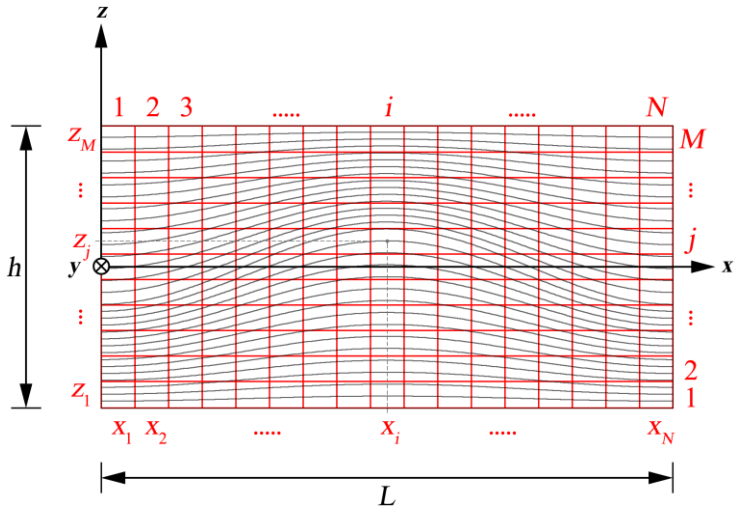

Fig. 5.8: Discretization of the representative volume element with graded waviness [81]

The sections are referred to $i \in [1; N]$ in x-direction and $j \in [1; M]$ in z-direction. The central point $(x_i|z_j)$ of element ij results from:

$$ \left(x_i = \left(\frac{2i-1}{2N}\right)L \,\middle|\, z_j = \left(\frac{2j-1-M}{2M}\right)h\right) \tag{5.13} $$

Assuming a stress σ_x that is subjected to the overall volume element, each section i is considered individually. Hereby, a constant strain ${}_G\boldsymbol{\varepsilon}_i$ in z-direction is assumed. Each element i is considered as a laminate with M plies and analyzed via the classical laminate theory (Fig. 5.8).

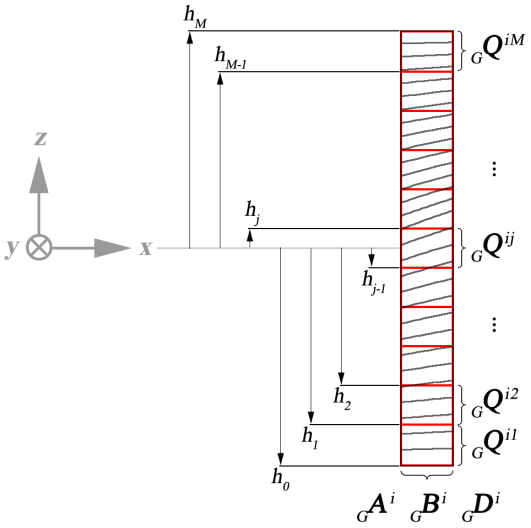

Fig. 5.9: Application of the classical laminate theory on the cut-out [81]

The previously derived local stiffnesses are used to determine a reduced stiffness matrix ${}_G\boldsymbol{Q}_{ij} = {}_G\boldsymbol{Q}(x_i, z_j)$ for every ply ij of the element i:

$$ {}_G\boldsymbol{Q}_{ij} = {}_G\begin{bmatrix} Q_{11} & Q_{12} & 0 \\ Q_{12} & Q_{22} & 0 \\ 0 & 0 & Q_{66} \end{bmatrix}_{ij} = {}_G\begin{bmatrix} \frac{E_x}{1-\nu_{xy}\nu_{yx}} & \frac{\nu_{xy}E_y}{1-\nu_{xy}\nu_{yx}} & 0 \\ \frac{\nu_{xy}E_y}{1-\nu_{xy}\nu_{yx}} & \frac{E_y}{1-\nu_{xy}\nu_{yx}} & 0 \\ 0 & 0 & G_{xy} \end{bmatrix}_{ij} \tag{5.14} $$

The height of the considered volume element being h, the relative distance h_j results to:

$$ h_j = \left(\frac{j}{M} - \frac{1}{2}\right) h \tag{5.15} $$

Therefore, the stiffness matrixes ${}_G\boldsymbol{A}_i$, ${}_G\boldsymbol{B}_i$ and ${}_G\boldsymbol{C}_i$ are determined by:

$$ {}_G\boldsymbol{A}_i = {}_G\boldsymbol{A}(x_i) = \sum_{j=1}^{M} {}_G\boldsymbol{Q}_{ij}(h_j - h_{j-1}) \tag{5.16} $$

$$ {}_G\boldsymbol{B}_i = {}_G\boldsymbol{B}(x_i) = \frac{1}{2}\sum_{j=1}^{M} {}_G\boldsymbol{Q}_{ij}(h_j^2 - h_{j-1}^2) \tag{5.17} $$

$$ {}_G\boldsymbol{C}_i = {}_G\boldsymbol{D}(x_i) = \frac{1}{3}\sum_{j=1}^{M} {}_G\boldsymbol{Q}_{ij}(h_j^3 - h_{j-1}^3) \tag{5.18} $$

Further, the stress-strain relation for the combined membrane plate element is applied:

$$ {}_G\begin{bmatrix}\boldsymbol{N}\\ \boldsymbol{M}\end{bmatrix}_i = {}_G\begin{bmatrix}\boldsymbol{A} & \boldsymbol{B}\\ \boldsymbol{B} & \boldsymbol{D}\end{bmatrix}_i \cdot {}_G\begin{bmatrix}\boldsymbol{\varepsilon}\\ \boldsymbol{\kappa}\end{bmatrix}_{i,0} \quad \text{or respectively:} \quad {}_G\begin{bmatrix}\boldsymbol{\varepsilon}\\ \boldsymbol{\kappa}\end{bmatrix}_{i,0} = {}_G\begin{bmatrix}\boldsymbol{a} & \boldsymbol{b}\\ \boldsymbol{b} & \boldsymbol{d}\end{bmatrix}_i \cdot {}_G\begin{bmatrix}\boldsymbol{N}\\ \boldsymbol{M}\end{bmatrix}_i \tag{5.19} $$

The approach to the stress analysis is based on ISHIKAWA and CHOU [82] [83]. Therein, in case of a bending-free state a modified law of elasticity is established. The assumption of a bending-free state is based on the fact that although under axial loading local shear deformations orthogonal to the ply are apparent, in global perspective shear deformations are omitted. Analytically, the bending-free state is implemented by applying local bending constraints, claiming the absence of curvatures ${}_G\boldsymbol{\kappa}_{i,0} = \boldsymbol{0}$ at existing moment ${}_G\boldsymbol{M}_i \neq \boldsymbol{0}$. Inserted in (5.19) it follows:

$$ {}_G\boldsymbol{M}_i = {}_G\left[-\boldsymbol{d}^{-1}\cdot\boldsymbol{b}\cdot\boldsymbol{N}\right]_i $$

$$ {}_G\boldsymbol{\varepsilon}_{i,0} = {}_G\left[\boldsymbol{a}\cdot\boldsymbol{N}+\boldsymbol{b}\cdot\boldsymbol{M}\right]_i = {}_G\left[\boldsymbol{a}\cdot\boldsymbol{N}-\boldsymbol{b}\cdot\boldsymbol{d}^{-1}\cdot\boldsymbol{b}\cdot\boldsymbol{N}\right]_i \tag{5.20} $$

Thus, the new law of elasticity according to ISHIKAWA und CHOU [83] is:

$$ {}_G\boldsymbol{\varepsilon}_{i,0} = {}_G\left[\boldsymbol{a}^*\cdot\boldsymbol{N}\right]_i \tag{5.21} $$

The new bending-free extensional compliance matrix ${}_G\boldsymbol{a}_{*i}$ is given as:

$$ {}_G\boldsymbol{a}_{*i} = {}_G\left[\boldsymbol{a}-\boldsymbol{b}\cdot\boldsymbol{d}^{-1}\cdot\boldsymbol{b}\right]_i \tag{5.22} $$

In the present case equation (5.22) can be simplified. Because of each element *i* being a mid-plane symmetrical laminate, the bending-extension coupling stiffness matrix follows as ${}_G\boldsymbol{B}_i = \boldsymbol{0}$. [29] Using block-wise matrix inversion according to [84], subsequent relation can be shown:

$$ {}_G\begin{bmatrix}\boldsymbol{a} & \boldsymbol{b}\\ \boldsymbol{b} & \boldsymbol{d}\end{bmatrix}_i = \left({}_G\begin{bmatrix}\boldsymbol{A} & 0\\ 0 & \boldsymbol{D}\end{bmatrix}_i\right)^{-1} = {}_G\begin{bmatrix}\boldsymbol{A}^{-1} & 0\\ 0 & \boldsymbol{D}^{-1}\end{bmatrix}_i \tag{5.23} $$

Hence, the new extensional compliance matrix ${}_G\boldsymbol{a}_{*i}$ can also be written by:

$$ {}_G\boldsymbol{a}_{*i} = {}_G\boldsymbol{a}_i = \left({}_G\boldsymbol{A}_i\right)^{-1} \tag{5.24} $$

Subsequently, the occurring stresses and strains are considered. The externally applied loading ${}_G\boldsymbol{\sigma}$, represented in global coordinates can be expressed as:

$$ {}_G\boldsymbol{\sigma} = {}_G\begin{bmatrix}\sigma_x\\ \sigma_y\\ \tau_{xy}\end{bmatrix} = {}_G\begin{bmatrix}\sigma_x\\ 0\\ 0\end{bmatrix} \tag{5.25} $$

From Equ. (5.21) and (5.24) the distribution of strains ${}_G\boldsymbol{\varepsilon}^i$ that are constant over the respective section i results:

$$ {}_G\boldsymbol{\varepsilon}_i = h \cdot ({}_G\boldsymbol{A}_i)^{-1} \cdot {}_G\boldsymbol{\sigma} = \begin{bmatrix} \varepsilon_x \\ \varepsilon_y \\ 0 \end{bmatrix}_{G,i} \tag{5.26} $$

The local stresses ${}_G\boldsymbol{\sigma}_{ij}$ in global coordinates succeed together with the reduced stiffness matrices ${}_G\boldsymbol{Q}_{ij}$ according to equation (5.14) to:

$$ {}_G\boldsymbol{\sigma}_{ij} = {}_G\boldsymbol{Q}_{ij} \cdot {}_G\boldsymbol{\varepsilon}_i = {}_G\boldsymbol{Q} \begin{bmatrix} \sigma_x \\ \sigma_y \\ 0 \end{bmatrix}_{ij} \tag{5.27} $$

Using the locational-dependent transformation matrix $\boldsymbol{T}_{ij}^{FG} = \boldsymbol{T}^{FG}(x_i, z_j)$ according to equation (5.9), the stresses of equation (5.27) can be transferred into the fiber coordinate system F:

$$ {}_F\boldsymbol{\sigma}_{ij} = {}_{FG}\boldsymbol{T}_{ij} \cdot \begin{bmatrix} \sigma_x \\ \sigma_y \\ 0 \\ 0 \\ 0 \\ 0 \end{bmatrix}_{G,ij} = \begin{bmatrix} \sigma_1 \\ \sigma_2 \\ \sigma_3 \\ 0 \\ \tau_{13} \\ 0 \end{bmatrix}_{F,ij} \tag{5.28} $$

Moreover, the strains expressed in the fiber coordinate system are determined by:

$$ {}_F\boldsymbol{\varepsilon}_{ij} = \boldsymbol{R} \cdot {}_{FG}\boldsymbol{T}_{ij} \cdot \boldsymbol{R}^{-1}\boldsymbol{\varepsilon} \begin{bmatrix} \varepsilon_x \\ \varepsilon_y \\ 0 \\ 0 \\ 0 \\ 0 \end{bmatrix}_{G,i} = \boldsymbol{\varepsilon} \begin{bmatrix} \varepsilon_1 \\ \varepsilon_2 \\ \varepsilon_3 \\ 0 \\ \gamma_{13} \\ 0 \end{bmatrix}_{F,ij} \tag{5.29} $$

In the event of uniform waviness, equation (5.28) can be simplified. Due to the independence in z-direction, all plies ij of the element i own the identical reduced stiffness matrices ${}_G\boldsymbol{Q}_{ij} = {}_G\boldsymbol{Q}_i$. The extensional stiffness matrix ${}_G\boldsymbol{A}_i$ follows by:

$$ {}_G\boldsymbol{A}_i = {}_G\boldsymbol{Q}_i \cdot h \tag{5.30} $$

Considering equations (5.26) and (5.27), it can be seen that the local stress ${}_G\boldsymbol{\sigma}_{ij}$ is equal to the global applied loading ${}_G\boldsymbol{\sigma}$. For uniform wavinesses, the stress distribution follows from the simple transformation:

$$ {}_F\boldsymbol{\sigma}_{ij} = {}_{FG}\boldsymbol{T}_{ij} \cdot \begin{bmatrix} \sigma_x \\ 0 \\ 0 \\ 0 \\ 0 \\ 0 \end{bmatrix}_G = \begin{bmatrix} \sigma_1 \\ 0 \\ \sigma_3 \\ 0 \\ \tau_{13} \\ 0 \end{bmatrix}_{F\,ij} \tag{5.31} $$

STRENGTH ANALYSIS ACCORDING TO PUCK CRITERION

The slightly adapted analysis approach according to [82] [4] is extended by a strength analysis based on the PUCK failure criterion following [85], enabling the distinction between fiber failure (FF) and inter-fiber failure (IFF). Stresses of equations (5.28) and (5.31) are used. The description confines itself merely to the essential principles.

The failure criteria for fiber failure and inter-fiber failure according to PUCK [85] are:

$$ f_{E_{FF}} = \frac{\sigma_{11}^{\pm}}{R_{11}^{\pm}} = \begin{cases} \dfrac{\sigma_{11}^{+}}{R_{11}^{+}} = 1 \;\forall\; \sigma_{11} \geq 0 \\ \\ \dfrac{\sigma_{11}^{-}}{R_{11}^{-}} = 1 \;\forall\; \sigma_{11} < 0 \end{cases} \tag{5.32} $$

$$ f_{E_{IFF}}(\theta_f) = \sqrt{\left[\left(\frac{1}{R_{22}^{+}} - \frac{p_{\perp\psi}^{+}}{R_{\perp\psi}^{A}}\right)\sigma_n\right]^2 + \left(\frac{\tau_{nt}}{R_{22}^{A}}\right)^2 + \left(\frac{\tau_{n1}}{R_{12}}\right)^2} + \frac{p_{\perp\psi}^{+}}{R_{\perp\psi}^{A}}\sigma_n = 1 \qquad \forall \;\; \sigma_n \geq 0 \tag{5.33} $$

$$ f_{E_{IFF}}(\theta_f) = \sqrt{\left(\frac{p_{\perp\psi}^{-}}{R_{\perp\psi}^{A}}\sigma_n\right)^2 + \left(\frac{\tau_{nt}}{R_{22}^{A}}\right)^2 + \left(\frac{\tau_{n1}}{R_{12}}\right)^2} + \frac{p_{\perp\psi}^{-}}{R_{\perp\psi}^{A}}\sigma_n = 1 \qquad \forall \;\; \sigma_n < 0 \tag{5.34} $$

For a loading in fiber direction $\sigma_{\parallel}^{\pm}$, it is stated:

$$ \begin{aligned} \sigma_{11}^{+} &= \sigma_{11} && \forall\, \sigma_{11} \geq 0 \\ \sigma_{11}^{-} &= |\sigma_{11}| && \forall\, \sigma_{11} < 0 \end{aligned} \tag{5.35} $$

Stresses σ_n, τ_{nt} and τ_{n1} result from the angle $\theta_f \in [-90°, 90°]$ using a coordinate transformation to the coordinate system of the fracture plane B:

$$ {}_B\begin{bmatrix} \sigma_n \\ \tau_{nt} \\ \tau_{n1} \end{bmatrix} = {}_{BF}\boldsymbol{T} \cdot \begin{bmatrix} \sigma_2 \\ \sigma_3 \\ \tau_{23} \\ \tau_{31} \\ \tau_{21} \end{bmatrix}_F \tag{5.36} $$

$$\boldsymbol{T}_{BF} = \begin{bmatrix} c^2 & s^2 & 2cs & 0 & 0 \\ -sc & sc & (c^2 - s^2) & 0 & 0 \\ 0 & 0 & 0 & s & c \end{bmatrix} \tag{5.37}$$

$$c = \cos\theta_f \qquad s = \sin\theta_f$$

The ratio $p_{\perp\psi}^{\pm}/R_{\perp\psi}^{A}$ is determined by an interpolation, using inclination parameters $p_{\perp\parallel}^{\pm}$ and $p_{\perp\perp}^{\pm}$ from [29]:

$$\frac{p_{\perp\psi}^{\pm}}{R_{\perp\psi}^{A}} = \frac{p_{\perp\parallel}^{\pm}}{R_{12}}\sin^2\psi + \frac{p_{\perp\perp}^{\pm}}{R_{22}^{A}}\cos^2\psi \tag{5.38}$$

$$\psi = \arctan\frac{\tau_{n1}}{\tau_{nt}} \tag{5.39}$$

For the fracture resistance in the action plane $R_{\perp\perp}^{A}$, it can be written:

$$R_{22}^{A} = \frac{\mathrm{R}_{22}^{-}}{2(1 + p_{\perp\perp}^{-})} \tag{5.40}$$

IMPLEMENTATION IN MATLAB

The previously depicted analytical approach is implemented into a code using the software MATLAB. The laminate height is set to a default relative value of $h = 1$. Results in the event of uniform waviness can always be derived by setting $z = 0$. Fig. 5.10 shows the procedure and sequence of the global and local stiffness calculation within the code.

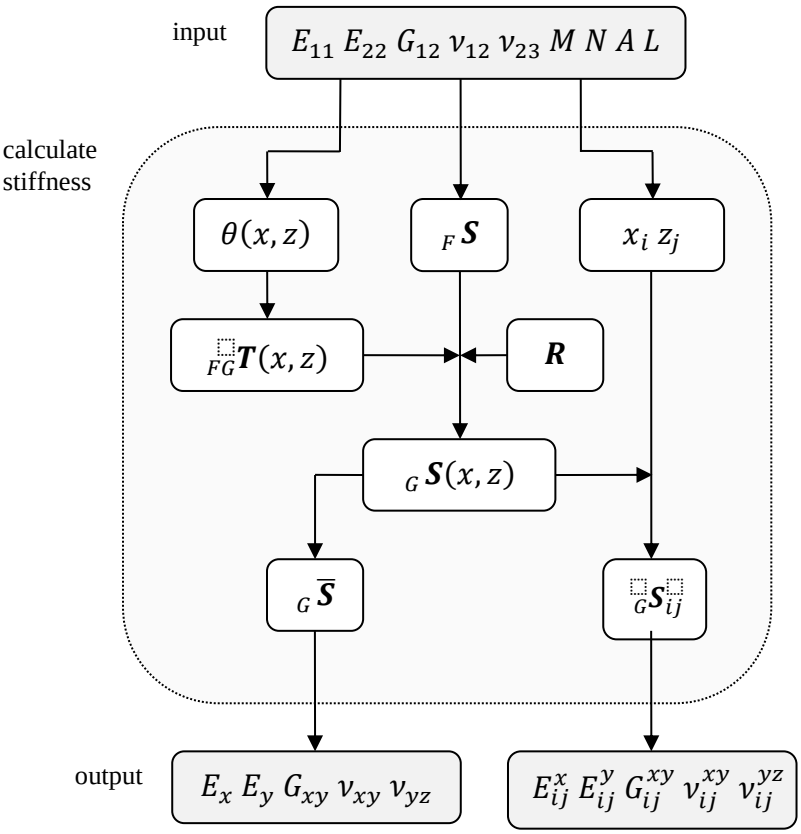

Fig. 5.1: Global and local stiffness calculation

In Fig. 5.11, the implemented process for calculating the stress/strain distributions is illustrated. Herein, the module of Fig. 5.10 is integrated to calculate stiffnesses.

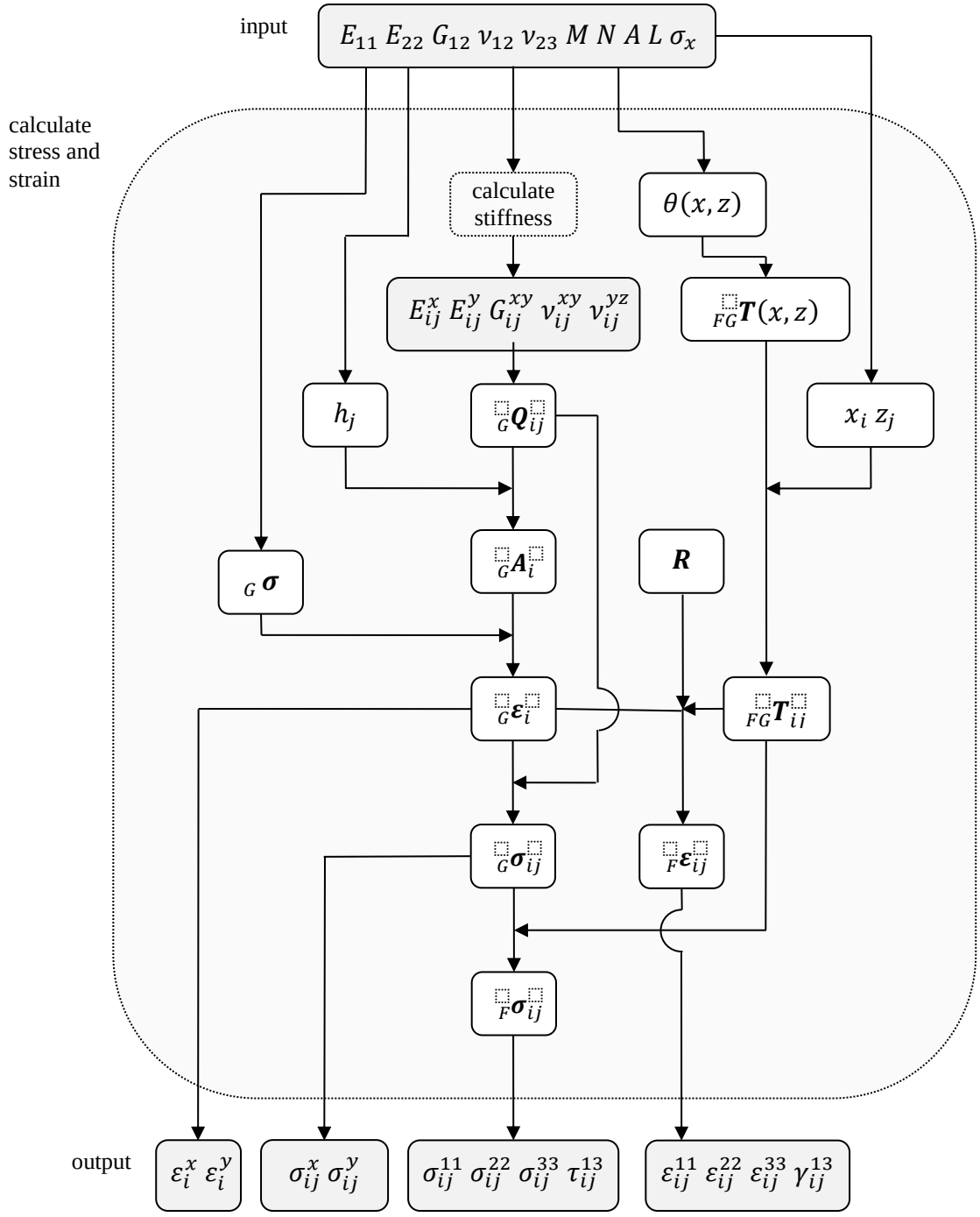

Fig. 5.11: Stress and strain calculation

The procedure of strength calculation is pictured in Fig. 5.12. In the process, the stress/strain calculation from Fig. 5.11 is used. The analytical strength prediction is conducted incrementally. The applied stress σ_x is increased iteratively, until one of the failure criteria has been reached. Furthermore, in each loading step various fracture planes θ_f are analysed for failure.

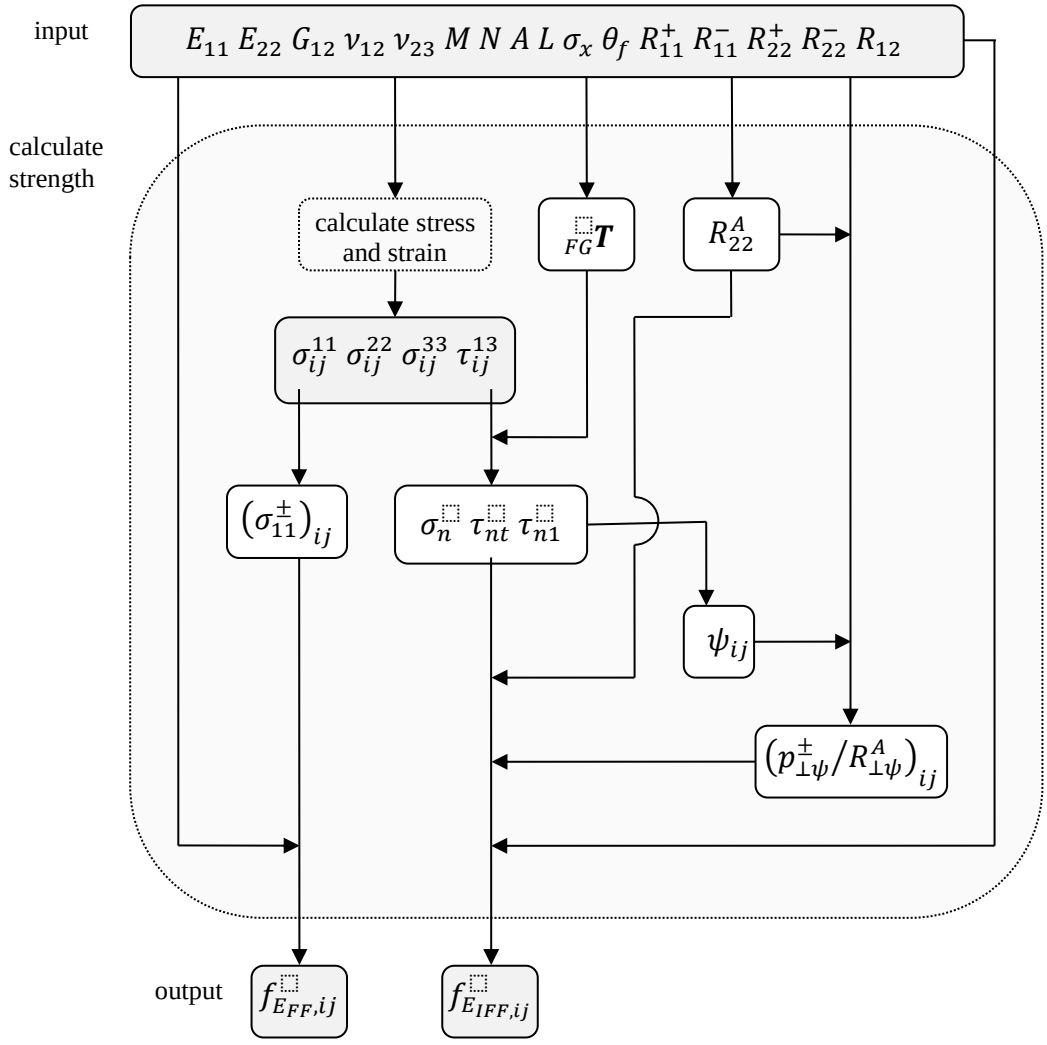

Fig. 5.2: Strength calculation by PUCK failure criterion

EXAMPLE OF GUI

The GUI is divided into multiple surfaces to calculate and visualize global and local stiffnesses, stress and strain distributions and the strength of laminates with ply waviness. To give an insight into the general functionality Fig. 5.13 shows the interface used to calculate local stress and strain distributions. It allows to quickly enter variable input parameters as stiffness properties, waviness severity, resolution of discretization and loading. After plotting, distributions of all interlaminar normal and shear stresses or strains can be displayed. Furthermore, the GUI makes it possible to choose between a fiber and global coordinate system and in case of graded waviness also to vary the height coordinate.

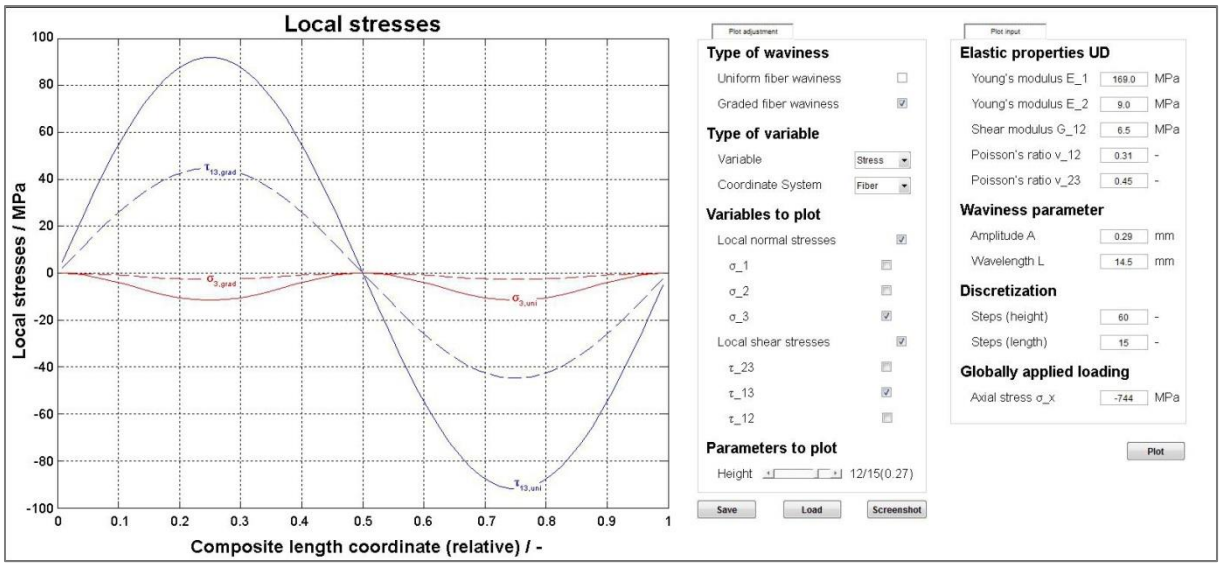

Fig. 5.13: GUI screen to calculate stresses and strains

VALIDATION OF MATLAB RESULTS

The distributions of the effective stiffnesses depending on the amplitude to wave-length ratio are in good agreement with several publications, applying analytical, numerical and also experimental approaches [82] [4] [86] [87] [88]. The example given in Fig. 5.14 shows analytical and experimental results from [88] confronted with results derived from MATLAB GUI.

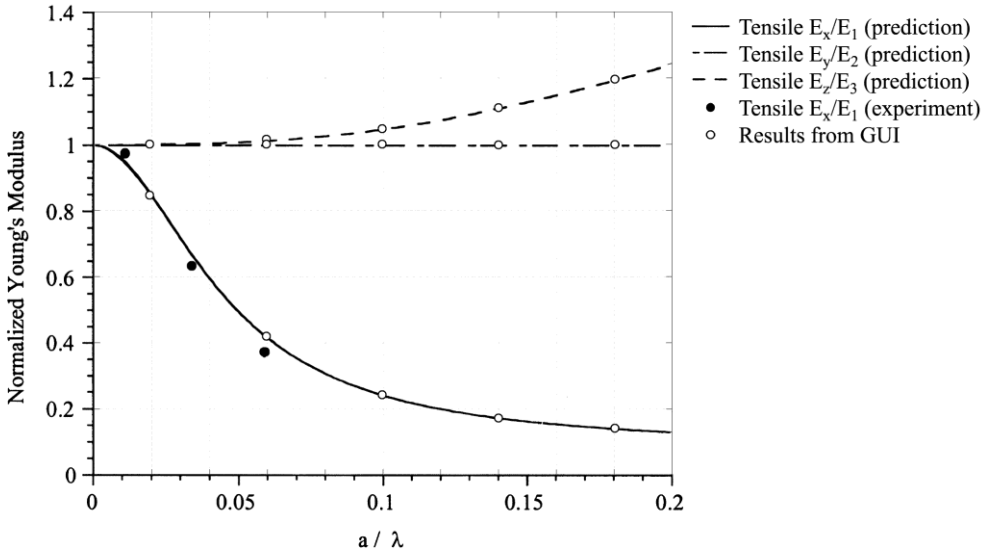

Fig. 5.14: Effective stiffnesses in case of uniform waviness

In [82], HSIAO and DANIEL calculate the strength to initial failure for a given configuration under compressive loading to be 744 MPa. Using the analytical approach presented gives a result of 748.73 MPa, showing good accordance to [82]. Moreover, failure takes place at the maximum fiber angle, also corresponding to the outcome of [82].

As HSIAO and DANIEL additionally perform an incremental analysis to calculate stresses at final failure, results from analytical approach presented cannot be compared directly due to the fact that the analytical approach only considers first ply failure. A further damage progression is not considered within this context. Nevertheless, initial and final failure stresses show a similar distribution, as seen in Fig. 5.15. The curves differ at a low amplitude to wavelength ratio, which may arise out of the distinction between fiber and interfiber failure drawn by the PUCK failure criterion. As carried out later, a change of failure mode takes place at low A/l values.

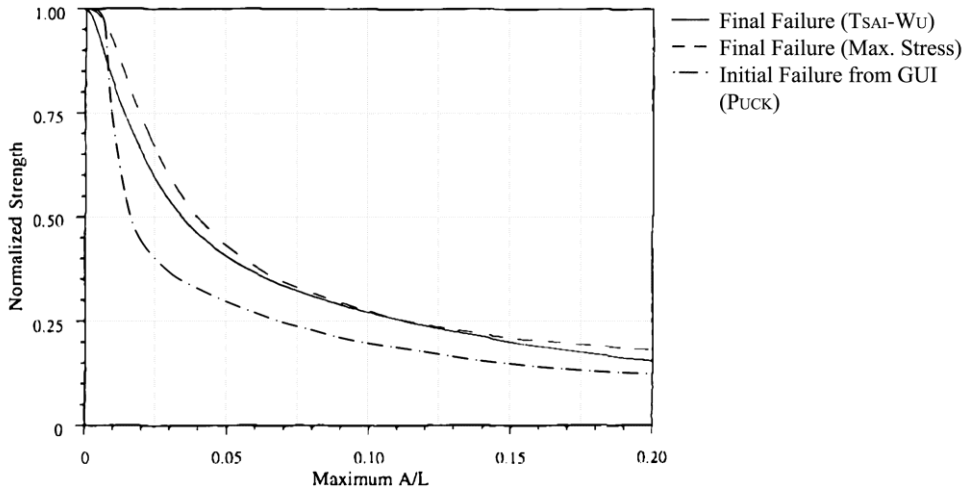

Fig. 5.15: Final failure stresses from [82] compared to initial failure stresses from GUI according to Hsiao/Daniel

ANNOTATION TO INTERLAMINAR STRESS STATE AND FAILURE IN WAVY LAMINATES

When loaded in fiber direction, ply waviness in composites leads to interlaminar shear stresses and induces compressive or tensile stresses perpendicular to the fiber. Vertical compressive stresses develop on compressive loading and accordingly tensile stresses on tensile loading. The largest arising stresses are found at the maximum fiber angle, where the laminate is assumed to fail.

After reaching a certain limit of waviness, the developing interlaminar stresses lead from fiber failure FF to inter-fiber failure IFF and strength drops rapidly with increasing A/l value. IFF is mainly caused by shear stresses but also influenced by stresses orthogonal to the fiber. Compressive stresses orthogonal to the fiber can prevent IFF, whereas superimposed tensile stresses can lead to earlier IFF. [29]

PARAMETRIC STUDY ON COMPRESSIVE STRENGTH BEHAVIOR

Hereinafter the influence of various UD strength parameters on strength to initial failure behavior of wavy laminates is investigated. A wavy composite of graded shape is considered. Therefore, a conventional glass fiber material and an EPOXY matrix system are applied. Using the rule of mixture (ROM), stiffness properties are specified. Strength parameters are estimated based on experimental test data. Hereby obtained mechanical data is given in Tab. 5.1. Inclination parameters are set to $p^{+}_{\perp\parallel} = 0.3$, $p^{-}_{\perp\parallel} = 0.25$, $p^{+}_{\perp\perp} = 0.2$ and $p^{-}_{\perp\perp} = 0.2$.

Tab. 5.1: Mechanical properties of GFRP

E_{11} [GPa]	E_{22} [GPa]	G_{12} [MPa]	υ_{12} [-]	υ_{23} [-]	R^{+}_{11} [MPa]	R^{-}_{11} [MPa]	R^{+}_{22} [MPa]	R^{-}_{22} [MPa]	R_{12} [MPa]
42.4	13.9	4055	0.292	0.43	891	807	76.5	144	48

The parametric study is conducted by both decreasing and increasing each strength value shown in Tab. 5.1 by 50 percent of its initial value while remaining strength values are kept constant. Corresponding distributions of the resulting strength to initial failure by PUCK are calculated using the previously described MATLAB GUI.

Generally noticeable in subsequent figures are kinks in all curves, where the resulting compressive strength drops rapidly. These kinks indicate a change of failure mode from fiber failure FF to inter-fiber failure IFF, which shall additionally be highlighted by circles.

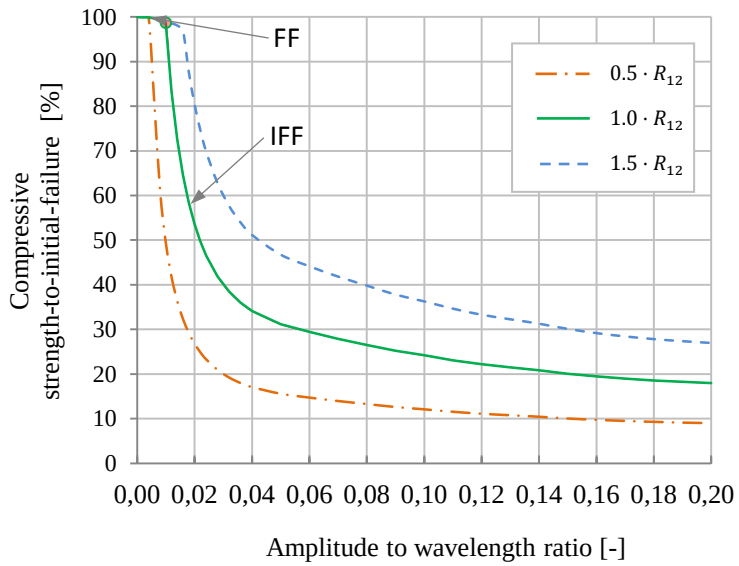

Fig. 5.16: Effect of R12 on the compressive strength

Variation of shear strength R_{12} shows significant impact on the resulting compressive strength of a wavy laminate, as can be seen in Fig. 5.16. In comparison to the base material, the compressive behavior of the degraded material is twofold: First, transition from fiber failure to interfiber failure takes place at smaller amplitude to wavelength ratio and second, after the transition strength is reduced more strongly. These two effects lead to a much more severe

impact of ply waviness to the compressive behavior of the laminate. In contrast, the material with increased shear strength shows a delayed transition to inter-fiber failure and a flatter descent of strength. Hence, the effect of ply waviness is weakened substantially.

Fig. 5.17 pictures the effect of compressive strength in fiber direction R_{11}^{-} on the effective compressive strength of wavy laminates. It shows that after inter-fiber failure takes place, compressive strength of the wavy laminate is not affected by R_{11}^{-}. However, the limit of A/l to change failure mode is influenced strongly. This can be taken to the extent that no fiber failure takes place at all for the degraded material, inducing a very insensitive behavior to waviness. Nonetheless, one has to consider this insensitivity only being due to a very weak material, failing on stress along its fiber orientation before any other failure can take place. On the other hand, ply waviness has severe impact on the strengthened material, as strength drops rapidly already at a low amplitude to wavelength ratio.

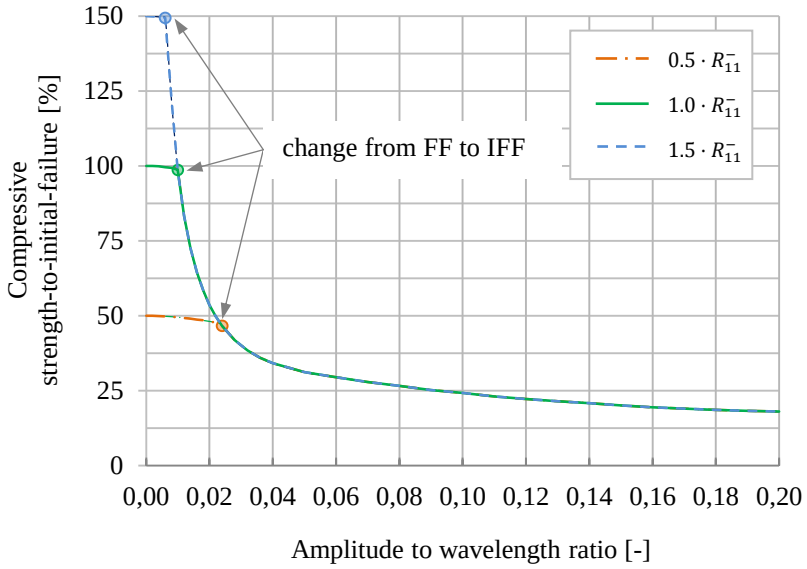

Fig. 5.17: Effect of R11- on the compressive strength

The variation of transverse strength R_{22}^{-} has a negligible influence on the resulting strength and thus is of no interest. The same applies for the effect of R_{11}^{+} on compressive strength and R_{11}^{-}on tensile strength.

In addition to the influence of strength parameters, the difference between graded and uniform wavinesses shall be taken into account, seen in Fig. 5.18. The compressive strength shows an increased impact of uniform waviness after inter-fiber failure takes place, although before change of failure mode waviness has a very light effect on the strength behavior.

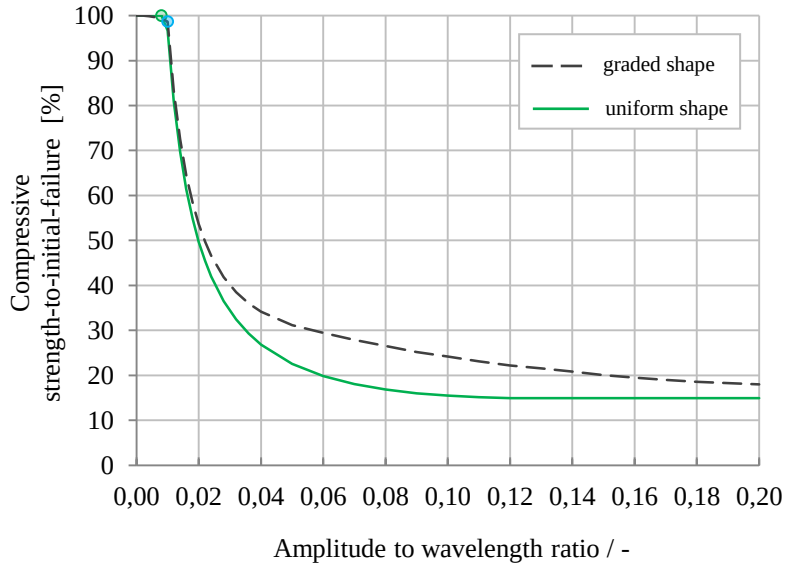

Fig. 5.18: Longitudinal compressive strength of uniform and graded ply wavinesses

CASE STUDY: DAMAGE TOLERANT MATRIX SYSTEM

Finally, after having identified the individual impact of each strength parameter a thought experiment shall be conducted. The aim is to design a composite`s properties featuring a high robustness against waviness. Based on the evaluated material, strength in fiber direction R_{11}^{-} is lowered by 50 percent and shear strength R_{12} is increased by 50 percent. This waviness-optimized composite is now compared to the original configuration with respect to the compressive strength depending on waviness severity.

Under compressive loading, the strength drop caused by waviness is reduced drastically, as can be seen in Fig. 5.19. Moreover, the optimized material shows no transition to inter-fiber failure at all, shown by the absence of a kink in the strength distribution. The relative loss in strength of the optimized configuration is lower than of the standard configuration.

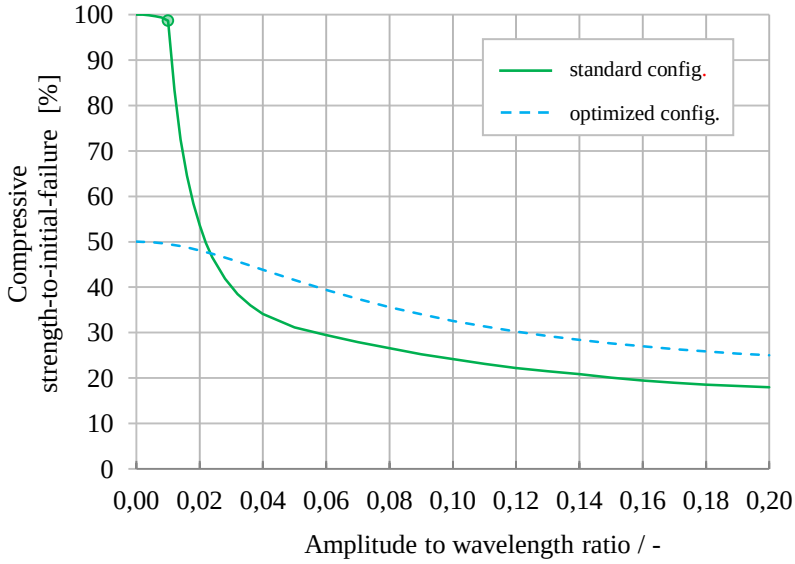

Fig. 5.19: Optimized system on the compressive strength

DISCUSSION

The previous findings can be summarized: Having very small waviness, fiber failure dominates. The fiber properties dominate the failure mechanism. As soon as waviness increases beyond a defined misalignment, the matrix properties dominate the strength behavior. Furthermore, the degradation is due to the matrix properties.

Previously shown effects shall now be regarded focusing on the influence of the matrix systems and their application for composite design. The matrix dominated shear strength R_{12} has been shown to have a strong impact on compressive failure behavior and thus bears great potential to minimize the effects of ply waviness in composites by utilizing adapted matrix systems. The longitudinal compressive strength R_{11}^{-} is dependent on both matrix and fiber and cannot be assigned clearly to one component by this analytical approach. Nevertheless, R_{11}^{-} allows to influence waviness tolerance on compressive loading by shifting the limit of waviness where inter-fiber failure sets in and strength drops rapidly.

In summary, a waviness robust composite design can be conducted by utilizing special matrix systems leading to increased shear strength R_{12} and decreased longitudinal compressive strength R_{11}^{-}. Nevertheless, one has to consider this only being a hypothetical study, as strength parameters are varied individually, while stiffness parameters are kept constant. Numerical and experimental studies need to be carried out verifying the outcome of this work. The outcome of this analytical approach can be used for a qualitative and quick assessment of wavy specimens. A deeper understanding of failure mechanisms at ply wavinesses discussed in the subsequent context could help to develop new matrix systems that are particularly robust to ply waviness.

5.2.2. Numerical simulation

A continuum damage model[26] developed together with TAUBERT and MANDEL [89] is incorporated within an ABAQUS user defined material subroutine VUMAT and described next. The aim is to incorporate failure and degradation mechanisms, which are typically occurring in wavy composites, within the numerical simulation. Findings in chap.5.1.3 also show that nonlinear shear effects have to be considered.

CONSTITUTIVE MATERIAL BEHAVIOR

The constitutive behavior of a single UD ply can be classified into the elasto-plastic hardening and the elasto-damage softening regime (Fig. 5.20). In the hardening regime the stress increases with ascending strain, whereby nonlinear material behavior has to be considered. After the failure initiation of the ply the softening regime begins. Within the softening regime an ascending strain leads to decreasing stresses representing the damage progression of the ply. This effect incorporated in the model is controlled by an energy-based linear stiffness degradation law.

The stress state is calculated by an ABAQUS user defined material subroutine VUMAT using the input of the total strain at the material integration point. The total strain $\boldsymbol{\varepsilon}$ consists of a plastic $\boldsymbol{\varepsilon}^{pl}$ and an elastic part $\boldsymbol{\varepsilon}^{ed}$.

$$\boldsymbol{\varepsilon} = \boldsymbol{\varepsilon}^{pl} + \boldsymbol{\varepsilon}^{ed} \tag{5.41}$$

The stress is defined by (5.42), where $\boldsymbol{C}^{d}$ denotes the damaged stiffness matrix.

$$\boldsymbol{\sigma} = \boldsymbol{C}^{d}(\boldsymbol{\varepsilon} - \boldsymbol{\varepsilon}^{pl}) \tag{5.42}$$

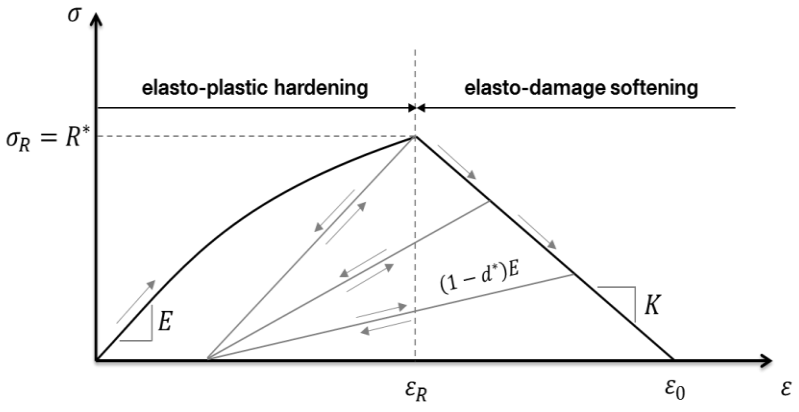

Fig. 5.20: Constitutive material behavior

[26] ply-based

NONLINEARITY

The idealized material behavior in the elasto-plastic assumed hardening regime in Fig. 3.1 is discussed next. Numerous references [90] [76] [68] show a significant influence of the plastic deformations on the failure behavior of thick laminates. In order to simulate the compression failure as a result of a kink band formation it is essential to include the nonlinear shear behavior of the composite material in the model. [90] [76] [68] This is also stated in chap.5.1.3.1.

The constitutive material behavior in the elasto-plastic regime can be defined as

$$\sigma_{ij} = \boldsymbol{C}^{ep}\varepsilon_{ij}. \tag{5.43}$$

The shear strain-stress relation is defined by

$$\varepsilon_{13} = \frac{\tau_{13}}{G_{13}} + \left\langle \left(\frac{\tau_{13}}{A_{nl}}\right)^{\frac{1}{n_{nl}}} \right\rangle. \tag{5.44}$$

Herein, the transcription $\langle \dots \rangle$ describe the MACAULAY brackets. The shear nonlinearity poses the main part of nonlinearities. Thus, the non-linear material behavior is approximated by a one-dimensional pure shear law. Moreover, it offers a facile numerical implementation. Only a few material parameters are needed.

The yield condition is defined as

$$f(\tau_{13}, \alpha) = |\tau_{13}| - r(\alpha) - \tau_{13}^{y} \tag{5.45}$$

where $r(\alpha)$ describes the hardening law with α as an internal hardening variable. As visualized in Fig. 5.20, the hardening is assumed to be isotropic defined by a uniform expansion of the yield point. The RAMBERG-OSGOOD type hardening power law shows a good correlation to experiments of the investigated material. It is defined as

$$r(\alpha) = A_{nl}(\alpha)^{n_{nl}}. \tag{5.46}$$

In case plastic material behavior occurs by assuming isotropic hardening, the elasto-plastic tangent modulus is

$$C^{ep} = \begin{bmatrix} \frac{E_1}{1-\nu_{13}\nu_{31}} & \frac{\nu_{31}E_1}{1-\nu_{13}\nu_{31}} & 0 \\ \frac{\nu_{13}E_3}{1-\nu_{13}\nu_{31}} & \frac{E_3}{1-\nu_{13}\nu_{31}} & 0 \\ 0 & 0 & \frac{G_{13}n_{nl}A_{nl}\alpha^{n_{nl}-1}}{G_{13}+n_{nl}A_{nl}\alpha^{n_{nl}-1}} \end{bmatrix}. \tag{5.47}$$

FAILURE INITIATION

The transition between hardening and softening regime is indicated by the strength limit of the unidirectional single ply. Therefore, the PUCK failure criterion following [29] [91] enables

the distinction between FF and IFF. The description confines itself merely to the essential principles. The failure criteria[27] for fiber failure and inter-fiber failure are:

$$f_{E_{FF}} = \frac{\sigma_{11}^{\pm}}{R_{11}^{\pm}} = \begin{cases} \frac{\sigma_{11}^{t}}{R_{11}^{t}} = 1 \; \forall \; \sigma_{11} \geq 0 \\ \\ \frac{\sigma_{11}^{c}}{R_{11}^{c}} = 1 \; \forall \; \sigma_{11} < 0 \end{cases} \tag{5.48}$$

Mode A:

$$\theta_{fp} = 0°; \; f_E = \sqrt{\left[\left(\frac{1}{R_{33}^{t}} - \frac{p_{31}^{t}}{R_{31}}\right)\sigma_{33}\right]^2 + \left(\frac{\tau_{31}}{R_{31}}\right)^2} + \frac{p_{31}^{t}}{R_{31}}\sigma_2 \qquad \forall \; \sigma_{33} \geq 0 \tag{5.49}$$

Mode B:

$$\theta_{fp} = 0°; \; f_E = \sqrt{\left(\frac{p_{31}^{c}}{R_{31}}\sigma_{33}\right)^2 + \left(\frac{\tau_{31}}{R_{31}}\right)^2} + \frac{p_{31}^{c}}{R_{31}}\sigma_{33} \qquad \forall \; \sigma_{33} \geq 0 \wedge \left|\frac{\sigma_{33}}{\tau_{31}}\right| \leq \left|\frac{R_{33}^{A}}{\tau_{31,c}}\right| \tag{5.50}$$

Mode C:

$$\theta_{fp} \neq 0°; \; f_E = \left[\left(\frac{\tau_{31}}{2(1+p_{33}^{c})R_{31}}\right)^2 + \left(\frac{\sigma_{33}}{R_{33}^{c}}\right)^2\right]\frac{R_{33}^{c}}{-\sigma_{33}} \qquad \forall \; \sigma_{33} \geq 0 \wedge \left|\frac{\sigma_{33}}{\tau_{31}}\right| \geq \left|\frac{R_{33}^{A}}{\tau_{31,c}}\right| \tag{5.51}$$

where:

$$\tau_{31,c} = R_{31}\sqrt{1 + 2p_{33}^{c}} \tag{5.52}$$

and

$$R_{33}^{A} = \frac{R_{33}^{c}}{2(1+p_{33}^{c})} \tag{5.53}$$

Inclination parameters are set to $p_{31}^{t} = 0.3$; $p_{31}^{c} = 0.25$; $p_{33}^{t} = 0.2$ and $p_{33}^{c} = 0.2$ assuming glass-fiber reinforced plastics (GFRP).

FAILURE PROGRESSION

Next, the idealized material behavior within the elasto-damaged softening regime shown in Fig. 5.20 is described. After the initiation of failure in one ply of a composite laminate - indicated and distinguished by the failure initiation criteria mentioned above - the bearable load of the laminate can be further increased considerably. Therefore, the processes leading to ultimate failure have to be numerically distinguished. Damage in thick laminates including kinking, occurs on micromechanical level. Considering the behavior of the constituents, namely fiber and matrix, offers the opportunity to take into account initial defects like fiber misalignments. Nevertheless, a micromechanical approach requires numerous material data

[27] See also chap.5.2.1.

and is computationally expensive. A common approach of damage idealization is the continuum damage mechanics (CDM), where a crack is smeared within an element and no initial crack tip is modeled.

Focusing on the modeling of the composites, a continuum damage approach is used to represent the failure mechanisms such as matrix cracking, fiber fracture, delamination and kinking. Due to these failure mechanisms energy is dissipated irreversibly. The idealization is carried out as a reduction of corresponding stiffnesses of homogenized continua with averaged material properties. The constitutive material behavior in the elasto-damaged assumed softening regime can be defined as

$$\sigma_{ij} = \boldsymbol{C}^d \varepsilon_{ij}^{ed}, \tag{5.54}$$

where C^d represents the damaged stiffness matrix. The elasto-damaged stiffness matrix of the material can be defined as

$$\boldsymbol{C}^d = \begin{bmatrix} \frac{(1-d_f)E_1}{1-(1-d_f)(1-d_m)\nu_{13}\nu_{31}} & \frac{(1-d_f)(1-d_m)\nu_{31}E_1}{1-(1-d_f)(1-d_m)\nu_{13}\nu_{31}} & 0 \\ \frac{(1-d_f)(1-d_m)\nu_{13}E_3}{1-(1-d_f)(1-d_m)\nu_{13}\nu_{31}} & \frac{(1-d_m)E_3}{1-(1-d_f)(1-d_m)\nu_{13}\nu_{31}} & 0 \\ 0 & 0 & (1-d_s)G_{13} \end{bmatrix}. \tag{5.55}$$

The damage variables d_i represent the state of the damage progression and, thus, the reduction of the corresponding stiffness. Herein, the damage variables are distinguished in d_f, d_m and d_s considering the damage progression of the fiber (longitudinal), matrix and shear direction. While undamaged material is idealized by $d_i = 0$, a fully damage state is defined by $d_i = 1$.

Plane stress elements representing the cross-section of the specimens are used. Due to the same fiber orientation of all plies, this is a numerical efficient way to consider the through the thickness stresses, allowing the model to represent delamination. In chap.5.5, the damage progression of a wavy specimen under a compression load is shown.

Determining the damage variables d_i the relation

$$d_i(f_E, K) = 1 + \frac{K_i}{E_i} - \frac{1}{(f_E)_i}\left(1 + \frac{K_i}{E_i}\right) \tag{5.56}$$

is used, where K_i characterizes the descent within the diagram (Fig. 5.20) and $(f_E)_i$ the stress exposure related to an undamaged stress state. K_i depends on the fracture toughness of the failure mode i and the element size. [92] [93]

The virtual specimen is described in chap.5.5. Therein, the numerical simulations are validated against experiments.

5.3. Experimental methods

First, the specimens` geometry (chap. 5.3.1) is defined, followed by the description of the fabrication method (chap. 5.3.2) and the specimens` characterization (chap. 5.3.3).

5.3.1. Definition of the specimens` geometry

Specimens containing artificially induced ply waviness are defined and generated in order to verify the simulation results. A wavy specimen`s geometry is derived from a DoE study.
The required specimen consists of a non-standard geometry. An appropriate standard specification is not available. CAIAZZO [57] conducted DoE studies for compression tests of a unidirectional specimen varying both the amplitude-to-length ratio, the free gauge length and the specimen`s thickness. "Results show an increasing mean compression strength with decreasing thickness. However, the scatter in the data also increases with decreasing thickness (…)." Further, [58] and [94] stated that "while prior research has shown strong tendencies for laminate mechanical response to scale according to WEIBULL scaling theories (critical defect sensitivity), there is no conclusive evidence to support that the response of flawed structures will follow the same trends." [94] Based on the literature it can be stated that it is not trivial to determine a unique specimen`s geometry that can be scaled arbitrarily. Own experiments concerning this matter are carried out in chap.5.4. Apart from this, it should become apparent that an increasing thickness of the specimen helps to minimize undesirable effects such as clamping effects. The specimen has be constructed based on its desired failure mechanisms. [61] Utilizing the analytical approach (chap.5.2.1) and the numerical model (chap.5.2.2), the wavy specimen`s geometry is defined and finally proposed in Fig. 5.21 (right). For the compression tests the specimen`s length l=164mm is taken and for tensile tests the specimen`s length l =250mm is taken.

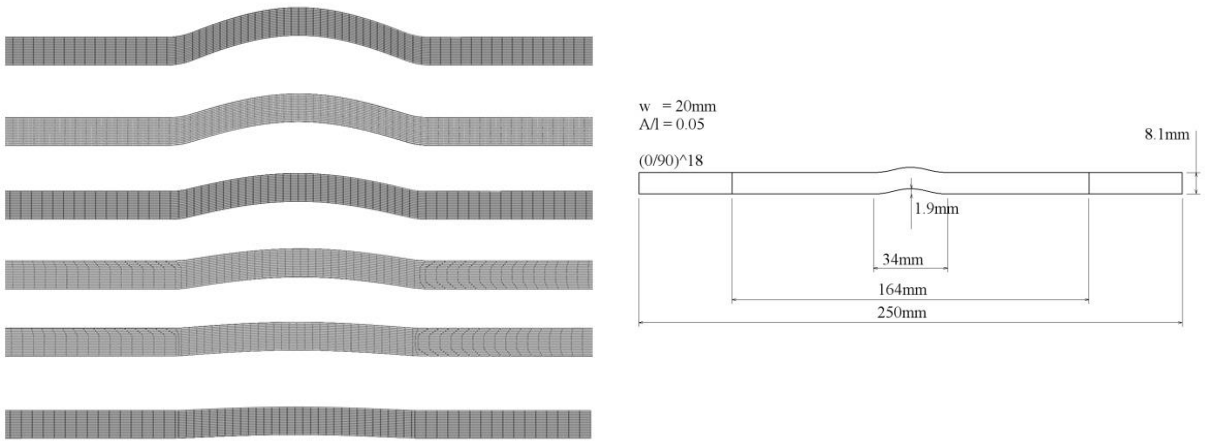

Fig. 5.21: Various ratios r (left); wavy specimen`s geometry (right)

Within this study, the specimen`s contour, the amplitude-to-wavelength ratio, the thickness of the specimen, and the free gauge length are varied in order to fulfill these mutual interacting requirements in Tab. 5.2. Thus, in order to induce matrix dominated failure mechanisms the specimen`s geometry is adjusted to a corresponding ratio $r = A/l$ and thickness t. It is desired that any failure that is induced by convenient test methods is driven by a combination of ILSS and ILTS, rather than through FF or local effects. Thus, while [65] shows matrix failure as initial failure mechanisms for little ratio r, [95] shows fiber failure occurring in greater ratio r. The aim is to define a wavy specimen geometry for material test and not for structural tests.

A representative thick wavy laminate of a real spar cap section (Fig. 5.42) of WTB is analyzed to determine A/l ratio that appear in reality (see also Tab. 5.6.). The specimen`s outer contour is dependent on the fabrication process and the scalability of its test data. A VAP® setup is used and further described in chap.5.3.2. The ratio r affects in turn the failure mechanism. The specimen is sized to prevent global buckling. The determined free gauge length l is a trade-off between the prevention of buckling effects and the feasibility of the application of non-contact measurements. Thus, the free gauge length is kept short to prevent global EULER buckling. Finally, the criteria of the determination of the thickness t for the specimen is twofold: First, it is recommended to design a preferably thick specimen in order to avoid that boundary conditions such as clamping effects are affecting the test data. Second, it is aimed to use standard test equipment. Thus, the maximum specimens` thickness is limited.

Tab. 5.2: Characteristics for determination of specimen`s geometry

characteristics	**design criteria**	**actions**
failure mechanisms	• matrix failure at the maximum inclinations • no initial fiber failure desired • probability of occurrence in reality	• A/l ratio r • thickness t
specimen`s contour	• reproducibility of fabrication • scalability of test data	• double curved specimen • VAP setup
A/l ratio r	• analysis of material behavior, no structural test • failure mechanisms • buckling effects • probability of occurrence in reality (literature data and existing evaluations)	• A/l ratio r
gauge length l	• buckling effects • feasibility of application of non-contact measurements	• gauge length l • thickness t
thickness	• clamping effects • use of standard test equipment	• thickness t • A/l ratio r

In the subsequent chap.5.3.2, the fabrication process is described.

5.3.2. Fabrication method of wavy specimen

An experimental technique is developed for the fabrication of specimen. The objective is to fabricate specimens, which contain artificially induced and predefined ply waviness that are manufactured by a reproducible and robust method. There are no standardized fabrication methods for wavy specimens. An excerpt of methods is cited from the literature:

- Resin stick method [3]: A sinusoidal wave of pure resin is fabricated in a first step. Subsequently, the plies are draped over the cured resin body, infiltrated and cured. [68]
- Fiber toe method [58]: Particular fiber toes are stacked in a pyramid fashion up til the desired ratio *r* is reached. The plies are draped thereon and finally form the wavy shape.
- Prepreg method [96]: Median plies are intercepted. Additionally, single fiber toes are positioned respectively. Finally, a straight sided specimen (top and bottom plies) is fabricated.
- Two-stage prepreg method [57]: Half of the laminate is pressed with roving orientated in 90° direction. Further, the additional half is assembled.
- RTM method [97]: An RTM tool contains circular bonded sticks at the top and bottom inner tooling side in an appropriate pattern.
- Clamping method: The dry plies are bent over the edge of a bench. In that position clamps are positioned at two opposite sides. Finally, the setting is positioned on a planar surface.
- Rotational injection method ROTAC[28] [98]: Similar to the RTM method. Injection pressure is applied via centrifugal forces.

Continuing fabrication methods are summarized in [99]. While some previously cited methods can only be applied to prepreg material, others indicate an insufficient reproducibility of artificially induced wavinesses. “In commercially produced composites it is inevitable that fibers are distributed unevenly and that clusters of fibers as well as resin-rich areas exist.“ [77]

For this reason, an appropriate fabrication facility is developed and proposed. In Fig. 5.22, a one-side tool containing defined sinusoidal waves is shown. The specimens are fabricated using a VAP® setup. The preforms, a peel-ply, a flow promoter, a VAP® membrane, a fleece, and an airtight membrane are placed. The fabrics are stacked in a constant sequence. This is done to avoid nesting effects. The preforms are individually draped into the sinusoidal curvature using a rod.

[28] Injection method for non rotation-symmetric composite parts using rotational forces.

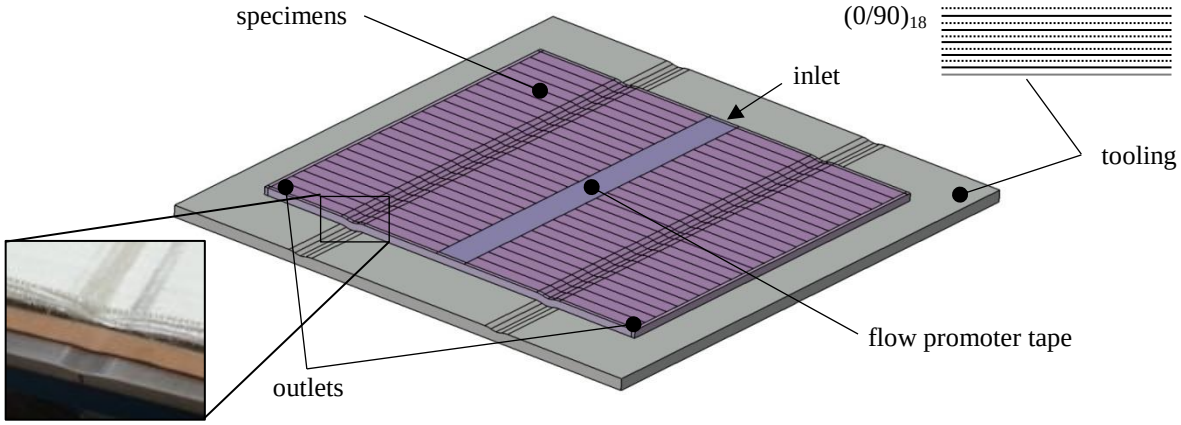

Fig. 5.22: Fabrication tool for specimen containing artificially induced PWs

The matrix system is mixed by hand. A vacuum is applied to the mixture for degasing issues. (Fig. 5.23) The matrix systems are given in Tab. 5.5. Having completed the infiltration under RT=25°C excessive matrix is exhausted at the inlet. Subsequently, a pressure equalization between inlet and outlets is applied. A pressure of 500mPa is applied. The layup is cured at 60°C for 15h. The equivalent procedure is conducted for all experimental setups in order to guarantee an equivalent FVC. Finally, the composition is prepared for the curing process in the oven. (Fig. 5.23) Hence, up to 50 specimens can be fabricated in one work step. This guarantees a high similarity of the specimens.

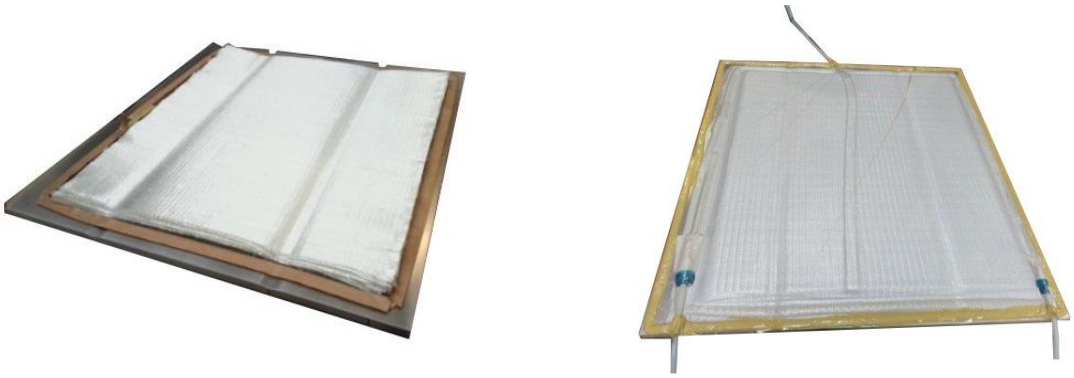

Fig. 5.23: Fabrication method: draped preform (left); ready for infusion (right)

If DCB and/or ENF tests are conducted, a TEFLON® foil may be embedded at previously defined positions. The rear side of tooling is used to fabricate uni-directional specimens without waviness. The cured composite part is removed from the mold and machined to the specimen dimensions required for the tensile and compressive testing. The specimens are cut from the mother plate into the dimensions suggested in chap.5.3.3 using both a buzz saw and water jet cutting. Finally, having roughened the bond area with sand paper and cleaned the surface, load tabs made of GFRP are placed following the instruction and equipment by [100].

5.3.3. Description of specimen and test plan

A mostly uni-directional preform material[29] that is commonly used in blade applications [101] is used. Relatively new fabrics (date of manufacture < half a year) are taken because the sizing on the fibers alter by time and may affect the failure mechanisms. The layup is $(0,90)_{18}$. The filler yarn remains within the preform. The grammage amounts to 591 g/m². The nominal ply thickness is 0.58mm.

Tab. 5.3: Preform architecture

	material [-]		grammage [g/m²]	size [-]
0°	E-Glass[30]	1200tex	520	PPG2002
90°	E-Glass	68tex	54	PPG2002
Thread	PES	110tex	17	

Two matrix systems are taken. First, a standard system of RIM135/RIM137H is used. In chap.5.4.2, several modified EPOXY based matrix systems are studied on neat matrix level. A matrix system RIM135/Trioxatridecandiamine (Tab. 5.5) is taken for comparison.

Tab. 5.4 summarizes the test plan for compression and tensile tests containing geometrical information, e.g. dimensions, layup, free gauge lengths, and measurement methods. The *setup* describes the corresponding plate of which the specimen are cut. Compression and tensile specimens are cut out of one experimental setup. It is pointed out that all wavy specimens consist of the equivalent geometrical wavy shape and layup. They are made of one specific glass fiber material. Only the matrix system is altered.

Specimens containing the same thickness as the wavy specimen are fabricated as reference specimens (Tab. 5.3). Therefore, standardized ASTM experiments are conducted to determine the ply-based strength parameters $R_{11}^t, R_{11}^c, R_{22}^t, R_{22}^c, R_{12}$.

Results are used as input parameters for the simulation model in chap.5.5 and to analyze the effect of matrix system of the stiffness and strength behavior of planar specimen while remaining properties stay unchanged.

[29] Material specification (Saertex): 30001209; textile structure 7000039.
[30] Hybon® 2002 roving that are compatible with Polyester, Vinylester, Phenolic and Epoxy resin systems are used. C. Hybon® 2002 is supplied globally by PPG Industries.

Tab. 5.4: Test plan for tension and compression tests

Description	Load type	Wave form	Layup	Dimension	Free gauge length	No. of specim.	Measurement method	Setup	Matrix system
	[-]	[-]	[-]	[mm]	[mm]	[-]	[-]	[-]	[-]
Wavy specimen	tensile	yes	0_{18}	250 x 20	150	20	Aramis system	1, 10	A, B
Wavy specimen	compression	yes	0_{18}	165 x 20	34	20	Aramis system	1, 10	A, B
Planar reference specimen	tensile	no	0_{18}	250 x 15	150	14	Aramis system	2, 11	A, B
Planar reference specimen	compression	no	0_{18}	164 x 15	34	14	Aramis system	2, 11	A, B
Planar reference specimen	compression	no	0_{18}	145 x 15	17	14	strain gauges	2, 11	A, B
ASTM R_{11T}	tensile	no	0_8	250 x 25	150	6	Aramis system	3, 12	A, B
ASTM R_{11C}	compression	no	0_8	150 x 25	20	6	strain gauges	3, 12	A, B
ASTM R_{22T}	tensile	no	0_8	250 x 25	150	6	Aramis system	3, 12	A, B
ASTM R_{22C}	compression	no	0_8	150 x 25	20	6	strain gauges	3, 12	A, B
ASTM R_{12}	tensile	no	$(45,-45)_s$	250 x 25	150	5	Aramis system	4, 13	A, B
ASTM OHT	tensile	no	(90,0,90)	300 x 36	-	4	-	5, 14	A, B
ASTM OHC	compression	no	(90,0,90)	300 x 36	-	4	-	5, 14	A, B
Neat matrix system (100/30)[31]	tensile	no	2mm	250 x 25	150	5	Aramis system	6	A
Neat matrix system (100/31)[32]	tensile	no	2mm	250 x 25	150	5	Aramis system	9	B
Neat matrix system (100/35)[31]	tensile	no	2mm	250 x 25	150	5	Aramis system	8	C
Neat matrix system (100/20)[31]	tensile	no	2mm	250 x 25	150	5	Aramis system	7	D

[31] RIM135/ RIMH137
[32] RIM135/Trioxatridecandiamine

The specimen grouped by the corresponding which tested exemplarily for the test series A are visualized in the Appendix B.

The specimen`s geometry is characterized using the DIC measurement system GOM ARAMIS-4M and caliper before experiments are carried out. Geometrical relevant information, e.g. the laminate thickness, width, and the ratio r are determined at predefined sections.

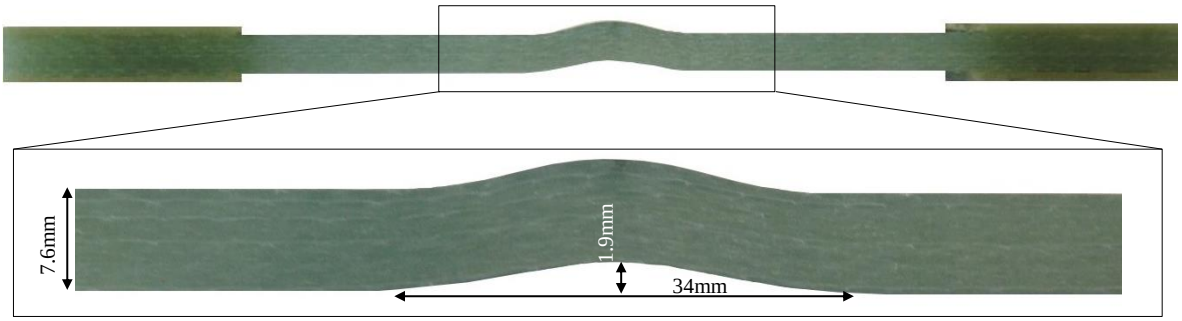

Fig. 5.24: Tensile specimen (ASTM-D-3039D)

A single specimen is exemplarily analyzed using a computer tomography (Fig. 5.25) in order to screen the specimen`s quality in consideration of manufacturing accuracy, such as fiber misalignment and void content. [102] The analysis of the selected specimen could detect three single voids. One is specifically pictured in Fig. 5.25 (right). It is assumed that voids also affect the failure mechanics. Nevertheless, the effects of void are neglected in the subsequent context.

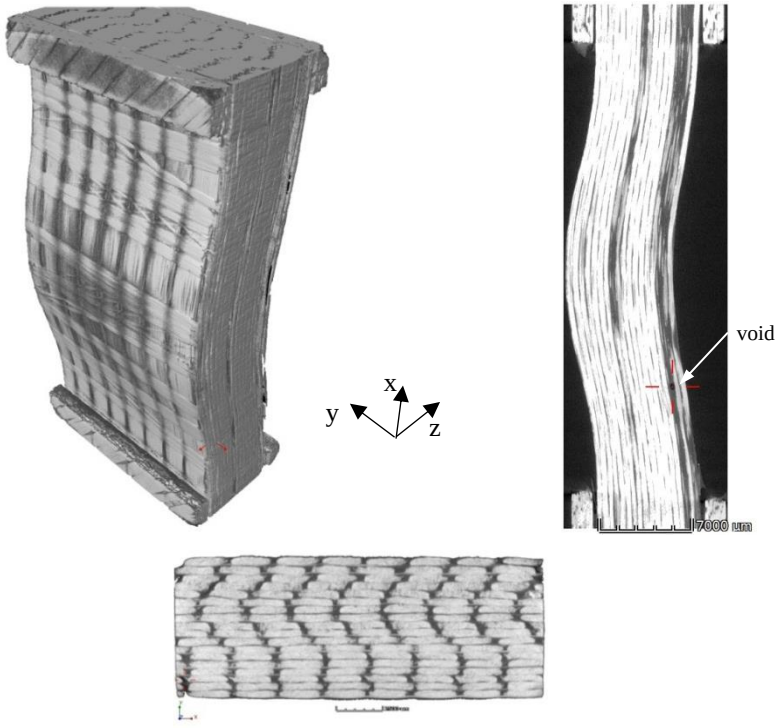

Fig. 5.25: Exposures of computer tomography (CT) of a specimen for a compression test

5.4. Experimental study and results

First, the test procedure is defined in chap.5.4.1. Experiments are carried out in order to gain insights at the following key issues:

- Effect of matrix`s mixture ratio on matrix properties on neat resin level (chap.5.4.2)
- Effects of matrix properties on the strength behavior on composite specimens (chap.5.4.3)
- Effects of ply waviness under compression (chap.5.4.4) and tensile loads (chap.5.4.5)
- Effects of wavy specimen on the stiffness and strength behavior compared to planar specimens (chap.5.4.6)

The corresponding failure mechanisms are also observed and discussed in the subsequent context. Results are validated against simulations in chap.5.5.

5.4.1. Definition of the test procedure

Compression and tensile tests are conducted for both planar and wavy specimens. The compression and tensile test methods of the non-wavy specimen are standardized by the American Society for Testing and Materials (ASTM) using ASTM-D-3039D-3039M for tension and ASTM D-6641 for compression tests. For the wavy specimens no standard test method exists. The tests are performed in a universal testing machine of HEGEWALD & PESCHKE INSPEKT 250 while recording the load/displacement curves via a digital image correlation (DIC). An optical system is the most effective way to analyze the failure mechanics even when a crack has formed. Due to the optical system the damage progression may be visually observed from initial to final failure. Therefore, the DIC measurement system GOM ARAMIS-4M is used. A 50mm glass object is used in measuring a volume of 65mm x 48mm. (CQ/CP20 55x44) The size of facets 10x5 is used. The measuring distance is constantly at 305mm. The exposure time is set to 85ms. Unless the application of the optical system is not possible due to geometrical constraints (

Tab. 5.4), strain gauges[33] are applied in a back-to-back pattern. If so, the mean value of both signals is calculated. Deviations of both signals that are greater than 10% indicate bending of the specimen. In that case, specimen tests are invalid. The strain rates for the tensile tests are 1.3mm/min. All tests are performed at ambient conditions (23-25°C). For compression tests an anti-buckling fixture - in the form of the WYOMING combined loading compression test fixture (ASTM D 6641; Tab. 5.2) - is used to prevent EULER buckling of the specimen (Fig. 5.26, left).

[33] Linear strain gauges of type FLA-3-11-1L

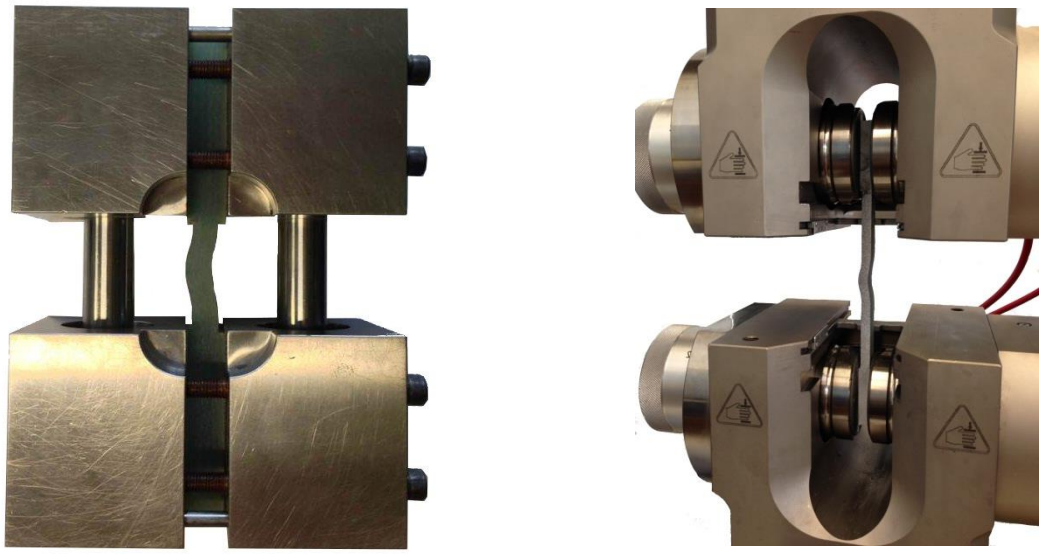

Fig. 5.26: Test procedure: Combined loading compression test fixture (left) and tensile test (right)

Utilizing the data analysis software of ARAMIS, virtual strain gauges measuring 20mm x 55mm are used in order to determine the present strain rates numerically. The Young`s Modulus is determined within the strain rate of 1000μm - 6000 μm. (D3039/D3039M) In order to screen out the noise of sensitive strain rates responses a SAVITZKY-GOLAY function implemented within a MATLAB script is utilized.

5.4.2. Matrix properties - Effects of various mixture ratios

The effects of the matrix`s mixture ratio on the stiffness and strength properties of the matrix system are discussed next. Further, an attempt is made to modify the strength parameters of the EPOXY based matrix system RIM135 in such a manner that the modified matrix systems (Tab. 5.5) obtain significantly reduced strength properties compared to the standard matrix system. Two polymers are wanted exhibiting a good interphase. Therefore, EPOXY is almost perfect. Both TALREJA [61] and WAAS [103] postulate that "it would be very useful to find two matrix materials that have similar Young`s Moduli and different yield stresses (or vice versa), or to find matrix materials with similar stiffness and strength, but exhibiting very different post-yield behavior, in order to determine the relative importance of the matrix stiffness or yield strength." [103] While the basic component RIM135 remains unchanged, the mixture ratio is varied. (matrix systems C and D). Matrix system B is generated by using the hardener *Trioxatridecandiamine*. Specimens of neat resin are subjected to tensile loading.

Tab. 5.5: Analyzed matrix systems

	system [-]	hardener [-]	mixture ratio [g/g]	cure temp. [°C]
matrix system A	RIM135	RIMH137	100/30	60
matrix system B[34]	RIM135	Trioxatridecandiamine	100/31	60
matrix system C	RIM135	RIMH137	100/35	60
matrix system D	RIM135	RIMH137	100/20	60

Alternatively, particles of Caoutchouc or EPOXY blends may be added to decrease the strength properties of the matrix systems intentionally. However, the viscosity of the system increases and is, therefore, not suitable for the fabrication method described in chap.5.3.2.

Fig. 5.27 shows the stress-strain curves of the standard and the modified matrix systems. Fig. 5.27a) depicts the averaged stress-strain curves of the standard EPOXY matrix system containing the proposed mixture ratio of 100:30. In Fig. 5.27c), the mixture ratio of 100:35 leads to a more brittle system, while the tensile strength is slightly reduced. In Fig. 5.27d), the lower proportion of the hardener (mixture ratio 100:20) creates a very ductile matrix system with an elongation to fracture of approx. 95%. The tensile strength is about one third of the value of the standard system. Matrix system B including the hardener *Trioxatridecandiamine* (Fig. 5.27b)) presents considerably reduced strength properties while the ductility of the system is slightly increased.

Matrix system B will be used as a reference system in the subsequent experiments. The matrix systems A and B exhibiting distinctively diverse strength properties are taken to experimentally observe the effect of various matrix properties on standard and wavy fiber reinforced specimens according to Tab. 5.4 and subsequent chapters.

[34] Recommendations by Dr. Fleischel (BASF SE AG)

a) Matrix system A: Mixture ratio 100:30

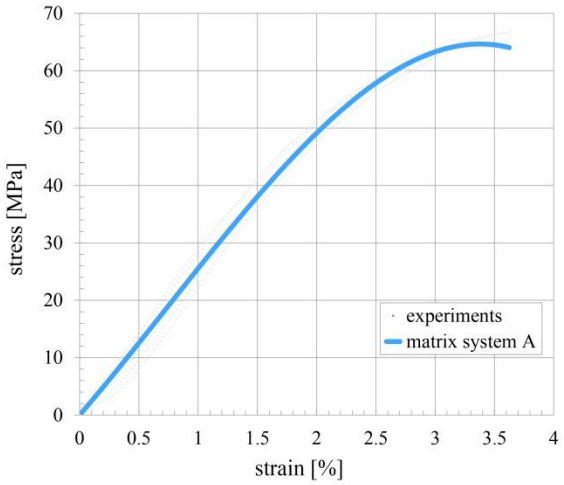

b) Matrix system B: Hardener Trioxatridecan

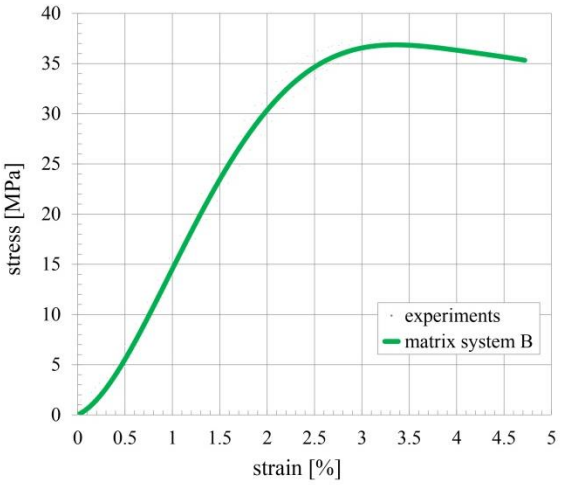

c) Matrix system C: Mixture ratio 100:35

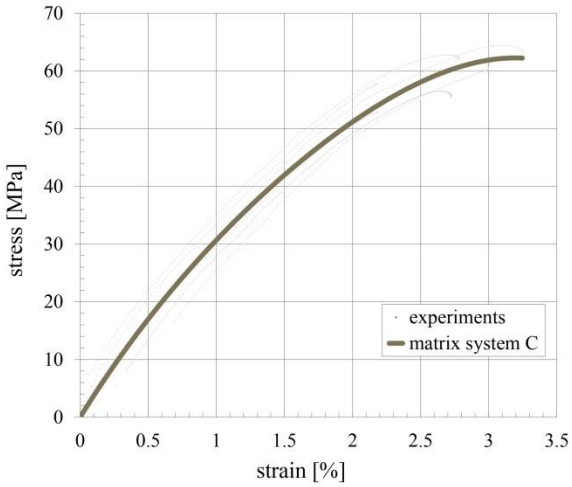

d) Matrix system D: Mixture ratio 100:20

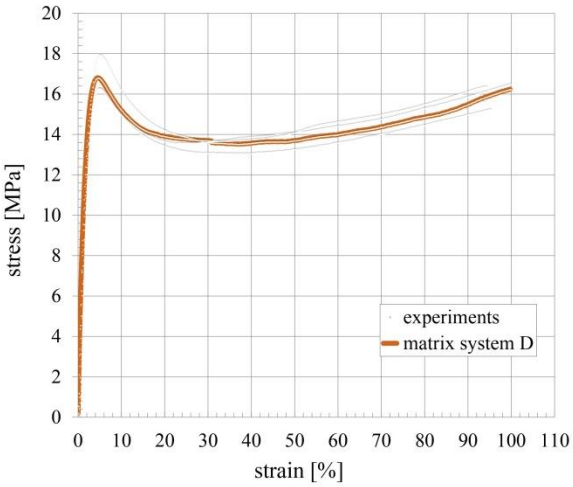

Fig. 5.27: Modified configurations of an epoxy based matrix system by adapted mixture ratios and an alternative hardener

While standard deviations of the Young Moduli are relatively large (>15%), the standard deviations for the tensile strength and strain-to-failure are fairly small (<10%).

5.4.3. Effects of matrix properties on stiffness and strength behavior of flat composite specimen

Tensile and compression tests are carried out according to ASTM-D-3039D-3039M [104] and ASTM-D6641D6641M [105] respectively and discussed next. While one distinct preform according to Tab. 5.3 is utilized, the matrix systems A and B (Fig. 5.27) are taken to experimentally determine the matrix dominated stiffness and strength behavior on the specimens` level.

The longitudinal tensile and compressive strengths are depicted in Fig. 5.28. The standard deviations of the Young`s Modulus E, the maximum strength σ_{max} and strain-to-failure ε_{max} are also appended. Results show that the longitudinal tensile strength is not affected by the chosen matrix system. In addition, the longitudinal compressive strength is slightly influenced by the matrix properties.

An additional experimental study analyzing sizing effects is conducted. The longitudinal compressive strength of specimens that exist of different laminate thickness and free gauge length are determined. Results show no clear trend of the strength behavior in dependence of the laminate thickness.

a) Longitudinal tensile strength (R_{11}^{+}) **b) Longitudinal compressive strength (R_{11}^{-})**

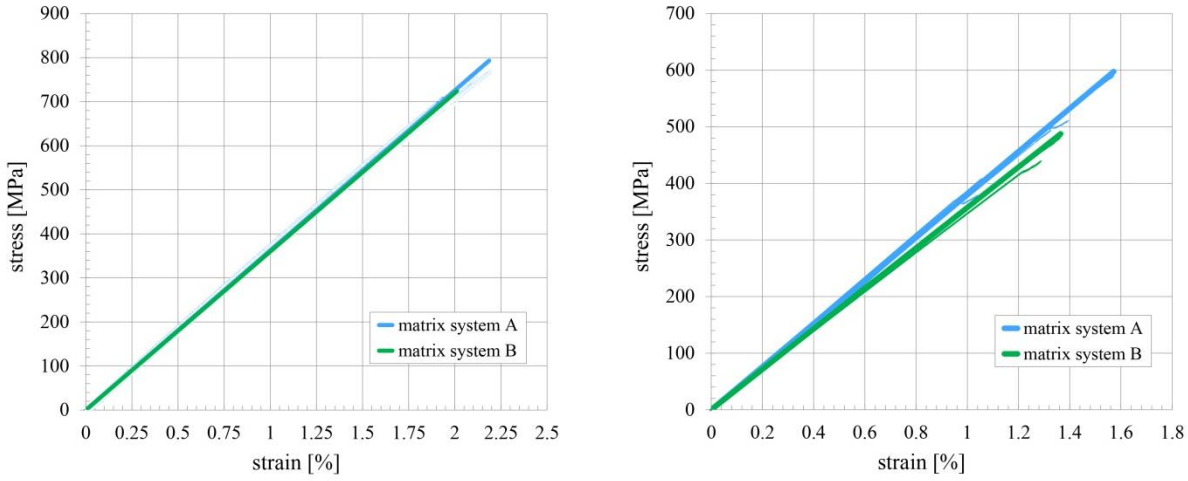

		MATRIX A		MATRIX B		MATRIX A		MATRIX B	
E	**[MPa]**	**37338**		**36923**		**38443**		**35983**	
S	[MPa], [%]	442	1.18	565	1.53	511	1.33	842.70	2.34
σ_{max}	**[MPa]**	**734**		**706**		**484**		**459**	
S	[MPa], [%]	33.80	4.61	8.24	1.17	66.58	13.75	17.20	3.75
ε_{max}	**[%]**	**2.05**		**1.99**		**1.31**		**1.29**	
S	[MPa], [%]	0.11	5.44	0.02	1.18	0.17	13.30	0.05	3.98

Fig. 5.28: Longitudinal tensile and compressive strength for matrix system A and B

Next, the effects of the matrix properties on the transverse tensile and compressive strength are observed in Fig. 5.29. Both strength properties are strongly affected by the matrix system. The curves of the transverse tensile strengths show a nonlinear trend beginning at 0.24

(matrix system A) and 0.1 (matrix system B) respectively. This indicates that inter-fiber failures (IFF) may occur. According to [106], composites loaded in tension normal to the fibers, the following initiation failure mechanisms can occur:

- Fiber/matrix debonding
- Yield in the matrix system
- Cavitation-induced brittle matrix failure

Further, in composites that have an irregular distribution of fibers, "it is expected that the local stress states would vary in the mix from deviatoric to purely dilatational. Thus, the matrix could yield in some regions while other regions could fail by cavitation-induced cracking. The fiber/matrix debonding depends on not only the stress state at the fiber/matrix interface but also on a range of other factors such as the adhesion and toughness of the interface." [106]

The transverse compressive strengths show a strong nonlinear behavior of both configurations. It is especially noted that the configuration containing the weaker matrix system B withstands a higher strength level. A reason for that could be that a composite with a lower shear strength (matrix system B) may tend to accumulate more sub-critical damage. Thus, its ultimate load carrying capacity is better than a matrix system containing a higher shear strength (matrix system A). "This is due to the fact that shear failure prohibits the load from being transferred to nearby fibers that are already highly stressed. The interlaminar failures serve to lessen the notch effect produced by the marcel, and more uniformly distribute the load throughout the cross section." [57] In summary, it is postulated that the transverse tensile strength is mainly affected by interphase cracking. The transverse compressive strength is predominately affected by the non-linear shear behavior of the matrix systems.

a) Transverse tensile strength (R_{22}^{+}) **b) Transverse compressive strength (R_{22}^{-})**

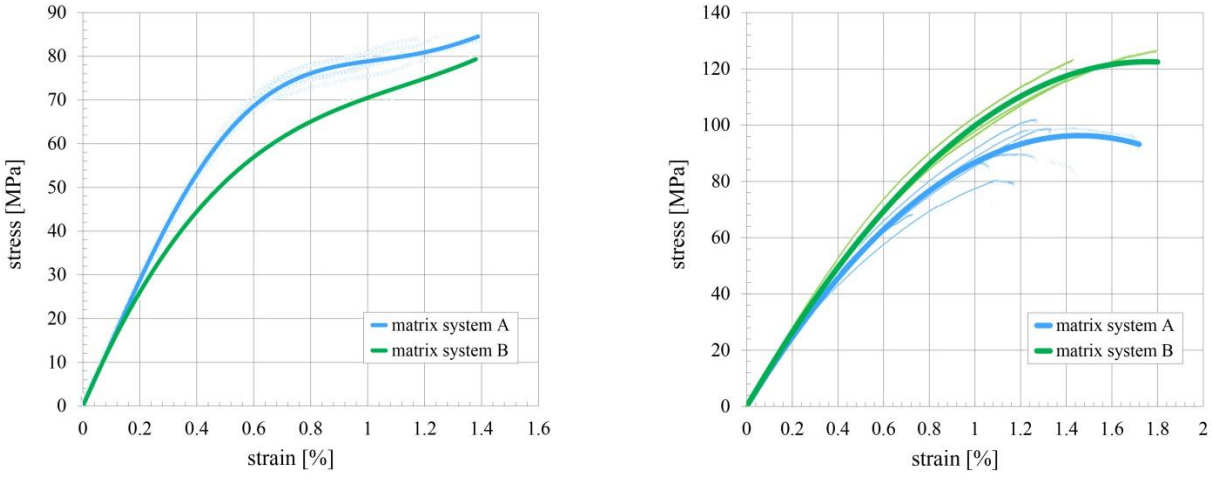

		MATRIX A		MATRIX B		MATRIX A		MATRIX B	
E	**[MPa]**	**10694**		**8586**		**9680**		**11229**	
S	[MPa], [%]	289	2.71	444	5.17	433	4.47	370	3.30
σ_{max}	**[MPa]**	**81**		**76**		**89**		**123**	
S	[MPa], [%]	2.28	2.79	3.81	5.00	11.86	13.36	4.23	3.44
ε_{max}	**[%]**	**1.16**		**1.28**		**1.17**		**1.56**	
S	[MPa], [%]	0.14	11.68	0.07	5.76	0.26	21.80	0.16	10.16

Fig. 5.29: Longitudinal tensile and compressive strength for matrix system A and B

The matrix properties affect the stiffness and strength behavior of composite specimen most when stressed under shear conditions shown in Fig. 5.30. The configuration that contains matrix system B (approx. 41% reduced tensile strength) leads to a shear strength reduction of approx. 35%. Both responses are highly nonlinear. In Fig. 5.30 (right), the shear strains of configuration A are visualized at 1.5% strain by the optical measurement system ARAMIS. The plot also shows the fitted curves of the materials behavior according to (5.44). The corresponding fitting parameters of matrix system A and B are also given and used as input parameters for the numerical simulations postulated in chap.5.2.2.

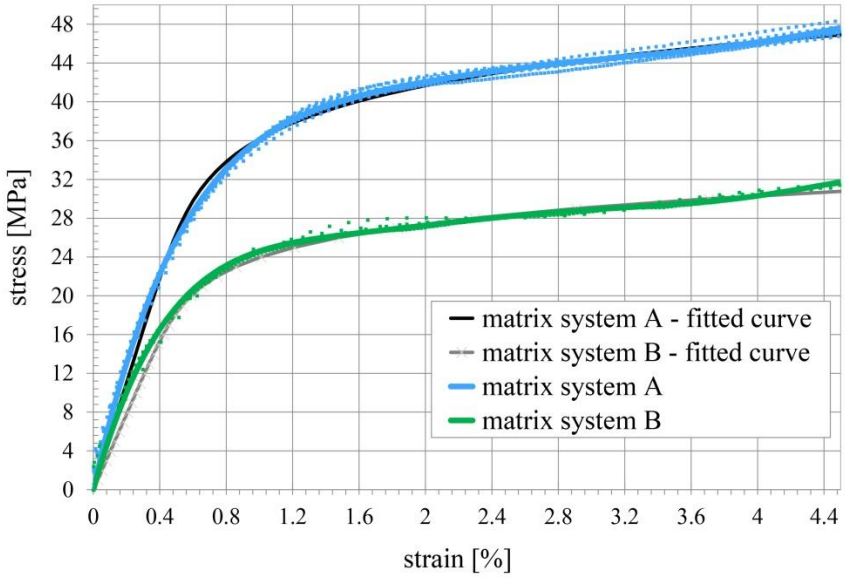

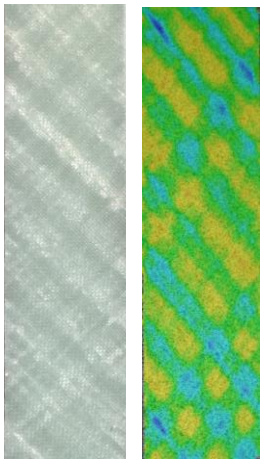

shear strains at 1.5%
(images by DIC)

		MATRIX A		MATRIX B	
G_{12}	**[MPa]**	**4238**		**2585**	
S	[MPa], [%]	145	3.44	64	2.48
σ_{max}	**[MPa]**	**49**		**32**	
S	[MPa], [%]	0.64	1.32	0.18	0.54
ε_{max}	**[%]**	**11.21**		**14.40**	
S	[MPa], [%]	1.05	9.40	0.57	3.94
Ramberg-Osgood parameters					
A	[-]	**67.5**		**44.4**	
n	[-]	**9.1**		**9.0**	

Fig. 5.30: Longitudinal shear strength R12 for matrix system A and B (DIN ISO 14129)

5.4.4. Compression test results of wavy specimen

Test results of wavy specimen (Fig. 5.24) subjected to compression are carried out and discussed next. The failure mechanisms are progressively observed. The phenomenological understanding is the first step. Thus, experiments are validated against the numerical model containing a continuum damage model. (chap.5.2.2.) The numerical model is described in chap.5.2.2.

The stress-strain curves of the two configurations are plotted. Therefore, the remote stress is calculated by the reaction forces of the testing machine. The remote strain is determined by the DIC system measuring Δx according to Fig. 5.36. The displacement of the peak point (Fig. 5.36) in y-direction is plotted later in chap.5.5. A total of 20 specimens are tested for each configuration in order to have a good statistical basis. The spread in the stiffness and strength is interpreted as a reflection of the variability in a misalignment angle from specimen to specimen. Experiments show that ply wavinesses produce spatially varying multi-axial stress states in the material subjected to simple uniaxial compressive far field load. The specimens show no global buckling failure mode. The EULER buckling is successfully inhibited by the anti-buckling fixture. (Fig. 5.26)

The ply waviness induces interlaminar shear stresses, and through the thickness normal stress under in-plane loads. The superposition of ILTS and ILSS leads to the subcritical interlaminar damage of the material at the maximum inclinations of the wavy shape. Observing the progressive failure mechanisms from state ② to state ④, the increasing shear strains leads to stress concentrations. The matrix takes up the mechanical loads especially in the shear loading direction and in transversal direction to the fiber orientations.

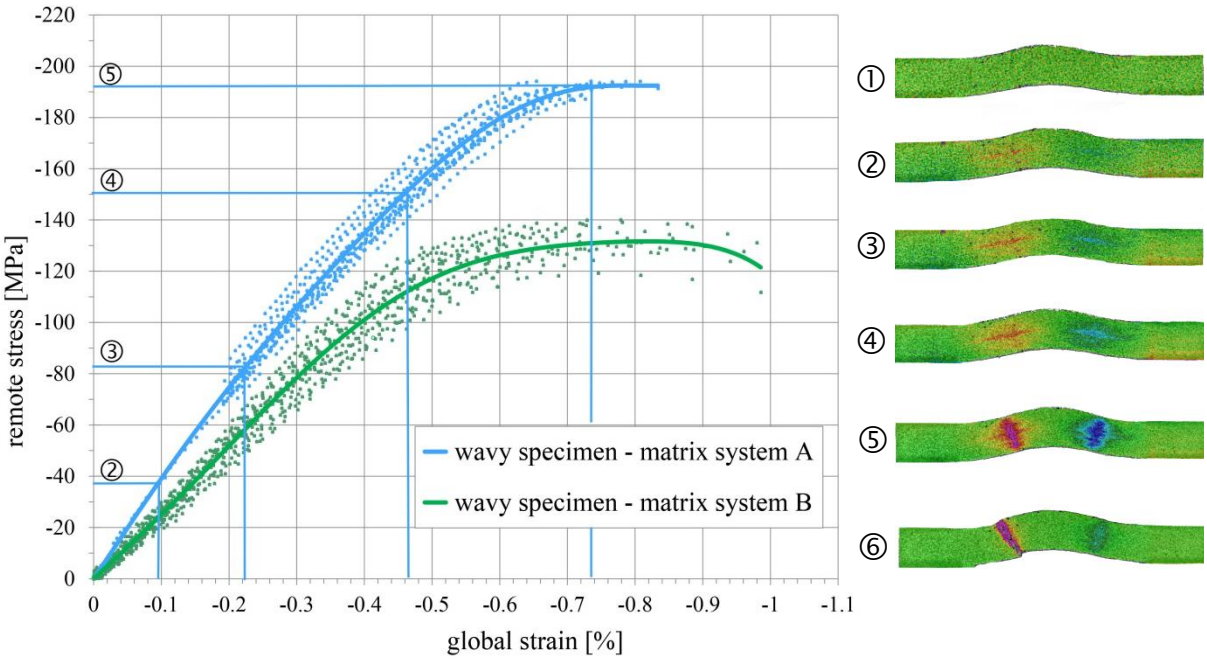

Fig. 5.31: Compression test results of wavy specimen incl. shear strain plots

The matrix system also supports the fibers during a compression load in fiber direction and bond adjacent layers together. Analogous loads are transferred. The failure mechanisms of a wavy specimen are strongly dominated by a nonlinear behavior. State ⑤ is taken immediately before a kink band suddenly formats (state ⑥). After the kink band has formed, a sudden drop occurs.

The key failure mechanism under a compression load is defined as the formation of a kink band due to due strongly nonlinear shear behavior of the matrix. The matrix failure controls the failure mechanisms. This is shown on the basis of the second wavy configurations containing matrix system B.

The kink band formation is a well-defined failure mechanism. Its critical conditions for its formations are observed phenomenologically, predicted by the numerical model introduced in chap. 5.2.2 and validated against experiments in chap.5.5. The kink band formations of the compression loaded specimen are shown in Fig. 5.32. Kinking most likely starts from the surface. It has to do with how the fibers on the surface are only supported from one side, so they can buckle easier. Fibers from inside are supported from two sides. It is also shown that a kink band occurs where max. shear stresses occur.

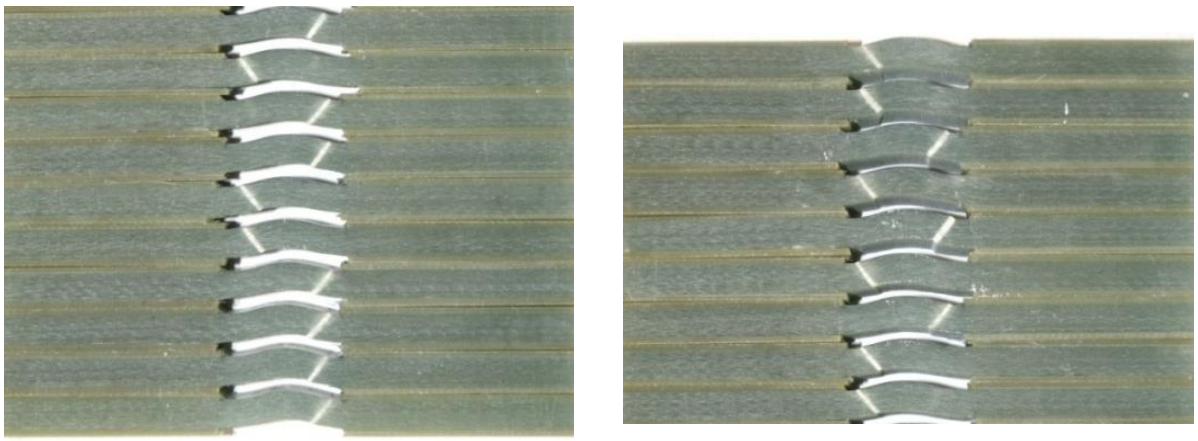

Fig. 5.32: Kink band formation of a compression loaded specimen

5.4.5. Tensile test results of wavy specimen

Subjecting the wavy specimen under tensile load, the wavy sections are continuously being pulled straight. (Fig. 5.33) Slightly curved plies are straightened first. The straightening of differently curved plies in through thickness pattern leads to ILTS and ILSS inducing the initial subcritical failure mechanism. At state ②, an interphase[35] failure mechanism is assumed [61] at the area of the maximum inclinations, but it cannot be finally proved. It is postulated that debonding begins on the fibers surface and then cracking from there occurs. The nonlinear behavior starting at point ③ may be indicated as gradual interphase failure between the matrix and fiber system. Thus, it is difficult to predict cracks from not cracks, the initiation of yielding is predicted. That is the first event. As yielding progresses it forms a shear band. If a further load is applied, the shear band becomes a crack. The matrix cracks leads to delaminations at state ④. Further delaminations at state ⑤ occur at the maximum inclinations before final fiber failure at state ⑥ arises. Analyzing the two configurations (A and B) it is found that the matrix properties affect the failure mechanism under tensile load in a negligible manner as expected.

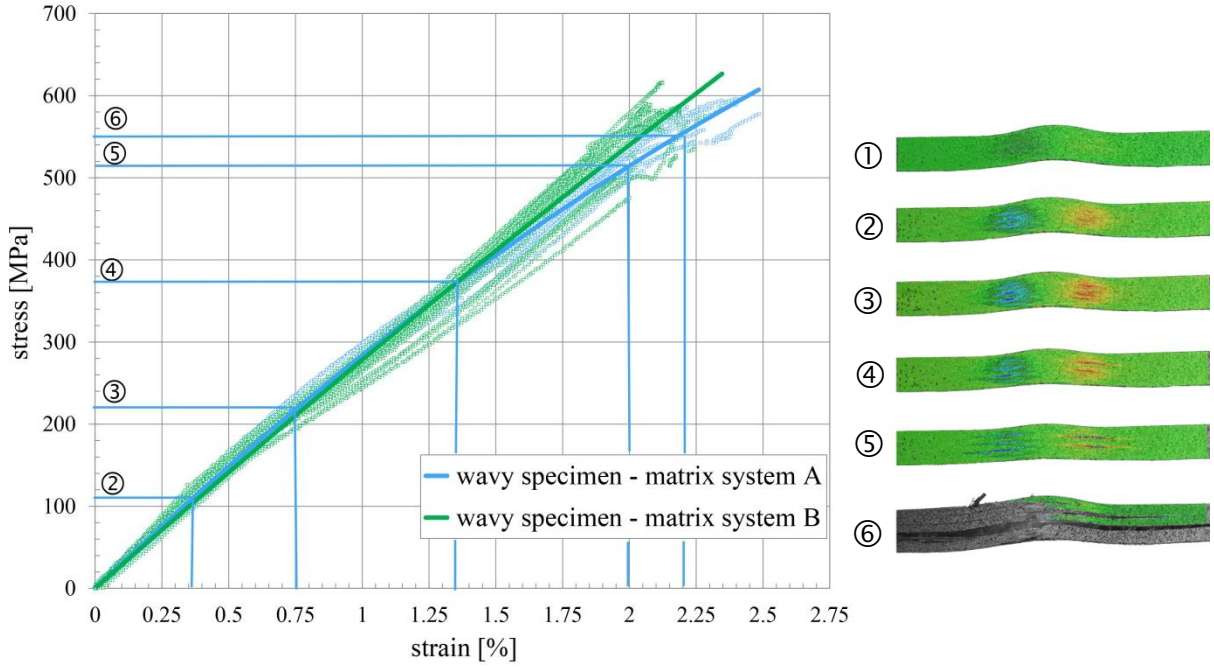

Fig. 5.33: Tensile test results of wavy specimen incl. shear strain plots

The observed failure mechanisms *delamination* (state ④) and *fiber failure* (state ⑥) are depicted in Fig. 5.34.

[35] Interphase: transition region between fiber and matrix.

State ④: Delaminations

State ⑥: Fiber failure

Fig. 5.34: Failure mechanisms - delamination and fiber failure of a tensile loaded specimen

5.4.6. Comparison of a planar and wavy specimen

In addition to the matrix dominated effects that are studied in chap.5.4.2 to chap.5.4.5, comparisons between the planar reference specimen and the wavy specimen are drawn under compression and tensile loads for the amplitude-to-length ratio 0.05. The compressive strength of the wavy specimen (A/l=0.05) is decreased by approx. 61% (matrix system A) and approx. 68% (matrix system B) respectively. Especially, the nonlinear behavior arises primarily when induced by the matrix properties. Most importantly, the waviness changes the failure mechanisms to a matrix dominated event.

The tensile strength and strain-to-failure under a tensile load is slightly affected by the wavy shape. Nevertheless, the stiffness is reduced by approx. 18% (matrix system A) and approx. 19% (matrix system B) respectively.

a) Compression load

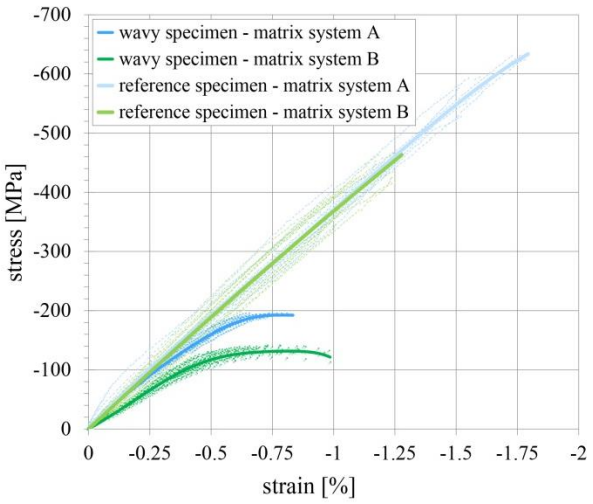

b) Tensile load

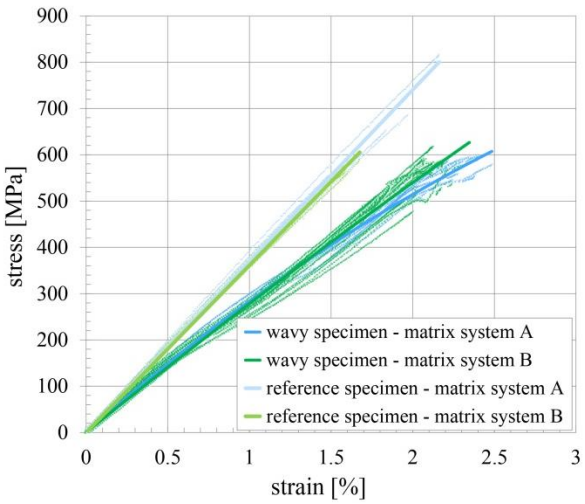

Planar specimen

		MATRIX A		MATRIX B		MATRIX A		MATRIX B	
E	**[MPa]**	**36408**		**38159**		**37320**		**36532**	
S	[-], [%]	2335	6.41	3157	8.27	1771	7.75	900	2.46
σ_{max}	**[MPa]**	**496**		**419**		**677**		**568**	
S	[-], [%]	110	22.12	33.40	7.98	108	15.98	14.19	2.50
ε_{max}	**[%]**	**1.35**		**1.14**		**1.86**		**1.59**	
S	[-], [%]	0.33	24.62	0.10	8.43	0.28	15.27	0.034	2.14

Wavy specimen

		MATRIX A		MATRIX B		MATRIX A		MATRIX B	
E	**[MPa]**	**27311**		**20272**		**30612**		**29489**	
S	[-], [%]	1474	5.40	1268	6.25	1325	4.33	1903	6.45
σ_{max}	**[MPa]**	**192**		**133**		**578**		**520**	
S	[-], [%]	3.02	1.58	4.75	3.57	15.15	2.62	30.49	5.86
ε_{max}	**[%]**	**0.63**		**0.86**		**2.33**		**1.95**	
S	[-], [%]	0.42	66.12	0.18	20.31	0.10	4.13	0.14	7.20

Fig. 5.35: Comparison of planar and wavy specimens

5.5. Validation of simulation results against experiments

The continuum damage model described in chap.5.2.2 is incorporated within a material user subroutine (VUMAT) of the FEA tool ABAQUS and applied to a virtual test specimen shown Fig. 5.36. The left edge of the mesh is constrained from moving in the x-direction. The edge is free to move in the y-direction except for the left bottom node that is constrained to prevent a rigid body motion. The right edges of the model are loaded uniformly by a velocity in x-direction. Using the explicit FE-code supplied by ABAQUS, the reaction forces RF, the displacement Δx and the displacement y of the peak point are computed for every time increment. From this data, the remote stress and strain curves are determined.

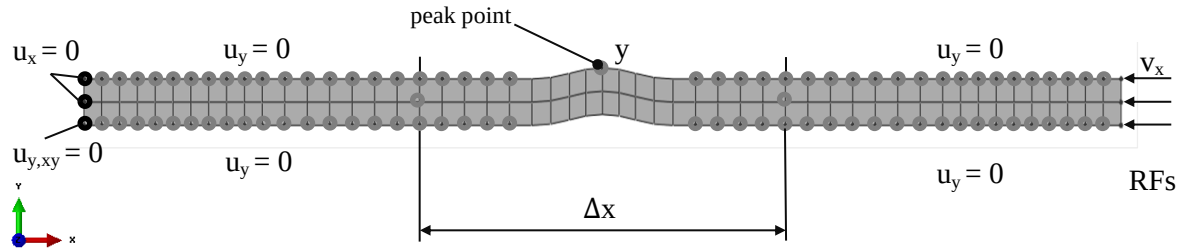

Fig. 5.36: Virtual specimen for compression tests

For visualization reasons, the specimen shown in Fig. 5.36 is meshed with a coarse mesh. Actually, the specimen contains 32 elements through its thickness. In total, approx. 25000 elements of the type *plane stress CPS4R* are used. To allow transverse contractions the element type "plane stress" is used.

On the basis of the numerical model, the sensitivity analysis in Fig. 5.37 (left) show the importance of taking non-linearities into account to exactly predict the strength behavior of thick wavy composites. The benchmark study depicted in Fig. 5.37 (right) demonstrate obviously the mesh independency of the continuum damage model (chap.5.2.2).

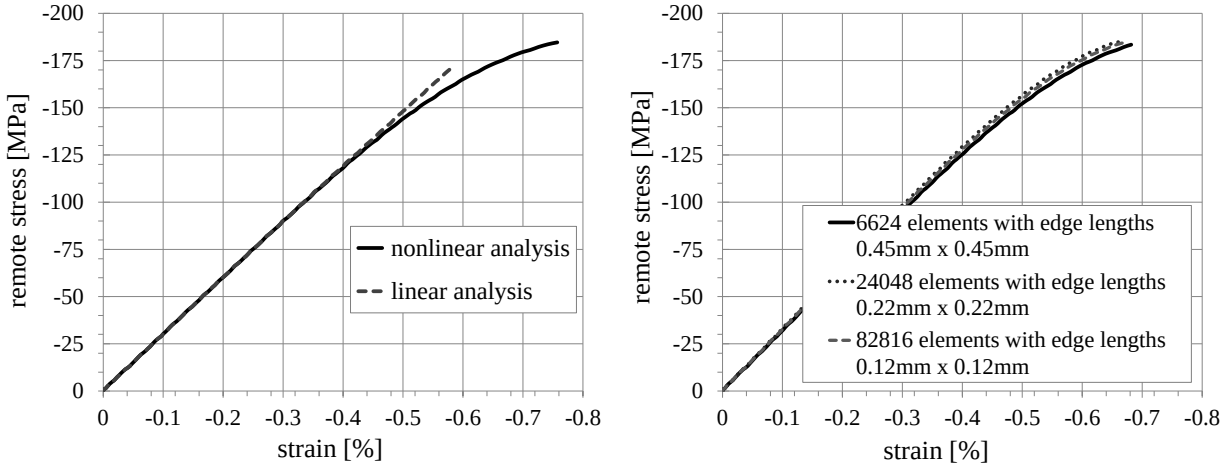

Fig. 5.37: Sensitivity studies: Nonlinear ag. linear analysis (left); mesh dependency (right)

Simulation results are validated against experiments that are carried out in chap.5.4. The remote *stress strain curves* of simulation results and experiments for the configuration of matrix system A are depicted in Fig. 5.38. Concurrently, the displacements of the peak point is plotted against the global strain. The global strain is determined by the displacement Δx (Fig. 5.36). This procedure is conducted for both experiments (using DIC) and numerical results. The displacement of the peak point gradually increases as the stress shows a nonlinear behavior. At locations of maximum inclinations, the matrix yield causes a narrow band of fibers which suddenly kinks. See also chap.5.1 and chap.5.1.3. This causes the global stress to drop.

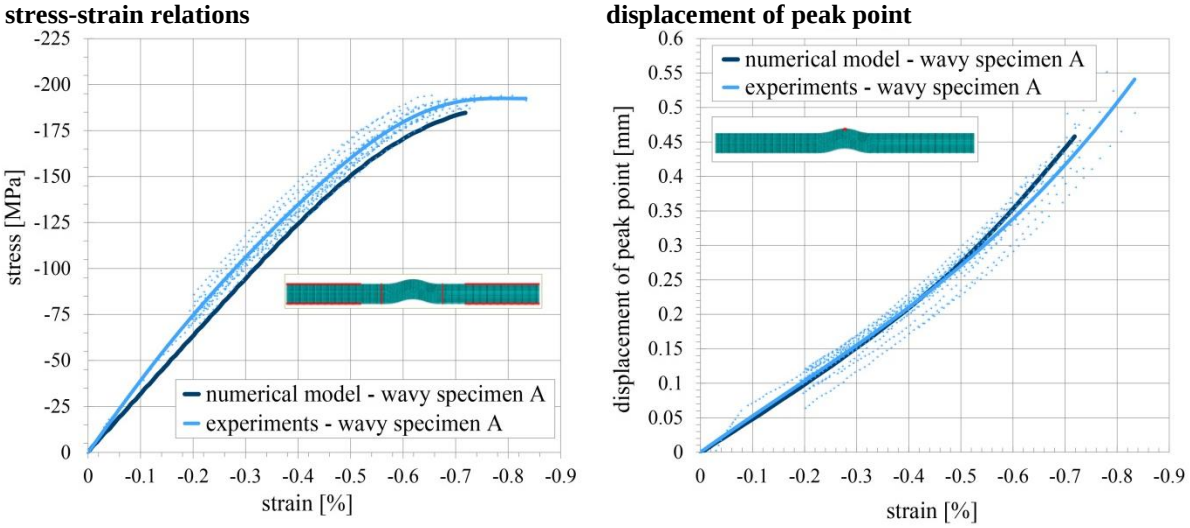

Fig. 5.38: Validation of simulation and experiments for configuration A

The equivalent procedure and analysis according to the previous context is conducted for the configuration of matrix system B in Fig. 5.39.

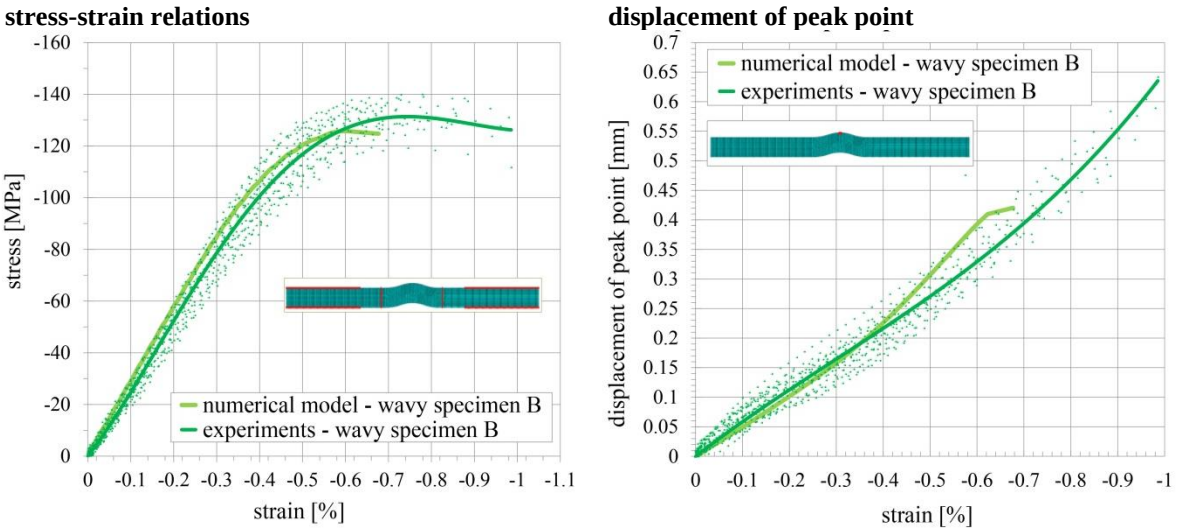

Fig. 5.39: Validation of simulation and experiments for configuration B

In summary, there is a good correlation between the numerical model and the experiments observing that the stress-strain curves and the displacement of the peak point fit well for both

configurations A and B. The numerical model also predicts the correct location and type of failure for compression tests. Shear strain plots (Fig. 5.40) indicate regions which undergo shearing strains of the opposite direction (positive and negative shear). Shear strain plots of DIC and numerical model are compared to each other. The failure mechanisms including the kink band failure are indicated. Both numerical results and experiments show the following phenomena: At the maximum inclinations of the wavy specimen broad shear zones (②) are induced by compression loading. Under increasing load the concentrated shear zones are localized to a small shear band (⑤). It is pointed out that shear stress of approx. 4.7% occur. The local shear concentrations induce the sudden formation of a kink band. (⑥).

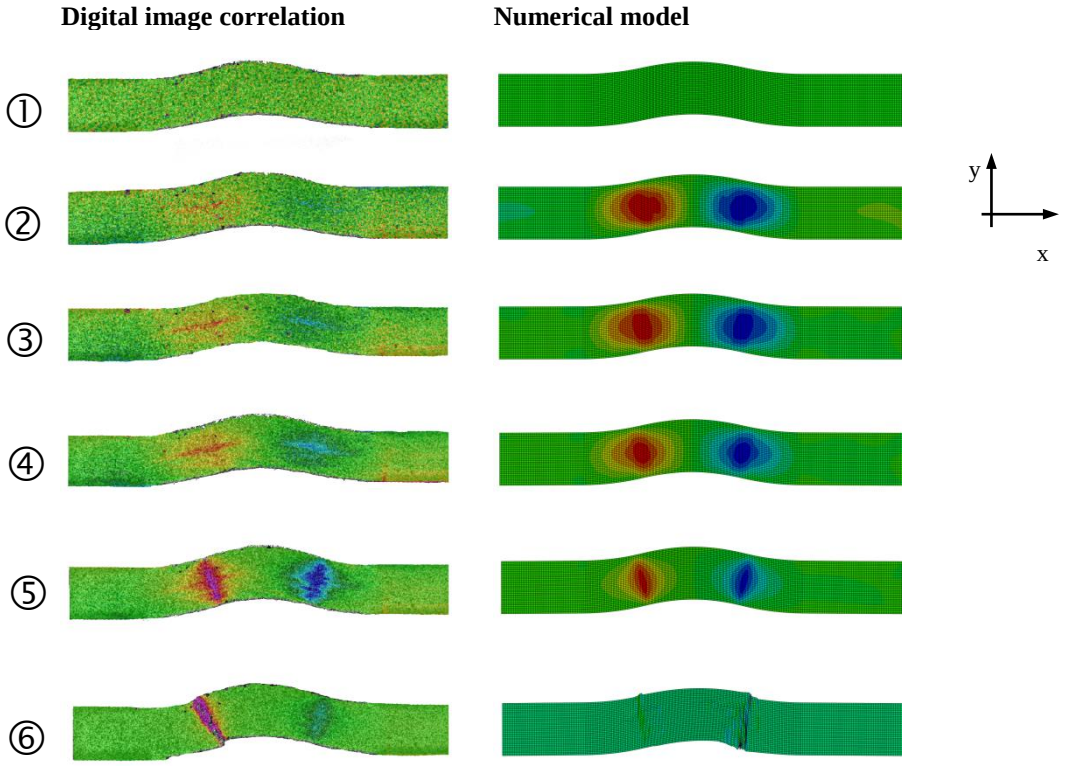

Fig. 5.40: Shear strain: Digital image correlation (DIC) vs. numerical results

The damage is viewed as a measurable state variable in order to describe the actual state of a physical system. The shear damage variable is shown in Fig. 5.41.

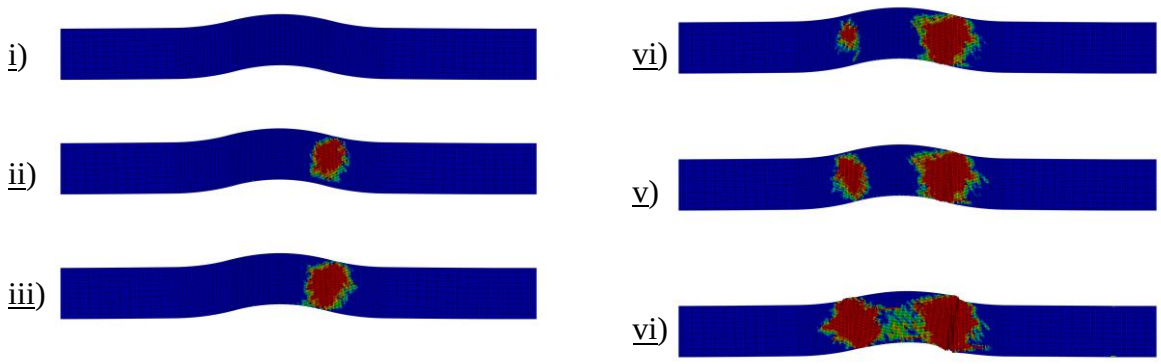

Fig. 5.41: Shear damage variable

5.6. Failure mechanisms in thick wavy laminates

Finally, the effects of wavy plies are studied on a thick wavy laminate. Therefore, a spar cap section of a conventional 40 meter long WTB is illustrated in Fig. 5.42 (left). The cross-section originates from a WTB that has been in operations under cyclic loading. The milky-white regions and the stretched failure patterns are indicators of delaminations of adjacent plies driven by matrix failure. JOYCE, BUSSE, GROSSE [107] [108] and al. study the application of non-destructive inspection methods (NDI) in thick laminates to determine in-situ defects such as ply waviness. An exemplary cross-section of a WTB containing several defects is shown in Fig.B2. Currently, only plies that are close to the laminate`s surface can be detected. For this reason, the spar cap is sliced into several pieces. One representative section[36] is analyzed in detail for several reasons: First, typical and characteristic shapes of ply wavinesses occurring in spar caps are determined. Second, the failure mechanisms in thick wavy laminates are observed numerically and discussed. Therefore, an image analysis[37] is utilized identifying the geometrics of the wavy plies. Data are taken as input parameters for numerical simulations.

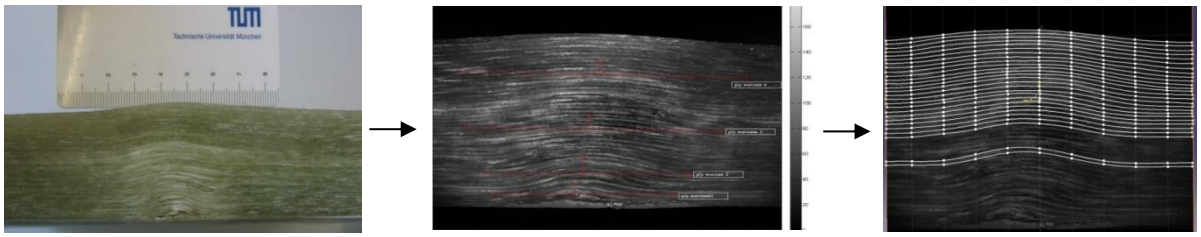

Cut through a spar cap (r=15m) **Image Analysis** **Determination of ply architecture**

Fig. 5.42: Ply waviness in thick laminates

The ply waviness traverses the overall thickness of the spar cap. The cross-section comprises 43 mostly unidirectional plies of a conventional glass fiber material[38]. Each ply contains a characteristic shape. Tab. 5.6 shows the geometrical descriptions of selected and representative wavy plies through the thickness of the section.

Tab. 5.6: Selected ratios of ply waviness through thickness

no. of ply		amplitude	wavelength	ratio	radius	ply thickn.
x		A [mm]	l [mm]	$\frac{A}{l}$ [-]	r [mm]	t [mm]
1	(1)	3.65	26.31	0.14	25	0.88
12	(2)	3.49	27.21	0.13	27	0.88
21	(3)	3.44	37.34	0.09	50	0.88
30	(4)	3.46	42.79	0.08	57	0.88
37	(5)	3.25	43.94	0.07	71	0.88
43	(6)	3.43	45.10	0.08	80	0.88

[36] The wavy section is cut out at 15m in the lengthwise direction of the spar cap structure.
[37] PROFACTOR: Image analysis sensor system using circulating lightning for rejection of reflections.
[38] NCF: (0,90) with (90%,10%)

Numerical models are implemented to analyze the predominant stresses and their superposition. The failure mechanisms are studied. Results of a 3D model based on volume elements show that edge effects can be neglected. (Fig. 5.43) Thus, further results are carried out utilizing a 2D model.

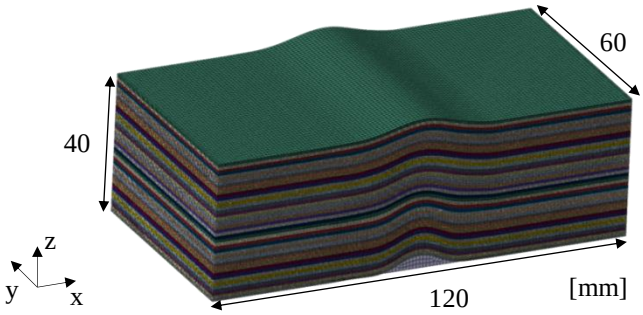

Fig. 5.43: Finite elemente discretization of a thick wavy laminate (spar cap)

Compressive and tensile loads are applied individually. The boundary conditions are applied analogous to the procedure described in Fig. 5.36. The stresses of specific plies highlighted in Fig. 5.44 are analyzed in lengthwise direction (x). While *ply 1* represents the ply at the very bottom, *ply 6* represents the top ply.

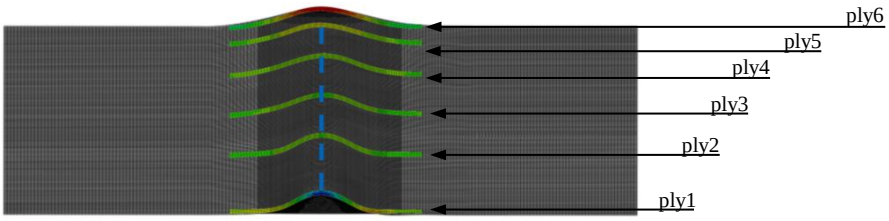

Fig. 5.44: FE-model: lengthwise and through thickness analysis

Fig. 5.45 shows the stresses σ_{11} in fiber direction each under compressive and tensile load respectively. While the embedded mid-plies manifest $\sigma_{xx}^{far\ field}$ along its lengthwise direction including minor changes, all plies follow a quite straight trend except for the top and bottom plies. The strong undulated bottom *ply 1* indicates an increase in σ_{11}. The top *ply 6* shows a continuous in-/decrease of σ_{11} til the wave peak is reached.

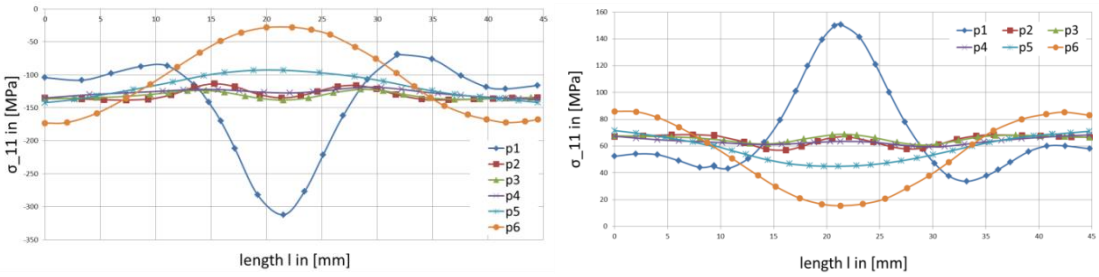

Fig. 5.45: Stresses in fiber direction loaded in compression (left) and tension (right)

Fig. 5.46 shows the interlaminar tensile stresses σ_{zz} in fiber direction. Compressive and tensile loads are applied individually. ILTS are maximum at the maximum inclinations of the

plies. Greatly curved plies show higher ILTS values than slightly curved plies. It cannot be concluded why *ply 2* and *ply 3* prevail higher values than the greatly curved *ply 1*. One reason may be the embedded location of the ply. The top *ply 6* prevails negligible ILTS. Considering the maximum values it is pointed out that

$$\sigma_{33,\ t/c}^{max} = \sim 0.24 \cdot \sigma_{xx,t/c}^{farfield}.$$

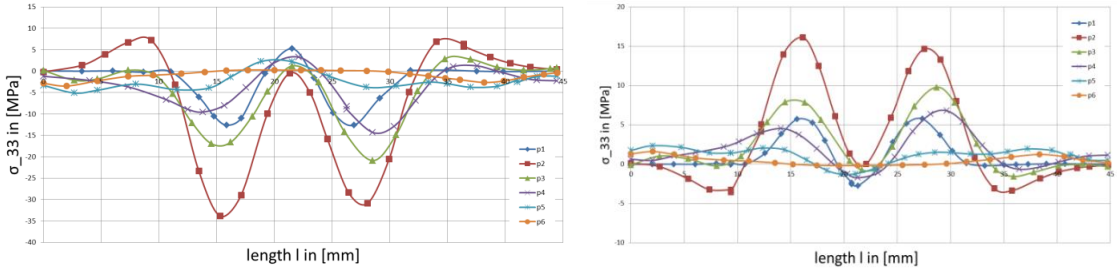

Fig. 5.46: Interlaminar tensile stresses loaded in compression (left) and tension (right)

Fig. 5.47 shows the corresponding stress plots according to Fig. 5.46.

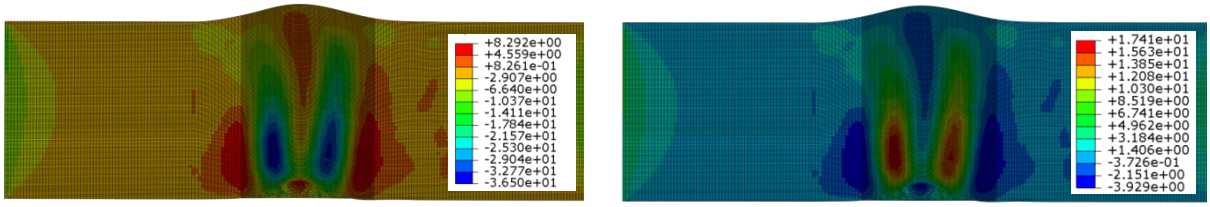

Fig. 5.47: Contour plots: interlaminar tensile stresses loaded in compression (left) and tension (right)

The curves shown in Fig. 5.48 indicate high interlaminar shear stresses reaching their maximum at the areas of maximum inclinations. The ILSS turns to zero at the wave peaks. High ILSS-values are one sign of the dominant effect of matrix systems to a failure and damage behavior in wavy composites.

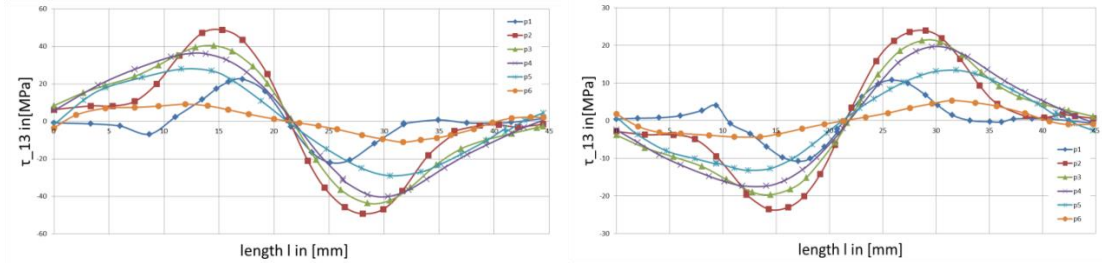

Fig. 5.48: Interlaminar shear stresses loaded in compression (left) and tension (right)

The corresponding ILSS are plotted in Fig. 5.49.

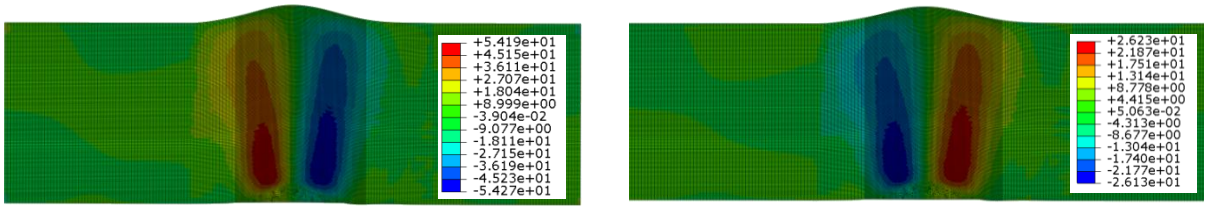

Fig. 5.49: Contour plots: interlaminar shear stresses loaded in tension (up) and compression (down)

Next, the failure mechanisms using progressive damage analyses are discussed for compressive and tensile loads respectively. Under a compression load, matrix shear failure is the initial failure mechanisms detected in Fig. 5.50. The initial failure originates at a local superposition of ILTS and ILSS. Although, failure mode B according to PUCK failure criteria is expected, the failure mode is close to the transition to mode C. In mode C, the fracture plane and action plane are no longer equal. Mode C implies the risk of delaminations between the fracture and the adjacent plies and in the worst case the risk of catastrophic wedge fracture. [109] At the critical *state iii*, the failure propagates not only along the thickness direction but also in loading directions. This failure mode can classically be defined as delaminations indicated by matrix failure. Delaminations may reduce the transverse backing of the fibers. Indications of fiber failure are observed at the wave peak. Ply buckling may occur in a further progressive load step. Under tensile load, matrix failure is also to be determined as the initial failure mechanisms. Herein, failure mode A is expected.

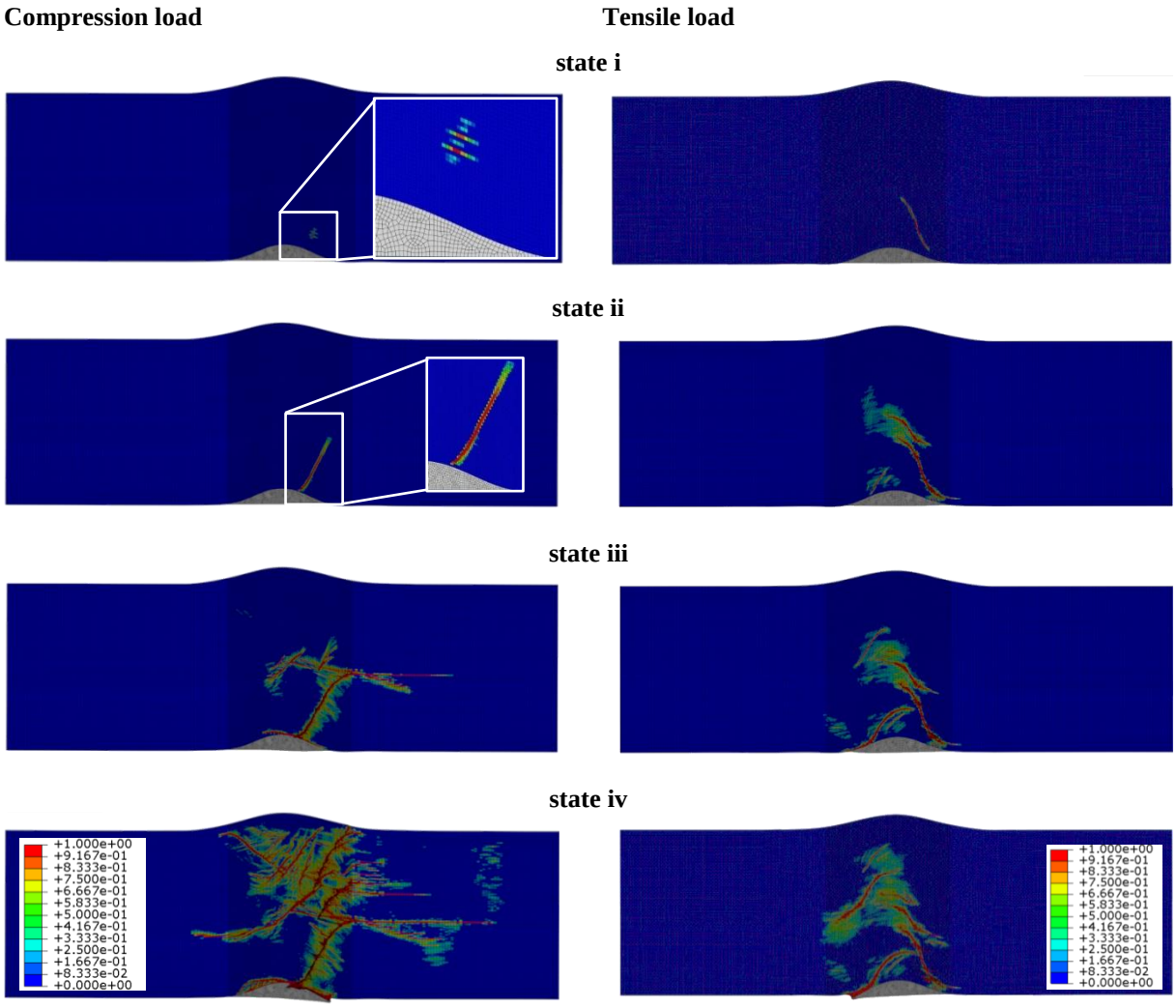

Fig. 5.50: Results of progressive failure analysis under compressive and tensile loads

It is shown that the failure mechanism of thick wavy laminates are strongly location-dependent. Plies containing a more severe inclination are more prone to initial failure. Depending on load type, the failure mode varies. It can also be numerically proven that once a

failure originates, stresses and shears will be redistributed and, hence generate a new initial situation. It is further demonstrated that the failure mechanisms are initiated and driven by a matrix dominated failure event for each load scenario.

6. Conclusion

Latest trends in the process chain of manufacturing WTBs run to a partial automatization of the single fabrication steps such as the *layup* and *finishing*. Although upcoming automation concepts promise savings in labor expenses and handling efforts, those concepts will very likely not be economically important in the near future.

Adjusting the material properties to their structural needs offers the greatest and most innovative potential to decrease the overall CoE.

The herein proposed WTB proposes a conventional and state-of-the-art composite design. While the latest matrix systems are primarily tailored to the manufacturers` needs, it is attempted to develop cost-efficient matrix systems that possess a low viscosity next to a low exothermal energy release rate. Associated therewith, the tuned matrix systems possess dissimilar stiffness and strength properties. These matrix dominated effects on the mechanical properties of a WTB are evaluated. It is noted that the Young`s Moduli of the matrix ranging between 1200MPa and 6000MPa are studied[39]. Following findings are made: The stiffness and stability effects on the blade structure are marginally influenced by the matrix properties. Therein, the thicknesses of the embedded plies and core materials are the crucial materials` parameters. Observing the strength performance of the structure it becomes obvious that the matrix properties play a crucial role. Especially, the dominant occurrence of the failure modes *fiber compression failure* (FF-) and *matrix tension failure* (IFF+) are strongly affected by the matrix properties. It is quantified that the blade`s composite structure is influenced by the matrix properties whenever exposed to shear stresses. Findings carried out on macroscopic level show that matrix systems, which contain slightly adapted matrix properties for manufacturing reasons, can be applied to conventional blade structures without any certain concerns. Referring to the presented findings, the author suggests that newly developing matrix systems should first be adapted to the manufacturing needs. Second, the effects of the matrix systems should be double-checked by the numerical analysis utilizing the workflow described within this work.

The crucial effects of matrix systems on a local level are considered next observing commonly fabrication defects such as ply wavinesses. An analytical method of HSIAO and DANIEL [82] enhanced by the PUCK failure initiation criterion [85] is postulated and incorporated within a MATLAB based GUI in order to assess the material`s strength behavior of wavy composites. The approach enables a quick and qualitative rating of wavy composites for the given geometrical shape and the material data. By using this method it is shown that the composite`s and, thereby, matrix`s shear strength strongly affects the failure initiation in wavy composites.

[39] The Young`s Modulus of commercial epoxy based matrix systems ranges between 2800MPa and 3200MPa.

A continuum damage model is developed to study the critical failure mechanisms in wavy composites numerically. The material user sub-routine takes the nonlinear shear behavior of the composites into account. The strong nonlinearities result in the formation of a kink band. Further, the numerical model is used for the virtual testing of the specimens.

Before experiments are carried out, a wavy specimen`s geometry is developed. The contour is designed for failure mechanisms that have been commonly observed in wavy laminates. Further, a fabrication method is presented to fabricate wavy specimen in a reproducible quality and robust way.

Numerical results validated against the experiments show good correlations. Findings point out that the initial and critical failure mechanisms are driven by matrix failure for both under compression and tensile loads. Under a compression load, the nonlinear shear behavior of the composites dominates the failure behavior that ends up in a kink band formation at regions of maximum shear stresses. Under a tensile load debonding between fiber and matrix is assumed to be the initial fiber mechanisms. A compression load is much more sensitive to wavy composites. In fact, already a very slight waviness causes a significant strength reduction. Herein, a wavy specimen of the amplitude-to-length ratio r=0.05 causes a strength degradation of approx. 60%. Observations are carried out for two matrix systems. They confirm the strong effects of the matrix systems, especially their nonlinear shear behavior.

The findings help to develop novel damage tolerant matrix systems. A high shear strength shall help to postpone the failure initiation in events where 3D stress states occur. Nevertheless, ply waviness can be reduced by the use of automated or robust manufacturing technologies, such as machine draping or tape placment technologies. However, waviness cannot be entirely avoided neither in highly automated manufacturing technologies nor in cost-efficient production lines. Hence, the idea of this work understanding the strength behavior of the material`s constituents in wavy laminates is crucial. Once, the matrix properties that affect the failure mechanisms are designated in detail, adjusted matrix systems can be configured and may diminish and delay the effects of waviness.

While on the macroscopic level the effects of various matrix properties ($2800MPa < E_m < 3200MPa$) are relatively moderate, the research on ply waviness carves out that the failure behavior is initiated and dominated by the matrix properties whenever a 3D stress state is present, e.g. ply drop-offs, voids, delaminations and etc. Thus, considering the trade-off between a cost-efficient material selection and sufficient mechanical properties the following proposal is submitted: The development of a low-cost matrix system for distinct sub-structures of WTBs (*aerody. shells* and *shear webs*) and the development of a damage tolerant matrix system containing a high shear strength for the subcomponent *spar cap*. Damage tolerant matrix systems may permit the manufacturers to allow a certain spectrum of fabrication intolerances. The usage of two distinct matrix systems tailored to the manufacturers` and structure`s needs will further decrease the overall material costs.

7. Outlook

The aforementioned remarks apply to static single and multi-axial load scenarios. The effect of matrix systems on the mechanical properties of WTBs may even increase if the behavior of the composite material under cyclic loadings is considered. As a long-term aim it may also be desired to automate the design process by incorporating the load calculation, the geometrical shape and the materials` selection within a fully automated routine. The herein discussed approach of *a reverse material selection* should also be conducted to other composite structures like automotive and airplane structures.

Having studied the effects of matrix systems on ply waviness, the initial and critical failure mechanisms are incorporated within the numerical model. Further failure mechanisms, such as delamination buckling may also be taken into account within a further improvement of the numerical model.

While the distinct focus within this research was on the matrix systems and GFRP, CFRP should also be experimentally studied in wavy composites. It is assumed that the anisotropic behavior of the fibers even decreases the strength behavior in wavy composites. The follow-up operations should study the effects of ply waviness under fatigue loadings.

Based on the current efforts to fully automatize the production of composite parts combined with a related defect rate, the field of *defects damage mechanics* is gaining in importance. Similar efforts should also be started by analyzing further manufacturing defects, such as voids and delaminations.

A. Appendix

A. Wind turbine blade data

A.1 Virtual plant data

Assumptions are made from compilation of several prevailing literature data [42] [43] [110]:

Tab. A.1: Assumptions for virtual energy plant

General characteristics of WEP	
Power	5MW
Operational area	onshore
Type, number of blades	horizontal, 3 blades
Rotor position	upwind

Operation and power output of WEP		**Dimensions of WEP**	
Wind class	I	Tower height	90m
Rated wind speed	10 m/s	Tower diameter (ground / head)	6m / 5m
Cut in wind speed	3 m/s	Rotor diameter	126m
Cut out wind speed	25 m/s	Tilt angle	5°
Rated speed frequency	11.16 rpm	Cone angle	2.5°
Cut off speed frequency	12.13 rpm	Pre-bending of blade	None
Pitch control	[0°, 90°]	Tower clearance	10.8m

Tab. A.2: Assumptions for wind turbine blade

Structural property	**Units**	**Values**
Natural frequency		
Flap 1	[Hz]	0.79
Flap 2	[Hz]	2.10
Edge 1	[Hz]	1.03
Edge 2	[Hz]	3.41
Tors 1	[Hz]	6.15
Buckling safety (analytical estimation)	[-]	1.8
Blade mass (FE-model)	[t]	26.44
Mass ratio (FE) GFRP – core material	[%]	90 : 10
Mass ratio (FE) PVC - Balsa	[%]	63 : 37
Bonding width web - shell	[mm]	140
Bonding width web - web	[mm]	110
Total blade mass (incl. bonding and matrix uptake)	[t]	27.21

A.2 Material data

Matrix systems

Matrix system [31]	Tension			Bending		Density
	Y. Modulus [GPa]	Strength [MPa]	Strain [%]	Modulus [GPa]	Strength [MPa]	[g/cm³]
Thermosets						
EPOXY	[2.8; 3.4]	[45; 85]	[1.3; 5.0]	[2.6; 3.6]	[100; 130]	>1.16
Unsat. POLYESTER	[2.8; 3.5]	[40; 75]	[1.3; 3.3]	[3.4; 3.8]	[80; 130]	[1.25; 1.30]
VINYLESTER	[2.9; 3.1]	~ 80	[3.0; 3.7]	[3.0; 3.7]	[120; 140]	~1.1
Thermoplastics						
POLYPROPYLENE (PP)	[1.3; 1.8]	[30; 40]	>50	[1.1; 1.6]	~30	[0.90; 0.91]
POLYETHYLEN-TEREPHTHALAT (PET)	[2.8; 3.5]	[55; 80]	>20	~2.3	~90	[1.38; 1.4]
POLYPHENYLEN-SULFID (PPS)	[3.3; 3.5]	[70; 110]	1.5	[3.5; 3.8]	[100; 140]	[1.30; 1.35]
POLYETHEREHTER-KETON (PEEK)	[3.5; 3.8]	[90; 105]	>50	>50	~150	1.32

Foam core materials

a) Foam core stiffness properties (PVC)

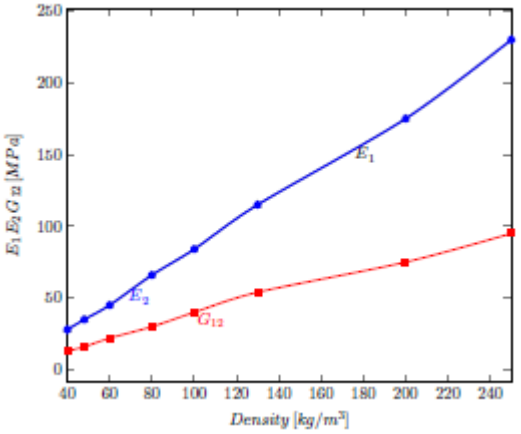

b) Foam core strength properties (PVC)

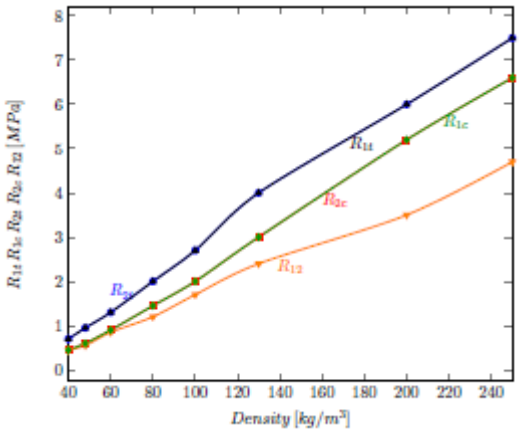

c) Balsa core stiffness properties

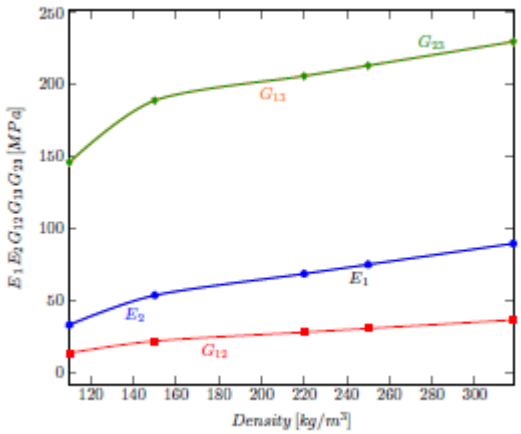

d) Balsa core strength properties

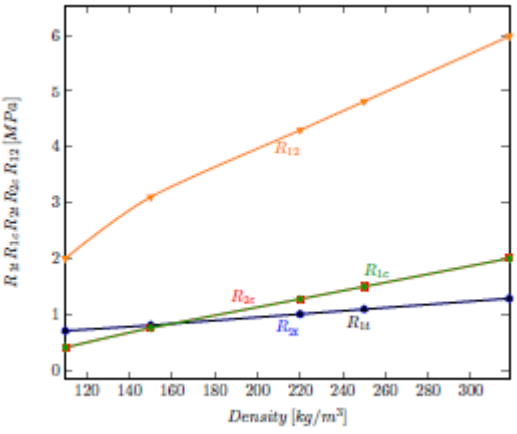

B. Appendix

B. Ply waviness data

B.1 Specimen

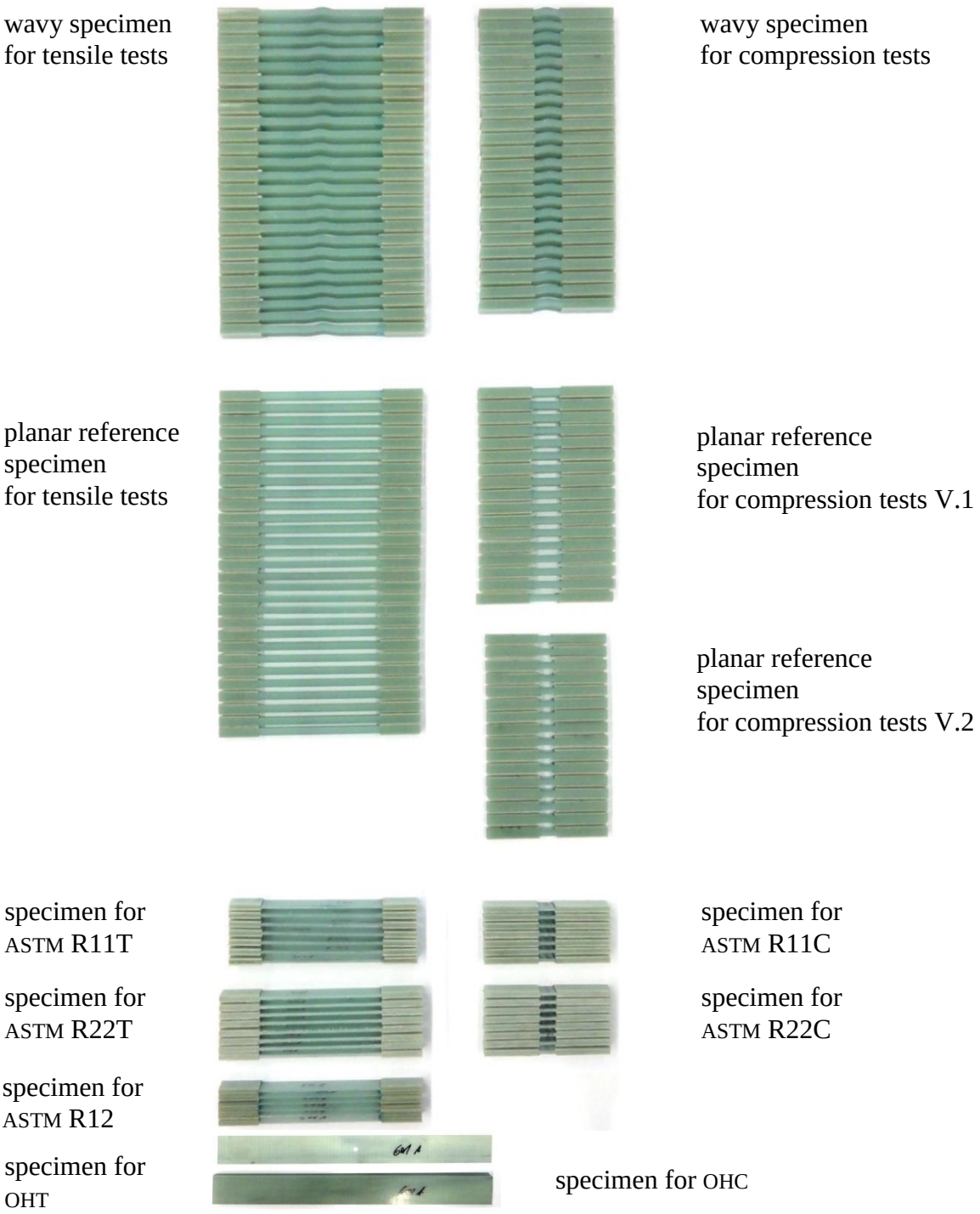

Fig. B1 Specimen of test series A

B.2 Blade`s cross-section with several defects

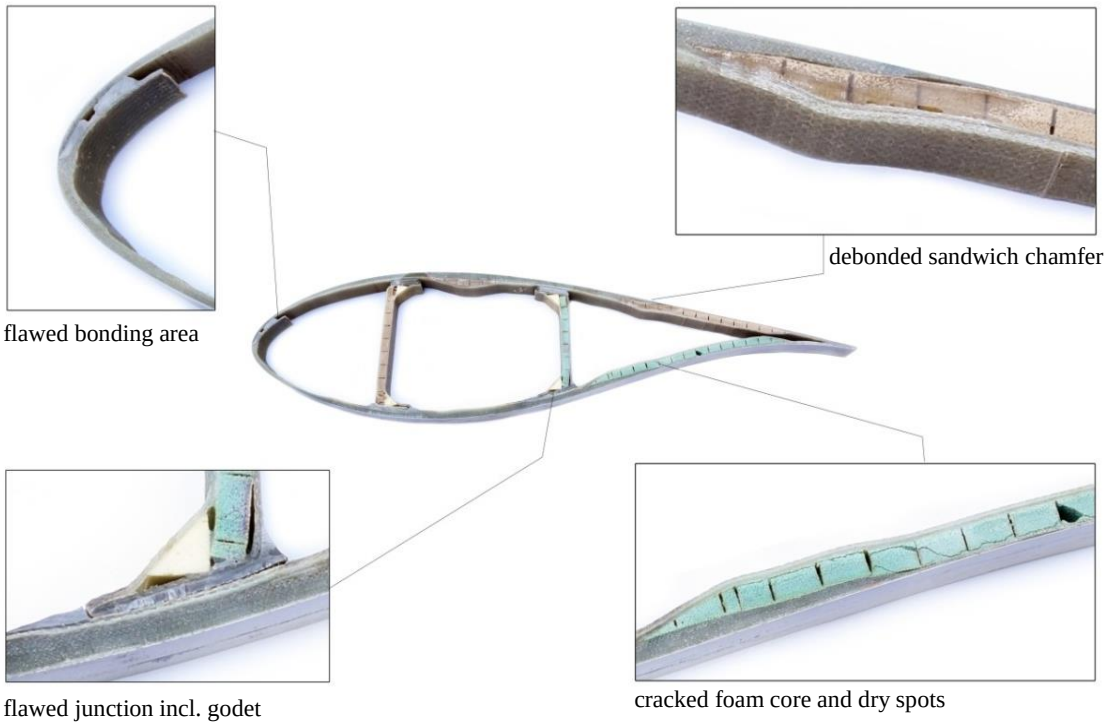

Fig. B2. Cross-section of a WTB with several defects

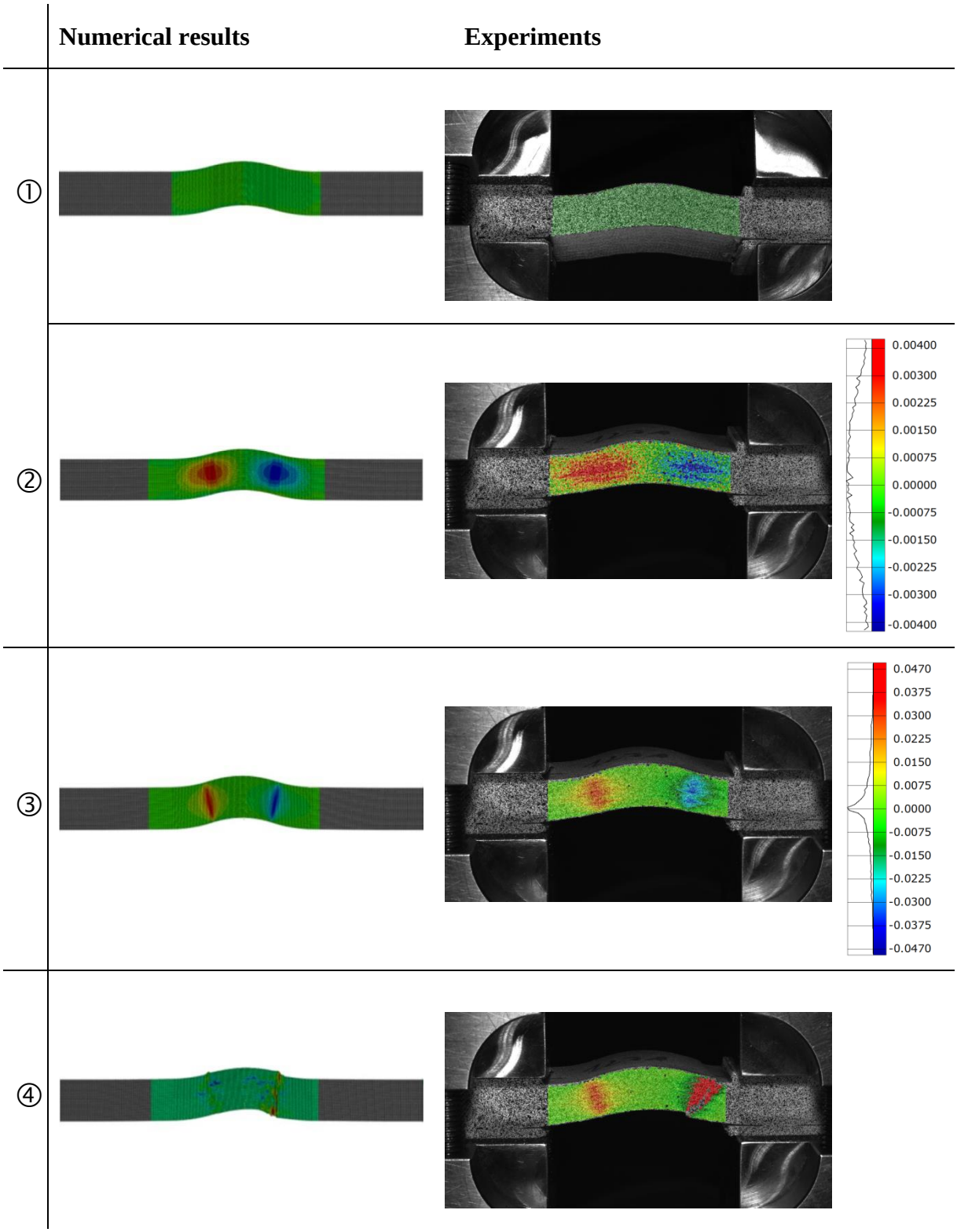

Fig. B3. Numerical results and experiments indicated by DIC

C. Appendix

C. Publications, supervised student theses and lectures

C.1 Publications

Journal Papers and Conference Papers

- ALTMANN A., GESELL P., DRECHSLER K.: Strength prediction of ply waviness in composite materials considering matrix dominated effects, Journal of Composite Structures, Composite Structures 127 (2015) 51–59.
- ALTMANN A., TAUBERT R., MANDEL U., HINTERHOELZL R., DRECHSLER K.: A Continuum Damage Model to predict the Influence of Ply Waviness on Stiffness and Strength in ultra-thick unidirectional FRPs, Journal of Composite Materials (submitted).
- ALTMANN A., TAUBERT R., MANDEL U., IGERZ S., HINTERHÖLZL R., DRECHSLER K., Strength prediction of wavy composites considering matrix dominated effects; Nafems Proceedings, Leipzig, 2014.
- ALTMANN A., TAUBERT R., MANDEL U., HINTERHÖLZL R., DRECHSLER K., A continuum damage model for strength prediction of ply waviness in ultra-thick laminates considering matrix dominated effects; Sampe Setec, Tampere, 2014.
- ALTMANN A., RUCKERBAUER R, ZAREMBA S, HINTERHOELZL R, DRECHSLER K. Novel injection process of long fiber material using rotation; Montreal ICCM19, 2013.

Patent

ALTMANN A., ZAREMBA S., Injection method for fiber reinforced composites, PCT/EP 2013/003299, 2014.

Publications and speeches

- ALTMANN A., HINTERHÖLZL R., DRECHSLER K., Strength prediction of ply waviness in composite materials considering matrix dominated properties, Fürstenfeldbruck 2015, Tuev Sued GFK Unlimited, 2015.
- HINTERHÖLZL R., ALTMANN A., HÖRMANN P., HALLER H., Mechanical Behavior of Composites Considering Manufacturing Effects, ESI Expert Seminar, Stuttgart 2015.
- ALTMANN A., IGERZ S., HINTERHÖLZL R., DRECHSLER K., Strength prediction of wavy composites considering matrix dominated properties, Nafems user conference, Leipzig, 2014.
- ALTMANN A., TAUBERT R., MANDEL U., HINTERHÖLZL R., DRECHSLER K., A continuum damage model considering ply waviness, Setec Sampe, Tampere, Finland, 2014.
- ALTMANN A., ZAREMBA S., Herstellverfahren von Karbonbauteilen mittels Rotation, Bayerischer Patentkongress 2013 (speech and poster presentation), München 2013.
- ALTMANN A., RUCKERBAUER R., ZAREMBA S., HINTERHÖLZL R., DRECHSLER K., Novel injection process of long fiber material using rotation. Proceedings of ICCM19, Montreal, 2013.

- ALTMANN A., ZAREMBA S., Neues Verfahren zur Tränkung und Aushärtung von Faserverbundstrukturen mittels Rotation. CCeV-Konferenz, Materials and process technologies, Donauwörth, 2013.
- ALTMANN A., DRECHSLER K., GROßE C., Introduction of the Institutes LCC and ZFP and presentation of current composite research topics, Bayern Innovativ, Garching, 2012.
- ALTMANN A., DRECHSLER K., New materials and design studies of wind turbine blades. Keynote lecture, Haus der Technik, Essen, 2011.
- DRECHSLER K., HEUMÜLLER R., DAUN G., New materials of wind turbine blades. WindChina 2011, Shanghai, 2011.
- MENDLER J., ALTMANN A., Structural design optimization of wind turbine rotor blades considering manufacturing costs, Conference on wind turbine blades, Düsseldorf, 2010.
- KATZENSCHWANTZ C., ALTMANN A., Optimization of a composite structure. Altair User Conference, Zürich, 2009.

C.2 Supervised student theses

[S1] MATHIS L., Investigation of individual blade adjustment and its possibilities for load reduction in wind turbines, semester thesis, 2011.

[S2] BLAISE F., Sensitivity analysis of bend-twist couplings on wind turbine blades, semester thesis, 2011.

[S3] TRAUB P., Design of the frame connection for a CFRP cargo floor structure, diploma thesis, 2011.

[S4] STAKELIES M., Finite element simulation and evaluation of manufacturing and operation related damages to wind turbine blades, diploma thesis in coop. with TUEV SUED, 2011.

[S5] SKREINIG H., Development and testing of an optimal CFRP space frame joint for large-scale applications considering structural characteristics and manufacturability, diploma thesis in coop. with SGL ROTEC, 2011.

[S6] SCHÄFER M., Integration of PUCK'S action-plane-related failure criterion as sub-routine for ABAQUS validated on a rotor blade section, semester thesis, 2012.

[S7] BOTZ M., GFRP-/CFRP hybrid design in rotor blades using analytical optimization methods, bachelor thesis, 2012.

[S8] SCHNEIDER D., Investigations into the assessment of the mechanical response of honeycomb sandwich structures to applied transverse static and dynamic loads, diploma thesis in coop. with AIRBUS, 2012.

[S9] KAETHER S., Development of a process chain for the structural optimization of composite materials in motor sport applications, diploma thesis in coop. with AUDI AG; 2012.

[S10] VOLLMER M., Implementation and validation of a pressure distribution upon a wind turbine blade, semester thesis, 2013.

[S11] RUCKERBAUER R., Design of a tools for an injection process using rotational forces, master thesis, 2013.

[S12] GLASER M., Composition and realization of material parameter studies regarding various materials in wind turbine blades, master thesis, 2013.

[S13] GESELL P., Stiffness and strength analysis of fiber waviness, semester thesis, 2013.
[S14] ALLOUN D., Programming of interfaces to transfer loads from a multi-body-simulation to a finite element method, master thesis in coop. with ACENTISS GMBH, 2013.
[S15] VORBERG C., Methods of characterization of matrix systems for wind turbine blade structures, semester thesis, 2013.
[S16] WIDMAIER M., Conceptional lightweight design with fiber-reinforced thermoplastics and integrated body shell mounting, diploma thesis in coop. with BMW GROUP, 2013.
[S17] TEBBE L., Injection process for composite parts by means of rotation – material characterization and implementation of a fill-level-sensor-system, bachelor thesis, 2013.
[S18] HECKEL C., Injection procedure of composite structures using rotation: parameter studies and implementation of a new resin feed, bachelor thesis, 2013.
[S19] LANZ A., Development and implementation of a routine to perform parametric studies and sensitivity analyses of a wind turbine blade FE model, master thesis, 2014.
[S20] IGERZ S., Experimental study on wavy specimen, bachelor thesis, 2014.
[S21] GESELL P., Numerical analysis on wavy composites using a multi-scale approach, 2014.
[S22] SASSL F., Modular rotor blade section, master thesis in coop. with GE GLOBAL RESEARCH, 2014.

C.3 Lectures at Faculty of Mechanical Engineering at Technische Universität München

- DRECHSLER K., HINTERHÖLZL R., HAHN C., ALTMANN A., Advanced mechanics of composite materials, Notes of the lecture "Analysis and design of composite materials", pages 40-55, 2010.
- DRECHSLER K., HINTERHÖLZL R., LEUTZ D., ALTMANN A., Joining technology, Notes of lecture "Analysis and design of composite materials", pages 4-56, 2010.
- DRECHSLER K., HINTERHÖLZL R., ALTMANN A., Analysis and design of sandwich structures, Notes of lecture "Analysis and design of composite materials", pages 1-44, 2010.
- DRECHSLER K., HINTERHÖLZL R., ALTMANN A., BRAND M., Composite structural design. Notes of lecture "Analysis and design of composite materials", pages 1-79, 2010.
- DRECHSLER K., HINTERHÖLZL R., KÖRBER H., ALTMANN A., Testing of composite materials, Notes of lecture "Analysis and design of composite materials", pages 1-37, 2010.
- DRECHSLER K., HINTERHÖLZL R., ALTMANN A., Damage tolerant design and repair, Notes of lecture "Analysis and design of composite materials", pages 1-39, 2010.
- DRECHSLER K., HINTERHÖLZL R., ALTMANN A., Fatigue of composites, Notes of lecture "Analysis and design of composite materials", pages 1-39, 2010.
- DRECHSLER K., ALTMANN A., FRÖHLICH F., FRÖHLICH P., Composites in wind energy applications, Notes of practical course "Materials and process technologies for carbon composites", pages 1-84, 2011.
- DRECHSLER K., LEUTZ D., ALTMANN A., LICHTINGER R., Mechanical Joining, Notes of practical course "Simulation of composite materials", 2011.

Bibliography

[1] B. Walsh, "The challenges of America's energy revolution," *Time Magazine,* p. 26, 28 10 2013.

[2] M. Vollmer, Implementation and validation of a pressure distribution upon a wind turbine blade, München: Institute for Carbon Composites, TU München, 2013.

[3] J. Nelson, T. Riddle and D. Cairns, Effects of defects in composite wind turbine blades round 1, Albuquerque: Sandia National Laboratories, 2012.

[4] M. Hsiao and M. Daniel, "Elastic properties of composites with fiber waviness," *Composite Part A,* pp. 27:931-941, 1996.

[5] A. Altmann, Bauweisenkonzept und numerische Simulation von Rotorblättern in der Windenergie unter Berücksichtigung spezieller Fertigungsverfahren, Ottobrunn: Institute for Carbon Composites, TU München, 2010.

[6] F. Sassl, Wind rotor blade joint concept comparison and subarticle development, München: Institute for Carbon Composites, TU München, 2014.

[7] A. Betz, Wind-Energie und ihre Ausnutzung durch Windmühlen, Göttingen: Ökobuch Verlag Vandenhoeck & Ruprecht, 1926.

[8] P. Jamieson, Innovation in wind turbine design, Chichester: Wiley & Sons Ltd, 2011.

[9] I. Philipson, Rotor design at Suzlon, Delft: TU Delft, 2011.

[10] E. Hau, Windkraftanlagen: Grundlagen, Technik, Einsatz, Wirtschaftlichkeit, Berlin: Springer Verlag, 2003.

[11] R. Gasch, J. Twele and P. Bade, Windkraftanlagen. Grundlagen, Entwurf, Planung und Betrieb, Wiesbaden: Vieweg und Teubner, 2010.

[12] Y. Golfman, Hybrid anisotropic material for wind power turbine blades, CRC Press Taylor & Francis Group, 2012.

[13] J. Manwell, J. McGowan and A. Rogers, Wind energy explained theory design and application, Cichester: Wiley, 2009.

[14] B. Eyb, "Berechnung und Verifikation der Ermuedung von Rotorblättern," in *CCeV-Conference,* Augsburg, 2013.

[15] S. Connors, "MIT Copyright Technology Review," 2006. [Online]. Available: http://www2.technologyreview.com/player/06/05/09Bullis/1.aspx.

[16] DNV, Guideline for design of wind turbines, Risø, 2002.

[17] F. Jensen, "Ultimate strength of a large wind turbine blade," PhD. Dissertation, Risø National Laboratory for Sustainable Energy, Risø , 2008.

[18] R. Seehase, Wind industry: globalization and cost pressure - demands towards suppliers, Bremen: IQPC, 2012.

[19] L. Weigel, Ways to manufacture rotor blades, Bremen: IQPC, 2012.

[20] G. Daun, "Schaltbare Haerter verbessern Rotorfertigung," *Kunststoffe*, pp. 74-77, 2009.

[21] K. Drechsler, G. Daun, R. Heumüller and A. Altmann, Selection of materials for offshore blades, Shanghai, China, 2011.

[22] J. Bhatia, Advanced material solutions for infusing carbon fibers and thick composite parts, 2012.

[23] R. Meier and A. Altmann, Rheological measurements at LCC, München: Institute for Carbon Composites, TU München, 2014.

[24] J. Mendler, C. Katzenschwanz and A. Altmann, Structural design optimization of WTB considering manufacturing costs, Düsseldorf: WTB conference, 2010.

[25] L. Forcier and S. Joncas, "Development of a structural optimization strategy for the design of next generation large thermoplastic wind turbine blades," *Journal of Structural and Multidisciplinary Optimization,* p. 45:889–906, 2011.

[26] K.-P. Jaquemotte, Personal communications, Bremen: SGL Rotec, 2011.

[27] H. Friedmann, Zustandsueberwachung im Fertigungsprozess und im Betrieb, Garching: Bayern Innoviatv Forum, 2012.

[28] M. Flemming and G. Ziegmann, Fertigungsverfahren mit duroplastischer Matrix, Berlin: Springer, 1999.

[29] H. Schürmann, Konstruieren mit Faser-Kunststoff-Verbunden, Berlin, Heidelberg: Springer, 2007.

[30] H. Baier, "Faserverbundwerkstoffe," in *Lecture Notes*, München, Institute for

Leightweight Structures, Technische Universität München, 2012.

[31] M. Neitzel and P. Mitschang, Handbuch Verbundwerkstoffe, Kaiserslautern/München: Hanser Verlag, 2004.

[32] SGL Rotec, "Production line of WTB," Lemswerder, 2010.

[33] A. Altmann, P. Fröhlich and F. Fröhlich, "Composites in wind energy applications," *Practical training,* 2011.

[34] I. Philipson, "Rotor design at Suzlon," 2011.

[35] P. Ermanni, "Aerospace structures," in *lecture notes*, IMES-ST, ETH Zuerich, 2008.

[36] F. Huerlimann, "Mass estimation of transport aircraft wingbox structures with a CAD/CAE based multidiscilpinary process," PhD. Dissertation, ETH Zuerich, 2010.

[37] M. Glaser, FE-Rotorblattauslegung für Windkraftanlagen und Sensitivitätsstudien zum Einfluss der Matrix- und Kernwerkstoffkennwerte auf die Struktureigenschaften, München: Institute for Carbon Composites, TU München, 2013.

[38] Abaqus, User manual Dassault Systemes, 2011.

[39] C. Bottasso, Interviewee, *GE/TUM Symposium.* [Interview]. 27 06 2013.

[40] M. Botz, GFRP/CFRP hybrid design in rotor blades using analytical optimization methods, München: Institute for Carbon Composites, TU München, 2012.

[41] D. Alloun, C. Katzenschwanz and W. Kurz, Optimization of the design process for wind turbine blades, Ottobrunn: Institute for Carbon Composites, TU Munich, 2013.

[42] P. Klausmann, W. Heydlauff, S. Kleinhansl and M. Mayer, Rotorblatt-Strukturentwicklung für eine Windenergieanlage, Neuhausen: Aero Dynamik Consult, 2011.

[43] J. Jonkman, S. Butterfield, W. Musial and S. Scott, 5MW Reference Turbine NREL, 2009.

[44] F. Blaise, Sensitivity analysis of bend twist couplings on wind turbine blades, München: Institute for Carbon Composites, TU München, 2011.

[45] Matrix system research group BASF AG, 2014.

[46] D. Montgomery, "Design and analysis of experiments," vol. International student

version, no. 7th edition, 2009.

[47] A. Lanz, "Development and implementation of a routine to perform parametric studies and sensitivity analyses of a wind turbine blade FE model," *Master Thesis*, 2014.

[48] H. Baier, "Multidisciplinary Design Optimization," in *Lecture Notes*, München, Lehrstuhl für Leichtbau, Technische Universität München, 2013.

[49] Z. Hashin, "Failure criteria for unidirectional fiber composites," *Journal of Applied Mechanics*, no. 47:329-334, 1980.

[50] D. Griffin, Evaluation of design concepts - design adaptive blades, Albuquerque: Sandia National Laboratories, 2002.

[51] J. Locke and U. Valencia, Twist coupled blades, Wichita: Wichita State University, National Institute for Aviation Research, 2004.

[52] M. Dugas, "A contribution towards the preliminary analysis and design of a composite wing," PhD. Dissertation, Institut fuer Flugzeugbau, Stuttgart, 2002.

[53] A. Altmann and K. Drechsler, "Latest wind energy related research topics at LCC," *Bayern Innovativ, Garching*, 2012.

[54] L. Zhuang and R. Talreja, Effects of voids on postbuckling delamination growth in unidirectional composites, 2013.

[55] J. F. Mandell, D. D. Samborsky and L. Wang, Effects of fiber waviness on composites for wind turbine blades, Montana: Montana State University, Department of Chemical Engineering, 2003.

[56] C. Bottasso, "Wavy spar cap laminate," München, Wind Energy Institute, Technische Universität München, 2014.

[57] A. Caiazzo, M. Orlet, H. McShane, L. Strait and C. Rachau, "The Effects of Marcel Defects on Composite Structural Properties," *Composite Structures*, 2000.

[58] J. Nelson, T. Riddle and D. Cairns, Effects of defects in composite wind turbine blades: round 2, Montana: Montana State University, 2012.

[59] B. Budiansky and N. Fleck, "Compressive kinking of fiber composites," *Journal of Mechanics and Physics of Solids*, no. 41:183-211, 1993.

[60] M. Garnich and G. Karami, Finite element micromechanics for stiffness and strength of wavy fiber composites, 2004.

[61] R. Talreja, Personal communications, 2014.

[62] T. Bogetti, J. Gillespie and M. Lamontia, "The influence of ply waviness with nonlinear shear on the stiffness and strength reduction of composite laminates," *Army Research Laboratory,* 1994.

[63] P. Jelf and N. Fleck, "Compression failure mechanisms in unidirectional composites," *Journal of composite materials ,* no. 26:2706-2726, 1992.

[64] K. Niu and R. Talreja, "Modeling of compressive failure in fiber reinforced composites," *International Journal of Solids and Strcutures,* pp. 37:2405-2428, 2000.

[65] T. Vogler, S. Hsu and S. Kyriakides, "Composite failure under combined compression and shear," *International Journal of Solids and Structures ,* pp. 37:1765-1791, 1998.

[66] H. Chai, C. Babcock and W. Knauss, "One dimensional modeling of failure in laminated plates by delamination buckling," *International Journal of Solids and Structures,* pp. 17:1069-1083, 1981.

[67] W. Slaughter and N. Fleck, "Microbuckling of fiber composites with random initial fiber waviness," *Jounral of Mechanical Physical Solids,* no. 42:1743-1766, 1994.

[68] P. Davidson and A. Waas, Effects of fiber waviness on the compressive strength of uni-directional carbon fiber composites, University of Michigan AiAA, 2012.

[69] S. Lemanski, J. Wang, M. Sutcliffe, K. Potter and M. Wisnom, "Modeling failure of composites specimens with defects under compression loading," *Comspostes Part A,* pp. 48:26-36, 2013.

[70] I. Daniel, J. Luo, P. Schubel and B. Werner, "Interfiber/interlaminar failure of composites under multi-axial states of stress," *Composite Science and Technology,* pp. 69:764-771, 2009.

[71] S. Pinho, L. Iannucci and P. Robinson, "Physically-based failure models and criteria for laminated fibre-reinforced composites with emphasis on fibre kinking: Part I development composites," *Composites Part A,* p. 37:63–73, 2005.

[72] S. Pinho, L. Iannucci and P. Robinson, "Physically-based failure models and criteria for laminated fibre-reinforced composites with emphasis on fibre kinking: Part II FE implementation," p. 37:766–777, 2005.

[73] S. Lee, C. Yerramalli and A. Waas, "Compressive splitting response of glass-fiber reinforced unidirectional composites," *Composites Science and Technology,* pp.

60:2957-2966, 2000.

[74] S. Basu, A. Waas and D. Ambur, "A macroscopic model for kink banding instabilities in fiber composites," *Mechanics of Materials and Structures,* pp. 1,6:979-1000, 2006.

[75] C. Schultheisz and A. Waas, "Compressive failure of composites. Part I: Testing and micromechanical theories," *Progress in Aerospace Sciences,* pp. 32:1-42, 1996.

[76] S. Lee and A. Waas, "Compressive response and failure of fiber reinforced unidirectional composites," *International Journal of Fracture,* pp. 100:275-306, 1999.

[77] L. Asp, A. Berglund and R. Talreja, "A criterion for crack initiation in glassy polymers subjected to a composite like stress state," *Composite Science and Technology,* pp. 56:1291-1301, 1996.

[78] I. Asp, A. Berglund and R. Talreja, "Prediction of matrix initiated transverse failure in polymer composites," *Composite science and technology,* pp. 56:1089-1097, 1996.

[79] G. Karami and M. Garnich, "Effective moduli and failure considerations for composites with periodic fiber waviness," *Composite Structures,* p. 67:461–475, 2004.

[80] M. Nedele and M. Wisnom, "Three-dimensional finite element analysis of the stress concentration at a single fibre break," *Composite Science and Technology,* pp. 53:517-524, 1994.

[81] P. Gesell, Effects of fiber waviness on stiffness and strength behavior of composite materials, München: Institute for Carbon Composites, TU München, 2013.

[82] H. M. Hsiao and I. M. Daniel, "Effect of fiber waviness on stiffness and strength reduction of unidirectional composites under compressive loading," *Composites Science and Technology,* no. 56(5):581–93., 1996.

[83] T. Ishikawa and T. Chou, "Nonlinear Behavior of Woven Fabric Composites," *Journal of Composite Materials,* no. 17(5):399–41, 1983.

[84] R. Horn and C. Johnson, "Matrix analysis. 2nd ed," *New York Cambridge University Press,* 2013.

[85] Verein Deutscher Ingenieure, Entwicklung von Bauteilen aus Faser-Kunststoff-Verbund - Berechnungen (VDI 2014, Blatt 3), 2006.

[86] H. Rai, E. Honein, R. Dibo and P. Ayoub, "The influence of fiber waviness on the critical buckling load of multilayered composites," *28th Risø International Symposium on Materials Science.*

[87] H. Rai, C. Rogers and D. Crane, "Mechanics of Curved Fiber Composites," *Journal of Reinforced Plastics and Composites,* no. 11(5):552–66, 1992.

[88] H. Chun, J. Shin and I. Daniel, "Effects of material and geometric nonlinearities on the tensile and compressive behavior of composite materials with fiber waviness," *Composites Science and Technology 2001,* no. 61(1):125–34, 2001.

[89] A. Altmann, R. Taubert, U. Mandel, R. Hinterhoelzl and K. Drechsler, A continuum damage model for strength prediction of ply waviness in ultra-thick laminates considering matrix dominated effects, Tampere, Finland: Setec SAMPE, 2014.

[90] T. Bogetti, J. Gillespie and M. Lamontia, "The influence of ply waviness with nonlinear shear," no. Army Research Laboratory, 1994.

[91] VDI2014, Development of FRP components Part 3, Düsseldorf, 2006.

[92] J. Lemaitre, "A course on damage mechanics," *Second Ed.,* vol. Springer, 1996.

[93] Z. Bazant and B. Oh, "Crack band theory for fracture of concrete," *Materials and Structures,* no. 16:155-177, 1983.

[94] M. Wisnom, The role of scaled tests in evaluating models of failure, University of Bristol, 2011.

[95] S. Pimenta, R. Gutkin, S. Pinho and P. Robinson, "A micromechanical model for kink band formation - Part I Experimental study and numerical modelling," 2009.

[96] P. Duangmuan, "Layer waviness effects on compression strength of composite laminates: Progressive failure analysis and experimental validation," PhD. Dissertation, University of Utah, Utah, 2012.

[97] B. Khan, K. Potter and M. Wisnom, "Simulation of process induced defects in resin transfer molded woven carbon fiber laminates and their effect on mechanical behavior," *FPCM8,* 2006.

[98] A. Altmann, R. Ruckerbauer, S. Zaremba, R. Hinterhoelzl and K. Drechsler, "A novel injection method for long fiber composites using rotation," in *ICCM19,* Montreal, 2013.

[99] J. Wang, K. Potter, K. Hazra and M. Wisnom, "Experimental fabrication and characterization of out-of-plane fiber waviness in continuous fiber-reinforced composites," *Journal of Composite Materials,* pp. 46:2041-2053, 2012.

[100] P. Kuhn and F. Hillreiner, Application of load tabs on CFRP, Garching: Institute for

Carbon Composites TU München, 2013.

[101] J. Serrano, "Composite materials for wind blade curent performance and future directions," *Wind Turbine Blade Workshop,* vol. Sandia National Laboraties, no. 2010.

[102] B. Plank, "Computer tomography," *FH oÖ F&E GmbH Wels Austria,* 2014.

[103] A. Waas and C. Schultheisz, "Compressive failure of composites part II experimental studies," *Progress in Aerospace Sciences,* pp. 32:43-78, 1996.

[104] ASTM International, "Standard Test Method for Tensile Properties of Polymer Matrix Composite Materials," no. 5th ed(ASTM-D-3039D-3039M), 2002.

[105] ASTM International, "Standard Test Method for Compressive Properties of Polymer Matrix Composite Materials using a combined loading compression (CLC) Test Fixture," no. 9th ed.(ASTM-D-3039DM), 2002.

[106] I. Asp, A. Berglund and R. Talreja, "Prediction of matrix initiated transverse failure in polymer composites," *Composite science and technology,* no. 56:1089-1097, 1996.

[107] P. Joyce, D. Kugler and T. Moon, "A technique for characterizing process-induced fiber waviness in unidirectional composite laminates using optical microsopy," *Journal of Composite Materials,* pp. 31:1694-1727, 1996.

[108] F. Schmidt, M. Rheinfurt, P. Horst and G. Busse, "Effects of local fibre waviness on damage mechanisms and fatigue behaviour," *Composites science and technology,* no. 72:1075-1082, 2012.

[109] K. Drechsler and R. Hinterhoelzl, "Lecture nodes of Analysis and design of composite structures," in *lecture notes,* München, Institute for Carbon Composites, Technische Universität München, 2013.

[110] Senvion AG, "5M Wind energy plant," [Online]. Available: http://www.repower.de/de/wind-power-solutions/windenergieanlagen/5m. [Accessed 15 5 2013].

[111] M. Jorkhof, TUM/GE Symposium, 2013.

[112] "Windkraft Journal," [Online]. Available: http://www.windkraft-journal.de/2012/01/12/20-mw-offshore-windanlagen-sollen-schon-bald-in-den-meeren-stehen/. [Accessed 22 04 2014].